# Numerical Modeling of River Ice Processes on the Lower Nelson River

by

**Jarrod Joseph Malenchak**

A thesis submitted to the Faculty of Graduate Studies in

partial fulfillment of the requirements for the degree of

**Doctor of Philosophy**

Department of Civil Engineering
University of Manitoba
Winnipeg, Manitoba, Canada

# Abstract

Water resource infrastructure in cold regions of the world can be significantly impacted by the existence of river ice. Major engineering concerns related to river ice include ice jam flooding, the design and operation of hydropower facilities and other hydraulic structures, water supplies, as well as ecological, environmental, and morphological effects. The use of numerical simulation models has been identified as one of the most efficient means by which river ice processes can be studied and the effects of river ice be evaluated. The continued advancement of these simulation models will help to develop new theories and evaluate potential mitigation alternatives for these ice issues.

In this thesis, a literature review of existing river ice numerical models, of anchor ice formation and modeling studies, and of aufeis formation and modeling studies is conducted. A high level summary of the two-dimensional CRISSP numerical model is presented as well as the developed freeze-up model with a focus specifically on the anchor ice and aufeis growth processes. This model includes development in the detailed heat transfer calculations, an improved surface ice mass exchange model which includes the rapids entrainment process, and an improved dry bed treatment model along with the expanded anchor ice and aufeis growth model (Chapter 3). The developed sub-models are tested in an ideal channel setting as somewhat of a model confirmation. A case study of significant anchor ice and aufeis growth on the Nelson River in northern Manitoba, Canada, will be the primary field test case for the anchor ice and aufeis model. A second case study on the same river will be used to evaluate the surface ice components of the

model in a field setting. The results from these cases studies will be used to highlight the capabilities and deficiencies in the numerical model and to identify areas of further research and model development.

# Acknowledgments

I would like to acknowledge the generous funding for this research provided by Manitoba Hydro, the Manitoba Graduate Scholarship program, and the Natural Sciences and Engineering Research Council of Canada, without which this research would not have been possible.

The guidance and direction of my thesis advisor Dr. Jay Doering, as well as the academic input provided by Dr. Hung Tao Shen of Clarkson University, have been extremely helpful.

I would like to acknowledge the input and support of the Manitoba Hydro line advocates for this project, Mike Morris, Efrem Teklemariam, and Bernard Shumilak.

My friends and colleagues at the University of Manitoba and Clarkson University. They have been the source of many insightful discussions and have helped make this experience most enjoyable.

My wife Tara, whose patience and support allowed me to commit the necessary time and effort to complete this thesis.

# Table of Contents

# List of Figures

# List of Tables

# Nomenclature

| Symbol | Units | Description |
|---|---|---|
| $a_0$ | [$m^2$] | surface area of a frazil particle normal to the a-axis |
| $A_N$ | [$m^2$] | contributing area of all elements surrounding a node |
| $A_p$ | [$m^2$] | ice parcel area |
| $\alpha$ | | probability of deposition of frazil ice particles reaching the river surface |
| $\alpha_b$ | | fraction of total water depth affected by bed friction |
| $\alpha_{ia}$ | [$W/m^2$] | constant for linear ice growth calculations |
| $\beta$ | [1/s] | re-entrainment rate of frazil ice at the river surface |
| $\beta_2$ | | deposition coefficient of frazil ice to river bed (Tsang, 1988) |
| $\beta_3$ | | deposition coefficient of frazil to river bed (Qu, 2006) |
| b | | wind fetch coefficient for dynamic border ice formation |
| $\beta_R$ | | fraction of solar radiation absorbed in the initial depth of water ($D_{ext}$) |
| C | | suspended frazil ice concentration |
| $C_a$ | | surface ice concentration |
| $C_c$ | [$1/10^{ths}$] | cloud cover |
| $c_f$ | | friction coefficient |
| $C_m$ | | area concentration of the $m^{th}$ bed particle size |
| $C_{nai}$ | | linear reduction factor for Manning's roughness due to anchor ice |
| $c_{ohb}$ | [$N/m^2$] | inter-particle resistance (bed particles) |

| | | |
|---|---|---|
| CV | | coefficient of variation |
| $C_v$ | | depth-averaged volumetric suspended frazil concentration |
| $C_v^{ent}$ | | portion of suspended frazil concentration attributed to rapids entrainment |
| $C_v^{g}$ | | portion of suspended frazil concentration attributed to thermal growth |
| $c_{wi}$ | | constant used for calculating heat transfer coefficient |
| DDF | [ºC-days] | degree-days freezing |
| $d_1$ | [m] | total thickness of surface ice layer for solar radiation extinction calculations |
| $d_2$ | [m] | water depth used in the solar radiation extinction calculations |
| $d_3$ | [m] | anchor ice thickness used in the solar radiation extinction calculations |
| $d_e$ | [m] | frazil disc thickness |
| $D_{ext}$ | [m] | initial depth used in solar radiation extinction calculations |
| $d_f$ | [m] | frazil disc diameter |
| $d_n$ | [m] | nominal diameter of undercover ice particles |
| $d_s$ | [m] | diameter of top layer of bed material |
| $d_w$ | [m] | water depth |
| $D_h$ | [m] | local hydraulic diameter |
| $D_{x,m}$ | [m] | bed particle diameter in the streamwise direction |
| $D_{y,m}$ | [m] | bed particle diameter in the vertical direction |
| $\Delta H_{cr}$ | [m] | critical water surface elevation change for ice breakup |
| $\Delta M_{ent}$ | [kg] | ice mass entrained at the rapids section |

| | | |
|---|---|---|
| $\Delta M_{ow}$ | [kg] | ice mass exchange with the open water area |
| $\Delta M_i$ | [kg/m$^2$] | total ice mass exchange per unit area |
| $\Delta M_{ic}$ | [kg] | ice mass exchange with ice covered area |
| $\Delta t_h$ | [s] | hydrodynamic time step |
| $\Delta t_i$ | [s] | ice dynamic time step |
| $\Delta_{tr}$ | [m] | hourly tailrace staging at the Limestone GS |
| $\eta_{e,m}$ | | deposition efficiency for the m$^{th}$ particle size |
| e | | generating unit efficiency |
| $e_a$ | | porosity of anchor ice |
| $e_{at}$ | [kpa] | vapour pressure corresponding to air temperature |
| $e_a^B$ | | bulk porosity of anchor ice / aufeis deposit |
| $e_{ba}$ | | geometric plane void rate at a depth into the river bed |
| $e_{bv}$ | | porosity of tightly packed bed material |
| $e_f$ | | porosity of frazil ice deposited at the river surface |
| $e_s$ | | porosity of snow |
| $e_{sat}$ | [kpa] | saturated vapour pressure |
| $\varepsilon_a$ | | emissivity of the atmosphere |
| $\varepsilon_i$ | [m$^{-1}$] | bulk extinction coefficient for ice |
| $\varepsilon_w$ | [m$^{-1}$] | bulk extinction coefficient for water |
| F | | shape factor for undercover ice particles |
| $F_{anb}$ | [N/m$^2$] | buoyant force of submerged anchor ice |
| $F_r$ | | Froude number ($F_r = V_w/(gd_w)^{0.5}$) |
| g | [m/s$^2$] | gravitational constant |

| | | |
|---|---|---|
| $\gamma$ | [m/s] | frazil ice accretion rate to the bed |
| $h_{an}$ | [m] | anchor ice thickness (including aufeis if applicable) |
| $h_{aufmax}$ | [m] | maximum thickness for a single aufeis layer |
| $H_{cr}$ | [m] | critical water surface elevation for breakup |
| $h_{f0}$ | [m] | initial parcel frazil ice thickness |
| $h_i$ | [m] | solid ice thickness (also aufeis layer thickness) |
| $h_{ia}$ | [W/m$^2$/°C] | linear coefficient for ice growth calculations |
| $h_{iws}$ | [W/m$^2$/°C] | heat exchange coefficient between anchor ice and substrate flow |
| $h_s$ | [m] | snow thickness |
| $h_{sb}$ | [m] | location of bottom surface of anchor ice relative to the centerline of the first layer of bed particles |
| htlow | [m] | minimum water depth on the finite element nodes |
| hthigh | [m] | water depth required before a “dry” node becomes “wet” |
| $h_{wa}$ | [W/m$^2$/°C] | linear heat transfer coefficient for open water and air |
| $h_{whi}$ | [m] | white ice thickness |
| $h_{wi}$ | [W/m$^2$/°C] | heat transfer coefficient between water and ice |
| $I_{so}$ | [W/m$^2$] | solar constant |
| $I_S$ | [mm/hr] | snowfall intensity |
| $I_R$ | [mm/hr] | rainfall intensity |
| $k_i$ | [W/(mºC] | thermal conductivity of black ice |
| $k_s$ | [W/(mºC] | thermal conductivity of snow |
| $k_{s2}$ | [m] | roughness height |
| $k_w$ | [W/(mºC] | thermal conductivity of water |

| | | |
|---|---|---|
| $k_{whi}$ | [W/(mºC] | thermal conductivity of white ice |
| $l_e$ | [m] | equilibrium length for an aufeis layer |
| $L_i$ | [J/kg] | latent heat of ice |
| n | | Manning's roughness of bed material |
| $n_i$ | | Manning's roughness for the underside of surface ice |
| $N_f$ | | number of frazil particles per unit volume |
| $N_u$ | | Nusselt number |
| $N_u^f$ | | Nusselt number for a suspended frazil particle |
| $\phi_A$ | [W/m$^2$] | heat transfer at water and river floor interface (Marcotte and Robert, 1986) |
| $\phi_{an}$ | [W/m$^2$] | heat flux from the anchor ice to the channel flow |
| $\phi_B$ | [W/m$^2$] | effective back radiation at the river surface |
| $\phi_{ba}$ | [W/m$^2$] | long wave radiation emitted by the atmosphere |
| $\phi_{br}$ | [W/m$^2$] | fraction of the atmospheric radiation reflected by the river surface |
| $\phi_{bs}$ | [W/m$^2$] | long wave radiation emitted by the river surface |
| $\phi_{cl}$ | [W/m$^2$] | short wave radiation reaching the earth surface under clear skies |
| $\phi_E$ | [W/m$^2$] | evaporative heat transfer at the river surface |
| $\phi_f$ | | critical dimensionless flow strength for undercover ice transport |
| $\phi_H$ | [W/m$^2$] | conductive heat transfer at the river surface |
| $\phi_i$ | [W/m$^2$] | heat flux between aufeis layer and ground or ice cover |
| $\phi_p$ | [W/m$^2$] | heat exchange at the river surface due to precipitation |
| $\phi_{pz}$ | [W/m$^2$] | short wave radiation absorbed by anchor ice |

| | | |
|---|---|---|
| $\phi_R$ | [W/m$^2$] | net short wave radiation at river surface |
| $\phi_{R1}$ | [W/m$^2$] | averaged amount of short wave radiation reaching the bottom of the surface ice layer |
| $\phi_{R2}$ | [W/m$^2$] | short wave radiation reaching the top of the anchor ice layer |
| $\phi_{R3}$ | [W/m$^2$] | short wave radiation reaching the bottom of the anchor ice layer |
| $\phi_{ri}$ | [W/m$^2$] | short wave radiation reaching the earth surface under cloudy skies |
| $\phi_T$ | [W/m$^2$] | net heat exchange at the water and/or ice surface |
| $\phi_{uc}$ | | dimensionless undercover ice transport capacity |
| $\phi_{wa}$ | [W/m$^2$] | heat flux between open water and the air |
| $\phi_{wi}$ | [W/m$^2$] | heat flux from ice cover to the river flow |
| $\rho_b$ | [kg/m$^3$] | density of river bed material |
| $\rho_i$ | [kg/m$^3$] | density of ice |
| $\rho_s$ | [kg/m$^3$] | density of snow |
| $\rho_w$ | [kg/m$^3$] | density of water |
| $q_w$ | [m$^2$/s] | water unit discharge |
| Q | [m$^3$/s] | discharge |
| $q_{ic}$ | [m$^2$/s] | volumetric rate of ice transport per unit width |
| $q_x$ | [m$^2$/s] | unit discharge in the x-direction |
| $q_y$ | [m$^2$/s] | unit discharge in the y-direction |
| R | | Bowen's ratio |
| $R_a$ | | rapids parameter (for entrainment at rapids) |
| $R_e$ | | Reynolds number ($R_e = V_w D_h/\nu$) |

| | | |
|---|---|---|
| RMSE | | root mean squared error |
| $R_t$ | | albedo (ice cover) or reflectivity (open water) |
| S | [m/m] | longitudinal channel slope |
| $S_*$ | [m/s] | deposition rate of frazil ice over the depth of the roughness layer (Qu, 2006) |
| $S_i(y)$ | [m/s] | deposition rate of frazil ice to river bed (Hammar and Shen, 1995) |
| t | [s] | time |
| $T_a$ | [°C] | air temperature |
| $T_{ak}$ | [°K] | absolute air temperature |
| $t_c$ | [s] | characteristic time used to define zone of active frazil adhesion (Tsang, 1988) |
| $th_i$ | [m] | total ice thickness |
| $th_{if}$ | [m] | frazil ice thickness of surface ice parcels |
| $th_{is}$ | [m] | solid ice thickness of surface ice parcels |
| $t_{intvl}$ | [s] | coupling time interval for hydrodynamic and ice dynamic calculations |
| $t_{intdry}$ | [s] | dry bed coupling interval |
| $T_m$ | [°C] | melting temperature of ice |
| $T_{dew}$ | [°C] | dew point temperature |
| $T_{cr}$ | [°C] | critical water surface temperature for border ice formation |
| $T_s$ | [°C] | ice surface temperature |
| $T_{sk}$ | [°K] | absolute river surface temperature |
| $T_w$ | [°C] | water temperature |
| $T_{ws}$ | [°C] | water surface temperature |

| | | |
|---|---|---|
| $\tau_{bx}$ | [N/m$^2$] | bed shear stress in the x-direction |
| $\tau_{by}$ | [N/m$^2$] | bed shear stress in the y-direction |
| $U_*$ | [m/s] | bed shear velocity |
| $u_{*i}$ | [m/s] | shear velocity on the underside of an ice cover or frazil ice jam |
| $U_{*max}$ | [m/s] | maximum bed shear velocity for frazil ice accretion |
| $U_{*min}$ | [m/s] | minimum bed shear velocity for frazil ice accretion |
| $\nu$ | [m$^2$/s] | kinematic viscosity of water |
| $v_b$ | [m/s] | average rise velocity of frazil ice in a turbulent flow |
| $v_b'$ | [m/s] | buoyant velocity of a frazil particle at the river surface |
| $V_c$ | [m/s] | maximum velocity for dynamic border ice growth |
| $v_{cr}$ | [m/s] | critical water velocity for static border ice formation |
| $V_i$ | [m/s] | ice velocity magnitude |
| $V_{isb}$ | [km] | visibility |
| $v_{sb}$ | [m/s] | substrate flow velocity |
| $V_w$ | [m/s] | water velocity magnitude |
| $v_z'$ | [m/s] | vertical turbulence velocity at the river surface |
| W | [m/s] | wind velocity magnitude |
| $W_{bi}$ | [m] | lateral dynamic border ice growth width |
| $w_{sb}$ | [N/m$^2$] | submerged weight of bed particles |
| x | [m] | horizontal (streamwise) coordinate |
| y | [m] | vertical coordinate |

CHAPTER 1

# Introduction

## 1.1 Background and Motivation

The existence of river ice can have a profound impact on water resources infrastructure development in cold regions of the world. As the winter season approaches, the cold air temperatures cause the water temperature in the river to drop. Continued heat transfer away from the river water may result in portions of, or all of, the river water to become supercooled (*i.e.*, < 0°C). At this point, various types of ice can form in the river depending on the meteorological and hydraulic conditions present.

Under quiescent conditions, tiny ice crystals will form at the surface of the water and rapidly grow to form surface ice in the form of skim ice and border ice. These ice runs can quickly form a static ice cover provided the turbulence level of the flow is relatively low. From here, the ice cover will experience either growth or decay depending on the meteorological and hydraulic conditions throughout the winter.

If the river flow is more turbulent, the ice particles formed at the surface may become entrained into the flow and will survive as active frazil ice provided the water is supercooled to a depth below the surface. It is believed that frazil ice is the origin of almost all forms of river ice at freeze-up time (Hammar and Shen, 1995). In the continued presence of supercooled water, active frazil particles will grow and agglomerate into flocs which can float to the water surface, provided they are large enough, and arrive on the surface as frazil ice pans (Figure 1.1). These frazil pans may insulate the river from further heat loss and can be transported downstream to contribute to the formation of a surface ice cover. These frazil pans will also grow and thicken from the continued deposition of suspended frazil ice on the underside of the pan and the freezing of the interstitial water at the surface. The above mentioned active frazil particles may also stick to underwater objects and produce what is known as anchor ice (Schaefer, 1950; Wigle, 1970; Tsang, 1982).

When approaching a solid or rubble ice cover, the floating surface ice pans can extend the ice cover further upstream in one of several cover progression modes. Theories on the different forms of surface ice accumulation and the associated ice jams ("narrow" or "wide" ice jam formation) have been developed (Pariset and Hausser, 1961). If the hydraulic conditions permit, the floating ice may be entrained under the ice cover and transported downstream along with any suspended frazil ice in the flow. When these transported ice particles arrive at an area of relatively low flow strength, they can be deposited on the underside of the cover and form a hanging dam or frazil jam (Wang and

Shen, 1995). A rise in water level is typically associated with any of these ice jam formations.

As spring approaches, breakup of the existing ice cover will occur. During a cool and dry spring, an existing ice cover will often deteriorate and melt out in place. Prior to this, a mechanical (premature) breakup can be initiated by the fragmentation of the ice cover by the hydraulic and mechanical forces associated with changes in water level and discharge. This can cause massive rubble ice runs to be transported downstream, which can initiate new surface ice jams further downstream before the ice is able to melt away. These processes can be very destructive to nearshore communities and structures but despite their importance, our current analytical understanding of the mechanical breakup processes is limited. A schematic illustrating all the aforementioned river ice processes can be found in Figure 1.2.

When studying river ice and the associated processes, inherent difficulties often arise. Adverse working conditions, the time scale of many of the formation processes, the unpredictability of many key events, the remote location of many study sites, and a general need for more advanced data collection instruments all are issues that are faced when attempting to conduct good quality field studies. These reasons, coupled with the difficulties encountered when transferring laboratory results to the field conditions, make the continued development of numerical simulation models for river ice processes invaluable. A good numerical model can also be used by researchers to isolate gaps and weaknesses in the current knowledge base of river ice processes. Traditionally, the

sophistication of the river ice theories at the time encouraged the development of 1-dimensional simulation models. It has been found though, that the complex flow conditions, geometry, and processes involved at many of the sites of interest often require that a 2-dimensional numerical model be used for adequate representation and analysis.

Major engineering concerns related to river ice are ice jam flooding, operation of hydropower facilities, inland navigation passages, water transfers and environmental, ecological, and morphological effects (Shen, 1996). It has been estimated that annual maintenance costs incurred at US Army Corps of Engineers projects as a result of ice problems were $33 million in 1992 (Haynes *et al.*, 1993). The ice conditions on an alluvial river can also have a significant effect on sediment transport and river bed change processes. As an explicit motivation for this research, river ice simulation models have a wide range of applications within the hydropower industry. These include but are not limited to the use of numerical models in the following applications (Shen, 2002):

1) in design, to evaluate extreme flow and ice conditions from the initial feasibility study to the detailed design,
2) in operations, to determine ice effects on generation efficiencies and to identify operation criteria that would induce favorable ice conditions, and
3) in environmental impact assessments, to quantify the wintertime impacts of hydropower and other river engineering projects on the eco-hydraulic and ice regime.

The above illustrates some general considerations of hydropower companies operating in cold regions of the world. For example, the ice management group at Manitoba Hydro deals with numerous ice issues annually. The importance of these issues is magnified by the fact that the worst ice conditions are found during the coldest periods which often coincides with peak demands for power. The continued development of river ice simulation models will help to develop and evaluate potential mitigation alternatives for these ice issues. A partial list of these river ice concerns includes the following:

1) Anchor ice (and aufeis) dams form annually at Sundance Rapids (Figure 1.3) and near the outlet of Clark Lake. These dams reduce the conveyance of the reach which causes increased staging and delayed flow through the river section (Girling and Groeneveld, 1999; Malenchak *et al*., 2006).
2) Ice bridging and hanging dams near Gull Rapids and Birthday Rapids annually affect the amount and rate of flow that can be passed through the river system leading up to Stephens Lake and on to the Lower Nelson River.
3) Ice cover formation on the forebay of the Jenpeg Generating Station has operational implications for Manitoba Hydro in regards to potential frazil ice buildup on the trash racks (Zbigniewicz, 1997; Bijeljanin and Clark, 2011).
4) The effects of operating the Jenpeg Generating Station on the stable ice cover of Cross Lake have both operational and safety implications that need to be considered annually.

5) Ice buildup in front of the Kelsey (Figure 1.4) and Grand Rapids Generating Station can create unwanted head loss and other concerns upstream of the stations.
6) How modifications to the operation of the Manasan Control Structure on the Burntwood River will impact the formation and breakup of a stable ice cover upstream from the City of Thompson needs to be assessed.

## 1.1.1 Formation and Evolution of Anchor Ice

### 1.1.1.1 Anchor Ice Initiation and Growth

The complete river ice process consists of numerous individual processes all acting interdependently with one another and anchor ice is one significant component. Anchor ice, or bottom ice (Wigle, 1970), refers to ice that forms on the bottom of rivers, lakes, and oceans. Anchor ice can be initiated by underwater nucleation or by the accretion of active frazil particles to objects below the water surface. Underwater nucleation occurs when supercooled water from near the surface is transported to a depth. Ice can then be directly nucleated on underwater objects to form anchor ice as indicated by Michel's theory (Michel, 1967). It has been established that the objects on which anchor ice nucleates need not be on the bottom, so long as they are submerged (Tsang, 1982).

Aside from underwater nucleation, anchor ice can also be initiated by the accretion of active frazil particles to the upstream side of underwater objects. These active particles must be transported to a depth by the turbulence of the flow. When the particles come

into contact with a submerged object, they usually stick to the object because of their adhesive nature (Carstens, 1966). The frazil particles will remain in the active state so long as the water is supercooled (Michel, 1963). The continued accretion of more frazil particles to existing layers of anchor ice can allow for anchor ice to accumulate very quickly. The surface of the anchor ice formed by frazil adhesion is much coarser than that formed by underwater nucleation and has distinct frazil crystals that are stuck to each other (Qu, 2006). Once the particles adhere to an object, they can experience accelerated thermal growth due to the higher relative velocity they have with the surrounding flow (Piotrovich, 1956; Osterkamp and Gosink, 1982).

Due to the location and environment of anchor ice initiation, this physical process is perhaps best studied in a laboratory setting and to date, a limited amount of laboratory studies have been conducted to directly observe the anchor ice initiation and growth process (Doering *et al*. 2001, Kerr *et al*. 2002, Qu 2007). These studies have increased our understanding and to some extent confirmed previous theories about this process.

A laboratory study on anchor ice initiation, evolution, and its hydraulic effect in channels with a gravel bed was conducted by Kerr *et al.* (2002). It was observed in these experiments that anchor ice was initiated by frazil attachment and was not observed to initiate below half of a gravel diameter from the top of the closely packed bed material. After initiation, three types of anchor ice forms were observed to develop depending on water velocity ($V_w$) and Froude number ($F_r$). These forms were termed tails, scales, and balls (Figure 1.5). At the lowest values of Froude number and velocity ($F_r < 0.2$, $V_w <$

0.25 m/s), tail type anchor ice formed and at the highest values ($F_r > 0.5$, $V_w > 0.45$ m/s), ball type anchor ice was observed with the scale type serving as the transition between the other types. After the initial stage of anchor ice growth, a transitional stage of growth followed which included a progressive flattening and joining of the protruding anchor ice which was then superseded by a final growth stage where the growth rate was found to be nearly constant so long as the other variables in the experiment were steady. It was observed that the anchor ice growth rate increased with heat loss and decreased with increased water depth. The combined bed/ice surface roughness initially increased with anchor ice growth but then decreased to a minimum value during the transition stage when the anchor ice grew out of the gravel bed. The overall hydraulic resistance of anchor ice was found to decrease with an increase in flow rate and depth, with an increase in flow drag serving to either flatten the anchor ice further or cause release. In all cases, individual anchor ice growths would eventually join together to form a mesh of anchor ice over the bed particles.

Doering *et al*., (2001) and Qu and Doering (2007) conducted experiments on anchor ice growth and evolution in a counter rotating flume. The observations obtained by Doering *et al*. suggested that the rate of anchor ice growth and the density of anchor ice have a dependence on Froude number. With the density of the anchor ice increasing with Froude number and a maximum growth rate of anchor ice observed at a Froude number of 0.27. These experiments also found that the attachment strength of the anchor ice to the bed material seems to be related to the Reynolds number ($R_e$), with anchor ice being released more easily at lower $R_e$ numbers but the exact nature of the relationship was unclear.

Qu and Doering (2007) investigated the process of anchor ice evolution around rocks and on gravel beds. These experiments were able to replicate in the counter rotating flume, and observe in more detail, many of the anchor ice formation types described by Kerr *et al*. These experiments showed that once incipient anchor ice forms by initial frazil adhesion to the bed, continued anchor ice growth occurs by a combination of frazil accretion and in situ growth of particles already attached to the bed. This in situ growth can account for some of the internal strength of an anchor ice mass and can increase the strength of the bond between the anchor ice mass and the substrate. A positive relationship between the density of anchor ice and the Froude number was demonstrated during the tests. It was also found that an increase in Reynolds number resulted in an increase in anchor ice density, a decrease in porosity, and a smoother anchor ice formation due to the close packing of the frazil particles on the bed material.

Several limitations on the thickness of anchor ice do exist in nature. In shallow rivers, the flow depth can initially provide an upper limit for the anchor ice thickness. Large anchor ice accumulations though are often associated with staging of the water level upstream of the ice deposits which can then allow even larger thicknesses to eventually form. In small streams, this staging can initiate the successive formation of numerous anchor ice dams along a reach that is conducive to the formation of anchor ice. This process results in the formation of a series of "steps" and "pools" as documented in field investigations (Yamazaki *et al.*, 1998; Tesaker, 1994). These dams are often large enough to be partially exposed at the surface where a process of "aufeis" or "naled"

growth (Kane, 1981; Schohl and Ettema, 1990) will continue to increase the size of the dam.

#### 1.1.1.2 Anchor Ice Release

While the formation and evolution of anchor ice is described above, the release of anchor ice is an equally important component of the process. Anchor ice is subjected to a buoyancy force and the drag forces of the surrounding flow. These forces increase proportionally with anchor ice thickness and can be significant. Tsang (1982) reported observations of large boulders and heavy anchors being floated by anchor ice in rivers and the hydraulic drag associated with anchor ice formations have affected the stability of field instruments mounted on the river bottom (Jasek, 2010). It has been observed that while anchor ice can form on any bed material, it preferentially exists on gravel and cobbles because these bed materials are more capable of resisting these forces (Kempema, 2002).

If the bond between the anchor ice and the bottom material is not strong enough to resist the combined action of these forces the anchor ice can be torn away or, in the case of a river with granular bottom material, individual particles can be "rafted" away by the released anchor ice if the buoyancy force of the ice is greater than the submerged weight of the granular pieces. This rafting mechanism can have a significant effect on sediment transport patterns at a particular location and sediment laden ice is often seen rising to the surface of northern rivers on mornings following cold, clear nights (Barnes, 1928; Wigle,

1970; Arden and Wigle, 1972; Michel, 1971; Foulds and Wigle, 1977; Kempema *et al.*, 2001).

Individual masses of anchor ice can mechanically release at any time, but anchor ice can also be thermally released from the bed in the morning when the sun warms the water (Michel, 1971; Arden and Wigle, 1972; Tsang, 1982). The solar energy input can offset the small levels of supercooling that occur in nature or as in the case of shallow, clear, rivers, will serve to weaken the bond between the ice and the river bottom allowing the ice to release and float to the surface. Generally, anchor ice cannot survive long when no supercooling exists but Parkinson (1984) observed the release of anchor ice on extremely cold days presumably under the influence of bright sunshine. Tsang (1982) also pointed out that the bond strength between the anchor ice and a riverbed may also be reduced in the presence of a bed heat flux to the underside of the anchor ice.

Generally, anchor ice formed in low velocity and low turbulence areas has been observed to be more porous and have a weaker bond with the bed material. In high velocity and high turbulence areas, the anchor ice has a stronger bond with the bed material and is less likely to release (Doering *et al.*, 2001; Stickler and Alfredson, 2009). This can be partially attributed to the higher amounts of turbulent heat transfer in high velocity and high turbulence areas.

#### 1.1.1.3 Field Observations and Implications of Anchor Ice

The effects of anchor ice on the hydraulic characteristics of the flow have been well documented (Arden and Wigle, 1972; Parkinson, 1984; Marcotte and Robert, 1986; Girling and Groeneveld, 1999; Malenchak *et al*., 2006). Anchor ice formation on the river bed changes the boundary roughness, raises the effective bed elevation, and reduces the conveyance of the channel. This can effectively "choke" off a portion of the flow and have significant impacts on water supplies and other industries dependent on the discharge. Sudden flow reductions of 20% to 30% have been observed in the upper Niagara River due to the growth of anchor ice in the night (Arden and Wigle, 1972). The modification of hydraulic conditions in a stream by anchor ice can be responsible for substantial reworking of the bed sediment (Osterkamp and Gosink, 1982). At locations where supercooled water can be drawn down from the water surface, at a water intake for example, evidence of anchor ice blocking these intakes has occurred up to a depth of 20 m (Daly, 1991).

Anchor ice can also have biological implications for invertebrates and fish which rely on an adequately aerated and physically stable river bottom for their spawning beds. Anchor ice formation can lead to the freezing of redds and eggs in the substrate of streams (Prowse and Gridley, 1993) and may also cause fish habitat exclusion and the freezing of invertebrates and macrophytes (Prowse, 2001; Huusko, 2007).

Early studies of anchor ice formation centered on field observations from cold regions around the world. Portions of the anchor ice process were verified and others were

expanded upon depending on the nature of the particular observations. A review of many of these field studies is appropriate as it will provide valuable insight into the anchor ice process as it has been observed to occur in nature.

Wigle (1970) observed that when water becomes supercooled, the frazil crystals adhere to underwater objects contributing largely to the underwater ice formations. Anchor ice formation was observed at all depths up to 20 feet in the Niagara River. He also found that anchor ice formed on rocky bottoms and not sandy bottoms due to the lack of anchoring effect of the sandy bottom.

Osterkamp and Gosink (1982) conducted field investigations of frazil and anchor ice formation as well as sediment transportation by anchor ice in Alaskan streams. At some locations, observed "sheets" of anchor ice that were partially lifted off the bed were observed to be moving slowly along the bottom of the stream in intermittent fashion, rafting a significant load of sediment with it.

Parkinson (1984) observed anchor ice formation, growth and release on Lake St. Louis, on the St. Lawrence River at Montreal. Results suggest that the water level in the lake reacts very quickly to the formation or release of anchor ice. The average porosities of the anchor ice were found to be 76% and a maximum water level rise on the lake of 0.9 m was attributed to anchor ice. Rapid anchor ice formation was observed at night often with some being released the following day due to an input of solar energy. This resulted in

daily rises and drops of up to 0.3 m in the water level of the lake that can be attributed to anchor ice.

Tesaker (1994) studied anchor ice in small Norweigian streams with slopes between 0.001 to 0.01. He observed that local, temporary damming by anchor ice is the common starting point for a chain of events that may eventually lead to formation of a stable ice cover. The formation of anchor ice in these small streams was found to occur at or below natural transitions from tranquil to rapid flow or where flow lines are converging to create increased turbulence in the flow.

Multiple field studies have been conducted in the Niuppu River and other small streams in Hokkaido, Japan (Yamazaki *et al.*, 1996; Hirayama *et al.*, 1997; Yamazaki *et al.*, 1998). Anchor ice was observed to be initiated in a rapid section (where the river bed gradient changes abruptly) and did not exist in milder/deeper sections of the stream. Anchor ice was also not found to any large degree in the sandy portions of the reach and when the water velocity was less than 0.7 - 0.9 m/s, anchor ice was hardly observed at that location in this small stream. It was found that when the freezing index is large, the minimum Froude number and critical velocity for anchor ice existence becomes smaller. The volume of the observed anchor ice masses becomes larger as the friction resistance of the bed increases and as air temperature decreases. The relative density of anchor ice masses obtained in these studies was between 0.3 and 0.7 and was found to be proportional to the flow velocity. The daily production of anchor ice was found to be proportional to the 6-hr freezing index.

Together, the above studies showed that anchor ice is more predominant in shallow, fast flowing sections of the stream having Froude number values ranging from 0.2 to 1.5. These field observations and the experimental results, discussed previously in section 1.1.1.1, have linked the local Froude number to anchor ice distribution and growth and this relationship has been questioned by other field studies (Kempema 2002; Stickler and Alfredsen 2009). The results from those particular field studies indicate that the growth mechanism and distribution of anchor ice may have a geographic component to it and that it also needs to be related to the overall hydraulic and geometric properties of the specific location. It is not surprising that the broad definition of anchor ice makes it particularly difficult to come up with a single set of formation and growth criteria.

Kempema *et al*. (2001) observed anchor ice in the nearshore zone of southwestern Lake Michigan during the winter. Lacustrine anchor ice was observed on sand, pebble, cobble, and boulder substrates in water depths up to 4 m. This anchor ice was released from the lake bed on mornings following formation events and was found to transport a significant amount of sediment along shore and offshore depending on the prevailing winds.

Kempema (2002) also observed ice rafting of coarse sediment from the Laramie River in Wyoming, USA. This rafting of sediment was observed to contribute significantly to the sediment transfer process in the Laramie River. The amount of anchor ice formed was found to be a function of the amount of open water and the ambient atmospheric conditions. The anchor ice always released the following morning. During large events,

sediment laden anchor ice between 20 to 30 cm thick was observed and the anchor ice was found to be capable of transporting all sediment sizes with the largest particle recovered weighing 1.7 kg.

As a continuation of the previous work on the Laramie River, Kempema (2004) observed that anchor ice formation can affect the local stage of rivers on a daily basis which in turn can affect the exchange of water and heat between the river and the adjacent aquifer (hyporheic zone). It was observed that the temperature in the shallow sediment beneath the streambed increased during nights when anchor ice formed. This heat exchange process could affect distribution of anchor ice on a streambed as Tsang (1982) pointed out that the bond between anchor ice and a riverbed is dependent on the heat balance of the water and therefore, heat flow from the bed may affect anchor ice adhesion.

Alfredsen *et al*. (2006) provided an overview of the ice formation processes in two small streams in Norway and Canada which were dominated by anchor ice formation and the creation of anchor ice dams. They found that the accumulation of frazil ice into anchor ice dams usually occurs in areas with large substrate and boulders, over natural weirs in the river, and in shallow or restricted areas of the stream. They also observed that anchor ice formed during cold nights and during nights with snow fall. It was also found that with prolonged cold conditions, the anchor ice dams may freeze and stabilize with sufficient strength to remain in place for prolonged periods of time.

As an extension of their 2006 work, Stickler and Alfredsen (2009) provided observations of anchor ice formation in three northern steep stream environments with different physical characteristics in Canada and Norway. The analysis of anchor ice growth and density showed that the anchor ice in these streams may be distinguished by two main types; Type I: lower density anchor ice on top of substrate, and Type II: higher density anchor ice forming between substrata and the interstitial spaces. The distribution of these two types of anchor ice suggests a relation between the growth pattern and density and the turbulence intensity which can be expressed by the Reynolds number. The Type II anchor ice, which has a higher relative density, was more frequently found at locations with a higher Reynolds number. A linkage between the spatial distribution of anchor ice and the Froude number was investigated but the data did not show one in these studies.

Kempema and Ettema (2009) observed large size ice crystals in anchor ice masses in the Laramie River, Wyoming, which indicates a significant amount of anchor ice forms as in situ ice growth once attached to the bed. Daly (2010) also observed very large amounts of in situ growth of ice crystals attached to a water intake in Lake Michigan where a supply of supercooled water was drawn towards the intake for a prolonged period of time.

### 1.1.2 Formation and Evolution of Aufeis

Aufeis (or sometimes termed “naled”, “icing”, or “taryn” depending on geographic location) is a sheet-like mass of layered ice which is a characteristic of many cold region streams where water (often under pressure) in the stream channel flows onto the existing ice cover or frozen ground, subsequently freezing as it flows over the surface (Kane,

1981; Yu *et al*., 2005). A simple classification of aufeis proposed by Alekseyev (1973) and utilized by Carey (1973) is according to the water source: 1) river and stream, 2) ground, and 3) spring. River aufeis may develop on rivers of nearly all sizes but shallow rivers and large braided rivers are the most affected (Slaughter, 1990).

Aufeis can occur under a number of conditions and typically forms on rivers and streams following the development of a complete ice cover and often occurs in response to increased resistance to flow in a stream which can be due to progressive channel constriction either by: 1) ice cover freezing from the top, 2) anchor ice growth from the bottom, or 3) cover depression due to snow cover or previous aufeis formation (Carlson and Kane, 1973; and Kane *et al*., 1973). An increase in piezometric head under the ice cover will force water to the surface which will flow in sheets over the pre-existing ice cover. Water flow during the formation of an aufeis layer is typically shallow and laminar (Schohl and Ettema, 1986b) and if present at the time of overflow, snow can be incorporated into the aufeis layer (Kane, 1981). These ice sheets (or layers) are of variable thickness and may range from less than an inch to as much as a foot or more (Alekseyev *et al*., 1973; Carey, 1973; Slaughter, 1990). Once an aufeis layer freezes solid, another layer may begin to form on top of it to create the laminated structure that is described in many published descriptions of aufeis. Multiple layers of aufeis can result in ice thicknesses that are two to three times the maximum ice thickness due to heat loss to the atmosphere (approximately 1.5 m) in deep, subarctic surface waters (Kane, 1981). Aufeis initially forms on any cold surface, but the subsequent growth always continues as a progressive accumulation of ice layers on top of ice.

Carstens and Lia (1998) observed aufeis growth and subsequent blockage of tunnel spillways and diversion tunnels in Norway. Similar to the process described above, they observed that aufeis growth can be initiated in one of two different ways:

1) When a shallow water stream freezes and is sealed to the ground.
2) When a floating ice cover fills the cross section of the underflow and water starts to flood the ice cover.

The formation of aufeis involves a complex combination of thermodynamic and hydrodynamic processes. The thickness of a single icing layer is influenced by the combination of weather, micro-topography, discharge, and water temperature (Hu *et al*., 1999). The sum of the surface and ground heat flux components (*i.e.*, heat loss) determines the rate at which the aufeis layer thickens which in turn affects the horizontal distance an aufeis layer will spread out. Consequently, very cold air temperatures cause water flowing over existing ice to freeze in relatively short distances (Carey, 1973; Schohl and Ettema, 1986a and 1990; Zufelt *et al*., 2009).

River aufeis processes can modify the hydraulic geometry of river channels and the importance of these processes to water resources research and their impact on northern engineering structures, along with the potential mitigation of these impacts, have been the focus of many studies (Carey, 1973; Sokolov, 1978; Kane, 1981; van Everdingen, 1982; Saarelainen and Vaskelainen, 1988; Slaughter, 1990; Lehtonen, 1991; Vinson and

Lofgren, 2003; Andersland and Ladanyi, 2003). The presence of aufeis in streams can cause increased channel and bank erosion and may induce or accelerate scour around piers and abutments of bridges and other in-stream structures. The temporary storage of water is a hydrologic consequence of large aufeis formations and can result in a redistribution of runoff from winter to spring and summer (Doganovskiy, 1973). As a relatively unique form of aufeis, periodic flooding of existing anchor ice formations downstream of a hydropower plant have resulted in ice dams of a significant thickness across the majority of the river width in northern Manitoba, Canada (Girling and Groeneveld, 1999; Malenchak *et al*., 2011).

Aufeis formation, while simple to describe in general terms, is very difficult to describe quantitatively given the general structure of the water flow through the aufeis which often combines conduit flow with surface sheet and active flow (Zufelt *et al*., 2009). Because of this, a significant portion of aufeis research conducted to date has centered on detailed field observations studies from locations around the world. Yu *et al*. (2005) observed aufeis (or icing) problems on roads in the Da Hinggangling Forest region in northwest China and proposed methods for the control of icings along roads. The methods in this paper focused on preventing the water from reaching the ground surface and providing a preferential path for the water to pass underneath the location requiring protection which in this case was a roadway.

Zufelt *et al*. (2009) carried out field observations of aufeis formation in Jarvis Creek, Alaska over 3 winters starting in 2006. Jarvis creek is a wide, braided channel which

flows over a large glacial outwash fan. Aufeis in Jarvis Creek was observed shortly after initial freezeup as channels with higher water surface elevations spilled out over the gravel bars into the channels with lower elevations. The exchange of flow between the braided channels throughout the winter promoted aufeis formation. At some locations, flow was directed to the overbank area and promoted aufeis formation in this area as well. Total aufeis thickness of almost 2.5 m thick was observed in Jarvis Creek with single layers being as small as 1 cm.

Hu *et al.* (1999) used a more quantitative approach in their study that focused on the temporal variations of energy fluxes during the formation of single or double icing layers in the North Fork Pass area of the Yukon Territory in Canada. They used an energy balance approach for the complete aufeis layer cycle and related the observed formation of aufeis to a range of climatic conditions.

#### 1.1.2.1 Laboratory Studies of Aufeis

Based on observations of aufeis growth (termed "naleds" in this study) in a refrigerated laboratory flume, a detailed description of the processes associated with aufeis growth is presented by Schohl and Ettema (1986a, 1986b, and 1990). In these experiments, two-dimensional (laterally confined) aufeis formations were observed to depend primarily on seven, independent, and dimensionless parameters. The experimental procedure was able to replicate the continuing, cyclic process by which slush layers form and eventually freeze solid resulting in the laminations that are a feature of aufeis formations. The

thickness of the ice laminations in these experiments were in the order of 1.4 to 2.4 cm thick.

Schohl and Ettema proposed, and confirmed by the experiments, the following equation for the equilibrium length ($l_e$) for aufeis which is the length of aufeis for which the source water flux is in equilibrium with the rate of freezing

$$l_e = \frac{q_w \rho_w L_i}{\phi_{wa} + \phi_i}, \qquad \textbf{(1.1)}$$

where $q_w$ = water unit discharge ($m^2/s$), $\rho_w$ = density of water ($kg/m^3$), $L_i$ = latent heat of ice (J/kg), and $\phi_{wa}$ = heat flux between the water surface and the atmosphere ($W/m^2$), and $\phi_i$ = heat flux between the aufeis layer and the ground or ice cover ($W/m^2$). It was observed in the experiments that aufeis formed under larger values of $\phi_{wa}$ not only has a shorter $l_e$, as expected from equation 1.1, but the aufeis layer also spreads more slowly and is thicker than aufeis formed under smaller values of $\phi_{wa}$.

An extension to the above work was conducted by Streitz and Ettema (2002), which investigated the spreading of aufeis formed on sloping planar surfaces subject to wind. The observations were largely qualitative and were focused on the trends in aufeis morphology under the influence of gravity and wind drag. The combination of the two driving mechanisms resulted in a variety of aufeis morphologies which included varying height and spacing of surface features on the ice layers.

## 1.2 Numerical Model Literature Review

Over thirty years ago, with the growing awareness and development around river ice engineering in North America, the American Society of Civil Engineers published a paper addressing the research needs of river ice (ASCE, 1974). Since then, significant progress has been made in all areas of river ice research by researchers from around the world. Specifically, the development of numerical models to simulate these complex phenomena has received the most attention because this method remains to be the most economical and efficient way to analyze the complete river ice regime and its evolution. The following literature review is intended to familiarize the reader with some of the more sophisticated river ice models developed since the eighties which may or may not still be in use today. It should be noted that many of these numerical models were developed to address the needs of a specific engineering problem or study and because of this limited scope; many limitations exist within the models themselves. This is especially evident when comparing the models to the current state of knowledge of river ice processes and the numerical computing methods available today. Each of the numerical models will be placed into one of the following two categories; 1) River Ice Models – aimed at simulating the formation and evolution of the complete river ice regime (or portion thereof) including freeze-up and/or breakup periods, and 2) Anchor Ice Formation Models – these are models that include the calculations for the formation and evolution of the anchor ice component of the river ice regime. The anchor ice models are singled out in this review because this research focuses primarily on the growth of anchor ice / aufeis and will be a key area of future development. The level of sophistication varies from model to model for each of the two categories.

### 1.2.1 Literature Review of River Ice Models

#### 1.2.1.1 SIMGLACE (Rousseau *et al*., 1983; Petryk, 1995)

This steady state, one-dimensional model simulates the processes of water cooling, ice generation, ice cover formation, melting, and breakup as functions of time, river bathymetry, and hydro-meteorological conditions. Input data for the model consists of river bathymetry, hydraulic roughness properties, as well as physical and mechanical properties of ice. Time dependant input data includes water temperature at the upstream end, discharge, and meteorological conditions. The model can output mean velocities, water levels, cover thicknesses, and quantities of ice generated and transported as functions of time and distance from the downstream end. The ice cover formation is governed by four criteria: frontal progression (narrow jam); shoving (wide jam); border ice growth; and erosion under ice jams. Anchor ice is ignored in this model.

#### 1.2.1.2 ICESIM/ICEDYN (Simonsen and Carson, 1977; Petryk, 1995)

The ICESIM model was originally developed in the late sixties by Acres International Limited and has been improved numerous times over the years. The current version is a one-dimensional, steady state program which considers, in discrete time steps, the various processes that affect the water surface profile along a river. Including, the rate of ice generation; ice cover advance by frontal progression; ice erosion/deposition/transport; border ice growth; ice cover shoving; and ice cover advance by staging. Most recently, provisions for the simulation of anchor ice processes have been incorporated into the

ICESIM model. As an extension to the ICESIM model, a dynamic model (ICEDYN) was developed which considered the fully dynamic or transient effects of hydropower peaking and the effect of falling or rising flows over a winter.

#### 1.2.1.3 JJT – The Finnish Ice Model (Huokuna, 1990)

The JJT-model combines a one-dimensional unsteady flow model with algorithms that simulate water temperature, ice cover formation, and ice cover growth and decay and was originally based on the model code of Shen and Yapa (1984). Many of the same equations used in the RICE models (see below) for water cooling and ice formation are included in the JJT-model. This allows border ice, skim ice, and frazil ice runs to be simulated. Locations of ice bridging are predicted using an empirical relationship and hanging dams are simulated using a critical velocity criterion. Dynamic ice cover formation includes narrow jam calculations but the stability of an ice jam (with respect to shoving) is not calculated. Anchor ice is also omitted from the JJT-model.

#### 1.2.1.4 ICEPRO/RIVICE (Petryk *et al*., 1990; TALAS, 1995)

An effort at developing a comprehensive river ice model RIVICE was initiated in Canada in the late eighties. Many of the algorithms and rationale used in the program were adopted for the ICEPRO model developed by KGS Group. The general capabilities of this steady state, one-dimensional model include, the estimation of ice generation as a function of air temperature; border ice simulation; and stability of the leading edge of the ice cover as well as stability of the cover in regards to shoving. The hydraulic module

contained within ICEPRO addresses the constant evolution of the water surface profile as ice accumulates. More recently, an unsteady flow model has been added to ICEPRO which now goes by the name VARY-ICE. Provisions for anchor ice formation are not included in any of the above models at this time.

#### 1.2.1.5 RICE/RICEN (Lal and Shen 1991, Shen *et al*. 1995, Shen, 2010)

RICEN is a one-dimensional, river ice simulation model that can simulate unsteady flow conditions for channel networks with ice. The thermal and ice condition sub-model simulates water temperature variation along the river (including supercooling events); frazil ice concentration; suspended and surface ice transport; border ice formation and growth; ice-cover progression and stability; undercover ice transport; and thermal growth and decay of ice covers. RICEN also allows for anchor ice growth, decay, and release. The model was improved to be applicable to rivers having shallow depth with large changes in channel geometry and applied to the lower Yellow River in China (Wang *et al.*, 1996). Two dimensional extensions of many of the formulations found in RICEN have been employed in the CRISSP2D model and will be elaborated on in Chapter 2.

#### 1.2.1.6 River1D (Andrishak and Hicks, 2008; She *et al*., 2008)

River1D is a hydraulic flood routing model developed at the University of Alberta, which uses the characteristic-dissipative-Galerkin finite element method to solve a conservation formulation for the Saint-Venant equations for rectangular channels of varying width (Hicks and Steffler, 1990 and 1992). The latest version of the model incorporates

thermal ice related processes, including water temperature, suspended and surface frazil ice, surface ice concentrations and solid surface ice, as well as ice front location (Andrishak and Hicks, 2008). At this point in time, border ice and anchor ice growth processes are not considered in the current version of the model.

Another component to the River1D model is an ice jam module capable of simulating river ice jam dynamics under various flow conditions. The model solves the 1D conservation of mass and momentum equations for water flow and ice motion using a finite element method in an uncoupled sequence. A one-seventh power law formulation is used to describe the internal resistance and strain rate relationship of a moving ice accumulation (She *et al*., 2008).

#### 1.2.1.7 MIKE-ICE (Theriault *et al*., 2010)

The MIKE-ICE model was jointly developed as an add-in module of the Danish Hydraulic Institute's MIKE11 software for river ice modeling. This unsteady numerical model computes the overall thermal balances and interactions between the flow and the different types of ice. The ice processes considered in the model include water temperature (including supercooling), frazil ice generation, formation of surface ice pans, upstream progression of ice cover due to juxtaposition, formation of hanging dams under an ice cover, border ice cover progression, and static ice cover thickness variations. It has been used to reproduce the ice regime in present conditions and the changes due to variations in water temperature and to an increase in winter flow.

### 1.2.1.8 One-Dimensional River Ice Jam Models

Various one-dimensional ice jam models exist and are in use today. These models typically simulate ice jam formations and their effect on the river stage and discharge. Inputs usually include discharge, river bathymetry and roughness, incoming ice discharge, as well as ice rubble characteristics. Thermal effects are omitted from these models which can be classified as equilibrium or non-equilibrium jam models. An equilibrium jam model relies on the assumption that the ice jam formed will be long enough to form an "equilibrium reach" where flow is uniform, ice thickness is constant, and the downstream forces are resisted entirely by the bank friction. The transition areas at the downstream (toe) and upstream (head) ends of the jam are then described using known equilibrium jam theories. Non-equilibrium jam models simulate the longitudinal configuration of a steady-state, wide ice jam regardless of whether or not the jam has reached equilibrium conditions. This is particularly useful in the simulation of an ice jam that forms with a limited ice rubble supply. Two examples of non-equilibrium jam models are RIVJAM (Beltaos, 1993) and ICEJAM (Flato, 1986; Healy and Hicks, 1999). One example of a model of the equilibrium type is ICETHK (Tuthill *et al*., 1998), which is used in conjunction with the HEC-2 backwater model developed by the U.S. Army Corps of Engineers and another is JAMSIM (Judge *et al*., 1997) which is a modified version of the ICESIM model described above.

In order to test and compare the performance of some the existing ice jam models (one- and two-dimensional models), the author contributed to a series of tests that were created and coordinated by a task force appointed by the Committee on River Ice Processes and

the Environment (CRIPE). The results indicate that the overall performance of the different ice jam models is good when calibration data is available, but considerably more varied when the models are applied in uncalibrated or "blind" mode. It was concluded that some of the diversity in the results can be attributed to the variations in perceptions of the physical processes and the specification of unknown boundary conditions by the modelers, as compared to the mechanics of the numerical computations (Carson and Beltaos *et al*., 2011).

#### 1.2.1.9 DynaRICE (Shen *et al*., 1993, 2000)

DynaRICE is a two-dimensional numerical model developed to simulate the dynamic transport and jamming of surface ice in rivers. The hydrodynamic component of the model uses an Eulerian finite-element method, while the ice dynamic component uses a Lagrangian discrete parcel method. Thermal effects are not considered in this ice dynamic model. DynaRICE was used as the starting point for the CRISSP2D model that will be employed and developed in this study. Therefore, a slightly more detailed description of the model can be found in chapter 2.

#### 1.2.1.10 RIVER2D Ice Model (under development)

The University of Alberta's River2D hydrodynamic model is currently being adapted to model ice formation processes in a purely Eulerian frame of reference (Wojtowicz *et al*., 2009). Processes included in the model include: water temperature and supercooling; border ice formation; frazil ice production, transport, and rise; and surface ice transport,

bridging, and frontal progression. The ice process model components are still being tested and validated, and so the application of the model to date has been limited to modeling open water and winter ice cover conditions (Wojtowicz, 2010).

### 1.2.2 Literature Review of Anchor Ice Formation Models

#### 1.2.2.1 Marcotte and Robert (1986)

An elementary mathematical model simulating the buildup and release of anchor ice was prepared and calibrated from observations. The basis of the model is a detailed heat transfer analysis where thermal exchanges at the water surface are used to determine the water temperature. When supercooled, part of the supercooling is used to generate various types of ice, including anchor ice. When the water temperature is positive, thermal erosion and subsequent release of anchor ice can occur. The water temperature is then adjusted depending on whether growth or decay of anchor ice takes place. In this model, the equation used to calculate the heat transfer at the water and river floor interface ($\phi_A$) is

$$\phi_A = -1.5 * 10^8 n^2 V_w T_w d_w^{-0.33}, \quad \textbf{(1.2)}$$

where $n$ = Manning's roughness, $V_w$ = water velocity, $T_w$ = water temperature, and $d_w$ = water depth. The heat transfer calculated above is used to adjust the volume of anchor ice on the riverbed and the subsequent thickness of anchor ice is a function of its density. The density of the anchor ice, as well as the release component of the anchor ice, is either

calibrated to direct observations or based on empirical relationships. It should be noted that this one-dimensional model does not include the accretion of frazil ice to the river bottom.

#### 1.2.2.2 Tsang (1988)

The growth of anchor ice in this one-dimensional model considers the adhesion of frazil particles to the river bottom as the only growth mechanism. A characteristic time ($t_c$) is used to define a zone of active frazil ice adhesion. This zone is assumed to extend from the point of frazil nucleation ($T_w$ = 0°C) to a location downstream that the water would travel during this characteristic time. It is further assumed in this zone that the distribution of frazil is uniform and equal to the concentration at the location that corresponds to $t_c/2$. This concentration and the location of frazil nucleation are predicted by the water cooling and frazil concentration sub-models and will move upstream and downstream with changing hydraulic and meteorological conditions. The model also contains a calibration parameter ($\beta_2$) that characterizes the rate of frazil adhesion to the river bottom and is site specific for various locations in the river. The increase in anchor ice thickness ($\Delta h_{an}$) at a point in the river is calculated by

$$\Delta h_{an} = \beta_2 C_v u_* \Delta t \,, \tag{1.3}$$

where $C_v$ = average suspended frazil concentration at $t_c/2$, $u_*$ = bed shear velocity, and $\Delta t$ = the time step.

The release of anchor ice is simulated by comparing the buoyant force of the anchor ice to the submerged weight of the bed particles. The effects of flow drag and the associated "peeling" of anchor ice is not considered in the model. A theory is formulated that relates the bond strength of the anchor ice to the amount of heat transferred to the ice when the water temperature rises above 0°C, but this theory was not implemented into the model.

#### 1.2.2.3 Wang and Shen (1993)

Wang and Shen formulated a one-dimensional model for anchor ice growth and release. Thermal growth and decay resulting from the turbulent heat transfer between the existing anchor ice and the river water is considered along with the accretion of active frazil particles to the bed material. The effect of incoming solar radiation on the decay of anchor ice is also considered in the model. The accretion of frazil ice to the river bottom is limited to occur only when the water is supercooled and when the critical shear velocity criterion are satisfied. The calibration parameter in this model is the accretion rate of frazil ice ($\gamma$) and the critical shear velocities. Thermal and mechanical release mechanisms are included in the model. With the mechanical release condition occurring when the buoyant force of the anchor ice overcomes the submerged weight of the bed particles and inter-particle resistance combined. This theoretical anchor ice model was incorporated into the RICEN model (see above) and subsequently the formulations were the basis for the anchor ice growth model presented below in section 3.4.

### 1.2.2.4 Hammar and Shen (1994, 1995, 1996)

This one-dimensional model considers the attachment of frazil ice to the channel bed as a process of particle deposition from a turbulent stream to a rough boundary. The formulation calculates the frazil accumulation on the bed particles in two stages. The first is the turbulent diffusion of frazil particles from the turbulent core to the roughness layer and the second is the attachment of frazil crystals to the bed material once inside the roughness layer. Outside the roughness layer, a traditional logarithmic velocity profile is used and the vertical frazil concentration is defined as a function of the buoyant velocity of the frazil particles and the surface eddy diffusivity. Inside the roughness layer, the rate of deposition of frazil on the roughness elements is dependent on the frazil concentration profile in the layer, which is a function of the turbulent mixing of the flow, as well as the geometry and distribution of the roughness elements themselves. The removal of frazil by the roughness elements is also governed in the model by a coefficient, $\eta_{e,m}$ , which is the deposition efficiency for the m$^{th}$ bed particle size. The value of $\eta_{e,m}$ is related to the size, density, and removal efficiency of the roughness elements and needs to be specified by the modeler. The heat exchange between supercooled water and the frazil and anchor ice is ignored in this model. The deposition rate ($S_i(y)$) can be expressed as

$$S_i(y) = \frac{3}{2}\frac{\eta_{e,m} C_m}{D_{x,m}} \int_0^{D_{y,m}} C(y) V_w(y) dy \,, \qquad \textbf{(1.4)}$$

where $C_m$ = area concentration of the m$^{th}$ bed particle size, $C$ = suspended frazil concentration, $V_w$ = water velocity, and $D_{x,m}$ and $D_{y,m}$ = bed particle diameters in the streamwise and vertical direction respectively.

#### 1.2.2.5 Qu (2006)

A one-dimensional mathematical model using a two-stage method (similar to Hammar and Shen, 1995) was developed to simulate the process of frazil ice transport and deposition to form anchor ice. Anchor ice growth due to frazil accretion and the growth and decay due to turbulent heat transfer are all considered in the model. The velocity distribution and frazil ice transport and deposition inside as well as outside the roughness layer are simulated with this model. The frazil ice concentration distribution inside the roughness layer along with a deposition coefficient ($\beta_3$) governs the accretion rate of frazil ice. The growth rate of anchor ice thickness ($h_{an}$) is expressed in this model as

$$\frac{dh_{an}}{dt}\frac{1}{1-e_a}\left(S_* + \frac{\phi_{an}}{\rho_i L_i}\right), \tag{1.5}$$

where $\phi_{an}$ = heat flux from the anchor ice to the channel flow, $\rho_i$ = density of ice, $L_i$ = latent heat of fusion of ice, and $e_a$ = porosity of anchor ice. The total deposition rate over the depth of the roughness layer ($S_*$) is written as

$$S_* = \int_{0.55k_{s2}}^{k_{s2}} \frac{\beta_3}{D_x} C(y) V_w(y) dy\,, \tag{1.6}$$

where $D_x$ = bed gravel diameter in the stream-wise direction, $k_{s2}$ = roughness height, $C$ = suspended frazil concentration, and $V_w$ = water velocity.

Predicted anchor ice growth rates from the numerical model above were compared to those obtained through physical experiments with good agreement. Thermal as well as mechanical release processes are also included in this model.

#### 1.2.2.6 Bisaillon and Bergeron (2009)

The meteorological and hydraulic conditions conducive to the formation of anchor ice were studied in three gravel bed rivers in southern Quebec. Ten continuous predictors related to air temperature and water temperature were used to develop a logistic regression model of anchor ice presence and absence. The statistical model found that the variables FDH-12 (freezing degree hours accumulated over 12 hours) and the local Froude number were the most effective in predicting the presence of anchor ice in these rivers. While the above are very site specific parameters, it is worth mentioning that the model indicated that anchor ice was most likely to form at Froude numbers greater than 0.1, which is slightly lower than the values of 0.148 found by Kerr *et al*., (1997) and 0.2 by Terada *et al*., (1998).

## 1.3 Objectives of this Study

As illustrated above, the impacts of river ice on engineering projects around the world are numerous. This is evident on a local level when considering the effects of river ice on hydroelectric power production in northern Manitoba. Limitations exist in laboratory and field work (section 1.1) and currently, the most efficient way to assess and study river ice phenomenon is through the development and application of numerical simulation models. Even though the present body of knowledge surrounding the analytical processes of river ice formation is at times limited, it continues to be developed. To this end, the further development of a numerical model has many advantages and will be the focus of this research. More specifically, the objectives of this research will be:

1) Obtain comprehensive knowledge of the CRISSP2D model structure and formulations;

2) Develop a coupled anchor ice and aufeis sub-module for CRISSP2D with the necessary refinements to the freeze-up components of the model;

3) Conduct ideal channel simulations to test developed model formulations (as a validation of the model) and conduct a sensitivity analysis on a few relevant model parameters;

4) Test the anchor ice and aufeis model using the Sundance Rapids case study;

5) Conduct a larger scale test on a section of the Lower Nelson River to test the applicability of the freeze-up model on a longer stretch of the river; and

6) Identify areas of future work and research.

**Figure 1.1 -** Frazil ice pans on the Nelson River, Manitoba, Canada – February, 2006.

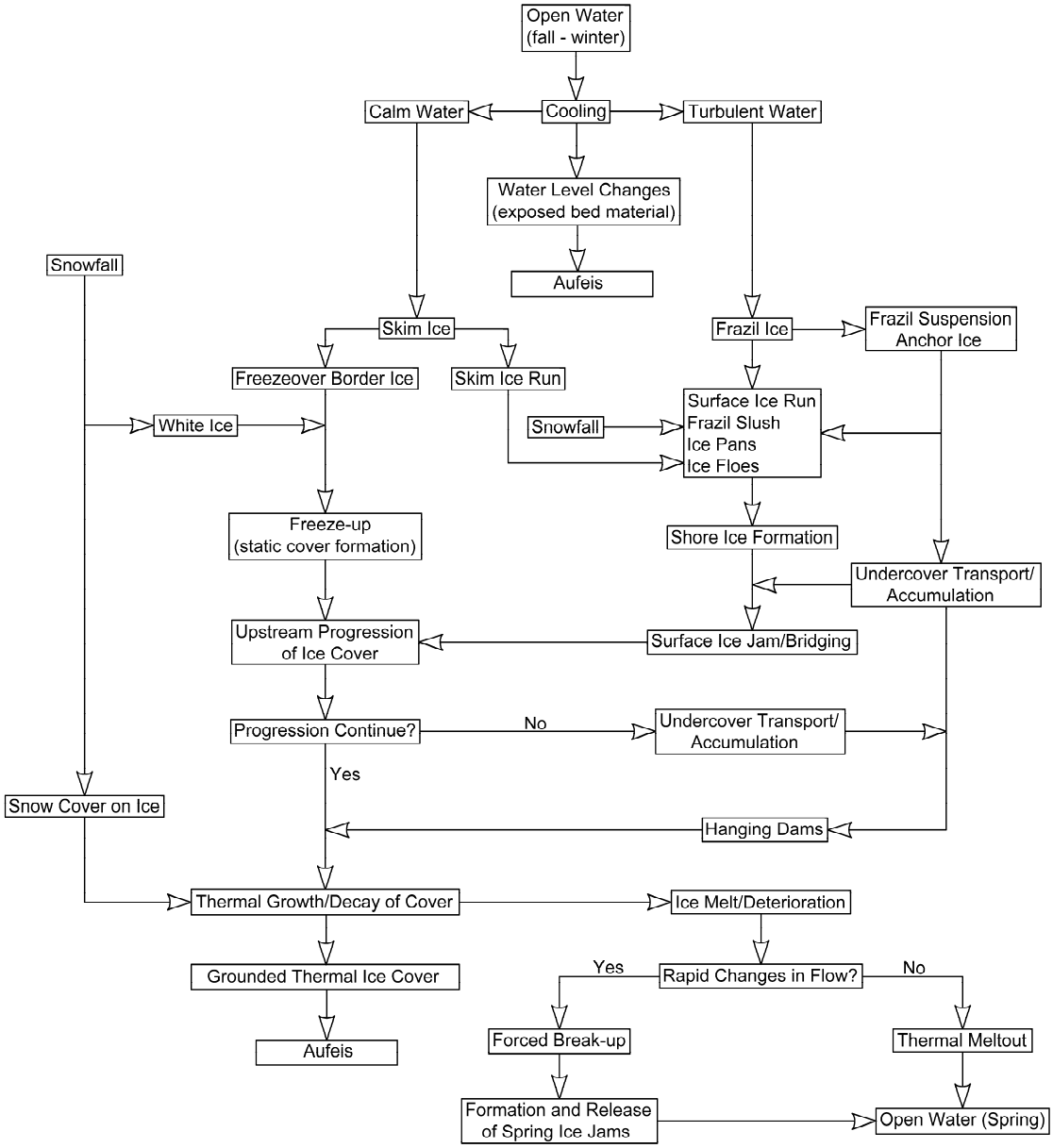


**Figure 1.2 -** Schematic of the complete river ice process. (after Shen, 2002)

**Figure 1.3 -** Anchor ice dam at Sundance Rapids, Manitoba, Canada – February, 2006.

**Figure 1.4 -** Ice buildup upstream of the Kelsey Generating Station, Manitoba, Canada.

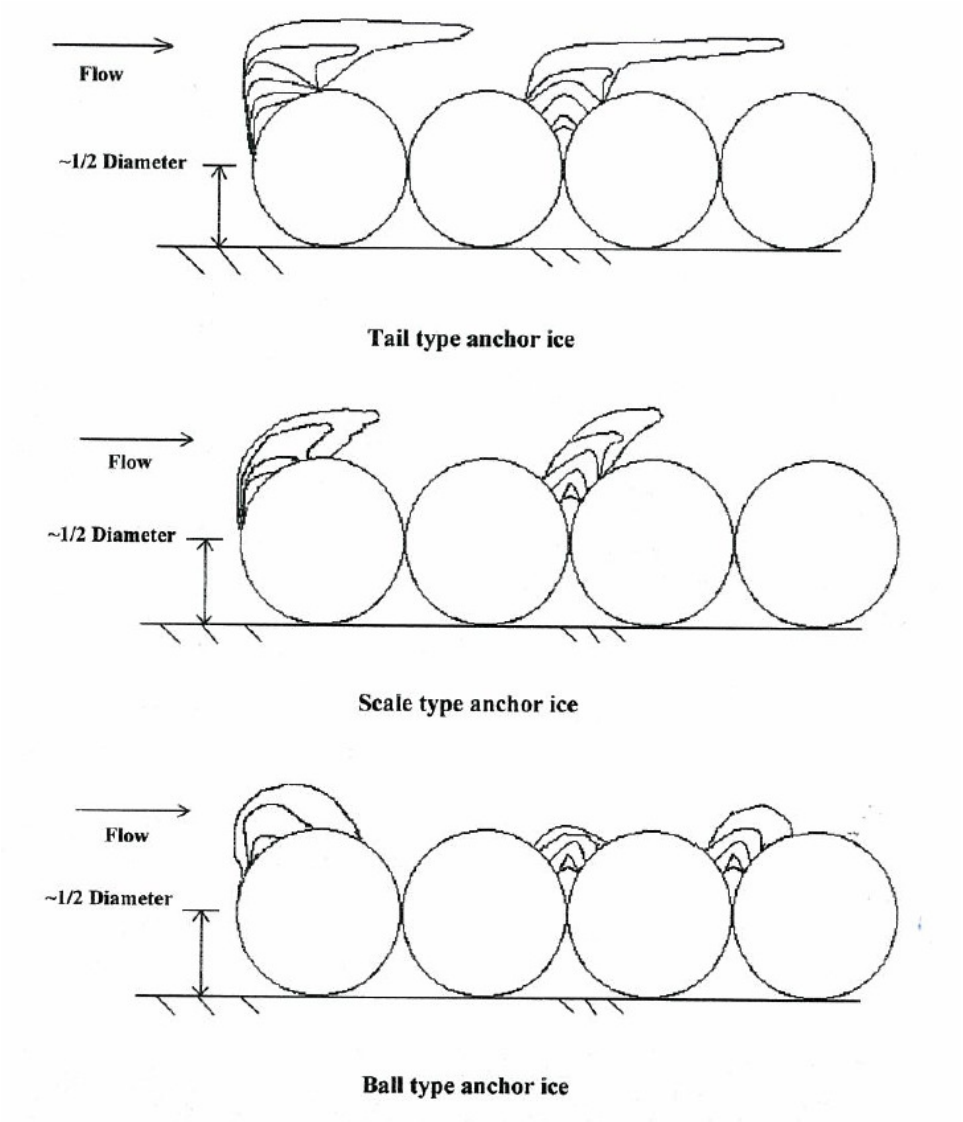


**Figure 1.5 -** Initial anchor ice growth forms (tails, scales, and balls). (Kerr *et al.*, 2002)

CHAPTER 2

# Numerical Model

## 2.1 Introduction to CRISSP

In September of 2000, a consortium of hydropower companies, including Manitoba Hydro, initiated the Comprehensive River Ice Simulation System Project (CRISSP). Each individual company had their own unique ice engineering issues to deal with and under the coordination of the Center for Energy Advancement through Technological Innovation (CEATI), it was determined that the development of a comprehensive numerical model that was capable of simulating the entire river ice process would benefit all parties involved. Since the development of a numerical model was underway at Clarkson University (Potsdam, NY), Dr. Hung Tao Shen and his group were chosen to be the primary researchers in the development of a 1-dimensional and 2-dimensional version of the program. This phase of the project reached completion in October 2005 with the release of CRISSP1D 1.0 and CRISSP2D 1.0. At this point, Manitoba Hydro expressed an interest in detailed testing of CRISSP2D and further model development with a

specific focus on freeze-up ice processes. To this end, some of the primary objectives of this research were establish (see Section 1.3).

CRISSP2D is a state-of-the-art 2-dimensional numerical model written using the FORTRAN 90 programming standard and is capable of simulating most hydrodynamic and ice formation/evolution processes. Its capabilities include but are not limited to the following:

1) an unsteady flow model capable of modeling transitional flow conditions, (*i.e.*, super-critical and sub-critical flows, and dry-wet bed conditions);
2) allowance for complete weather data input;
3) water temperature calculations that include supercooling events;
4) simulation of freeze up processes including frazil ice, anchor ice, border ice, skim ice, and surface ice runs;
5) simulation of the dynamic transport of surface ice and ice jam evolution; and
6) simulation of thermal growth/decay of ice covers as well as mechanical breakup conditions.

Given that one objective of this thesis was to obtain comprehensive knowledge of the current state of the CRISSP2D model, the following sections will review the general structure of the program. Generalized discussions of the model formulations and the capabilities of the sub-model components will also be referenced and presented in this chapter. Since this thesis will be focused primarily on the freeze-up river ice processes,

and more specifically the anchor ice and aufeis growth processes, the components of the model that are essential to these specific processes will be further developed in this thesis and presented in detail in Chapter 3.

### 2.1.1 General Structure

CRISSP2D 1.0 was the numerical model initially used in this research with only minor modifications. A sub-model was then developed to include other freeze-up processes (see Chapter 3) and the code from version 1.0 was cleaned up and streamlined where required. The general computational structure of the program is consistent between the versions so the following discussions on the structure of the model in this chapter are relevant.

The computational engine of CRISSP2D is programmed in structured modular form using INTEL Visual FORTRAN (formerly DIGITAL Visual FORTRAN), which follows FORTRAN 90 and 95 standards (Shen, 2002). The structured modular form was chosen because it allows future developers to conveniently update individual formulations as new relationships are developed. The computational logic of a CRISSP2D simulation can be broken down into 5 distinct steps. Each of these steps is summarized below and with the help of Figure 2.1, illustrates the flow of calculations in a complete CRISSP2D simulation where all of the sub-models have been activated.

Step 1 – Initialization of Simulation and Input of Data

This step is done once at the beginning of every simulation. The input parameters and geometry data are read and setup. Timing tables are constructed for the input data (weather, variable boundary flux and elevations, inflow water temperatures, and ice fluxes) and output data (longitudinal profiles, discharge and elevation output). Optimal time steps are checked and boom data is read if available. For a hotstart simulation, hydrodynamic (water levels and velocities) and ice dynamic (water temperatures, border ice locations, ice cover thicknesses and ice parcel locations and properties) values are initialized. If hotstart data is not available, default values are used as a starting point for the simulation and a "spin-up" period is often required.

Step 2 – Finite Element Calculations

These calculations are explicitly carried out for each hydrodynamic time step ($\Delta t_h$) and continue until the next coupling interval of hydrodynamics and ice dynamics is reached ($t_{intvl}$), see Figure 2.1. They include the finite element calculations for: 1) hydrodynamics, 2) the advection and diffusion of water temperature, and 3) the advection and diffusion of suspended frazil concentration. The output timing tables are referenced and output data are printed to the appropriate file if required. Boundary condition timing tables are also referenced at each of these time steps and updated if necessary.

Step 3 – Initial Coupling Interval Calculations

These calculations are done once at every coupling interval ($t_{intvl}$). They are done primarily on a node by node or element by element basis. They include ice cover

breakup checks, border ice, skim ice, anchor ice, thermal growth of frazil ice concentration, and thermal growth/decay of ice cover calculations. Nodal and elemental parcel statistics are calculated and ice mass exchanges between the suspended and surface ice layers are evaluated. The undercover transport calculations are also carried out at each coupling interval along with the checks for jammed ice parcels. An update of the weather timing table is carried out at this time interval as well.

Step 4 – Ice Dynamic Calculations

The ice dynamic calculations are initiated at each new coupling interval time, they jump back to the previous coupling interval time and continue incrementally to the current coupling time using the ice dynamic time step ($\Delta t_i$), see Figure 2.1. The most recent finite element data calculated in Step 2 is used throughout this portion of the simulation. For example, if the coupling interval is 900 seconds, the finite element data calculated at time = 900 s is used in the ice dynamic calculations from time = 0 – 900 s. In this way, the hydrodynamic and ice dynamic calculations are said to be loosely coupled. Ice flux calculations are carried out at each of these time steps. Ice parcel positions, velocities, and properties (area, concentration, mass density, and internal stress) are evaluated. An ice parcel within CRISSP2D is a surface ice quantity that is of a variable size that carries the abovementioned information. It is these parcels that enable the Lagrangian calculations to be carried out during the ice dynamic calculations. Free drift calculations are carried out at this time (if parcel interaction is not required and only parcel position needs to be tracked) along with ice boom conditions and parcel image information. Smooth lengths in the SPH calculation of ice dynamics are updated and the wind and

gravity forces are applied. If required, the ice dynamic data is output to the appropriate file.

Step 5 – Final Coupling Interval Calculations

In this step, the final coupling calculations are completed. These include nodal ice thicknesses, nodal and elemental parcel statistics and parcel images around the boundaries. Essentially, this portion of the calculations prepares the data for the next round of finite element calculations (Step 2) if required. If the simulation is complete, then all open files are closed and saved which completes the simulation.

## 2.2 Model Components

CRISSP2D was developed as a generalization of the DynaRICE model (Shen *et al*., 2000), which simulated the coupled dynamics of ice motion and water flow but did not consider any thermal effects. Thermal characteristics were added to DynaRICE by utilizing 2-dimensional extensions of the river ice formulations developed for the RICE (Lal and Shen, 1991) and RICEN (Shen *et al*., 1995) models previously. The CRISSP2D model has been applied to an assortment of field cases (Malenchak *et al.*, 2006 and 2008; Wojtowicz *et al.*, 2009; Brayall and Hicks, 2009; and Bijeljanin and Clark, 2011) that showed many of the capabilities of the model but also identified some limitations and areas of further refinement. Brief summaries of the individual model components will be shown in the bullets below and detailed references regarding the formulations and implementation can be found in Li (2005) and Liu and Shen (2005). As mentioned

previously, a detailed discussion of the model formulations relevant to the simulation of the anchor ice and aufeis growth processes will be in chapter 3. This includes an expanded presentation of the energy budget calculations, the surface ice mass exchange formulation (including rapids entrainment), anchor ice and aufeis growth processes, and an improved dry-bed treatment formulation.

- **River Hydrodynamics**

The hydrodynamic sub-model solves the two-dimensional, depth-averaged, unsteady free-surface shallow water flow equations using an explicit finite-element implementation of the streamline upwind Petrov-Galerkin concept (Liu and Shen, 2003). With this formulation, the model is capable of simulating all flow regimes including transitional and super-critical flows. A modified explicit time integration technique called the leapfrog method is applied, which is conditionally stable provided the time step is chosen sufficiently small to meet the stability criteria (Liu and Shen, 2005). Also included is the effect of surface ice on the flow and the seepage flow through the surface ice layer. This enables the model to simulate the flow through an ice jam, which in turn allows the model to simulate grounded ice jams, which is a property exclusive to this model. A simplified dry-bed treatment was originally included in the model and this formulation is improved and expanded upon in section 3.6.

- **Water Temperature and Frazil Concentration**

An equation was developed to describe the transport of thermal energy for an ice-water mixture (*i.e.*, river water with suspended frazil ice). This equation includes the advection

and diffusion related transport of thermal energy, the source and sink terms due to heat transfer at the river bottom and the surface, the heat exchange between the suspended frazil and the river water, as well as the mass exchanges between suspended and surface ice. The solution of the above transport equation can be divided into 2 parts. The first is a lumped formulation (no upwinding) of the Galerkin finite element method which is employed to solve the conservation equations of water temperature and suspended frazil concentration including the advection, diffusion, and heat source/sink terms at the top and bottom boundaries (Liu and Shen, 2005).

In addition to the finite element calculations above, changes in water temperature and frazil concentration due to the thermal growth of the suspended frazil ice are calculated on a nodal basis using a Lagrangian form of the equations. Suspended frazil ice concentration is calculated volumetrically in the model and a constant frazil particle size (frazil particle diameter ($d_f$) and thickness ($d_e$)) must be specified by the modeler. The change in suspended frazil concentration due to thermal growth of the frazil particles ($DC_v^g/Dt$) is calculated using a finite difference form of the following equation

$$\frac{DC_v^{\,g}}{Dt} = -\frac{1}{\rho_i L_i}\frac{N_u^{\,f} K_w}{d_e} a_o T_w N_f, \qquad \textbf{(2.1)}$$

where $\rho_i$ = density of ice (kg/m$^3$), $L_i$ = latent heat of fusion of ice (J/kg), $N_u^f$ = Nusselt number (specified by the modeler and used to characterize the average heat transfer coefficient between a frazil particle and the water), $K_w$ = thermal conductivity of the water (W/mºC), $a_o = \pi d_f d_e$ (surface area of a frazil particle normal to the a-axis

(thickness) of the frazil disc, $m^2$), $T_w$ = water temperature (ºC) and $N_f$ = number of frazil crystals per unit volume. As indicated above, the Nusselt number in equation 2.1 ($N_u^f$) is a dimensionless parameter to be specified by the modeler and is defined as the ratio between the convective and conductive heat transfer. It is a function of the frazil particle size, shape and orientation to the flow as well as the turbulent heat transfer between the frazil particle and the water.

The changes in frazil concentration due to frazil mass exchanges with the water surface and the bed material are also calculated in this nodal manner. These changes are then coupled with the finite element results to obtain a complete solution for the water temperature (including supercooling events) and suspended frazil concentration. The size of suspended frazil particles in the model is a user defined parameter that does not change throughout a simulation. Any thermal growth over time simply serves to increase the volumetric suspended frazil concentration and not the size of the particles themselves.

- **Energy Budgets**

In order to accurately simulate river ice processes, one must be able to calculate the energy fluxes that occur between the water, the atmosphere, the ice cover, the anchor ice and the riverbed. The prevailing portion of heat transfer occurring through the top surface of the river water. Provided that complete weather data is available, detailed calculations regarding this heat transfer can be completed. These calculations include contributions from solar radiation, back or terrestrial radiation, evaporative heat transfer, conductive heat transfer, and heat transfer due to precipitation (Liu and Shen, 2005).

When required, linear heat exchange approximations can be used in the absence of complete weather data records. This component of the model will be presented in detail in section 3.2.

- **Thermal Growth and Decay of Ice Floes and Cover**

Thermal growth and decay of an ice floe or an ice cover is an important part in the simulation of river ice processes. The existence of surface ice can have a significant effect on the flow regime and the thickness of the ice cover plays an important role in cover stability and breakup. In this sub-model, an ice floe is considered the same as a moving ice cover when calculating thermal growth and decay (Liu and Shen, 2005). Depending on the direction of the heat transfer at the boundaries with the atmosphere and the river water, an ice cover can melt from the bottom, melt from the top, grow from the bottom, or any combination of the three. This sub-model also takes into account the insulating effects of snow on top of an ice cover as well as the presence of frazil ice deposited on the underside of an ice cover, which can serve to accelerate the growth or decay of the cover at the bottom boundary. The principles of thermal growth and decay of an ice cover (Shen and Chiang, 1983; Shen and Yapa, 1985) are extended to include the formation of a solid crust thickness within an ice jam as well as in the formation of individual solid aufeis layers (see section 3.5).

- **Mass Exchange Between Suspended and Surface Layers**

The total ice discharge in the model is divided up into a suspended layer and a surface layer. Mass exchanges between these two layers as well as exchanges between the

suspended layer and the river bottom are important considerations in river ice formation and simulation. Suspended frazil particles may be deposited to the surface layer in areas of open water as frazil slush, or deposited to the underside of an existing ice cover or ice floe. This mass exchange process is quantified by the coefficient $\alpha$. This deposition can increase the frazil portion of the thickness of ice cover or ice floe which will then be subject to thermal growth and decay. Under turbulent conditions, frazil ice on the undersurface of ice floes can be entrained back into the suspended layer which is quantified by a separate coefficient, $\beta$. These coefficients, along with the average rise velocity of frazil particles ($v_b$), help this sub-model simulate the effect of turbulent conditions on these exchange processes. Mass exchange between the suspended layer and the river bottom is accounted for in the anchor ice sub-model. The calibration of these mass exchange parameters is often necessary when applying the model to field cases and should be chosen carefully by the modeler. An extension of this sub-model to include the entrainment of surface ice parcels at a rapids section of the river is presented in section 3.3.

- **Border Ice and Skim Ice Formation**

Typical ice cover on a river often first appears as static border ice developed in the form of skim ice along the banks. The existence of static border ice is calculated empirically using the thermal and mechanical conditions defined by Matousek (1984) coupled with an attachment criteria. These calculations are carried out on a node by node basis and if the following four criteria are met, the node will be considered border ice:

1) water surface temperature ($T_{ws}$) is less than a critical water temperature ($T_{cr}$) which is less than 0ºC;
2) buoyant velocity of a frazil particle at the surface ($v_b$`) is greater than the vertical turbulence velocity ($v_z$`);
3) local depth averaged velocity ($V_w$) is greater than a critical value ($V_{cr}$); and
4) an attachment criteria that requires that a new border ice node be attached to either a bank node or an existing border ice node.

The surface water temperature ($T_{ws}$) is calculated using the following empirical relationship (Matousek, 1984a, 1990)

$$T_{ws} = T_w - \frac{\phi_{wa}}{1130u + bW}, \qquad \textbf{(2.2)}$$

where $T_w$ = local water temperature (ºC), $u$ = local water velocity (m/s), $\phi_{wa}$ = rate of heat loss to the atmosphere (W/m$^2$), $W$ = wind velocity at an elevation of 2 m above water surface (m/s), and $b$ = wind fetch coefficient related to the width of the channel surface (B) in the wind direction (where B is taken as the square root of the nodal area in the model).

$$b = 15.0 \qquad \text{(B <= 15.0 m)} \qquad \textbf{(2.3a)}$$

or

$$b = -0.9 + 5.87 \ln B \qquad \text{(B > 15.0 m)} \qquad \textbf{(2.3b)}$$

The buoyant velocity of the frazil particles at the surface ($v_b$`) is also determined using an empirical equation (Matousek, 1990) relating $v_b$` to $T_{ws}$

$$v_b^{'} = -0.025T_{ws} + 0.005, \quad \textbf{(2.4)}$$

Matousek (1990) also developed an equation for $v_z$`, which considered bed shear effects only, but as a modification to this criteria Lal and Shen (1989) developed an equation that considered both bed and wind shear effects at the water surface using the approach for vertical mixing in lakes (Fischer, *et al*., 1979).

In areas of particularly low water velocity and low turbulence intensity, skim ice can form on the river surface. The formation of skim ice in the model is also calculated using the empirical criteria defined by Matousek (1990) but in this case the calculations are performed on the finite elements. The criteria for skim ice formation in the model requires:

1) surface water temperature ($T_{ws}$) < 0ºC;
2) buoyant velocity of surface frazil particles ($v_b$`) > ($v_z$`); and
3) element not covered by border ice or an ice cover.

In both the static border ice and skim ice criteria above an important part of the formulation is the consideration of the turbulent fluctuations at the surface.

In addition to static border ice formation and in locations where static border ice does not form a complete ice cover across the river, dynamic border ice growth may occur due to the accretion of floating surface ice to the existing static ice. It is this ice cover growth that allows for the progressive closure of a river surface from the banks as the border ice grows towards the center. Relationships to describe the dynamic border ice growth mechanism have been developed by Michel *et al*. (1982), Newbury (1968) and Miles (1993). The dimensionless relationship developed by Michel *et al*. (1982), which is based on field observations in the St. Anne River, is employed in the model. The rate of lateral border ice growth ($dW_{bi}/dt$) is calculated using

$$\frac{dW_{bi}}{dt} = \frac{\phi_{wa}}{\rho_i L_i} 14.1 V_*^{-0.93} C_a^{1.08}, \qquad \textbf{(2.5)}$$

where $\phi_{wa}$ = rate of heat loss to the atmosphere (W/m$^2$), $\rho_i$ = density of ice (kg/m$^3$), $L_i$ = latent heat of fusion of ice (J/kg), $V_* = V_w/V_c$ (where $V_c$ is a maximum velocity for dynamic border ice growth, and $V_w$ = the local water velocity, m/s), and $C_a$ = surface ice concentration adjacent to the existing border ice edge. A range for $V_c$ has been observed in the field between 0.4 m/s (Matousek, 1984; Shen and Van DeValk, 1984) and 1.2 m/s (Michel, 1982).

- **Anchor Ice and Aufeis Formation**

The simplified analytical formulation developed by Wang and Shen (1993) and Shen *et al*. (1995) forms the basis for the anchor ice sub-model. Here, the formation of anchor ice is assumed to be initiated by the attachment of frazil crystals to the bed material in

supercooled water. This accretion of frazil crystals is further assumed to begin at a theoretical bed level below the crown of bed material. The continued growth of anchor ice is considered to be due to the turbulent heat exchange between the supercooled river water and the anchor ice as well as due to the continued accretion of frazil ice. The anchor ice will not completely fill the voids between the bed particles and as such, a channel of substrate flow will form on the underside of the anchor ice. This flow can either contribute to the growth of the anchor ice, if supercooled conditions exist, or erode the anchor ice from the substrate surface.

The release of anchor ice is a very important but complicated process that has both thermal and mechanical components, both of which are considered in the current model. The anchor ice is assumed to release thermally when the substrate flow erodes the under-surface of the ice to a level of $0.4d_s$ ($d_s$ = diameter of top layer of bed material) above the centerline of the bed material (see section 3.4). The anchor ice can also be mechanically detached from the bed. This occurs when the buoyant force of the anchor ice overcomes the submerged weight and inter-particle resistance of the bed particles combined. Once the anchor ice is released, it floats to the surface where it is added to the frazil portion of the surface ice concentration and/or floe thickness. The above formulation is developed further in Chapter 3 of this thesis and an aufeis growth mechanism is added to the formulation.

- **Undercover Transport and Frazil Jams**

When suspended (frazil) ice approaches a competent ice cover it can be transported underneath the cover, deposited on the underside, or a combination of the two. This process is simulated in the model using a 2-dimensional extension of the frazil transport capacity theory developed by Shen and Wang (1995). This theory states that for given flow conditions and ice particle characteristics, a corresponding frazil transport capacity exists. If the incoming suspended ice discharge is greater than this capacity, deposition will occur. Erosion of the frazil layer on the underside of the cover will occur if the ice discharge is less than the defined capacity. This theory is analogous to many sediment transport theories and allows for the simulation of frazil (hanging) jams. The ice transport capacity is estimated by

$$\phi_{uc} = 5.487\left(\theta_f - \theta_{fc}\right)^{1.5}, \tag{2.6}$$

where $\theta_{fc}$ = 0.041, and is the critical flow strength below which there is no ice transport and,

$$\phi_{uc} = \frac{q_{ic}}{d_n F\sqrt{g d_n \Delta}}, \tag{2.6a}$$

$$\theta_f = \frac{{u_{*i}}^2}{F^2 g d_n \Delta}, \tag{2.6b}$$

where $q_{ic}$ = volumetric rate of ice transport per unit width (or ice transport capacity) ($m^2/s$), $d_n$ = nominal diameter of undercover ice particles (m), $u_{*i}$ = shear velocity on the underside of an ice cover or frazil jam (m/s), $F$ = shape factor for ice particles (approximately 1.0 for spherical particles), and $\Delta = (\rho_w - \rho_i)/\rho_w$.

- **Dynamics of Surface Ice Transport**

The previously developed DynaRICE model (Shen *et al*., 2000) is included as a sub-model in order to simulate the dynamics of surface ice transport. This is done using a Lagrangian discrete parcel method (Shen *et al*., 1993). The basic concept of this method is that river ice, considered a continuum, can be represented by a sufficiently large number of ice "parcels". Each individual parcel is tracked through the model domain and carries mass, momentum, and energy. The properties of each parcel include position, velocity, thickness, density, mass, concentration, internal stress and strain. The non-advective terms from the above list are calculated using the properties of parcels within an appropriate distance of the reference parcel through kernel interpolation (Liu and Shen, 2005). This interpolation is based directly on the Lagrangian parcels themselves. A viscoelastic-plastic (VEP) model is used to calculate the internal stresses (Ji *et al*., 2004). This formulation allows forces to be calculated at the boundaries of the model and at the locations of ice booms. The model is also able to simulate grounded ice jams when this formulation is coupled with the previously mentioned hydrodynamic sub-model. The model also allows for the ice dynamic calculations described above, which can be computationally intensive, to be replaced by free drift calculations which only track the

ice parcel evolution as it travels down the river without including the interaction of other parcels (*i.e.*, does not consider the internal stresses in the parcels).

- **Ice Cover Breakup**

River ice breakup typically falls into one of two broad categories, either mechanical breakup or thermal meltout. Mechanical breakup occurs when an otherwise competent ice cover is forced to breakup by hydraulic (river wave) or mechanical (incoming rubble ice) forces. Thermal meltout occurs when the ice cover melts in place with little to no movement or adjustment of the deteriorating cover and is considered in the thermal growth and decay portion of the model. A clear analytical formulation for the occurrence of mechanical breakup of river ice currently does not exist. Therefore, empirical predictive methods are used to determine when and where breakup will occur. In this sub-model, the user can simulate this breakup using one or all of the following four methods:

1) user specified time and location of breakup;
2) a critical water surface elevation ($H_{cr}$) for breakup may be specified;
3) a critical change in water surface elevation ($\Delta H_{cr}$) over a specified time period can induce mechanical breakup; and
4) the $\Delta H_{cr}$ can be related to the thickness of the ice cover at any given time which tries to provide a measure of the cover stability.

## 2.3 Model Requirements

The typical procedures involved with a CRISSP2D model study are not unlike those carried out for most other studies that are numerical in nature. In a general sense, the steps include: 1) collection and preparation of input data, 2) calibration and verification of hydrodynamic components, 3) calibration and verification of thermodynamic and ice dynamic components (if data is available), 4) carry out scenario simulations, and 5) analyze the results obtained. The detail that steps 2) and 3) may be carried out depends on the available data. It has been documented that the absence of good quality field data has been in the past and will continue to be an impediment to future development and use of river ice numerical models (Shen, 2003). Whenever data is not available, the default or "typical" model parameters are used for the primary simulations and later iteratively modified. This can be a very time consuming process considering the complex interactions that take place throughout the river ice formation and evolution process. The existence of extended (see below) sets of input data would be beneficial in this regard as it would help to streamline the calibration of some of these model parameters.

In the two lists below, typical and extended sets of input data will be identified. The primary data being the sets required for even the most basic simulations and the extended data being those that would serve to calibrate the river ice process components and make the simulations more accurate. This will illustrate how little data is actually required to set up a model and also how extensive the input data set can be if it is available. It is important to note that a higher quantity of good quality field data will typically increase

the accuracy of any numerical model which will assist in the accurate specification of the boundary and initial conditions for the model.

**Typical Input Data Sets**

- reach boundary geometry and river bed bathymetry;
- input and/or output river flows;
- water levels at flow boundaries and/or other monitoring locations; and
- air temperature data or seasonal norms (most basic weather data accepted).

**Extended Input Data Sets**

- complete weather data (air temperature, atmospheric pressure, dew point, cloud cover, precipitation, etc.);
- boundary ice fluxes;
- water temperature measurements;
- frazil ice particle size and concentration (observation tools currently being developed);
- surface ice conditions (border ice extents, ice floe concentration and velocity);
- anchor ice locations and thicknesses (bed particle size distributions);
- location of leading edge of ice cover;
- stable ice cover thickness;
- river ice jam and hanging jam location and thicknesses;
- strengths of rubble ice floes and accumulations; and

- location and times of river ice breakup and associated measurements of water/ice velocity and water levels.

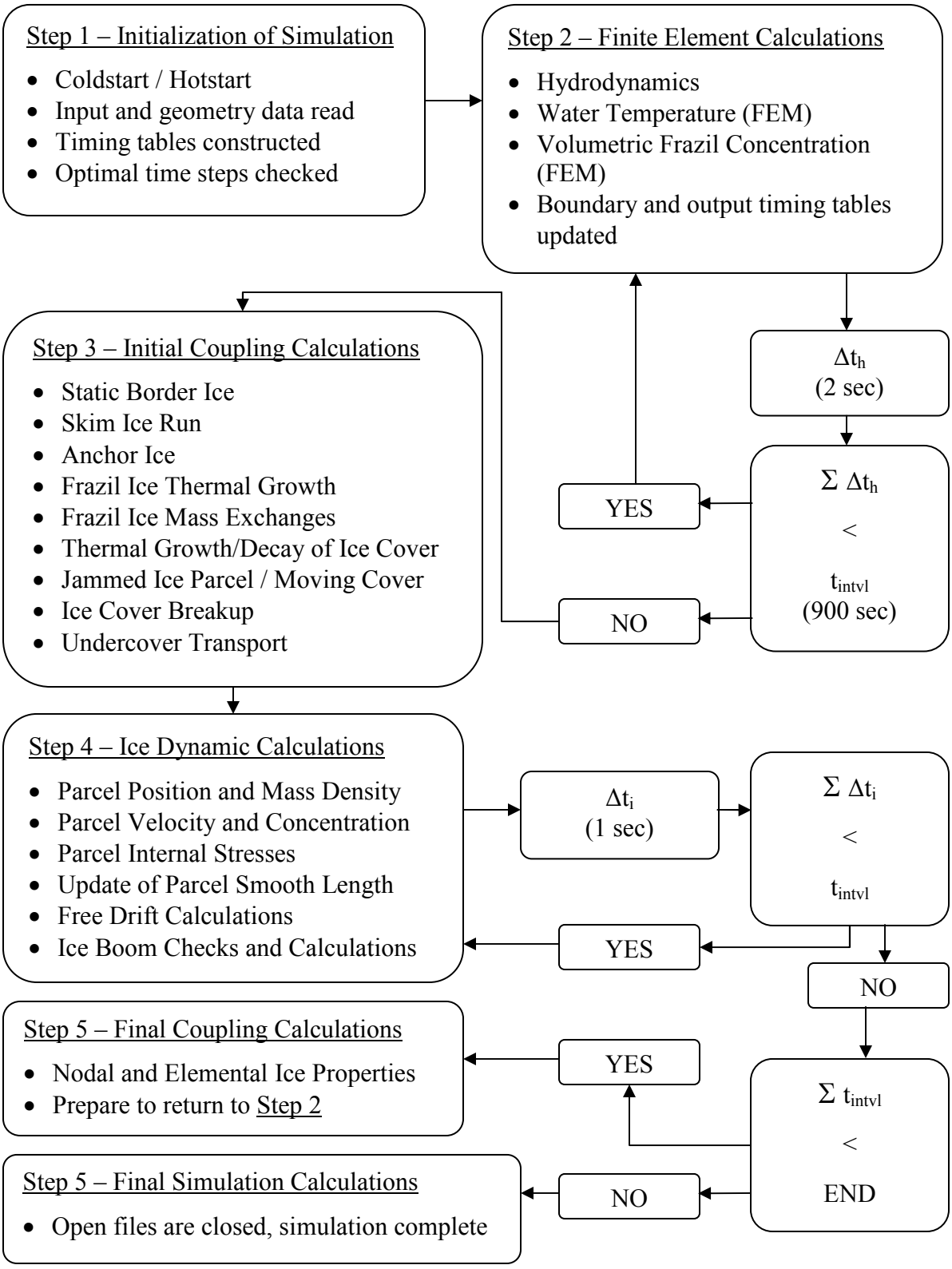


**Figure 2.1 -** Computation structure of the CRISSP2D program.

CHAPTER 3

# Aufeis and Anchor Ice Growth

## 3.1 Introduction

The formation and evolution of aufeis and anchor ice are very complex processes and as such, many numerical models either neglect or simply approximate these phenomena. While an overview of the two-dimensional model components can be found in Chapter 2, the following sections will detail the numerical model formulations developed for this thesis and those most significant to the formation and evolution of aufeis and anchor ice. The development of the sub-models for this application is focused primarily on these components which include: 1) energy budget, 2) suspended and surface ice exchange, 3) anchor ice growth and release, 4) aufeis growth and release, and 5) dry bed treatment.

## 3.2 Energy Budget

An important component in any river ice model is the ability to model the heat transfer (or energy budget) at the surface of the river. In many numerical models, the components of the energy budget are often approximated using a single linear heat transfer coefficient that relates the amount of heat transfer at the river surface to the difference in air and water temperatures. This is an important approximation in cases where detailed meteorological data is not available at the site and/or where the ice processes being modeled are not particularly sensitive to the diurnal variations in the heat transfer rate.

### 3.2.1 Linear Heat Transfer Method

For an open water area, the heat loss at the river surface ($\phi_{wa}$) is calculated as

$$\phi_{wa} = h_{wa}(T_w - T_a), \tag{3.1}$$

where $h_{wa}$ = open water heat transfer coefficient (W °C$^{-1}$ m$^{-2}$), $T_w$ = water temperature (°C), and $T_a$ = air temperature (°C). For rivers in the northern United States, the value of the heat exchange coefficient $h_{wa}$ is of the order 20 W °C$^{-1}$ m$^{-2}$ (Lal and Shen, 1991) and is a calibration parameter that can vary significantly at each specific location. A similar linear heat transfer relationship is used to calculate the heat exchange between the river water and ice at the ice-water interface (ice cover or anchor ice interface). For the ice covered area, the heat exchange between the ice and water ($\phi_{wi}$) is calculated by

$$\phi_{wi} = h_{wi}(T_w - T_m), \quad \textbf{(3.2)}$$

where $h_{wi}$ = water-ice heat transfer coefficient (W °C$^{-1}$ m$^{-2}$), $T_w$ = water temperature (°C), and $T_m$ = melting temperature of ice (0 °C). The water-ice heat transfer coefficient $h_{wi}$ is a function of the water temperature and flow conditions at that particular location. For fully developed turbulent flow, *i.e.*, when the Reynolds number ($R_e$) is greater than 2200, $h_{wi}$ is calculated using the following formula (Liu and Shen, 2005)

$$h_{wi} = c_{wi} \frac{V_w^{0.8}}{D_h^{0.2}}, \quad \textbf{(3.3)}$$

where $V_w$ = water velocity magnitude (m/s), $D_h$ = local hydraulic diameter (m, $D_h = 4*d_w$ ($d_w$ = water depth) for open water conditions, or $D_h = 2*d_w$ for ice covered conditions), and $c_{wi}$ = an input constant that is a function of water temperature (m$^{0.4}$s$^{0.8}$, 1118 for supercooled conditions ($T_w$ <= 0°C), or 1448 for $T_w$ > 0°C). The length and velocity scales used in the calculation of $R_e$ is hydraulic diameter (m) and water velocity (m/s), respectively. The values for $c_{wi}$ can vary substantially when flow and ice conditions change and therefore are accepted as inputs to the model.

For specific cases where fully developed laminar flow exists, *i.e.*, substrate flow between the undersurface of anchor ice and the river bed particles ($R_e$ < 2200), $h_{wi}$ is calculated using (Liu and Shen, 2005)

$$h_{wi} = \frac{N_u K_w}{D_h}, \tag{3.4}$$

where $N_u$ = Nusselt Number (ratio of convective to conductive heat transfer), and $K_w$ = thermal conductivity of water ($Wm^{-1}°C^{-1}$). Since detailed studies of anchor ice are limited, the Nusselt number for the substrate flow under anchor ice is accepted as input data.

The total heat transfer at the river surface is calculated as the combination of the heat exchange over the open water area and the heat exchange at the ice-water interface using

$$\phi_T = (1 - C_a)\phi_{wa} + C_a\phi_{wi}, \tag{3.5}$$

where $C_a$ = surface ice concentration (stated as a ratio between 0 and 1), and $\phi_{wa}$ and $\phi_{wi}$ are as defined above. This last formula is the same for the detailed thermal budget calculations with the difference being that $\phi_{wa}$ is calculated in a more rigorous manner (see section 3.2.1 below).

The heat transfer between the river water and the bed material is not considered in the model. For most rivers with open water areas, the heat exchange at the surface is the dominate component of the thermal budget calculations (Shen and Yapa, 1984). In rivers that are completely ice-covered over long distances the heat exchange at the bed is a more important component of the river's heat budget (Shen and Chiang, 1983).

### 3.2.2 Detailed Thermal Budget Calculations

For certain cases, when the diurnal variations in heat transfer are important to the river ice processes being simulated or the individual contributions to the overall thermal budget are needed, detailed heat exchange calculations are necessary. The five components considered in the total heat loss at the air-water interface ($\phi_{wa}$) include the net short wave radiation ($\phi_R$), effective back radiation ($\phi_B$), evaporative heat transfer ($\phi_E$), conductive heat transfer ($\phi_H$), and heat exchange due to precipitation ($\phi_P$). The total heat loss at the air-water interface can be written as

$$\phi_{wa} = -\phi_R + \phi_B + \phi_E + \phi_H + \phi_P , \qquad \textbf{(3.6)}$$

The heat transfer at the ice-water interface ($\phi_{wi}$) is calculated as described for the linear case above and the total heat transfer at the river surface is calculated using equation 3.5.

#### 3.2.2.1 Short Wave Radiation

The computation of short wave radiation is a detailed formulation that is based on several astronomical and geographical relationships that are detailed in (Wang and Shen, 1993) and employed during this study. The model's geographic location (*i.e.*, latitude and longitude), the local apparent time (true solar time), the local mean time and the solar constant ($I_{so}$) are the primary inputs into the calculation of the extraterrestrial incident short wave radiation for a simulated time period. The solar constant is accepted as an

input parameter but Ashton (1986) recommends a value of 1380 $Wm^{-2}$ be used for the solar constant in winter time. The net short wave radiation ($\phi_R$), is calculated using the following energy balance equation

$$\phi_R = \left(1 - R_t\right)\phi_{ri}, \tag{3.7}$$

where $\phi_{ri}$ = short wave radiation reaching the earth surface under cloudy skies ($Wm^{-2}$), and $R_t$ = albedo (ice cover surface) or reflectivity (open water surface). The albedo of the ice cover surface is accepted as an input parameter and the reflectivity of the open water surface is estimated using the formulation developed by Anderson (1954) and Brady *et al*. (1969). The short wave radiation reaching the earth surface under cloudy skies ($\phi_{ri}$) is determined using the following equation (Kennedy, 1944)

$$\phi_{ri} = \phi_{cl}\left(1 - 0.0065{C_C}^2\right), \tag{3.8}$$

where $\phi_{cl}$ = short wave radiation reaching the earth surface under clear skies ($Wm^{-2}$), considering an atmospheric attenuation factor, and $C_c$ = cloud cover (in tenths), where $C_c$ = 0 for a clear day and 10 for a cloudy day.

### 3.2.2.2 Effective Back Radiation

The net effective back (or long wave) radiation ($\phi_B$) is often a major component of the total heat loss at the river surface. This is especially the case on clear winter nights and is

the main reason why supercooled water has been observed overnight even if the air temperature is not that cold (Andersson and Andersson, 1992; Morse and Richard, 2009). This component of the total thermal budget is also calculated using an energy balance equation that is written as

$$\phi_B = \phi_{bs} - \left(\phi_{ba} - \phi_{br}\right), \tag{3.9}$$

where $\phi_{ba}$ = the long wave radiation emitted by the atmosphere, $\phi_{br}$ = is the fraction of the atmospheric radiation reflected back by the river surface, and $\phi_{bs}$ = is the long wave radiation emitted by the river surface. The components of the above equation are calculated using primarily the Stefan-Boltzman law with appropriate emissivity coefficients applied (Liu and Shen, 2005 and Shen, 2006). Combining the various components into a single equation, the net effective back radiation is calculated using

$$\phi_B = 0.97\sigma\left[T_{sk}{}^4 - \varepsilon_a\left(1 + kC_c{}^2\right)T_{ak}{}^4\right], \tag{3.10}$$

where $\sigma$ = Stefan-Boltzman constant, 5.67 x $10^{-8}$ ($Wm^{-2}K^{-4}$), $T_{sk}$ and $T_{ak}$ = the absolute river surface temperature and atmospheric air temperature respectively (°K), $\varepsilon_a$ = emissivity of the atmosphere calculated using the Satterlund formula (for $T_{ak}$ <= 273.16 ºK) and the Idso-Jackson formula (for $T_{ak}$ > 273.16 ºK), $k$ = an empirical constant, and $C_c$ = cloud cover (in tenths) as defined for the short wave radiation calculations.

### 3.2.2.3 Evaporative Heat Transfer

A review of 63 evaporation formulas by Paily *et al*. (1974) recommended the Rimsha-Donchenko formula (1957) be used for winter conditions. According to this formula, the evaporative (latent) heat transfer ($\phi_E$) is calculated as

$$\phi_E = \frac{4.1855}{8.64}(1.56K_n + 6.08W)(e_{sat} - e_{at}), \quad \textbf{(3.11)}$$

where $K_n$ = 8.0 + 0.35*($T_w$ - $T_a$) with $T_w$ and $T_a$ being the water and air temperature respectively (°C), $e_{sat}$ = saturated vapour pressure corresponding to the temperature just above river surface (water temperature), $e_{at}$ = vapour pressure corresponding to the air temperature at z = 2 m above the river surface, $W$ = wind velocity (m/s) at z = 2 m. If the wind velocity is not measured at z = 2 m, then the following formula is used to transform the measured value ($W_{az}$ = wind velocity (m/s) at height $z$ (m))

$$W = W_{az}\left(\frac{2}{z}\right)^{0.15}. \quad \textbf{(3.12)}$$

### 3.2.2.4 Conductive Heat Transfer

The conductive heat transfer ($\phi_H$) at the river surface is defined as a fixed ratio of the evaporative heat transfer ($\phi_E$) using the Bowen's ratio ($R = \phi_H / \phi_E$). This approach includes the added heat transfer that occurs when a wind velocity exists. Using a

combination of the Rimsha-Donchenko formula above and the Bowen Ratio the conductive heat transfer is calculated as

$$\phi_H = \frac{4.1855}{8.64}(K_n + 3.9W)(T_{sk} - T_{ak})\,. \tag{3.13}$$

### 3.2.2.5 Heat Exchange due to Precipitation

When precipitation falls over the river surface in the form of snowfall or rainfall it can be a significant form of heat exchange ($\phi_p$). This portion of the total thermal budget can be calculated directly using the following formula provided the snowfall intensity ($I_S$) or rain intensity ($I_R$) is known in mm/hr (Ashton, 1986)

$$\phi_p = \left(92.778 - 0.567T_a\right) I_S \frac{\rho_s}{\rho_w} + 1.163(T_w - T_a) I_R\,, \tag{3.14}$$

where $\rho_s$ = snow density (a user input, kg m$^{-3}$), $\rho_w$ = water density (kg m$^{-3}$), $T_w$ and $T_a$ are the water and air temperature respectively (°C). The snowfall intensity ($I_S$) and/or rain intensity ($I_R$) are often not readily available in weather data records. An alternative is to estimate the snowfall intensity using Mellor's formula (1966) and the visibility data (measured in km) if available. Mellor's formula determines $I_s$ using

$$I_S = \frac{3270.83}{\rho_s} V_{isb}^{\ -2.375}\,, \tag{3.15}$$

where $V_{isb}$ is the visibility reported in km, and $\rho_s$ is the user defined snow density (kg m$^{-3}$). This formula is found to be applicable for visibilities in the range of 1 to 10 km under calm conditions and caution should be exercised when using the above approximation as visibility may not always be directly correlated with snowfall intensity.

## 3.3 Suspended and Surface Ice Mass Exchange

The ice mass exchange between the suspended and surface layers of the river is an important component in the simulation of any freeze-up ice process. Suspended frazil particles grow in size, flocculate together, and rise to the river surface when the buoyant forces on the suspended ice are greater than the turbulent mixing intensity of the flow. This exchange process can lead to ice pans on the river surface that can first, partially insulate the river from further heat loss, and if the ice pan concentration at the surface gets large enough these surface ice pans can contribute to the initiation of an ice cover. This ice mass exchange is also an important component in the simulation of the suspended frazil ice concentration and therefore the water temperature, specifically when supercooled conditions exist. The two-layer mass exchange concept by Shen *et al*. (1991, 1995) is used in the current model to quantify the mass exchange between the suspended and surface ice layers. The total ice mass exchange per unit area ($\Delta M_i$) can be summarized as

$$\Delta M_i = \left[ \alpha v_b C_v C_a - \beta th_{if} C_a \left(1 - e_f\right) + \alpha v_b C_v \left(1 - C_a\right) \right] t_{\text{int}\,vl} \rho_i \,, \qquad \textbf{(3.16)}$$

where α = probability of deposition of frazil ice particles reaching the surface, $v_b$ = buoyant velocity of suspended frazil particles (m/s), $\beta$ = re-entrainment rate of frazil ice at the surface ($s^{-1}$), $C_v$ = volumetric suspended frazil ice concentration, $C_a$ = surface ice concentration, $th_{if}$ = thickness of frazil ice in the surface ice parcels (m), $e_f$ = porosity of frazil deposited at surface, $t_{intvl}$ = coupling time interval (s), and $\rho_i$ = density of ice (kg $m^{-3}$). The total ice mass exchange from above can be divided into two separate components. The first being the mass exchange with the open water area ($\Delta M_{ow}$) which can be written as

$$\Delta M_{ow} = \left[ \alpha v_b C_v \left(1 - C_a\right) \right] t_{\mathrm{int}vl} \rho_i , \qquad \textbf{(3.17)}$$

where the parameters are the same as defined above in equation 3.16. This component of the ice mass exchange will either increase the concentration of existing ice parcels or create new ice parcels in open water areas where none presently exist (see section 2.2 for the concept of ice parcels). In the limiting case, the maximum amount of frazil that can be deposited to the surface over a single time interval is the amount of frazil available in the entire water column, i.e. $\alpha v_b t_{intvl} <= d_w$ ($d_w$ = water depth (m)). Any new parcels will initially consist entirely of the frazil ice mass exchanged to the surface and then thermal growth of the parcels may establish a solid ice thickness which will grow down into the frazil ice layer (see Figure 3.1).

The second component is the ice mass exchange with the ice covered portion of the river surface ($\Delta M_{ic}$) which can be written as

$$\Delta M_{ic} = \left[ \alpha v_b C_v - \beta th_{if} \left(1 - e_f\right) \right] C_a t_{\text{int}\,vl} \rho_i \,, \qquad \textbf{(3.18)}$$

where again the parameters in this equation are as defined in equation 3.16. Depending on the $\alpha$, $v_b$ and $\beta$ values in equation 3.18, the result of the mass balance equation can either be a net deposition or a net entrainment of frazil ice, which will either increase or decrease the frazil ice thickness ($th_{if}$) of the surface ice parcels. In the case of net entrainment of frazil from existing parcels (*i.e.,* $\alpha = 0$, $\beta > 0$), the amount of ice mass that can be entrained into the suspended layer is limited to the amount of frazil ice mass that exists in the ice parcels.

In areas of the river where border ice has progressed in from the banks or in areas where the ice parcel density is large enough that the ice parcels form a slow moving ice cover and possibly an ice jam, these mass exchange parameters need to be adjusted to account for the increased deposition that occurs when an ice cover is present. Under these conditions the $\alpha$ parameter is either, 1.0 (when under border ice), or the $\alpha$ value for that specific location is multiplied by a factor of 2 for all forms of parcel ice cover. In all cases of ice cover, the β parameter is set to be 0 as any undercover erosion process will be taken care of by the undercover transport sub-module.

While it is not a requirement for the model to run, it is recommended that for cases where significant frazil ice deposition occurs (either under an ice cover or border ice) and the transport of this deposited frazil is an important process to be considered, the undercover transport calculations be included in the model. In the formulation described above, frazil ice mass that is deposited under border ice or ice cover parcels will not be transported from the location deposited but will be subject to thermal growth and decay processes.

In more turbulent river conditions, such as in a river rapids, entire portions of parcels or entire parcels themselves may be entrained (often temporarily) into the suspended layer. Under these conditions, both the solid portion of the surface ice parcels ($th_{is}$) as well as the frazil portion ($th_{if}$) can be entrained and generally the surface concentration of ice parcels ($C_a$) will be reduced. When this process occurs, it is expected that the entrained ice mass that has existed at the surface for some time will have a larger particle size and therefore different mass exchange properties ($\alpha$, $\beta$, $\gamma$, $v_b$) when compared to frazil particles already existing in the suspended layer. Typically, these larger particles will have larger $\alpha$ and $v_b$ values and lower $\beta$ and $\gamma$ due to the increased buoyant forces on these particles. In order to account for this component of the mass exchange process and the distinct properties of these particles entrained at the rapids section, a second class of suspended frazil particles ($C_{vB}$) needed to be accounted for in the calculations whenever ice mass exchange at a rapid section occurs. This additional class of suspended frazil particles will help the model better represent the surface and suspended ice concentrations throughout and after the rapids section in the river. Similar mass exchange parameters will be used to quantify the ice mass exchange of this new class of frazil

particles ($\alpha_B$, $\beta_B$, $\gamma_B$, $v_{bB}$). This second class of frazil particles is accounted for using the same finite element methods and nodal calculations used when a single class of suspended frazil particles is present. The physical interaction (*i.e.*, flocculation and disintegration of colliding particles) of these two classes of particles is not accounted for in the model and the combined concentration of the suspended frazil is assumed not to impact the hydrodynamic properties of the flow. These assumptions are valid provided the total volumetric suspended frazil concentration ($C_v$) is small.

In order to initiate the ice mass entrainment process at a rapids section, a rapids parameter ($R_a$) is defined. $R_a$ can have a value between 0 and 1 where 0 indicates no rapids entrainment and 1 means the entire ice parcel will be entrained over one coupling time ($\Delta t_{intvl}$). Conceptually, $R_a$ is the fraction of the parcel concentration and therefore also the fraction of the parcel mass that will be entrained over a coupling time. The change in surface parcel concentration ($\Delta C_a$) over a coupling time is calculated using

$$\Delta C_a = C_a R_a , \tag{3.19}$$

where $C_a$ = surface parcel concentration, and $R_a$ = elemental rapids parameter value. Using $\Delta C_a$ from above, the ice mass entrained ($\Delta M_{ent}$) over the coupling time can be calculated by

$$\Delta M_{ent} = \left( th_{is} + th_{if}(1 - e_f) \right) \Delta C_a A_p \rho_i , \tag{3.20}$$

where $\Delta M_{ent}$ = ice mass entrained (kg), $th_{is}$ = thickness of the solid portion of the ice parcel (m), $A_p$ = area of the ice parcel ($m^{-2}$) and the remaining parameters are as defined above. This entrained ice mass will become a mass source divided equally over the 3 nodes of the element that contains the parcel and distributed over the next coupling time interval ($\Delta t_{intvl}$). This source term will be added to the mass conservation equation of suspended frazil at the finite element nodes

$$\frac{DC_{vB}}{Dt} + p_v C_{vB} = q_v \,, \tag{3.21}$$

where,

$$p_v = \frac{\alpha_B v_{bB} + \gamma_B}{d_w} \,, \tag{3.22}$$

and

$$q_v = \frac{\beta_B th_{if}(1-e_f)C_a}{d_w} + \frac{DC_{vB}^{g}}{Dt} + \frac{DC_{vB}^{ent}}{Dt} \,. \tag{3.23}$$

$p_v$ and $q_v$ are sink and source terms in the mass conservation equation, respectively. The second term on the right hand side of equation 3.23 quantifies the suspended frazil concentration change due to thermal growth or decay and the third term is the added term for rapids ice mass entrainment and can be represented by

$$\frac{DC_{vB}^{ent}}{Dt} = \frac{\sum(\Delta M_{ent}/3)}{\rho_i A_N d_w t_{\text{int}\,vl}}, \qquad \textbf{(3.24)}$$

where the numerator on the right hand side is the summation of the entrained ice mass from all parcels surrounding a particular node (kg), $A_N$ = contributing area of all elements surrounding a node ($m^2$), and the other variables are as defined above. The mass conservation equation (equation 3.21) is solved on the finite element nodes using a Lagrangian explicit integration scheme and combined with the finite element advection and diffusion calculations to obtain a complete solution for the two classes of suspended frazil concentration. A graphical representation of the mass exchange processes discussed in this section is shown in Figure 3.1.

## 3.4 Anchor Ice Growth Model

Over the years, anchor ice has been the focus of many research efforts but to date, the attempts to model the growth process with a field application has been limited. This is primarily due to the fact that the formation and evolution of anchor ice is a very complex process and as such, many numerical models neglect this phenomenon (see Chapter 1). Experimental observations of anchor ice initiation and growth in a laboratory setting (Doering *et al*. 2001; Kerr *et al*. 2002; Qu, 2006) and numerous field observations studies (section 1.1.1.3) have increased our understanding and to some extent confirmed previous theories about this important component of river ice.

The model as described below will be utilized on the finite element nodes whenever the nodes are classified as *"wet"* to describe anchor ice formation, evolution, and release. This is typically whenever the water surface elevation is above the bed level (including any previous anchor ice growth) by a relatively small amount (see Section 3.6 below). For the case when the finite element nodes become *"dry"*, the anchor ice calculations are no longer carried out in the model and the aufeis growth model as presented below in Section 3.5 is activated.

The simplified analytical formulation developed by Wang and Shen (1993) and Shen *et al*. (1995) is the basis for the anchor ice sub-model and is expanded on in the current model. Here, the formation of anchor ice is assumed to be initiated by the attachment of frazil crystals to the bed material in supercooled water. This accretion of frazil crystals is further assumed to begin at the theoretical bed level of $0.2d_s$ below the crown of the semispherical bed material having a nominal diameter $d_s$ (Einstein and El-Samni, 1949), see Figure 3.2. In this model, the growth of anchor ice is considered to be due to the turbulent heat exchange between the supercooled river water and the bottom ice as well as due to the continued accretion of frazil ice. Considerations to account for the heat transfer due to the absorption of solar radiation by the existing anchor ice layer is also included in the model and will be expanded on in the discussion below. The contribution of heat transfer due to solar radiation can be significant under shallow water conditions. The rate of growth and decay of the anchor ice thickness at the top surface of the anchor ice is calculated by

$$\frac{dh_{an}}{dt} = \frac{1}{1-e_a}[\gamma C_v + \frac{(\phi_{wi} - \phi_{pz})}{\rho_i L_i}] \ , \qquad \textbf{(3.25)}$$

where $dh_{an}/dt$ is the growth rate of the top surface of anchor ice, $e_a$ is the porosity of the growing anchor ice, $\phi_{wi}$ is the heat flux from the ice to the flow, $\phi_{pz}$ is the heat flux due to absorbed solar radiation by the ice layer, $C_v$ is the depth averaged frazil ice concentration, $\gamma$ is the frazil ice accretion rate to the bed, with $\rho_i$ and $L_i$ being the density and latent heat of ice, respectively.

The calculation of $\phi_{wi}$ is the same formulation used for the heat flux from an ice cover at the surface to the flow and was described in Section 3.2. In order to calculate the amount of solar radiation reaching and being absorbed by the anchor ice layer, a modified version of the Beer's or Bouguer-Lambert exponential law (Bolsenga, 1978; Martin *et al*., 1999 ) is employed in the model to calculate the exponential decay of solar radiation as it passes through the water column and ice layers. For these calculations the river column is divided into 3 layers: 1) surface ice layer (if present), 2) water layer, and 3) bottom ice layer.

For a surface ice layer with a concentration of $C_a$ and a thickness of $d_1$, the amount of solar radiation at the bottom of this layer ($\phi_{R1}$) is the averaged value of the solar radiation passing through the ice layer and the radiation passing through the same depth of water and is calculated using one of the following two equations:

when $d_1 > D_{ext}$,

$$\phi_{R1} = \phi_R \left[ C_a e^{-\varepsilon_i d_1} + (1 - C_a)\left((1 - \beta_R) e^{-\varepsilon_w (d_1 - D_{ext})}\right)\right] \quad \textbf{(3.26)}$$

or when $d_1 <= D_{ext}$,

$$\phi_{R1} = \phi_R \left[ C_a e^{-\varepsilon_i d_1} + (1 - C_a)\left(1 - \beta_R \frac{d_1}{D_{ext}}\right)\right]. \quad \textbf{(3.27)}$$

$\phi_R$ = the incoming net solar radiation ($Wm^{-2}$), $C_a$ = surface ice concentration, $\varepsilon_i$ and $\varepsilon_w$ = extinction coefficients for ice and water respectively ($m^{-1}$), and $\beta_R$ = fraction of solar radiation absorbed in the initial water depth $D_{ext}$.

For the second and third layers, the solar radiation reaching the bottom of the water column ($\phi_{R2}$) and the solar radiation reaching the bottom of the anchor ice layer ($\phi_{R3}$) is calculated in a similar fashion using a continuation of the above approach and

$$\phi_{R2} = \phi_{R1} e^{-\varepsilon_w d_2} \quad \textbf{(3.28)}$$

and

$$\phi_{R3} = \phi_{R2} e^{-\varepsilon_i d_3}, \quad \textbf{(3.29)}$$

where $d_2$ and $d_3$ are the depth of water and thickness of the anchor ice layer, respectively. The amount of solar radiation absorbed by the anchor ice layer ($\phi_{pz}$) is calculated as the difference between $\phi_{R2}$ and $\phi_{R3}$ from above ($\phi_{pz} = \phi_{R2} - \phi_{R3}$).

A schematic representation of this formulation is shown in Figure 3.3 and the equations above show that the amount of solar radiation reaching the bed level decreases with

increases in both the water depth and the surface ice concentration. The solar extinction parameters for the Lower Nelson River water are 2.79 $m^{-1}$, 0.85, and 0.6 m, for the extinction coefficient for water ($\varepsilon_w$), linear decay coefficient ($\beta_R$), and the depth over which $\beta_R$ is calculated ($D_{ext}$), respectively (Tetres, 2004). The bulk extinction coefficient ($\varepsilon_i$) can vary greatly due to the range in ice properties and the inconsistencies in the ice layers themselves. This coefficient can vary from 0.6 $m^{-1}$ for clear ice (Bolsenga, 1978) to a range of 10 to 25 $m^{-1}$ for snow covered cloudy ice (Ashton, 1980). The bulk extinction coefficient for the surface and anchor ice is 22 $m^{-1}$ in the current model.

In the current model, the frazil accretion rate is set to zero ($\gamma = 0$) when the water temperature rises above 0°C. For this condition the suspended frazil is no longer in the "active" state and will not accumulate on the river bottom. The accretion rate parameter is also set to zero when the river surface is covered by an ice cover (border ice or a parcel ice cover) and when the shear velocity at the bed (U*) is either less than $U^*_{min}$ or greater than $U^*_{max}$. If $U^* < U^*_{min}$, it implies there isn't enough turbulent mixing in the flow to bring frazil particles into contact with the bed and if $U^* > U^*_{max}$, it implies the shear strength of the flow is too high for particles to attach directly to the bed. Under these conditions the growth of the anchor ice layer will be primarily due to the turbulent heat exchange between the ice and the supercooled water. These effects on the attachment criteria have been quantified in the past through the observation of the impact of the Froude and Reynolds numbers on anchor ice growth (Terada *et al*., 1998; Doering *et al*., 2001; Kerr *et al*., 2002; Bisaillon and Bergeron, 2009; and Stickler and Alfredson, 2009).

The shear velocity is calculated using the bed shear stresses which take into account the influence of any surface ice. The bed shear stresses are calculated using

$$\tau_{bx} = c_f \rho_w \frac{q_x \left( q_x{}^2 + q_y{}^2 \right)^{\frac{1}{2}}}{d_w{}'^2} \tag{3.30}$$

and

$$\tau_{by} = c_f \rho_w \frac{q_y \left( q_x{}^2 + q_y{}^2 \right)^{\frac{1}{2}}}{d_w{}'^2}, \tag{3.31}$$

where $d_w'$ = water depth under the surface ice layer (m), $q_x$ and $q_y$ = unit width discharges in the x and y directions respectively ($m^2s^{-1}$), and $c_f$ = a friction coefficient that can be expressed as a function of the Manning's roughness coefficient for the bed ($n$) using

$$c_f = \frac{n^2}{(\alpha_b d_w')^{1/3}} g, \tag{3.32}$$

where $\alpha_b$ = the fraction of the total water depth that is affected by the bed friction. The value of $\alpha_b$ is 1.0 when there is no surface ice present ($C_a = 0$) and is calculated using the following formula for wide channels when $C_a > 0.0$

$$\alpha_b = \frac{1}{1 \pm \left( C_a \frac{n_i{}^2 \left( V_w - V_i \right)^2}{n^2 V_w{}^2} \right)^{3/4}}, \tag{3.33}$$

where $n_i$ = Manning's coefficient for the undersurface of the surface ice, and $V_w$ and $V_i$ are the velocity magnitudes for water and ice respectively (m/s). The sign between the terms in the denominator is positive when $V_w > V_i$ (common case) and negative when $V_w < V_i$ (rare case).

The growth of anchor ice impacts the conveyance or carrying capacity of a river channel by decreasing the flow depth and changing the surface roughness. The overall flow resistance resulting from the combined effect of the change in surface roughness and the reduction in flow area due to anchor ice growth was quantified in the laboratory experiments of Kerr *et al*. (2002) through the calculation of the gross Manning's roughness coefficient. This roughness coefficient was on the order of 0.05 – 0.2 in these experiments. In this model, the effect of anchor ice growth on the flow depth (and cross-sectional flow area) is included by step-wise adjusting the bed elevation to include the existence of the anchor ice layer. The change in surface roughness of the river bed during the formation of anchor ice has been observed to be an increase in roughness initially, as the initial irregular deposits of anchor ice form on the bed particles, but a smoothing effect occurs after a period of time once the anchor ice begins to form a complete blanket over the entire bed. This effect was observed in the experiments conducted by Kerr *et al*. (2002) and to some extent in the experiments of Qu (2006). In this model, the temporary initial increase in surface roughness is neglected and the bed roughness is reduced linearly by a user specified fraction ($C_{nai}$) of the calibrated Manning's roughness ($n$) as the anchor ice grows from an initial thickness of 0.0 to 1.5*$d_s$ ($d_s$ = diameter of top layer of bed particles (m)). Once the anchor ice layer exceeds a thickness of 1.5*$d_s$ then no

further reduction in surface roughness will occur. The approximate fractional reduction of Manning's surface roughness observed in Kerr's experiments was 0.5. Future experimental observations of this phenomenon would help to refine this simplified formulation.

As alluded to above, anchor ice will not completely fill the voids between the bed particles and as such, a channel of substrate flow will form on the underside of the anchor ice. One may conclude that an existence of a bed heat flux would contribute to the melting of the anchor ice from underneath. However, a heat budget analysis (Shen *et al*., 1995) showed that unless the bed is fully covered over a distance of several kilometers, the substrate water temperature would not be significantly different than the river water temperature. Therefore, the rate of melting or growth at the bottom of the anchor ice is calculated by

$$\frac{dh_{sb}}{dt} = \frac{1}{(1-e_a)\rho_i L_i}[h_{iws}(T_w - T_m) + \phi_{R3}] \ , \qquad \textbf{(3.34)}$$

where $dh_{sb}/dt$ is the growth rate of bottom surface of anchor ice (measured relative to the centerline of the first layer of bed particles), $\phi_{R3}$ is the short wave radiation reaching the bed material as calculated above, $h_{iws}$ is the heat exchange coefficient between the anchor ice and the substrate flow, with $T_w$ and $T_m$ being the water temperature and the melting temperature of ice, respectively. The heat exchange coefficient ($h_{iws}$) is calculated in a similar manner as $h_{wi}$ from above (see section 3.2) with the difference being the

substitution of the substrate flow depth and velocity into the equation. The substrate flow velocity ($v_{sb}$) is determined using the Manning's equation for $v_{sb}$ (Wang and Shen, 1993)

$$v_{sb} = \left( \frac{e_{bv} h_{sb}}{d_w} \right)^{2/3} V_w \,, \qquad \textbf{(3.35)}$$

where $e_{bv}$ = porosity of the tightly packed bed material with diameter $d_s$ and the other variables are as defined previously.

The release of anchor ice is a very important but complicated process that has both thermal and mechanical components, both of which are considered in the current model. The anchor ice is assumed to release thermally when the substrate flow erodes the under-surface of the ice to a level of 0.4*$d_s$ above the centerline of the bed material (Figure 3.2). This thermal release mechanism is somewhat analogous to the bond strength formulation proposed by Tsang (1988) in that as the bottom surface of the anchor ice grows downward it is effectively building up a form of bond strength that can subsequently be thermally eroded prior to anchor ice release.

The anchor ice can also be mechanically detached from the bed. This will occur when the buoyant force of the anchor ice ($F_{anb}$) overcomes the submerged weight of the bed particles ($w_{sb}$) and the inter-particle resistance ($c_{ohb}$) together. This is expressed (in N/m$^2$) by

$$F_{anb} > w_{sb} + c_{ohb} \tag{3.36}$$

where

$$w_{sb} = \frac{\pi}{3\sqrt{3}} g\left(\rho_b - \rho_w\right) d_s \tag{3.37}$$

and

$$F_{anb} = \left( h_{an} - \left(1 - \frac{e_{ba}}{2}\right)\left(\frac{d_s}{2} - h_{sb}\right)\right) * \left(\rho_w - \rho_i\right) * \left(1 - e_a\right) g \,. \tag{3.38}$$

$e_{ba}$ = geometric plane void rate at a depth into the river bed, $\rho_b$ = density of bed material (kg $m^{-3}$), $g$ = gravitational constant (m $s^{-2}$) and the other variables are as defined previously.

Once the anchor ice is released from the bed, either thermally or mechanically, it floats to the surface where it is added to the surface ice run and will increase the surface ice concentration and/or increase the existing floe thickness. If the anchor ice is released at a location covered by border ice, the released ice will be added to the frazil thickness under the ice cover.

While the above model of anchor ice formation and evolution is quite detailed, it is important to note that it is still a relatively simplified formulation of a very complex process and future laboratory and field studies would serve well to better understand the

process and improve the formulation. In some cases, additional ice processes need to be considered in conjunction with anchor ice formation. One such process is aufeis formation and will be discussed in section 3.5.

## 3.5 Aufeis Growth Model

Research on and observations of the formation and evolution of aufeis have largely focused on cases where the progressive flooding of an ice cover or ground surface has resulted in significant *"layered"* ice masses (Kane, 1981; Schohl and Ettema, 1986 and 1990; Slaughter, 1990; Carstens and Lia, 1998; and Hu *et al.,* 1999). Aufeis can also be an important ice process in river environments where portions of the bed surface, or a combination of the bed surface and anchor ice, can be exposed to the cold atmosphere due to changing river hydraulic conditions. This can be quite common downstream of hydropower generating stations that frequently adjust their operating conditions over the winter. Aufeis growth can have significant effects on the ice conditions in the river and when coupled with the anchor ice growth process can contribute to considerable impacts on the water regime (Girling and Groeneveld, 1999). The aufeis growth model calculations will be activated whenever the finite element nodes are *"dry"* (*i.e.*, when a cycle of flow goes below the top of the bed material or anchor ice).

Generally, anchor ice will have some initial porosity (denoted as $e_a$ in section 3.4 above) and when this anchor ice is exposed to the atmosphere (*i.e.*, when the location is *"dry"*) a solid crust will begin to form on the surface as a form of aufeis growth. This aufeis layer

will thicken using a similar method to the growth of a solid ice cover downward through a porous ice layer. Using a similar approach to Dingman and Assur (1969), a linear formulation of the heat exchange at the air-ice interface is

$$\phi_T = \alpha_{ia} + h_{ia}(T_s - T_a) - \phi_{pz} \ , \qquad \textbf{(3.39)}$$

where $\phi_T$ is the net heat exchange to the atmosphere from the ice layer, $\phi_{pz}$ is the net heat flux due to absorbed solar radiation by the ice layer, $T_s$ and $T_a$ are the ice surface and air temperatures, respectively, and $\alpha_{ia}$, $h_{ia}$ are linear coefficients that can be derived from the complete heat exchange process. By neglecting internal heating of the ice layers and therefore assuming a linear temperature gradient across the layers, the steady state heat flux across each layer in the ice cover will be the same. Greene (1981) and Ashton (1982) showed that a linear temperature distribution is applicable to river ice covers because of the relatively small thickness. Employing the above assumptions, Shen and Lal (1986) showed that solid ice thickness growth downward through a porous layer (with porosity $e_a$), and considering the effects of a multi-layer formation, can be expressed as

$$\frac{dh_i}{dt} = \frac{1}{e_a \rho_i L_i}\left( \frac{\alpha_{ia} + h_{ia}(T_m - T_a) - \phi_{pz}}{h_{ia}\left( \frac{1}{h_{ia}} + \frac{h_s}{k_s} + \frac{h_{whi}}{k_{whi}} + \frac{h_i}{k_i} \right)} - h_{wi}(T_w - T_m) \right) , \qquad \textbf{(3.40)}$$

where $h_i$ and $k_i$ are the thickness and thermal conductivity of solid black ice with similar parameters for white ice (subscript *whi*) and snow (subscript *s*). The other parameters in the formula are as defined previously.

Under natural conditions, this growth of the aufeis layer will strengthen the anchor ice deposit through continued growth of the underside of the aufeis layer. This will progressively reduce the overall porosity ($e_{aB}$) of the anchor ice/aufeis deposit using a simple weighted average formula and assuming the porosity of the solid aufeis layer to be 0, the formula can be written as

$$e_{aB} = \frac{(h_{an} - h_i)e_a}{h_{an}} \quad , \tag{3.41}$$

where $e_{aB}$ = new bulk porosity of combined aufeis and anchor ice deposit, and the remaining parameters are as defined previously. A simplified graphical representation of this process can be found in Figure 3.4. The decrease in the bulk porosity due to aufeis growth can affect the eventual release of the anchor/aufeis in a couple of ways. The first is to increase the buoyant force on the ice once it is flooded again and the second will be to effectively reduce the rate the undersurface is eroded, which in some ways helps to capture the "strengthening" that occurs when aufeis growth occurs. For example, a combination anchor ice/aufeis deposit that has been exposed to the atmosphere has been observed to be significantly stronger (Girling and Groeneveld, 1999; Malenchak *et al*., 2006 and 2011) than an anchor ice deposit that has not been exposed. This stronger

deposit will conceivably require more thermal heat transfer from solar radiation and/or warm water to release.

This aufeis layer will continue to grow downward until the ice growth is flooded with water, and the anchor ice calculations take over again, or when a limiting thickness is reached. The specification of a limiting thickness is partially due to the fact that aufeis growths are typically layered. With the thickness of the layers being a function of many factors (Hu *et al*., 1999) including heat transfer, riverbed topography, and the nature of the water source (groundwater, overflow, etc.). In this model formulation, the limiting aufeis layer thickness will be a user defined parameter. Hu *et al*. (1999) observed icing (or aufeis) layer thicknesses in the north-central Yukon Territory (Canada) between 2 and 8.1 cm with multi-layer thicknesses greater than 2 m being observed by Carstens and Lia (1998) in the interior of southern Norway. Since each aufeis layer will typically overlay a relatively porous anchor ice growth below, water will eventually drain away as the surrounding water level drops and thereby limiting the layer thickness. In locations where the spatial extent of the aufeis formation is large and/or the surrounding geometry will not allow the water to drain away, the thickness of a single aufeis layer may be larger.

As the aufeis layer is thickened, snow may deposit on the surface. This snow will absorb some moisture from the surrounding open water areas as it approaches the river surface and will likely be quite dense once deposited. This snowfall will insulate the ice layer and slow the growth of the aufeis layer downward. If supercooled conditions exist when the aufeis layer is flooded again, this snow thickness is added to the total thickness of the

anchor ice/aufeis growth as a layer of white ice. This is done because once the already cold, dense, and moisture rich snow deposit is saturated with supercooled water, it will gain enough strength very quickly to avoid being washed away by the overflow. It is expected that for cases where large amounts of snow has fallen between periods of flooding and when the areal extent of the aufeis growth is quite large, some of this deposited snow may be washed away as the water flows overtop. Nonetheless, there does exist the potential for large amounts of this snow layer to be solidified enough to contribute significantly to the total thickness of the aufeis/anchor ice growth. This is especially the case when the aufeis layer is flooded gradually over a period of time and the deposited snow is allowed to absorb some water through capillary action and then solidify. It has also been observed in nature that the very cold air temperatures common in northern climates cause water flowing over existing ice to freeze quickly and in relatively short distances (Schohl and Ettema, 1986 and 1990; Zufelt *et al*., 2009). Figure 3.5 contains a photo of this process occurring at Sundance Rapids, Manitoba, Canada in February, 2000. If supercooled conditions do not exist when the aufeis layer is flooded, the deposited snow is assumed to be washed away by the relatively warm water and is not added to the anchor ice/aufeis growth thickness.

The bottom surface of the anchor ice growth will continue to grow down (or decay upward) at this time in much the same manner as described in the section above (using equation 3.34). This growth (or decay) will continue as long as the water surface elevation surrounding the aufeis/anchor ice growth is greater than the bed elevation. The porous nature of the anchor ice near the bed material will allow for the continued action

of the water on the undersurface of the ice deposit. The continuation of this process is especially important in the release mechanisms, which are carried through as described above in anchor ice growth formulation (see section 3.4).

During a period of melting, the aufeis layer may be eroded at the top surface of the layer if appropriate thermal conditions exist. If snow is present on the surface of the aufeis layer, the snow accumulation is melted according to the following formula

$$\left(1-e_s\right)\rho_i L_i \frac{dh_s}{dt} = \alpha_{ia} + h_{ia}(T_s - T_a) - \phi_{pz} \ , \qquad \textbf{(3.42)}$$

where $e_s$ = the porosity of snow deposit. The surface temperature ($T_s$) in the above formula is assumed to be 0ºC during a melting period. When there is no snow layer present, the snow porosity is removed from the above formula and the thickness of the aufeis layer ($h_i$) is substituted for the snow thickness ($h_s$). When the aufeis layer is decayed in this manner, the total thickness of the anchor ice/aufeis growth ($h_{an}$) is reduced by an equal amount and the bulk porosity of the ice growth ($e_{aB}$) is adjusted.

One of the prerequisites of the above formulation is that a thickness of anchor ice must exist prior to an aufeis layer being calculated. It should be acknowledged that an aufeis layer could form in nature where no anchor ice exists and the aufeis formulation proceeds as described above in the absence of the porous anchor ice under the aufeis layer. It is

anticipated that without supercooled conditions, and therefore no subsequent anchor ice growth when the aufeis layer is flooded, any small aufeis layer that is formed periodically may be removed by the warmer water and no significant thickness will be able to develop. This case is considered to be relatively unique and it is expected that the limiting aufeis layer thickness in this case will need to be chosen carefully.

Similar to the anchor ice formulation presented in section 3.4, this model of aufeis formation and evolution is also a simplified formulation of a very complex process and future studies would serve well to better understand the process and potentially improve the formulation.

## 3.6 Dry Bed Treatment

Often an essential component to the simulation of large accumulations of anchor ice and aufeis growth is the ability to model dry bed or exposed bed conditions. As indicated previously, significant anchor ice and aufeis growths can occur in regions that experience cyclical drying and wetting conditions (Girling and Groeneveld, 1999). These conditions are commonly found in reaches downstream of hydropower generating stations that operate in a "peaking mode of operation", meaning the flow through the generating station fluctuates on an hourly and daily basis to match power demand cycles (Malenchak *et al*., 2006). A robust (and computationally stable) formulation is required to more accurately simulate drying and wetting conditions within the two-dimensional model.

The finite element hydrodynamic calculations are carried out without any special treatment (see Section 2.2) until the water depth at a particular node (including the effects of surface ice and anchor ice / aufeis) reaches a user specified value, "*htlow*", and the node is then classified as "*Dry*". *htlow* is the minimum water depth on the finite element nodes and this minimum value is required to be greater than 0 for model stability because the dry nodes are not removed from the hydrodynamic calculations completely. All of the nodes in the simulation are checked against the "*Dry*" criteria once every dry bed coupling time step ($t_{intdry}$).

Once a node is identified as "*Dry*", the surrounding nodes are flagged and these nodes create a temporary land boundary around the dry node(s). The discharge calculated on these temporary land boundary nodes is rotated along the neighbouring element faces (with zero-normal flux) much the same as it is done with the permanent land boundary nodes in the model. This treatment allows the discharge at the dry nodes to be 0.0 and effectively creates a temporary island at the dry node locations.

A node that is identified as "*Dry*" will remain that way until a sufficient depth, "*hthigh*", is reached at which point the node will then be reclassified as "*Wet*" and there will be no more special treatment on this node. It is necessary that "*hthigh*" be larger than "*htlow*" by an adequate amount so that the node does not oscillate between a "*Dry*" and "*Wet*" state every coupling time unnecessarily. This method for the treatment of dry bed conditions is a computationally efficient method that works especially well for cases

where the "*Dry*" areas are relatively small and localized, which is often the case in rapids areas and other locations where significant anchor ice and aufeis can form. Computational errors can existent with this method when large floodplains are modeled which is due to the existence of the minimum depth, "*htlow*", at all of the dry nodes.

A summary of the different nodal states is as follows:

- water depth < *htlow*, node is "*Dry*"
- *htlow* < water depth > *hthigh*, node stays "*Wet or Dry*"
- water depth > *hthigh*, node is "*Wet*"

(a)

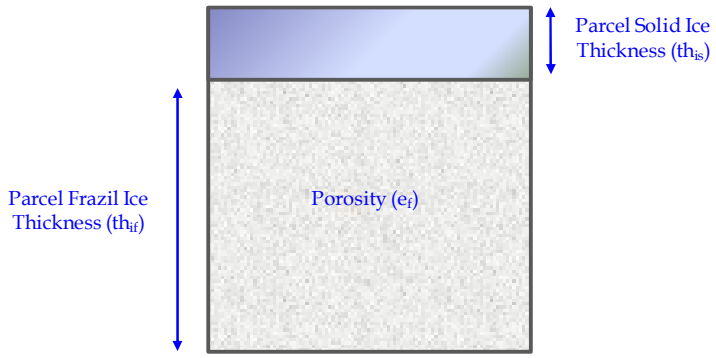


(b)

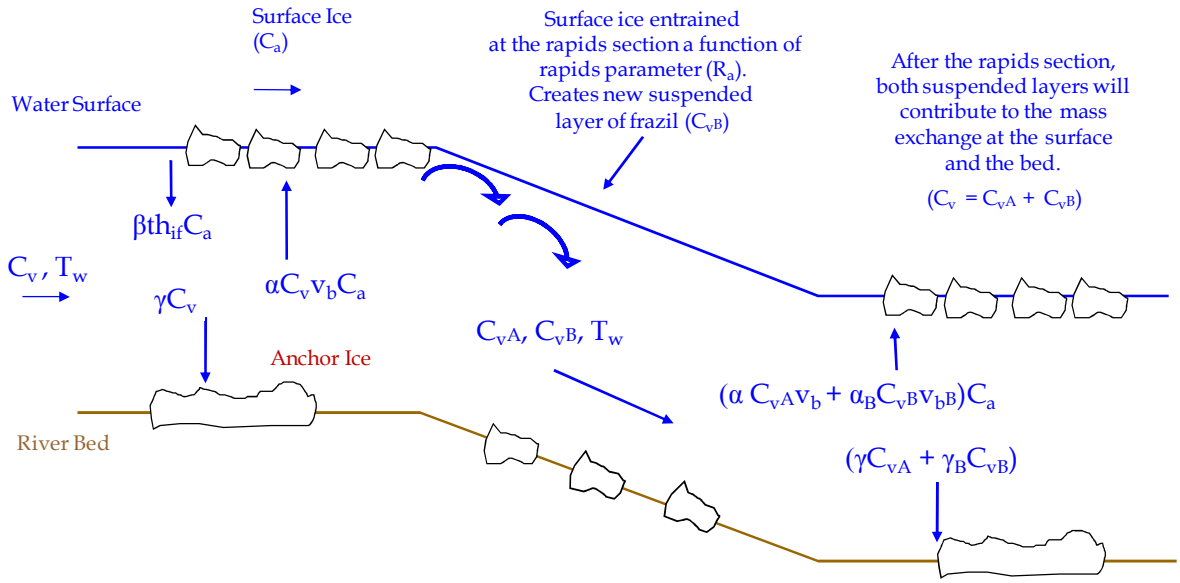


**Figure 3.1 -** Schematic representation of (a) the ice parcel thickness layers (top) and (b) ice mass exchange parameters (bottom).

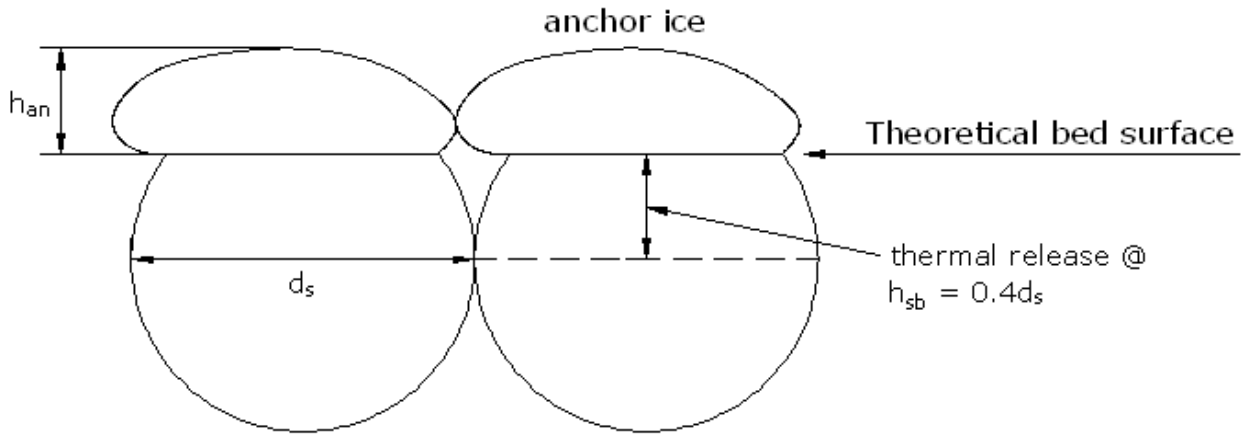


**Figure 3.2 -** Location of the theoretical bed surface for the initiation of anchor ice. (adapted from Wang and Shen, 1993)

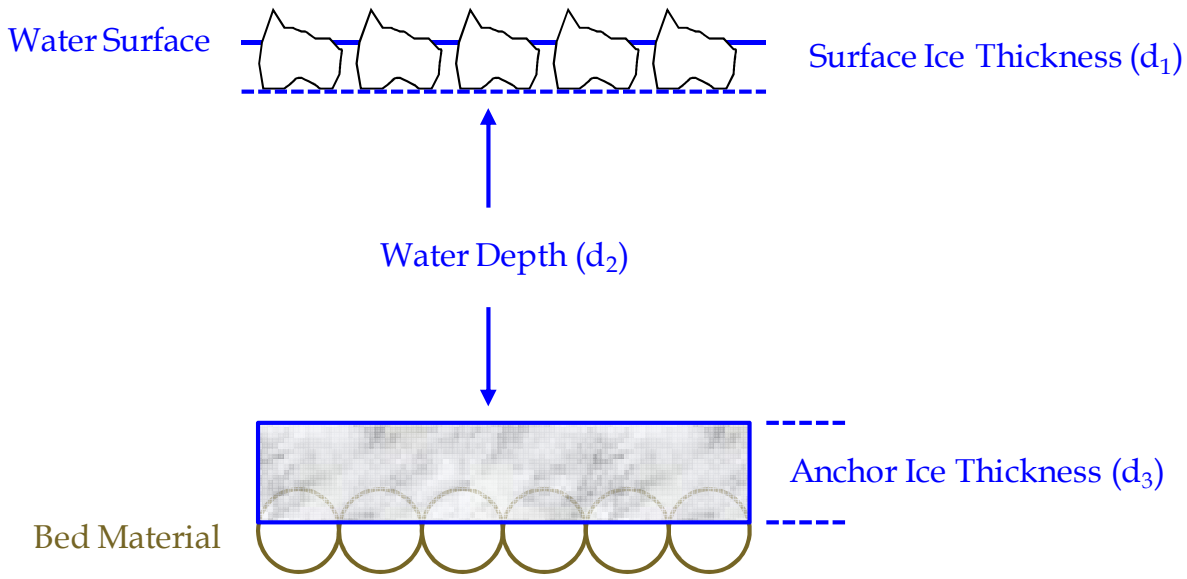


**Figure 3.3 -** Schematic representation of river layers used to calculate the solar radiation extinction.

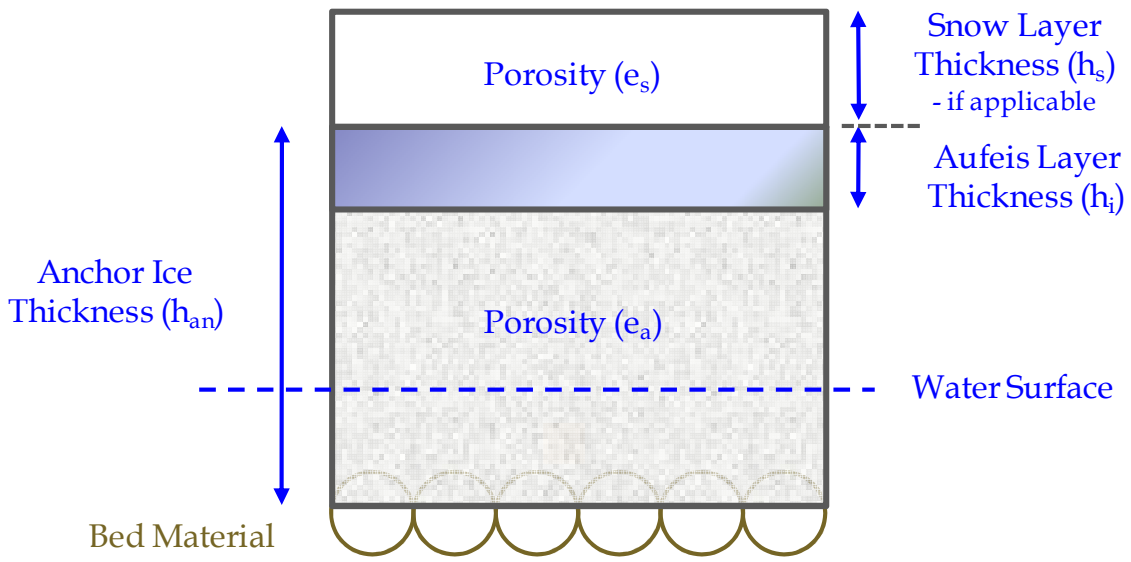


**Figure 3.4 -** Simplified representation of the aufeis growth layer model.

**Figure 3.5 -** Snow deposited and flooded on an aufeis layer caused by water level fluctuation at Sundance Rapids, which is located downstream of the Limestone Generating Station in Manitoba, Canada. (February 4, 2000)

CHAPTER 4

# Ideal Channel Simulations

## 4.1 Ideal Channels

The sections below will present the results of selected model runs, which will serve as a test of the model formulations discussed in Chapter 3. These tests were conducted in an ideal channel setting and focused specifically on the following sub-models: 1) energy budget model, 2) suspended and surface ice exchange model, 3) anchor ice model, 4) aufeis model, and 5) dry bed treatment model. Specific tests were setup in order to validate each of the above sub-models separately. The last section in this chapter will be a sensitivity analysis of selected model parameters that was carried out to determine the effects these parameters had on the growth rates of anchor ice in an ideal channel setting. A set of eight model parameters were tested and compared to a base case in order to observe how changing these parameter values would impact the simulated anchor ice growth rates. The data from this analysis can then be used to assist in the calibration of these same model parameters for the simulation of more unique river situations. This

data will establish a "relative importance" of the parameters as they pertain to the growth of anchor ice and should not be confused with the actual values a modeler would choose (or calibrate) for a given simulation setup.

Four different 10 km long by 1 km wide ideal channels will be used throughout these tests. These channels were developed to allow for proper testing of the specific model formulations. The geometric extents and the bed elevations of these ideal channels are shown in Figures 4.1 and 4.2. The main characteristics of the four channels are listed below:

1) *Rectangular Channel* –has a rectangular bed elevation profile with a constant slope throughout (see Figure 4.1).
2) *Rectangular Berm Channel* – at 7 km from the upstream boundary there is a 2.5 m high berm that extends halfway across the channel. The crest of the berm is 500 m wide by 150 m long (see Figure 4.1).
3) *Rectangular 1-Outcrop Channel* – has a single outcrop in the center of the channel 7 km from the upstream boundary. The crest of this single outcrop is 200 m by 200 m and is 3.0 m high (see Figure 4.2).
4) *Rectangular Multiple Outcrops Channel* - at 7 km from the upstream boundary, 3 – 3 m high outcrops exist with one 250 m square outcrop in the center of the channel and two along the left and right bank. At 7.5 km from the upstream boundary, 2 – 2 m high, 200 m square, outcrops exist that are offset from the previous row of outcrops (see Figure 4.2).

As evident from the list above, each channel is unique in its own way but there are also some similarities between the channels. In general, the mesh density of the ideal channels is a 100 m by 100 m triangular mesh. The mesh density is higher in the areas surrounding some of the bed outcrops where a greater resolution is required. Other similar characteristics of the channels are the main channel slopes ($S$ = 0.001) and the Manning's roughness values specified ($n$ = 0.03). Other model parameters specific to the case being tested will be included in the simulation descriptions below.

## 4.2 Energy Budget

The energy budget calculations are carried out in the model as described in section 3.2. The following tests and discussions will be focused on the detailed energy budget calculations over the open water area because the linear heat transfer approximations are relatively straightforward calculations. The Rectangular Channel shown in Figure 4.1 will be used for this simulation. The boundary conditions used for this simulation are shown in Table 4.1.

**Table 4.1** – Boundary conditions for the energy budget model runs.

| Boundary Condition | Value |
|---|---|
| Upstream Inflow | 4000 cms |
| Downstream Water Level | 2.23 m |
| Upstream $T_w$ | 0.05 °C |
| Heat Transfer | Variable |
| Simulation Length | 48 hrs |

The surface ice mass exchange calculations were not included in this simulation so that the existence of surface ice would not interfere with the open water heat transfer calculations. Other important parameters related to these calculations is the channel is located at 49.5ºN latitude, the elevation above sea level is 218 m, the density of snowfall ($\rho_s$) is assumed to be 170 kg/m$^3$, and the inflow water temperature ($T_w$) is chosen to limit the amount of water temperature change throughout the channel; this was done because the water temperature at a specific location impacts the heat transfer rates calculated to some degree. The height the wind data is measured is 10 m and the relative humidity is assumed to be 50% throughout the simulation. The relative humidity is captured in the input dataset through the specification of the dew point temperature ($T_{dew}$) for a given air temperature ($T_a$). The start date and time is March 1, 2006 @ 0:00 AM (midnight). The input weather parameters for the 48 hour simulation are shown in Table 4.2.

**Table 4.2** - Weather input parameters used for the energy budget simulation.

| Time (hr) | $T_a$ (°C) | Visibility (km) | Cloud Cover (1/10ths) | $T_{dew}$ (°C) | Wind Magnitude (m/s) | Wind Direction (°) |
|---|---|---|---|---|---|---|
| 0 | -25 | 24 | 0 | -31.75 | 0 | 270 |
| 4 | -25 | 24 | 0 | -31.75 | 0 | 270 |
| 8 | -22 | 24 | 0 | -28.91 | 0 | 270 |
| 12 | -15 | 24 | 0 | -22.30 | 0 | 270 |
| 16 | -15 | 24 | 0 | -22.30 | 0 | 270 |
| 20 | -23 | 24 | 0 | -29.86 | 0 | 270 |
| 24 | -30 | 2 | 10 | -36.48 | 9.722 | 270 |
| 28 | -30 | 2 | 10 | -36.48 | 9.722 | 270 |
| 32 | -28 | 2 | 10 | -34.59 | 9.722 | 270 |
| 36 | -21 | 2 | 10 | -27.97 | 9.722 | 270 |
| 40 | -20 | 2 | 10 | -27.02 | 9.722 | 270 |
| 44 | -24 | 2 | 10 | -30.80 | 9.722 | 270 |
| 48 | -25 | 2 | 10 | -31.75 | 9.722 | 270 |

The heat transfer over the open water area is calculated on the finite element nodes and the averaged values over the channel are plotted in Figure 4.3. From the figure it can be seen that the conductive heat transfer plays a significant role in the amount of heat transfer from the open water surface. This component is largely a function of the temperature difference between the air and water surface and is increased in the second day of the simulation when the temperature drops and the wind velocity increases to

9.722 m/s (35 km/h). The wind direction specified (270º) corresponds to a north wind in the model.

The next most significant components of the total heat transfer from the channel surface are the effective back radiation and the short wave (solar) radiation. The effective back radiation is largely a function of the water surface temperature and to a lesser extent the ambient air temperature as well. The level of effective back radiation is decreased slightly during the second day of the simulation when significant cloud cover was specified. Short wave radiation can be a significant source of heat gain and is a function of the geographic location, time of day and year, and the cloud cover. From Figure 4.3, it can be seen that during a clear day in early March (first day of the simulation), the short wave radiation at midday can result in a net heat gain for a short period of time even though the ambient air temperature is -15ºC. The level of short wave radiation is significantly reduced, but not completely eliminated, in the second day of the simulation when a complete (10/10ths) cloud cover is specified.

When compared to the other heat transfer components, a modest level of heat loss occurs (< 80 $W/m^2$) during the second day of the simulation when an equivalent snowfall intensity is calculated using a visibility measurement of 2 km. This visibility corresponds to an approximate snowfall intensity of 3.71 mm/hr (see equation 3.14). Out of all the heat transfer components, the evaporative heat transfer is the least significant (< 20 $W/m^2$) but would be slightly larger during periods of lower relative humidity.

Given the large range in the total heat transfer values in Figure 4.3, from a 100 W/m$^2$ net heat gain to a maximum heat loss of 960 W/m$^2$, it is important to relate the daily total heat transfer back to the linear heat transfer approximation described at the beginning of section 3.2. For the first day of the simulation, the average air temperature was -21.3ºC and the average heat loss was 258.5 W/m$^2$, which assuming a water temperature close to 0ºC, gives a linear heat transfer coefficient ($h_{wa}$) of 12.1 W/(m$^2$ ºC) using equation 3.1. Similarly, for the second day of the simulation, the average air temperature was -25.1ºC, the average heat loss 785.6 W/m$^2$, which gives a value for $h_{wa}$ of 31.3 W/(m$^2$ ºC). When considering both days of the simulation together, the average value for $h_{wa}$ of 22.4 W/(m$^2$ ºC) is close the value of 20 W/(m$^2$ ºC) recommended by Lal and Shen (1991) for use on northern United States rivers. It is worth noting again that $h_{wa}$ can vary significantly with location and should be calibrated with field data whenever possible. This comparison shows that even when there is a large variation in the total heat transfer components, if the modeler is not interested in the diurnal variations in the heat transfer rate or when limited weather data exists, it may be possible to approximate the daily heat transfer rates using the linearized formulation.

## 4.3 Suspended and Surface Ice Mass Exchange Model

The expanded surface and suspended ice mass exchange model is described in section 3.3 and this component of the model will be evaluated using the Rectangular Channel. In order to evaluate the ice mass exchange formulation, the mass exchange parameters will be adjusted throughout the channel to demonstrate the different characteristics of this

component of the model and are not intended to be representative of a physical change in the channel geometry or flow structure. The boundary conditions used for this simulation are shown in Table 4.3.

**Table 4.3** – Boundary conditions for the mass exchange model runs.

| Boundary Condition | Value |
|---|---|
| Upstream Inflow | 500 cms |
| Downstream Water Level | 6 m |
| Upstream $T_w$ | 0.02 °C |
| Heat Transfer | 380 W/m$^2$ |
| Simulation Length | 12 hrs |

At approximately 6.5 km from the upstream end of the channel, a section of the channel is designated as "Rapids" in order to test the rapids entrainment formulation presented in Chapter 3. This is also the location where the water depth begins to transition from a normal depth of 0.55 m to the eventual maximum depth of 6 m at the downstream boundary.

The above parameters were chosen to provide sufficient travel time for suspended frazil and surface ice to develop in the channel. Other user defined parameters relevant to these simulations are an initial parcel frazil thickness ($h_{f0}$) of 0.15 m, a thermal suspended frazil

particle diameter of 2 mm with a diameter to thickness ratio (*d/t*) of 15:1, and an entrained frazil particle diameter of 2 cm (*d/t* = 15). Once the surface ice parcels are initiated at the river surface, there may be a net entrainment or a net deposition of suspended frazil to them as they travel downstream. This depends on the solution of the following equation at each point in the channel and is a function of the mass exchange parameters and the parcel properties at that particular spatial location

$$\alpha v_b C_v - \beta th_{if}(1-e_f) > 0, \qquad \textit{net frazil deposition} \qquad \textbf{(4.1a)}$$

and

$$\alpha v_b C_v - \beta th_{if}(1-e_f) < 0, \qquad \textit{net frazil entrainment} \qquad \textbf{(4.1b)}$$

where the parameters in the above equations are as defined previously in Chapter 3. The above equations can also be used by a modeler to identify/specify areas where net entrainment or net deposition of frazil to or away from the surface ice parcels is desired.

A snapshot of the simulation described above with no rapids entrainment ($R_a$ = 0) is found in Figure 4.4 and illustrates the distribution of surface ice concentration ($C_a$), ice thickness ($th_i$) and suspended frazil ice concentration ($C_v$) throughout the channel. The surface ice concentration slowly increases for the first 5 km and then increases significantly near the downstream end of the channel as the suspended ice concentration increases and the slower water velocity at the downstream end gives more time for suspended frazil to be deposited on the open water surface (which will increase the

surface ice concentration), as well as on the underside of the existing surface ice parcels (which will increase the ice parcel thickness). From the plot of ice thickness, it can be seen that surface ice parcels are initiated near the upstream end of the channel at an approximate thickness of 0.15 m and this thickness stays relatively constant until approximately the 8 km mark of the channel. The net deposition to the surface ice layer over the last 2 km of the channel is greater than the thermal growth of the suspended frazil ice concentration and therefore results in a decrease in the suspended ice concentration.

The rapids entrainment formulation is illustrated in Figures 4.5 – 4.7 where the rapids entrainment parameter ($R_a$) is varied from 0.25, 0.5, and 1.0 respectively. A rapids entrainment parameter value of 1.0 represents complete entrainment of the parcel in a single coupling interval. From these figures it can be seen that upstream of the "rapids" location, that the ice concentration(s) and thickness are basically identical to the case with no rapids entrainment. At the rapids location, the surface ice concentration is decreased with each coupling interval and the suspended frazil ice concentration increases. The number of coupling intervals that a parcel is expected to remain in the rapids should be considered when choosing an appropriate value for $R_a$ if the value is intended to be less than 1.0. This is because with a $R_a$ value of 0.5, half of the surface ice parcel will be entrained in the first coupling interval and half of the remaining surface ice parcel will be entrained in the next interval and this will continue until the parcel exits the rapids area. Depending on the amount of entrainment expected throughout the entire rapids area, the coupling time ($t_{intvl}$) and $R_a$ should be chosen carefully.

Immediately downstream of the rapids location, an increase in the surface ice thickness of existing parcels is typical due to the elevated suspended ice concentration after the rapids. If the surface ice parcels are completely entrained at the rapids ($R_a$ = 1.0), new ice parcels must be initialized at the initial frazil ice thickness ($h_{f0}$) and will be allowed to accumulate frazil from that point on. The suspended ice concentration is highest when $R_a$ is specified as 1.0 and it peaks at a value of 0.0075 (Figure 4.7) which is almost 10 times the maximum suspended frazil concentration when no rapids entrainment exists ($C_v$ = 0.0008).

Due to the relatively short travel time in the above simulation setup, the thermally generated parcels do not generate a lot of ice mass that can be entrained at the rapids. In order to test the entrainment of larger volumes of surface ice, an ice run simulation needed to be setup as well. The boundary conditions used for this simulation are shown in Table 4.4.

**Table 4.4** – Boundary conditions for the mass exchange model runs (with ice run included).

| Boundary Condition | Value |
|---|---|
| Upstream Inflow | 3345 cms |
| Downstream Water Level | 2 m |
| Upstream $T_w$ | 0.02 °C |
| Heat Transfer | 380 W/m$^2$ |
| Simulation Length | 12 hrs |

Ice parcels were input at the upstream boundary and allowed to float down the channel to where they were completely entrained in one coupling time (Figure 4.8). These parcels had a surface ice thickness ($th_{is}$) of 0.15 m and a frazil ice thickness ($th_{if}$) of 0.15m. The larger surface ice volumes at the rapids in this simulation resulted in higher suspended ice concentrations at the rapids ($C_v$ = 0.015) and the higher water velocities in the channel carry the suspended frazil ice further downstream than in the previous simulation. Once through the rapids, the ice mass exchange to the surface initiates new parcels once again and the suspended frazil ice concentration begins to decrease due to the net deposition to the surface after the 8 km mark of the channel (Figure 4.8).

## 4.4 Anchor Ice Growth Model

The anchor ice growth model described in section 3.4 will be demonstrated by a series of rectangular channel simulations. The boundary conditions used for these simulations are shown in Table 4.5.

**Table 4.5** – Boundary conditions for the anchor ice model runs.

| Boundary Condition | Value |
|---|---|
| Upstream Inflow | 3345 cms |
| Downstream Water Level | 2 m |
| Upstream $T_w$ | 0.02 – 0.5 °C |
| Heat Transfer | 100 - 500 W/m$^2$ |
| Simulation Length | 48 - 192 hrs |

For these simulations, the mass exchange parameters will be set so that little to no surface ice develops which will allow the suspended frazil ice concentration to be at its highest value possible for the flow and heat transfer conditions specified. The porosity of anchor ice ($e_a$) will be 0.4 unless indicated otherwise, the frazil ice accretion rate to the bed ($\gamma$) will be 6 x $10^{-4}$ m/s and there will be 5 material types in this channel to allow for a range of parameters to be tested at the same time.

The simulation of anchor ice growth and mechanical release is shown in Figure 4.9. A range of bed particle sizes ($d_s$) from a diameter of 0.5 cm to 5 cm are specified throughout the channel and the anchor ice thickness ($h_{an}$) is tracked at these locations over the course of the simulation. The smaller bed particle sizes are specified at the upstream channel locations and the bed particles get progressively larger as you move downstream. From Figure 4.9, it can be seen that the anchor ice growth rates increase slightly in the downstream direction. This is due to the thermal growth of the suspended frazil ice concentration with increased travel time and will in turn increase the rate of anchor ice growth if the accretion rate to the bed material is held constant (see equation 3.25). With the inter-particle resistance ($c_{ohb}$) set to 0, it can be seen that there is a linear relationship between $d_s$ and the thickness of anchor ice that this bed material can support before the buoyant force of the anchor ice overcomes the submerged weight of the bed particles. Closely packed bed particles with a diameter of 1 cm can hold 0.2 m of anchor ice with a porosity of 0.4 and similarly 5 cm diameter bed particles can hold 1.0 m of anchor ice with the same porosity. This is expected given the relative submerged weights of the bed particles ($\rho_b$ = 2650 kg/m$^3$) and the anchor ice ($\rho_i$ = 917 kg/m$^3$). A higher porosity for anchor ice would mean the same bed material could support a greater thickness prior to release and vice versa. Once the anchor ice is released another growth cycle begins immediately on the same bed material.

As discussed in section 3.4, once anchor ice is released from the bed through either a mechanical or thermal release mechanism it is added to the surface as a surface ice parcel. To illustrate this component of the model, the surface ice concentration is tracked

during the simulation above and the first 96 hours of the simulation is shown in Figure 4.10. It can be seen that anchor ice is released periodically at specific locations and there are associated spikes in the surface ice concentration ($C_a$) when these new ice parcels pass over this location. Because there is a positive gradient in the anchor ice thickness in the downstream direction, there is progressive release of anchor ice in areas with the same bed material properties which can result in extended periods of surface ice concentration during each release event. This is evident in the multiple spikes of surface ice concentration in Figure 4.10.

Similar to the simulation above with a range of bed particle sizes, a range of inter-particle resistance values ($c_{ohb}$) yields similar results. Inter-particle resistance values between 50 and 250 N/m$^2$ with a small bed particle diameter ($d_s$ = 0.001 m) shows another linear relationship between the inter-particle resistance and the anchor ice thickness just prior to release. It is evident form Figure 4.11 that a $c_{ohb}$ value of 100 N/m$^2$ will support 0.2 m of anchor ice with a porosity of 0.4. The submerged bed particle weight will be a force in addition to the inter-particle resistance to counteract the buoyant force of the anchor ice.

The second form of anchor ice release considered in the model is a thermal release mechanism and is illustrated in Figure 4.12. Here, anchor ice is allowed to grow under supercooled conditions for the first 48 hours of the simulation. During this time, the substrate layer thickness ($h_{sb}$) decreases slowly from its initial value of 0.03 m. After hour 48 of the simulation, the inflow water temperature is raised from 0.02 ºC to 0.5 ºC and the heat transfer away from the surface is decreased from 500 W/m$^2$ to 100 W/m$^2$. This

causes the supercooled water at the monitored location to be replaced by much warmer water which thermally erodes the anchor ice thickness at the surface as well as the substrate layer thickness because the substrate water temperature is assumed to be equal to the water temperature above it. It can be seen from the plot that the thermal erosion is relatively high at the top surface of the anchor ice which is due to the higher water velocity that increases the heat transfer and subsequent melting rate. It is also evident from the figure that the thermal erosion of the undersurface of the anchor ice is at a higher rate than the thermal growth which occurred in the first 48 hours of the simulation. This is expected because the water is usually only supercooled by a few hundredths of a degree Celsius so it freezes quite slowly and the warmer water during a melting period is often more than a few hundredths of a degree above 0. Once the substrate layer thickness reaches the thermal release value (0.04 m) the anchor ice is released and no new growth is started because the water is no longer supercooled. A final observation from Figure 4.12 is the small increase in supercooling just prior to the arrival of the warm water from the upstream boundary. This is also expected because the location of peak supercooling is often just downstream of the 0ºC isotherm prior to significant thermal growth of frazil ice. This isotherm will be moving downstream as the incoming warm water from upstream travels through the channel.

Another component of the model that will impact the growth and decay of anchor ice is the amount of solar radiation reaching the anchor ice. The model also considers the presence of surface ice in this calculation and Figure 4.13 shows the results from a 48 hour simulation used to illustrate these components of the model. The first 24 hours of

the simulation has no surface ice and the solar radiation reaching the water surface ($\Phi_R$) is tracked along with the solar radiation reaching the top of the anchor ice ($\Phi_{R2}$). Solar radiation first appears in the simulation around hour 8, peaks shortly after hour 12, and is gone before hour 18. The solar radiation extinction coefficients for this simulation are the same as those identified for the Nelson River in section 3.4 (Tetres, 2004). During the second 24 hours of the simulation, a surface ice run is passed through the channel with a thickness ($th_i$) of about 0.3 m which does not impact the solar radiation reaching the water surface ($\Phi_R$) but the reduction in solar radiation reaching the anchor ice ($\Phi_{R2}$) due to the passing surface ice is clear from the plot (Figure 4.13).

## 4.5 Aufeis Growth Model

One complete aufeis growth cycle (node is *wet*, *dry*, then *rewet*) is simulated using the Rectangular Multiple Outcrops Channel and the node at the top of the center outcrop (7.0 km from upstream) is tracked in Figure 4.14. The boundary conditions used for this simulation are shown in Table 4.6.

**Table 4.6** – Boundary conditions for the aufeis model runs.

| Boundary Condition | Value |
|---|---|
| Upstream Inflow | 1000 - 1500 cms |
| Downstream Water Level | 1.375 - 3 m |
| Upstream $T_w$ | 0.02 °C |
| Heat Transfer | 500 W/m$^2$ |
| Simulation Length | 60 hrs |

In this simulation, the outcrop is flooded for the first 34 hrs and anchor ice thickness is accumulated at a porosity of 0.4. After hr 34 the incoming discharge is decreased from 1500 to 1000 cms and the downstream level boundary is lowered from 3 to 1.375 m to expose the anchor ice on the outcrop to the atmosphere and to activate the aufeis growth calculations. The aufeis layer ($h_i$) grows using the formulation presented in section 3.5 until it reaches the maximum aufeis layer thickness ($h_{aufmax}$) which is specified to be 0.05 m for this simulation. The aufeis layer is able to reach this thickness in about 6 hrs with the heat transfer rate of 500 W/m$^2$. This growth of the solid aufeis layer also reduces the bulk porosity ($e_{aB}$) of the anchor ice / aufeis layer from the initial value of 0.4 to 0.29.

Once the outcrop is "*dry*", a snow thickness begins to accumulate on the surface at a rate of about 6 mm/hr for about 14 hrs. After the snowfall event is complete the discharge at

the upstream boundary and the downstream level boundary are increased again to flood the snow and aufeis layers. Once the node is "*rewet*" the aufeis and snow layers are reset to 0 and the snow layer is added to anchor ice thickness because of the supercooled conditions. This results in a step up in the total anchor ice / aufeis thickness and a step down in the bulk porosity (Figure 4.14). From this point on, the anchor ice growth calculations proceed as presented in section 4.4 above. In the case of consecutive drying and wetting cycles, the aufeis growth and decay formulation would function the same as outlined above, and in Figure 4.14, on a repeatable basis.

## 4.6 Dry Bed Treatment

The dry bed treatment outlined in section 3.6 will be tested using three ideal channel setups, the Rectangular Berm channel (Figure 4.1), the Rectangular 1-Outcrop channel (Figure 4.2), and the Rectangular Multiple Outcrops channel (Figure 4.2). The simulation setups will be fairly straightforward in that a given discharge will be set at the upstream boundary of the channel and the downstream level boundary will be progressively lowered until portions of the outcrops in the channel become "*dry*". In the case of the Rectangular 1-Outcrop simulation, the downstream level boundary will be subsequently raised until the outcrop is defined as "*wet*" again.

For the Rectangular 1-Outcrop setup, the inflow boundary condition was set at 3000 cms, the dry bed coupling time ($t_{intdry}$) was 300 s, the hydrodynamic time step was 0.75 s ($\Delta t_{hd}$), the dry bed (*htlow*) and rewet (*hthigh*) depths were set as 0.05 m and 0.1 m,

respectively. The minimum depth at the downstream boundary is 2.5 m to allow for portions of the single outcrop to become "*dry*" and then the boundary was raised to a depth of 6.0 m to allow for the outcrop to be "*rewet*". Figure 4.15 shows the simulated results when the downstream boundary is at its lowest level. The coloured contour in the figure is the water depth and the directional flow vectors are plotted on top of the contours to show the flow lines around the dry portion of the outcrop. An element in this figure is blanked (*i.e.,* no colour shown) when all 3 nodes of that element are "*dry*". Some of the small irregularities in the simulated results near the single large outcrop can be attributed to the relatively coarse mesh around this outcrop and serves to highlight the importance of a refined mesh in areas where drying and wetting are likely to occur. The other two setups used for this section are more refined around the outcrops. Figure 4.16 is plotted in the exact same manner as Figure 4.15 but this figure contains the simulated results from the end of the simulation when the raised downstream boundary condition has made all the nodes in the channel "*wet*" again. From these two figures, it can be seen that the dry bed treatment employed in the model is able to reasonably simulate the drying and rewetting of a single large outcrop in a rectangular channel.

Another simulation was setup using the Rectangular Multiple Outcrops channel and a similar procedure was used to illustrate the dry bed treatment of the model. Figure 4.17 shows this channel with portions of the outcrops "*dry*" (discharge = 1800 cms, downstream water level = 1.375 m). The water depth contours and flow vectors in the plot show that the model is able to simulate the flow patterns around these multiple

outcrops. The smoother contours around the outcrops and the symmetrical flow vectors are partially due to the more refined mesh around the outcrops in this channel.

The last simulation used to illustrate the dry bed treatment was setup with the Rectangular Berm channel and the water depth contours and flow vectors are shown in Figure 4.18 once portions of the berm are "*dry*" (discharge = 1000 cms, downstream water level = 4 m). This figure shows that even though the flow is required to turn 90 degrees at the berm, the flow patterns appear reasonable even downstream of the berm where a small re-circulation eddy is apparent as well. The current dry bed treatment in the model illustrated in Figures 4.15 – 4.18 is a marked improvement over the dry bed treatment employed by the model previously and is an important component in the simulation of anchor ice and aufeis growth.

The nodal dry depth (*htlow*) and rewet depth (*hthigh*) should be specified while taking into consideration the mesh and bed geometry. Small *htlow* values will require small hydrodynamic time steps to remain stable throughout the explicit solution scheme. Larger *htlow* (and *hthigh*) values will result in a more stable simulation but will result in a more inaccurate solution near the locations of drying and wetting and in extreme cases can introduce significant continuity errors into the simulation. For these reasons, the *htlow* and *hthigh* parameters should be chosen carefully by the modeler.

# 4.7 Sensitivity of Anchor Ice Model Parameters

A sensitivity analysis of selected model parameters was carried out to determine the effects these parameters had on the growth rates of anchor ice. A set of eight model parameters were tested and compared to a base case in order to properly observe how changing these parameter values would impact the simulated results. The data from this analysis can then be used to assist in the calibration of these same model parameters for the simulation of unique river situations. This data will establish a "relative importance" of the parameters as they pertain to the growth of anchor ice and should not be confused with the actual values a modeler would choose (or calibrate) for a given simulation setup.

## 4.2.1 Simulation Setup

The channel used in each of the simulations was the Rectangular Channel (Figure 4.1). Each of the simulations was conducted using an identical setup, with the exception of the parameter being tested. Each simulation was run for 350 hours with a hydrodynamic time step of 5.0 seconds and a coupling time of 900 seconds. The time frame was chosen as such because it allowed for substantial anchor ice growth without running into extremely thick anchor ice deposits which can alter the flow patterns in the channel significantly.

In order to reduce the required length of channel for proper formation of active frazil and anchor ice the inflow water temperature was set to 0.05 °C and the heat transfer from the channel surface was approximately 500 $W/m^2$. While most of the other model parameters

were left as default for the base case simulation, the coefficient quantifying the rate of re-entrainment of surface frazil ice ($\beta$) was raised to 5 x $10^{-5}$ $s^{-1}$ and the net rise velocity of frazil ice in the turbulent flow ($v_b$) was reduced to 0 m/s, which represents the condition that the buoyant velocity of frazil is balanced by the vertical turbulent mixing of the flow. The values of these two parameters were set to help prevent the formation of surface ice runs throughout the sensitivity simulations. The diameter of the bed particles was set to 0.25 m to limit any mechanical release of anchor ice. The channel setup described above and the other model characteristics were chosen to facilitate the simulation of typical anchor ice conditions which allowed for an accurate analysis of the parameters affecting anchor ice formation and evolution within the model.

In total, eight parameters were tested in this portion of the sensitivity analysis. Each parameter has one "Base Case" value along with a "Case A" and a "Case B" value. When a given parameter is being tested, each of the other parameters was set back to the base case value. All of the parameters tested and their respective values for each of the cases are shown below in Table 4.7.

**Table 4.7** - Model parameters and the case values used in the sensitivity analysis.

| Model Parameter | Base Case | Case A | Case B |
|---|---|---|---|
| Inflow Water Temperature (°C) | 0.05 | 0.02 | 0.035 |
| Nusselt Number | 4 | 2 | 6 |
| Frazil Disc Diameter (mm) | 2 | 0.2 | 20 |
| Frazil Disc Thickness (mm) | 0.3 | 0.03 | 3 |
| Porosity of Anchor Ice | 0.4 | 0.2 | 0.6 |
| Accretion Rate of Frazil to the Bed ($\gamma$) | $1.0 \times 10^{-3}$ | $1.0 \times 10^{-4}$ | $1.0 \times 10^{-2}$ |
| Manning's Roughness of Bed (n) | 0.035 | 0.02 | 0.05 |
| Depth (m) | 3.5 | 2.5 | 4.5 |

### 4.2.2 Results

In order to properly illustrate the results of the sensitivity analysis, the anchor ice thickness was tracked as a function of time at three locations in the channel. These locations were 3 km, 5 km, and 7 km from the upstream boundary of the channel. The nodes across the width of the channel were averaged at each location and output at one hour intervals for the entire simulation. It was observed that under these conditions the increase in anchor ice thickness has a linear relationship with time. To summarize the results of the simulation and to facilitate proper discussion, the slopes of each of these lines (anchor ice growth rates) were calculated and are presented in Table 4.8.

From the results in the table, comments can be made about the impact each of the assessed model parameters have on the growth rates of anchor ice in the ideal channel. It should be noted that the relationships are only valid for the range of model parameters tested and the conditions simulated in this analysis.

- In all cases, the growth rate of anchor ice at each location increased with increasing distance from the upstream boundary. This is expected because without any surface ice to insulate the flow, continued heat loss from the ice/water mixture must be balanced with thermal growth of the suspended frazil ice concentration. This increased frazil concentration will result in more active ice particles attaching to the bed material, which will further increase the anchor ice growth rate.

**Table 4.8** - Anchor ice growth rate (mm/hr) at each measured location in the channel.

| | | Anchor Ice Growth Rate (mm/hr) | | |
|---|---|---|---|---|
| | | **3 km** | **5 km** | **7 km** |
| **Inflow Water Temperature** | **Base Case** | 0.280 | 1.875 | 5.205 |
| | **Case A** | 1.233 | 4.444 | 6.596 |
| | **Case B** | 0.670 | 3.136 | 6.015 |
| **Nusselt Number** | **Base Case** | 0.280 | 1.875 | 5.205 |
| | **Case A** | 0.282 | 1.405 | 3.436 |
| | **Case B** | 0.294 | 2.520 | 5.326 |
| **Frazil Disc Diameter** | **Base Case** | 0.280 | 1.875 | 5.205 |
| | **Case A** | 0.584 | 3.434 | 5.448 |
| | **Case B** | 0.284 | 1.280 | 2.451 |
| **Frazil Disc Thickness** | **Base Case** | 0.280 | 1.875 | 5.205 |
| | **Case A** | 0.584 | 3.434 | 5.448 |
| | **Case B** | 0.284 | 1.280 | 2.451 |
| **Porosity of Anchor Ice** | **Base Case** | 0.280 | 1.875 | 5.205 |
| | **Case A** | 0.213 | 1.396 | 3.894 |
| | **Case B** | 0.407 | 2.868 | 7.838 |
| **Accretion Rate of Frazil Ice to Bed Material** | **Base Case** | 0.280 | 1.875 | 5.205 |
| | **Case A** | 0.231 | 0.979 | 0.957 |
| | **Case B** | 0.843 | 1.775 | 3.763 |
| **Manning's Surface Roughness** | **Base Case** | 0.280 | 1.875 | 5.205 |
| | **Case A** | 0.344 | 1.780 | 5.013 |
| | **Case B** | 0.254 | 2.059 | 5.249 |
| **Depth** | **Base Case** | 0.280 | 1.875 | 5.205 |
| | **Case A** | 1.963 | 6.396 | 8.146 |
| | **Case B** | 0.000 | 0.560 | 1.705 |

- A colder inflow water temperature results in higher anchor ice growth rates, with the influence being greater near the upstream end of the channel (a 340% increase in growth rate was observed at 3 km compared to a 27% increase at 7 km, when comparing the minimum and maximum parameter values). This can be attributed to the fact that the influence of the upstream water temperature decreases as the ice/water mixture approaches a state of thermal energy equilibrium further downstream.

- A higher Nusselt number results in higher thermal growth rates of the suspended frazil concentration (see section 2.2) and therefore, higher anchor ice growth rates as well. This is due to the increase in convective heat transfer associated with a higher Nusselt number. This increase in heat transfer can be caused by a change in particle shape/orientation to the flow, an increase in turbulent heat transfer or a combination of the two. The effect of the Nusselt number is minimal at 3 km (4% increase in growth rate from min to max values) and is much greater at 7 km (55% increase for same values). It should also be noted that the growth rates at 7 km for the base case and case B values (max value) are very close to one another. This potentially could signify a decrease in the effects of a higher Nusselt number as you move further downstream towards equilibrium.

- Thermal conductivity was not included in table 4.8 above but it was found that the effects of changing the thermal conductivity coefficient between the frazil

ice and water are identical to the effects of changing the Nusselt number so long as each of the values were modified by a common factor. This behavior is in fact required by the model formulation (section 2.2). Since the thermal conductivity is a property of the fluid and the amount of supercooling is quite small, this coefficient should remain very close to a value of 0.56594 W/(m*°C).

- Throughout a period of supercooling, frazil ice discs of constant size are assumed to exist throughout the water column. Both the diameter and the thickness of these discs must be specified by the modeler. At all locations, a smaller frazil disc diameter ($d_f$) corresponds to a larger growth rate of anchor ice. This is a byproduct of the fact that the suspended ice concentration is calculated volumetrically. For a given volume of suspended ice produced, there will be a greater number of particles when they are smaller in size. Based on the model formulation (section 2.2), this greater number of particles will increase the thermal growth portion of the frazil concentration (through accelerated heat transfer) and therefore will do the same for the anchor ice growth rate. Another observation is that at 3 km, the base case growth rate is very close to the case B rate (largest diameter of frazil), but at 7 km, the base case has moved up to be very close to the case A rate (smallest diameter of frazil). This indicates that the impact of various frazil sizes on the growth rate of anchor ice may diminish with time for certain sizes of particles. This effect should not be understated though as the particle size is one of the least

measured values in the field and at 7 km, the difference between the case A ($d_f$ = 0.2 mm) growth rate and the case B ($d_f$ = 20 mm) growth rate is 122%.

- At all observed locations in the channel, a smaller frazil disc thickness ($d_e$) corresponds to a larger growth rate of anchor ice. It was observed that the effects of changing the frazil disc thickness were identical to those found when changing the frazil disc diameter. Since the base case values for each parameter were modified +/- a factor of 10 to establish the case A and the case B values, the model formulation for the thermal growth of frazil concentration (section 2.2) requires that this in fact be the case.

- It was found that a higher porosity of anchor ice corresponded to a larger growth rate in the anchor ice thickness. While this was an expected result (section 3.4), it should be noted that the differences in the growth rates at each of the observed locations were much more consistent throughout than for other parameters. The base case growth rate was 33% higher on average than the case A growth rate, and the case B growth rate was on average 50% higher than the base case values.

- As indicated in the model formulation for the growth of anchor ice (section 3.4), the accretion rate ($\gamma$) of frazil ice to the bed material is a primary contributor to the growth of anchor ice. As expected, the higher accretion rate (case B) is attributed to the largest growth rate of anchor ice at the 3 km

location. By the 5 km location though, the middle accretion rate (1 x $10^{-3}$ m/s) has overtaken the largest accretion rate (1 x $10^{-2}$ m/s) in terms of anchor ice growth which is still the case at the 7 km location as well. This occurs because in our ideal channel scenario, the highest accretion rate is able to remove enough of the suspended frazil concentration in the early stages of supercooling to impact the results further downstream. Eventually, as the flow approaches a state of thermal equilibrium it is anticipated that the higher accretion rate (case B) will catch up and likely surpass the base case values.

- For the range of values tested, the Manning's roughness (n) of the bed material had the smallest impact on the anchor ice growth rates. At 7 km, there was only a 5% difference between the smallest anchor ice growth rates (case A) and the highest (case B). Generally, a higher Manning's roughness value corresponded to marginally higher anchor ice growth rates but at the upstream end of the channel (3 km location), it was observed that the lowest Manning's roughness value at this location was attributed to higher anchor ice growth rates. After reviewing the model formulation, the Manning's bed roughness was not expected to impact the frazil ice production or the growth rate of anchor ice in any meaningful way. This was confirmed through this sensitivity analysis.

- It was found that a shallow flow depth produced much higher anchor ice growth rates than a deeper flow. This is consistent with the fact that a deeper

flow is able to store much more thermal energy so it will take a more severe event to supercool the water to a point where significant frazil ice and anchor ice growth will take place. Providing for a deeper flow depth will delay the onset of supercooling, and therefore the initiation of anchor ice, and sometimes can prevent it from forming altogether. These results are important to keep in mind when considering any mitigation alternatives directed at reducing the anchor ice formation in a given reach. This effect of water depth was observed in the experiments of Kerr *et al*., (2002) that showed a larger water depth had lower anchor ice growth rates.

The results discussed above indicate that the model parameters tested impact the anchor ice growth rates to varying degrees. Keeping in mind that this was an ideal channel setup, any numerical modeler wishing to simulate the growth of anchor ice with the model could use the insight gained from the above results as a guide when choosing values for some of the model parameters.

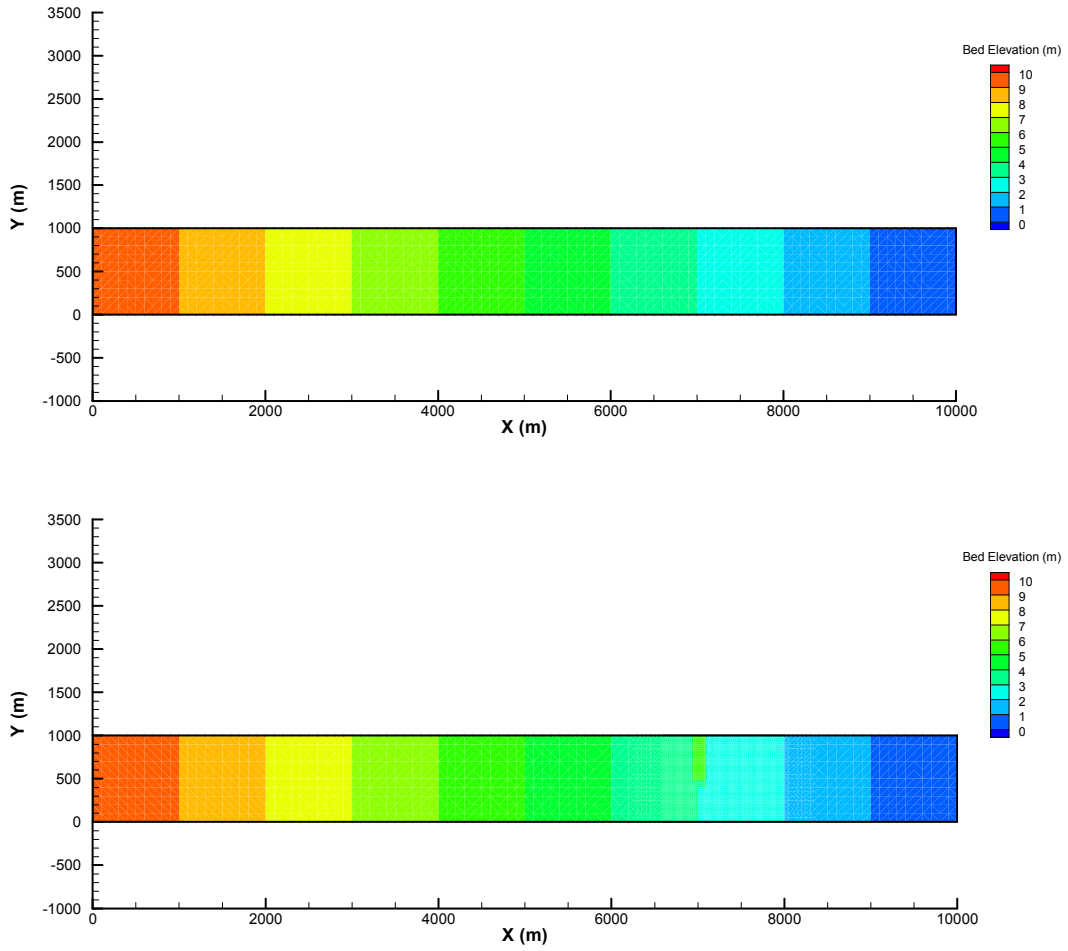


**Figure 4.1 -** Bed elevation profile for Rectangular Channel (top) and Rectangular Berm Channel (bottom).

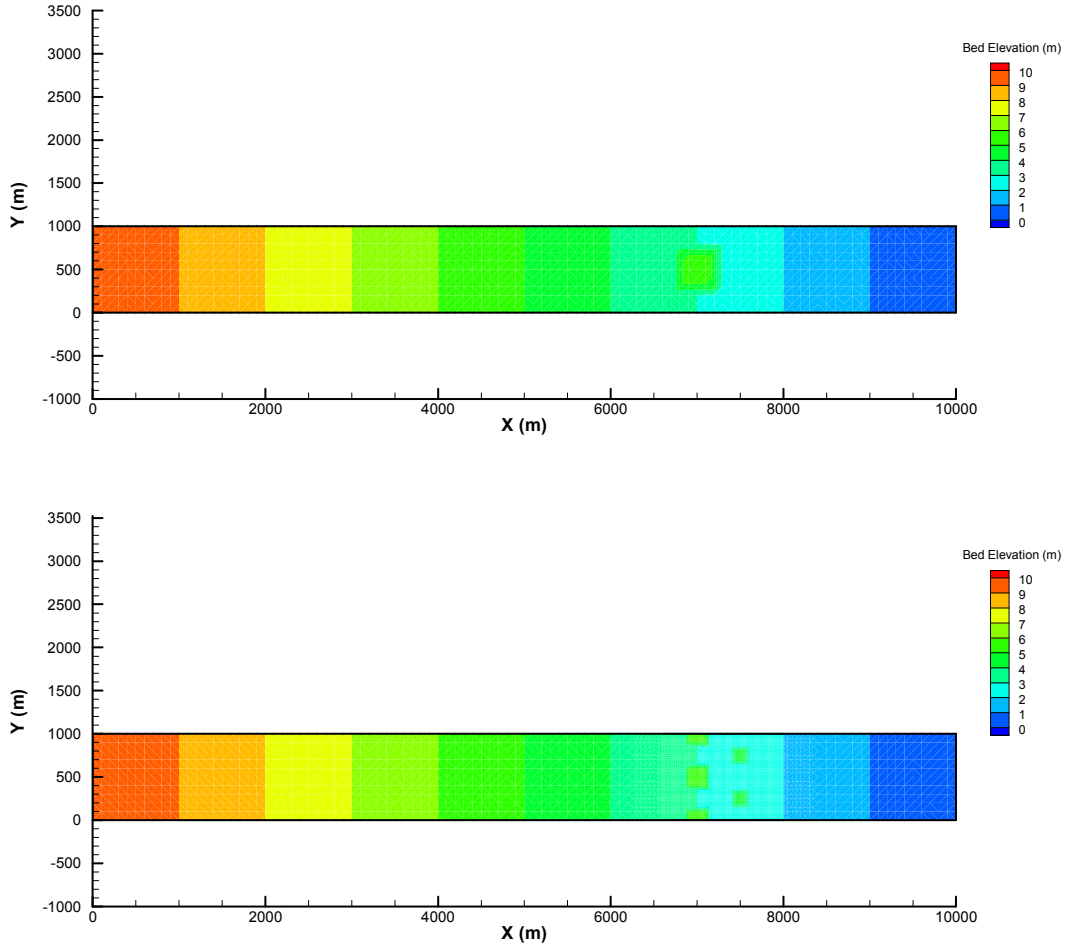


**Figure 4.2 -** Bed elevation profile for Rectangular 1-Outcrop Channel (top) and Rectangular Multiple Outcrops Channel (bottom).

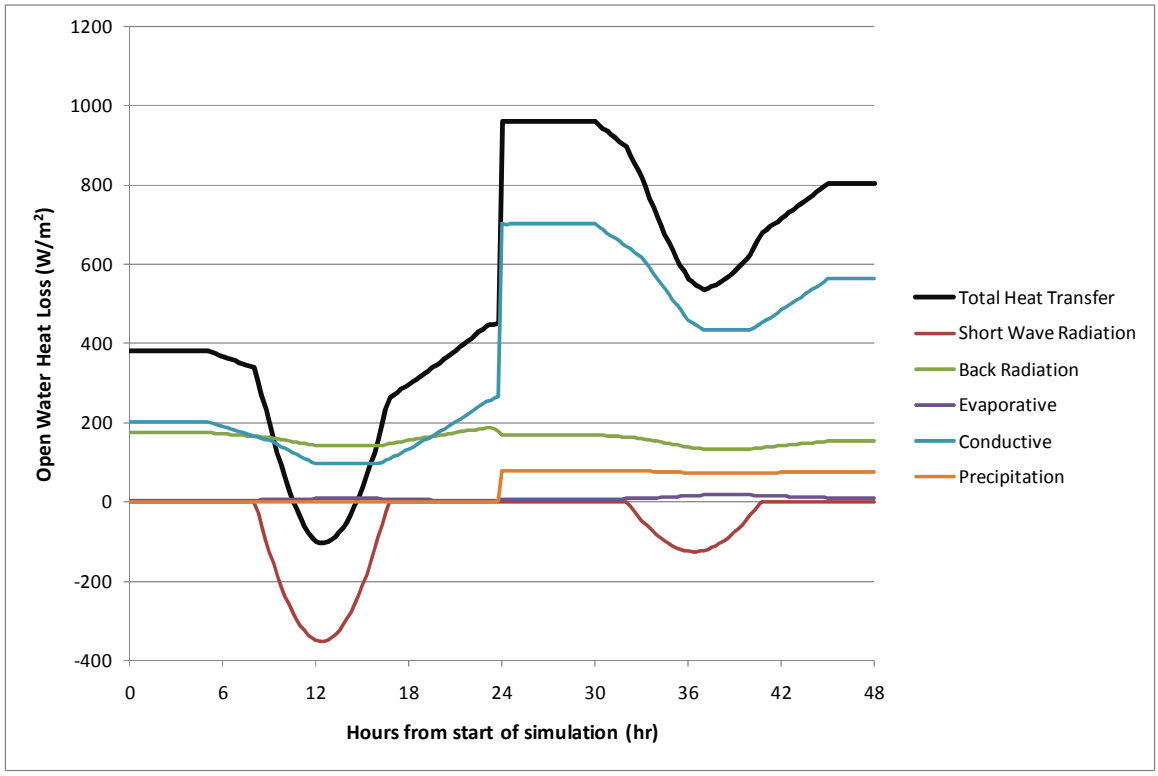


**Figure 4.3 -** Total heat transfer and detailed heat transfer components over a 2-day simulation.

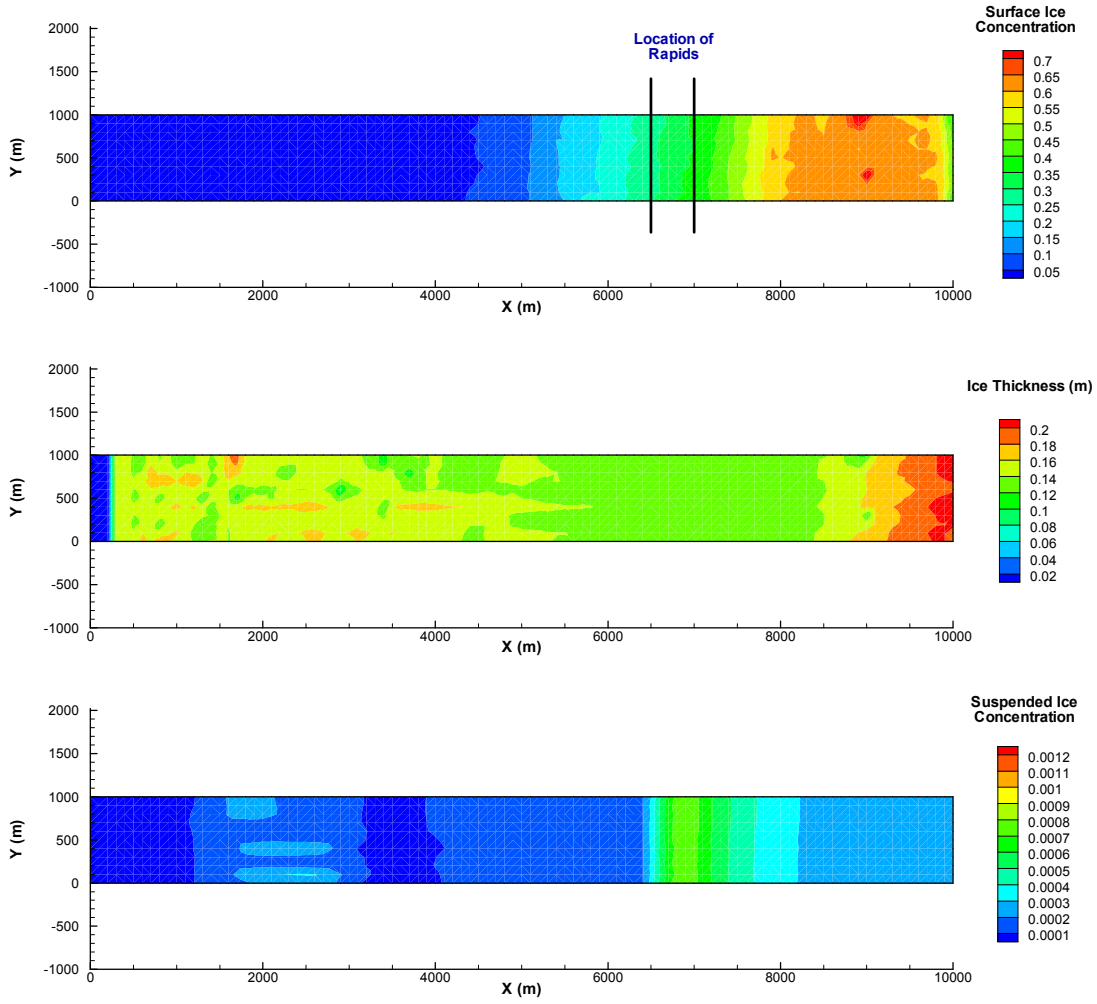


**Figure 4.4 -** Rectangular channel simulation with rapids entrainment off ($R_a$ = 0.0). Showing surface ice concentration, ice thickness, and suspended frazil concentration.

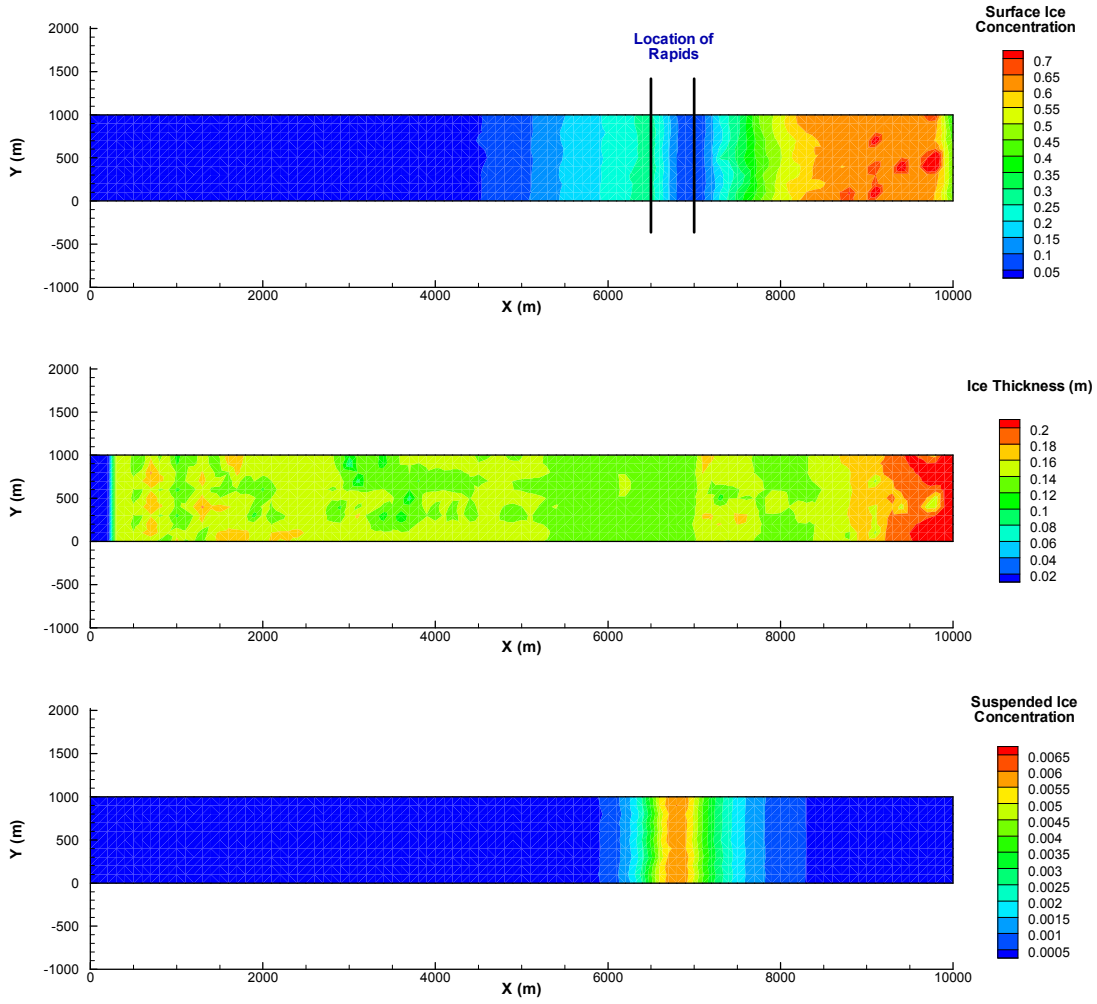


**Figure 4.5 -** Rectangular channel simulation with rapids entrainment on ($R_a$ = 0.25). Showing surface ice concentration, ice thickness, and suspended frazil concentration.

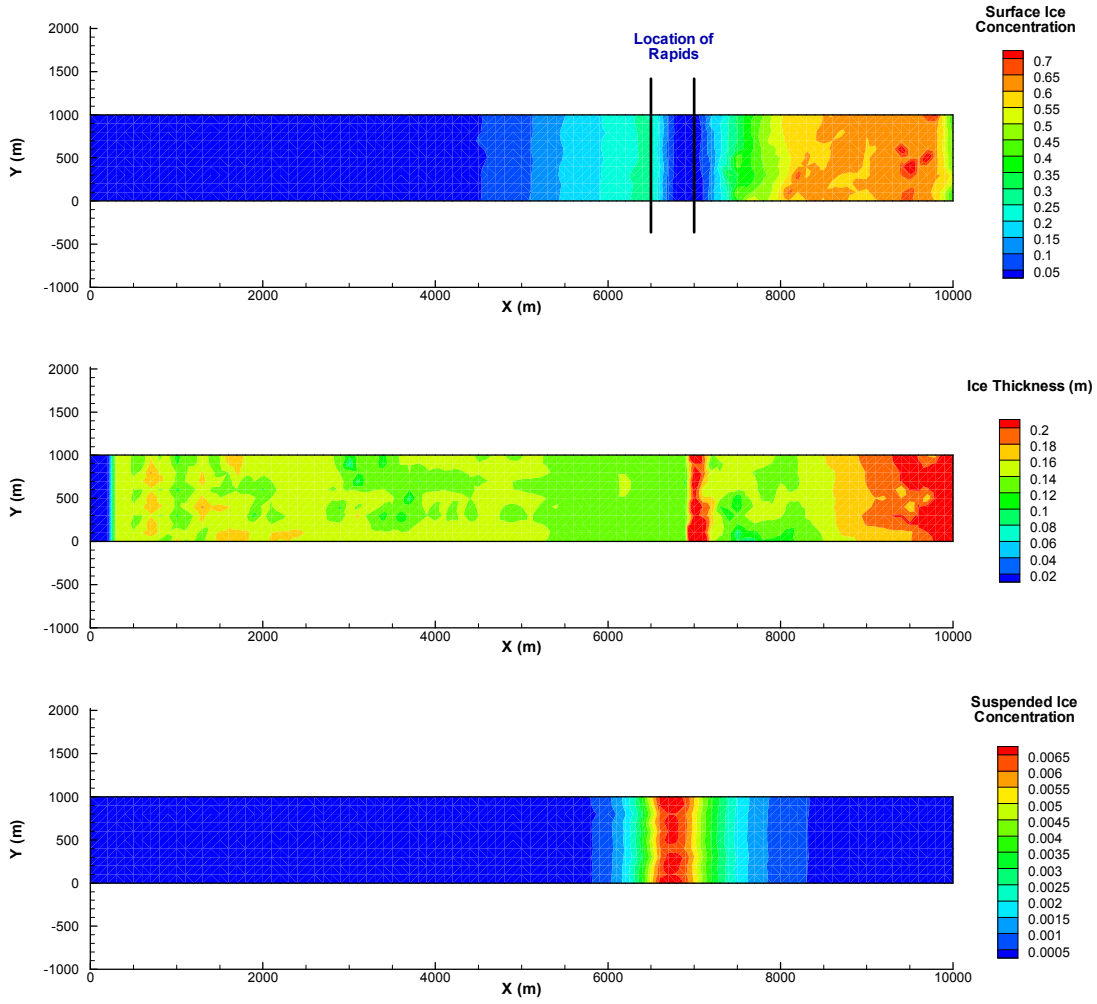


**Figure 4.6 -** Rectangular channel simulation with rapids entrainment on ($R_a$ = 0.5). Showing surface ice concentration, ice thickness, and suspended frazil concentration.

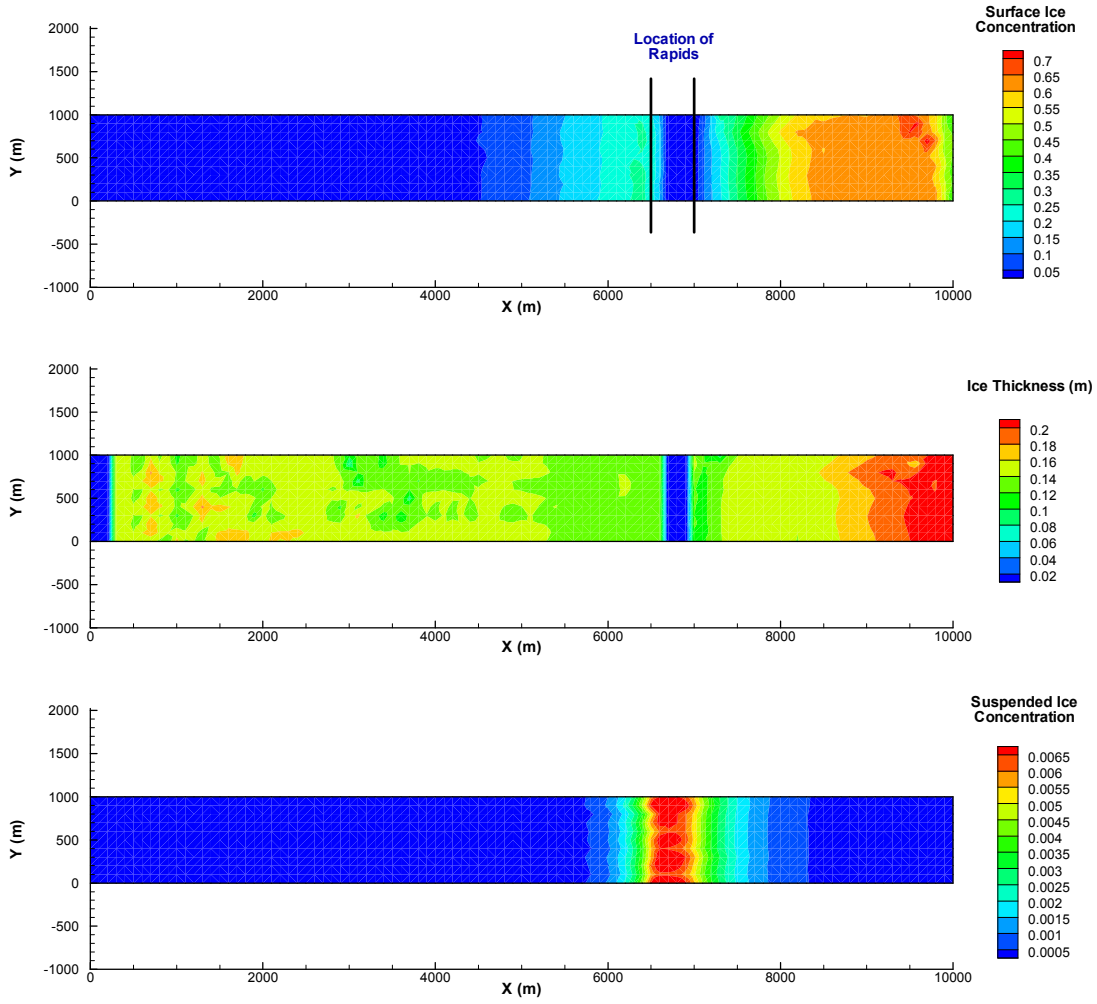


**Figure 4.7 -** Rectangular channel simulation with total rapids entrainment ($R_a$ = 1.0). Showing surface ice concentration, ice thickness, and suspended frazil concentration.

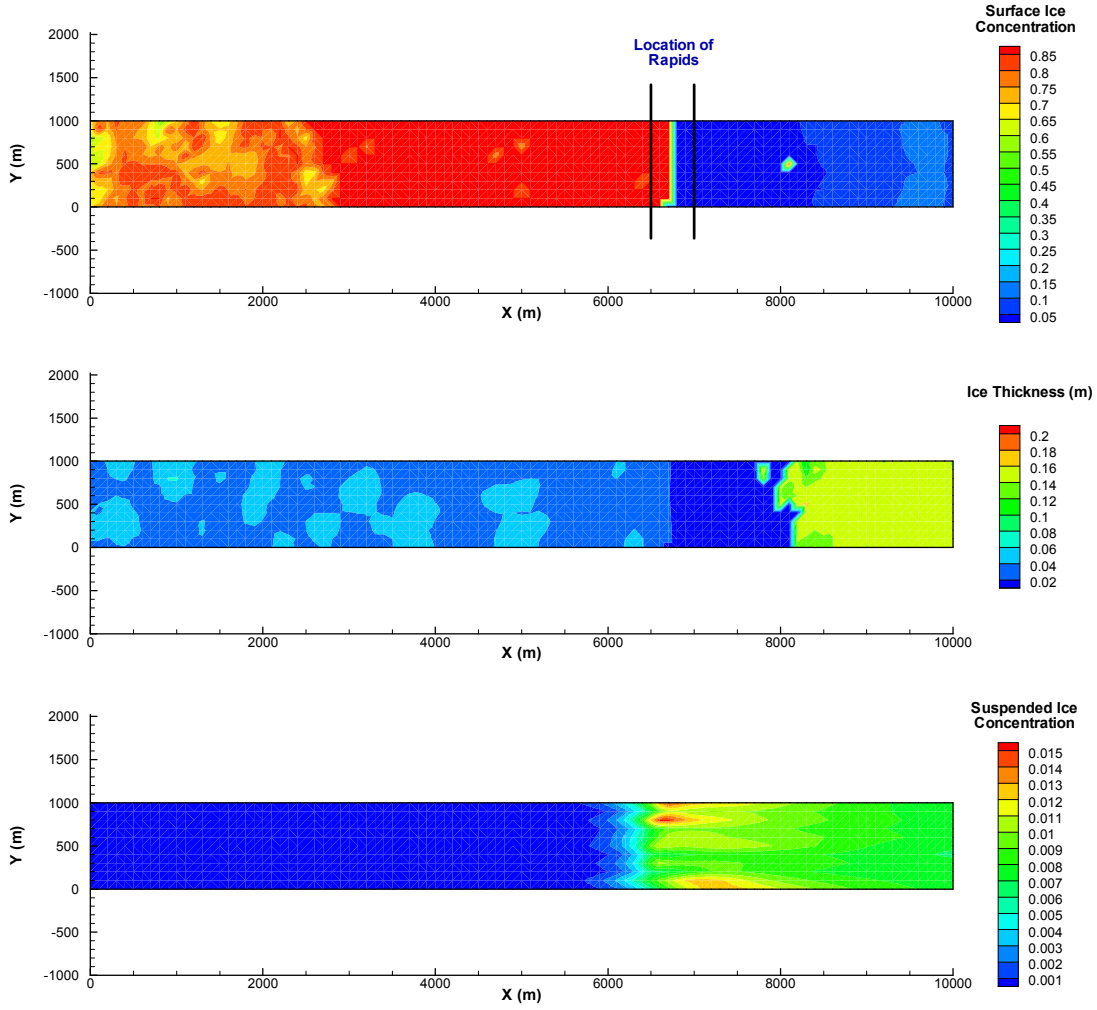


**Figure 4.8 -** Rectangular channel simulation with total rapids entrainment ($R_a$ = 1.0) and an incoming ice run. Showing surface ice concentration, ice thickness, and suspended frazil concentration.

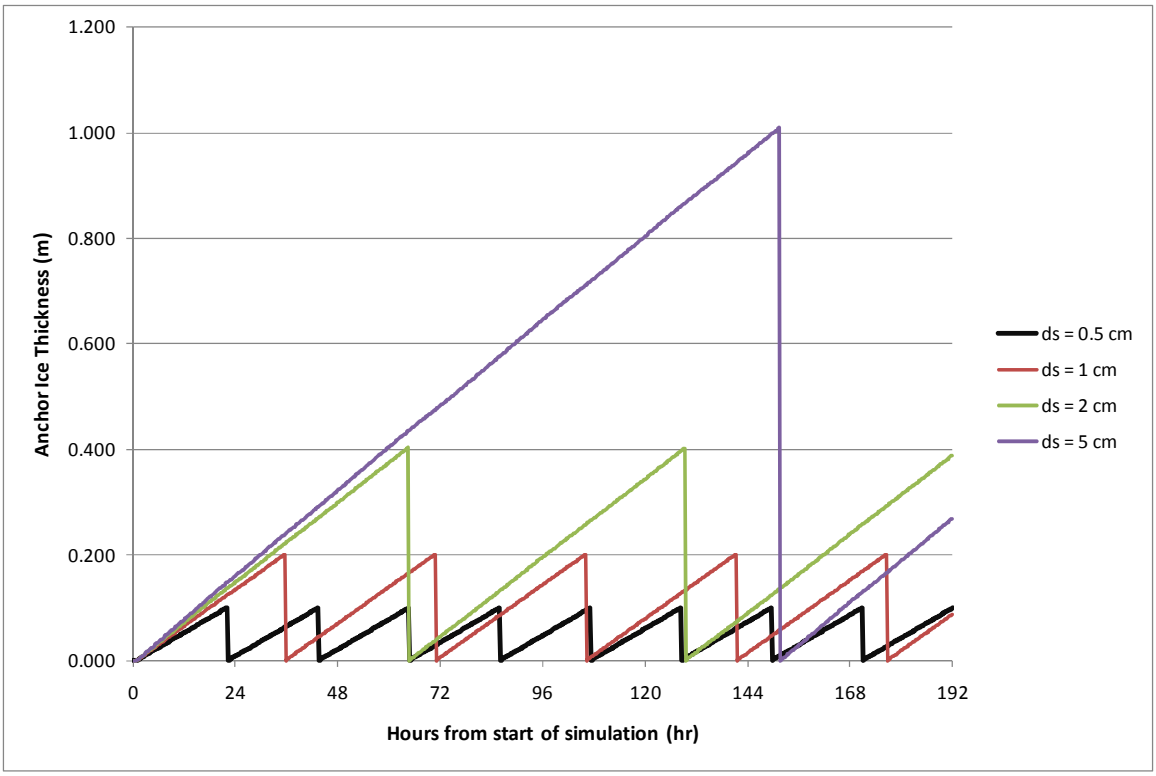


**Figure 4.9 -** Anchor ice growth and release with different bed particle sizes ($d_s$) and no inter-particle resistance ($c_{ohb} = 0$).

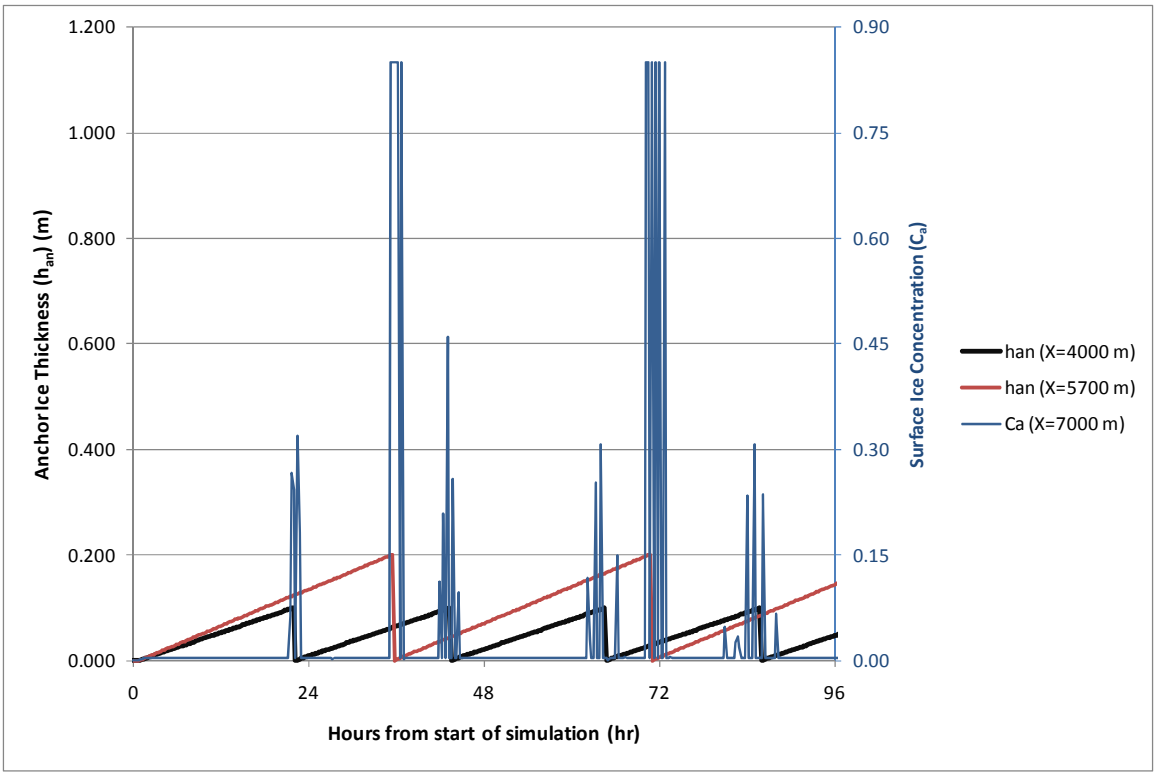


**Figure 4.10 -** Anchor ice growth and release with surface ice concentration ($C_a$) tracked (first 96 hrs).

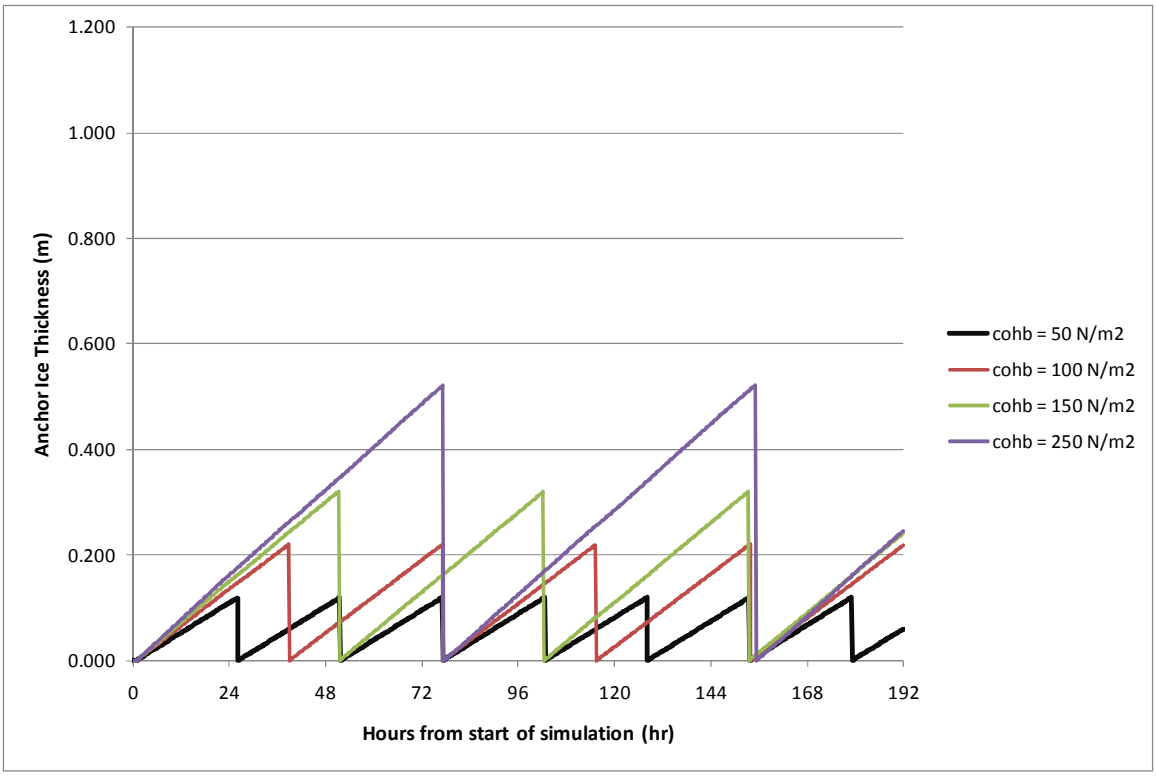


**Figure 4.11 -** Anchor ice growth and release with different inter-particle resistance ($c_{ohb}$) and small bed particle size ($d_s$ = 0.001 m).

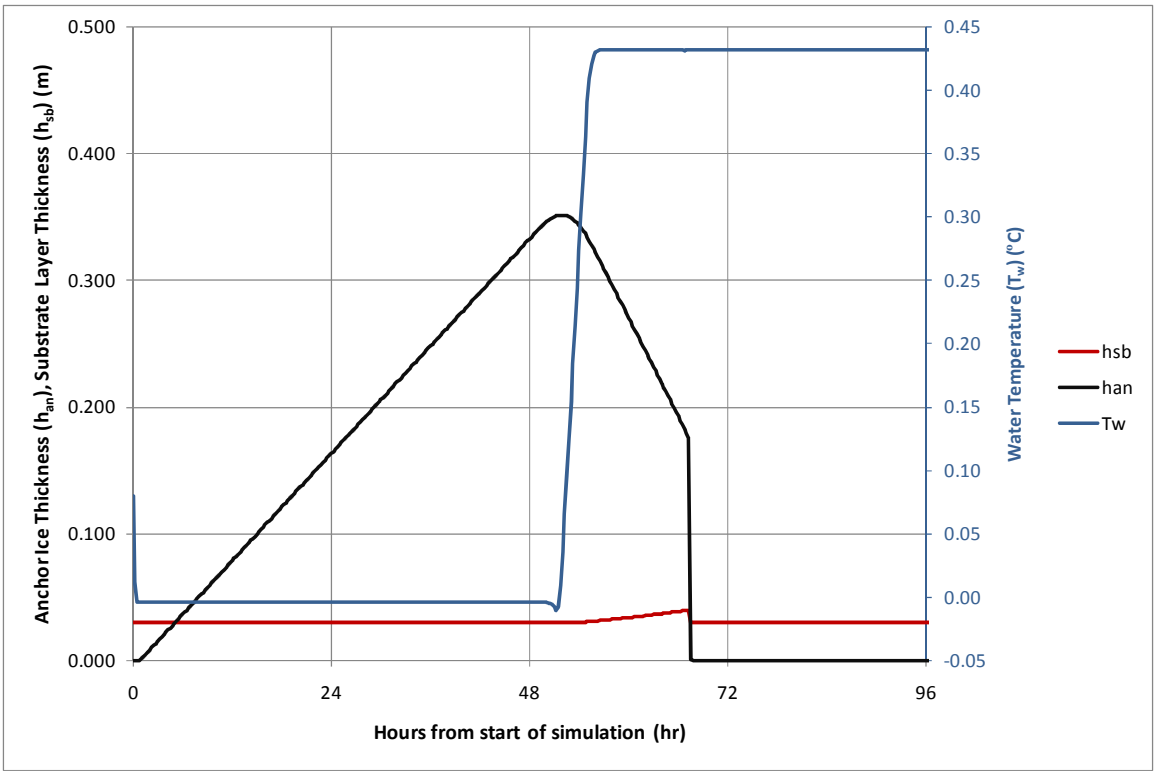


**Figure 4.12 -** Anchor ice growth and release with thermal release (first 96 hrs).

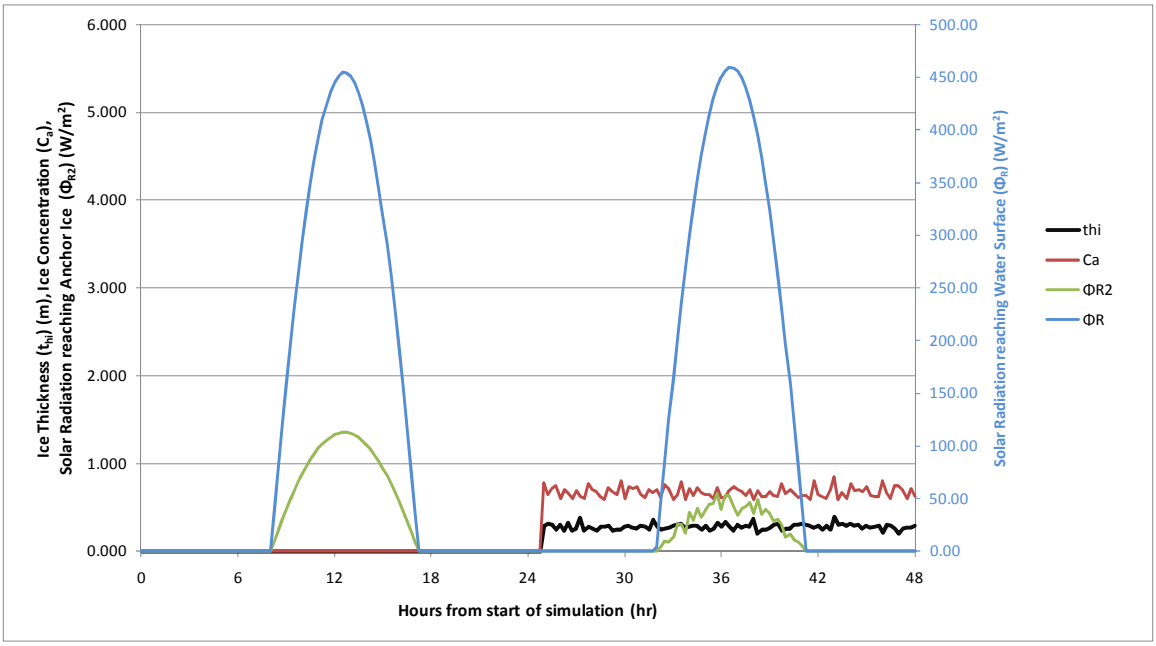


**Figure 4.13 -** Solar radiation reaching the water surface ($\Phi_R$) and the surface of anchor ice ($\Phi_{R2}$) with and without surface ice.

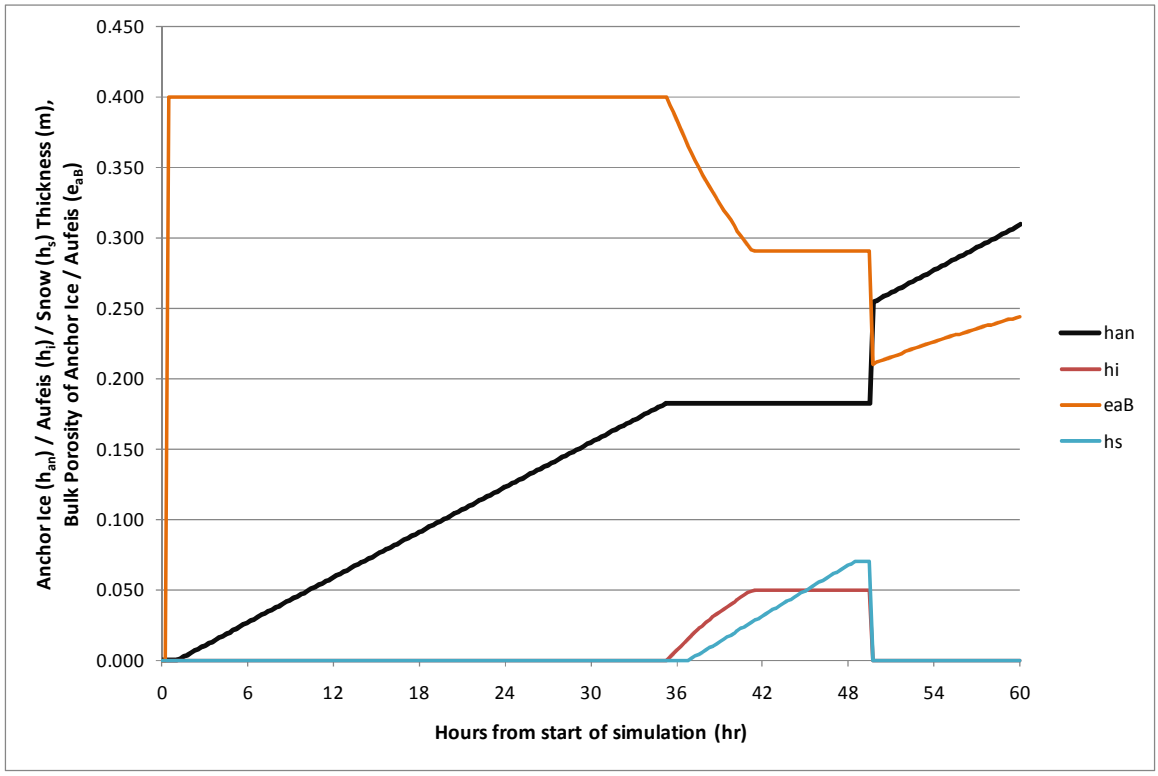


**Figure 4.14 -** One complete aufeis growth cycle including snowfall thickness.

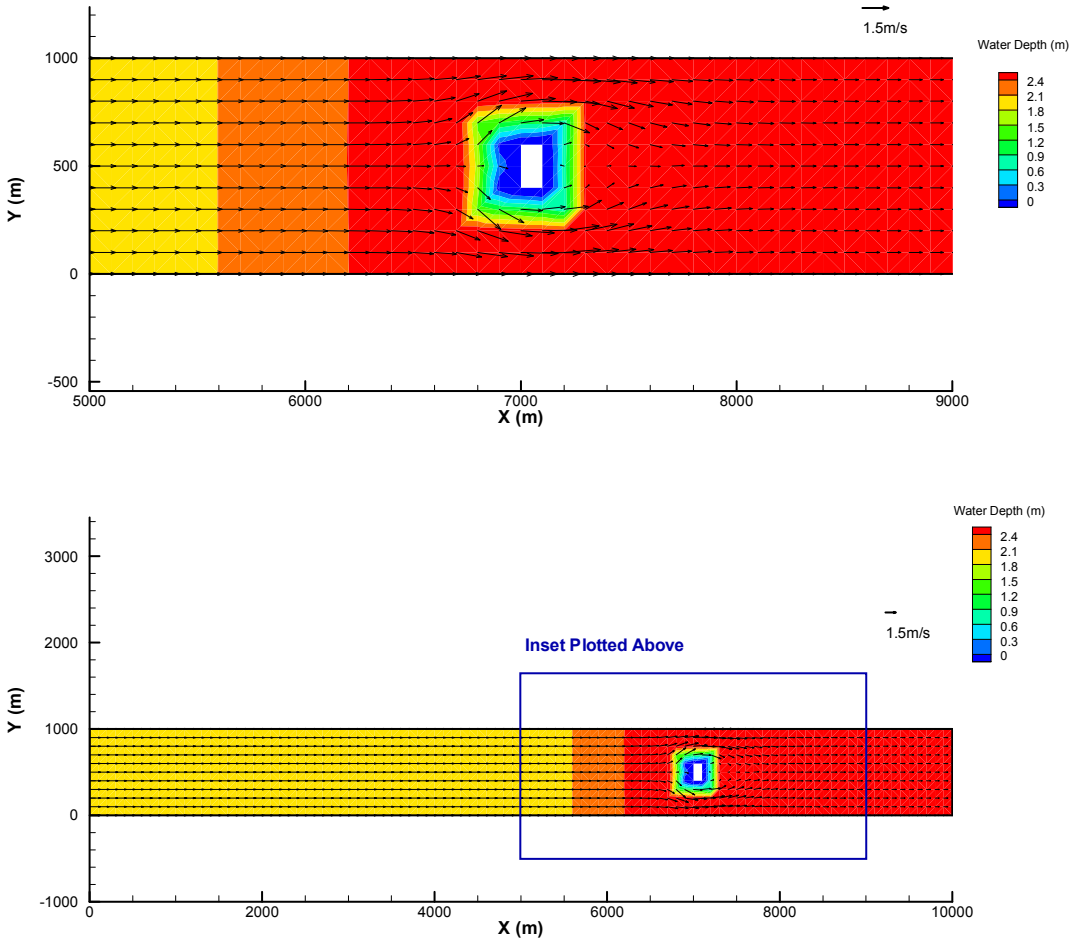


**Figure 4.15 -** Rectangular 1-Outcrop channel with portions of the channel "*dry*".

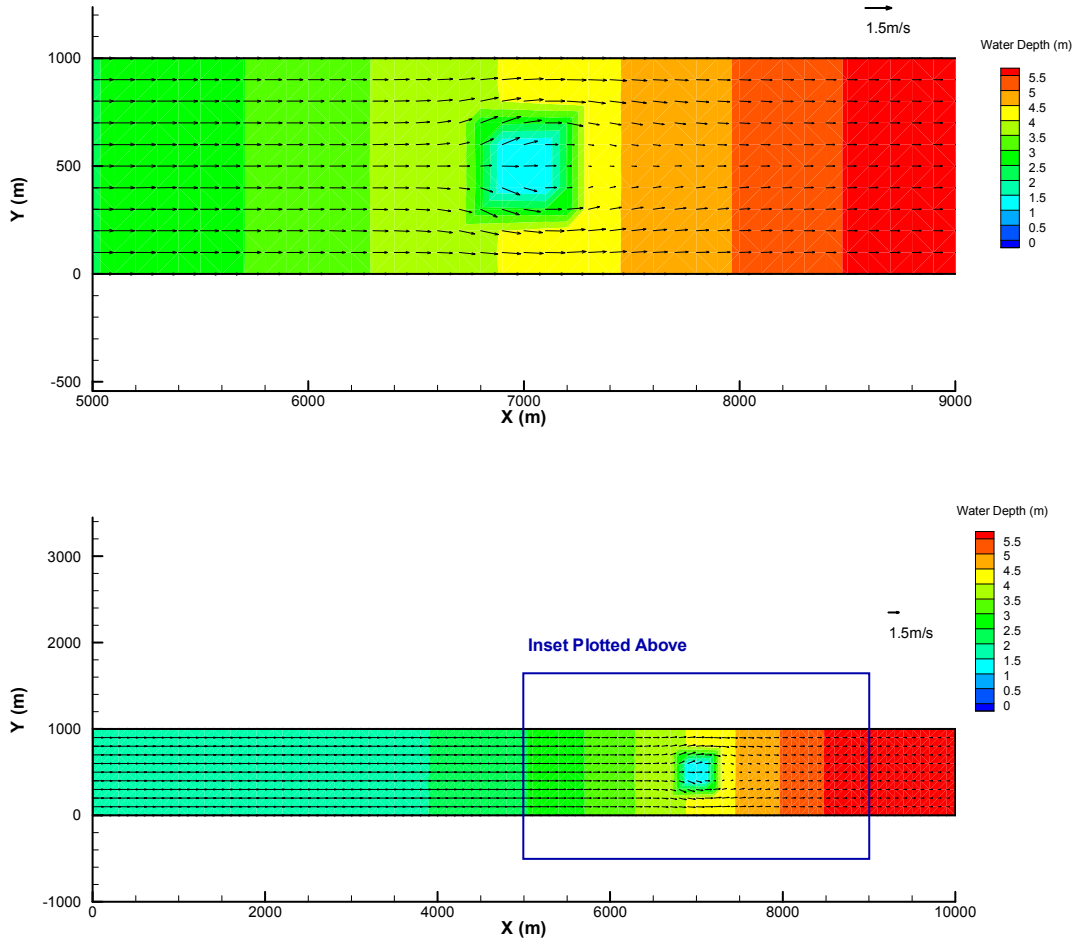


**Figure 4.16 -** Rectangular 1-Outcrop channel with the entire channel "*wet*".

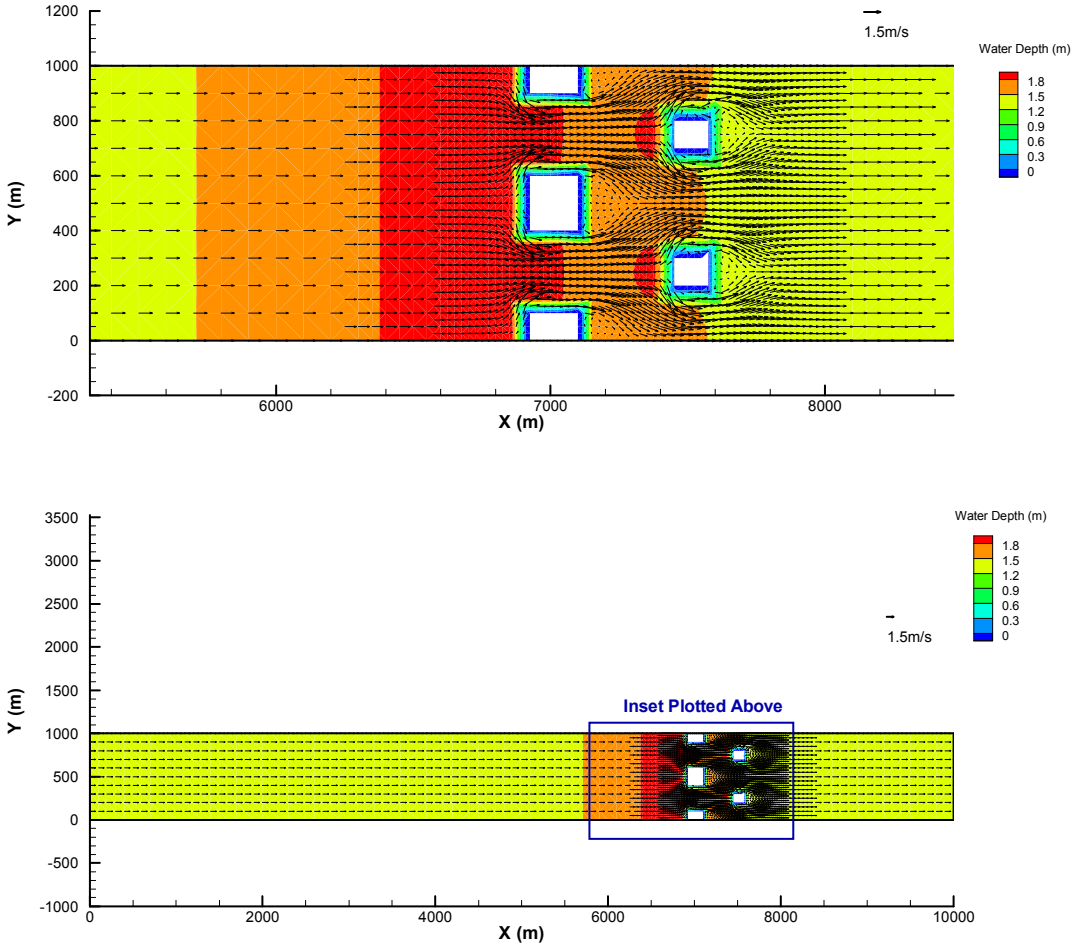


**Figure 4.17 -** Rectangular Multiple Outcrops channel with portions of the channel "*dry*".

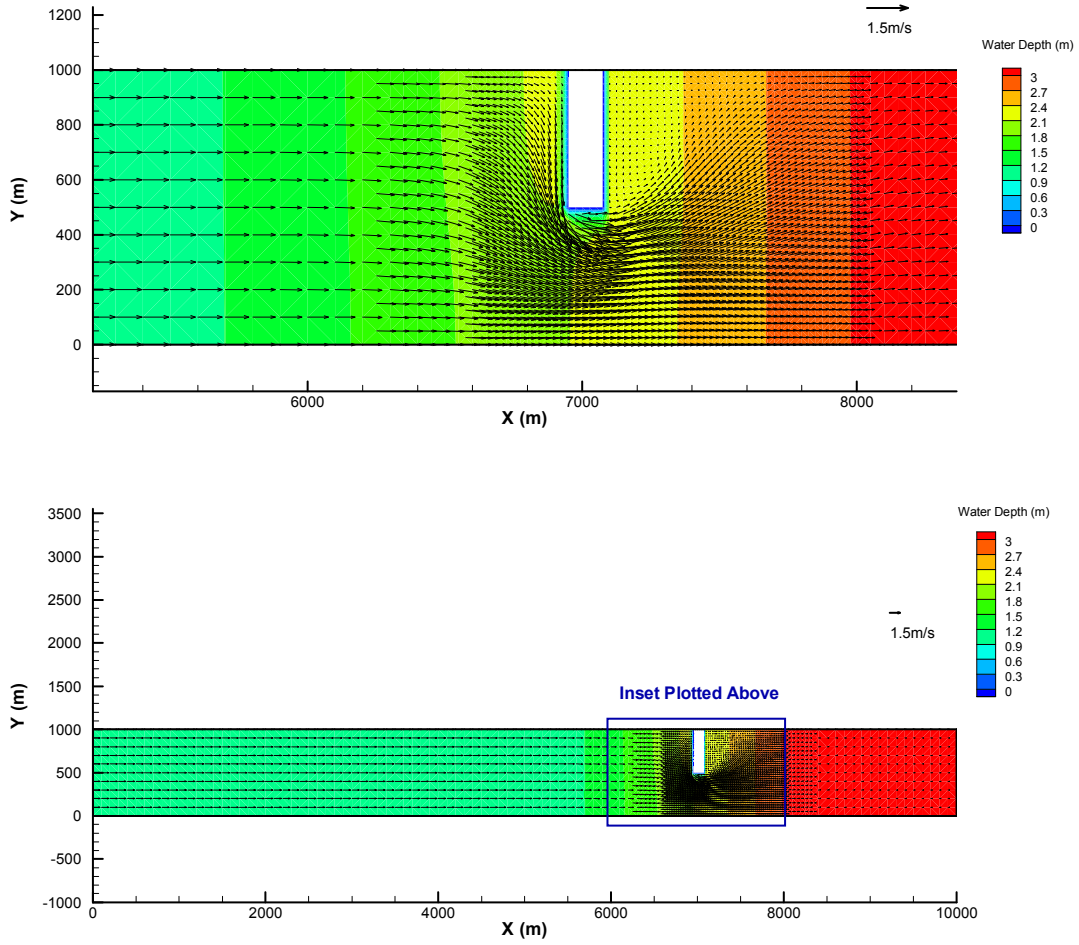


**Figure 4.18 -** Rectangular Berm channel with portions of the channel "*dry*".

CHAPTER 5

# Field Applications

## 5.1 Case Study 1: Sundance Rapids

The Limestone Generating Station (GS) is located on the Nelson River about 775 km north of Winnipeg, Manitoba, Canada (Figure 5.1). It is currently the largest generating station in Manitoba Hydro's system with an installed capacity of 1340 MW with 10 generating units. Approximately 3.25 kilometers downstream of the plant is Sundance Rapids. The cyclic nature of the flow through the station coupled with the unique bed geometry found at the rapids makes this an ideal location for large quantities of anchor ice to form each winter. The anchor ice at the rapids usually grows to a level where an ice dam forms across the entire width of the river leaving only a few channels open. An example of one such ice dam is shown in Figure 5.2. Since the ice dam forms only about 3 km away from the generating station, this restriction of flow causes staging (*i.e.*, water level rise above the ice free water level) to develop at the station's tailrace. While the initiation of anchor ice is largely governed by the meteorological conditions at the site,

the first staging effects are often realized in early December, peak in mid-February, and typically last until the end of March. The levels of staging measured at the tailrace are frequently around 1.0 to 1.5 m but have been measured as high as 3.0 m over the normal open water tailrace levels. The staging effects realized at the tailrace of the Limestone station impact the ability to produce electricity and therefore have both operational and financial implications for Manitoba Hydro.

Field monitoring programs at this location began in the winter of 1991-92 and largely consisted of water levels and aerial photos of the ice dam formation at Sundance Rapids. The data collected since 1991 has shown that the anchor ice accumulations and ice dam formations have been relatively consistent in nature and extent each year, in spite of the variability in hydrologic and meteorological conditions from year to year (Girling and Groeneveld, 1999). Collectively, the field observations provided valuable information regarding the principal ice processes contributing to the anchor ice / aufeis dam at Sundance Rapids and the subsequent effects realized at the Limestone GS. Girling and Groeneveld (1999) provided the following detailed description of complicated ice dam formation and evolution process:

- Frazil ice formation in the reach between the Limestone station and Sundance Rapids is the dominant process in the ice accumulation process.
- This turbulent reach provides an ideal environment for the formation of active frazil flocs which are largely still suspended in the flow and have not yet

accumulated into large frazil pans on the surface yet. The accumulation of active frazil flocs on shallow rock outcrops forms the initial blanket of anchor ice.

- The subsequent flow cycling at the Limestone station causes shallow overtopping of the rock outcrops and the established ice accumulations in the rapids. This will cause an additional accretion as a form of aufeis growth that over time, and many cycles, creates a significant blockage. It was observed that this growth may initially be cyclical, with periods of growth followed by periods of decay and collapse.
- Border ice forms upstream of the rapids during nightly low flow cycles and portions can release during the high flow cycle which can contribute an additional volume of ice that can adhere to the shallow outcrops and/or previously initiated anchor ice.
- The ice dam continues to grow through a combination of aufeis growth during high flow cycles, accretion of suspended frazil ice from the frazil-laden flow over-topping the ice accumulation, and to a small degree the accumulation of surface ice to the leading edge of the ice dam.
- As the ice dam thickens, the flow is redistributed across the channel causing localized high flow locations where the majority of the flow is conveyed. The locations of these high flow channels in the ice dam are relatively consistent from year to year.

Time-lapsed photography was collected from the north bank of the rapids over the 1999-2000 winter. A series of photos in Figures 5.3 – 5.4 shows the progression of the anchor ice dam through this particular winter.

Since the Limestone GS was commissioned in 1993, an almost continuous record of flow through the station and water level in the tailrace has been generated. Using this hydrometric data, weather data from the Gillam airport weather station, and a one-dimensional HEC-RAS model for the reach of the Nelson River from the Limestone station to Hudson Bay, the effects of the ice dam at Sundance Rapids is quantified in Table 5.1 for the 13 winters from 1993/94 to 2005/06. The HEC-RAS model mentioned above was calibrated as part of the planned Conawapa Generating Station studies by Manitoba Hydro and was used to generate a time series of open water or "ice-free" water levels at the Limestone tailrace to help quantify the staging effects each winter in this analysis.

The values in the table are meant to illustrate the variation, as well as the consistency, of the ice dam effects on the tailrace water levels and associated lost generation revenue. The staging values are calculated as a 24-hr running average to smooth out some of the noise generated when comparing the measured hourly tailrace levels to the hourly open water levels from the HEC-RAS model. While it is acknowledged that this running average may underestimate the peak levels of staging slightly, it still provides a sufficient basis for comparison between the years. The standard deviation of the discharge through the GS gives a measure of the amount of cycling that winter and the Cumulative Degree-

Days Freezing (DDF) provides the severity of the winter from a temperature perspective. The maximum staging and cumulative staging gives the basis for comparing the impacts of the annual ice dam and the generation revenue lost ($ Lost) combines the staging, flow, and cycling effects into one single parameter for comparison. In Table 5.1 below, the 3 highest values are highlighted in red and the 3 lowest values are highlighted in blue to try and identify any relationship between tailrace staging and the other parameters.

**Table 5.1** – Summary of staging effects at the Limestone GS, 1993-2006.

| Year | Date of Maximum Staging | Maximum Staging (m) | Average Discharge (cms) | Discharge Standard Deviation (cms) | Cumulative DDF (°C*day) | Cumulative Staging (m*hr) | $ Lost (million) |
|---|---|---|---|---|---|---|---|
| 93-94 | Feb 15 | 0.970 | 3201 | 1007 | 2631 | 1264 | 2.325 |
| 94-95 | Feb 19 | 0.800 | 3148 | 1058 | 2816 | 990 | 1.761 |
| 95-96 | Feb 16 | 1.262 | 3058 | 966 | 3499 | 1714 | 2.978 |
| 96-97 | Feb 13 | 1.877 | 3625 | 777 | 3296 | 2114 | 4.114 |
| 97-98 | Feb 14 | 1.438 | 3854 | 810 | 2591 | 1656 | 3.517 |
| 98-99 | Feb 10 | 1.302 | 2802 | 1128 | 2381 | 1082 | 1.786 |
| 99-00 | Feb 16 | 2.479 | 3254 | 981 | 2543 | 2190 | 4.052 |
| 00-01 | Feb 24 | 1.730 | 3692 | 1083 | 2861 | 2127 | 4.546 |
| 01-02 | Mar 11 | 0.745 | 3199 | 1125 | 2957 | 778 | 1.374 |
| 02-03 | Mar 10 | 1.211 | 2959 | 1177 | 3084 | 1283 | 2.185 |
| 03-04 | Feb 12 | 1.225 | 1837 | 692 | 3098 | 1652 | 1.675 |
| 04-05 | Feb 9 | 1.779 | 3960 | 887 | 3011 | 2291 | 5.054 |
| 05-06 | Feb 13 | 1.254 | 4209 | 693 | 2294 | 1138 | 2.663 |
| **Avg** | **Feb 19** | **1.390** | **3292** | **953** | **2851** | **1560** | **2.925** |

Upon a visual inspection of the values in Table 5.1, no trend is apparent between the levels of staging and other parameters like average discharge, amount of cycling, or

severity of winter. Over the 1996-97 winter, a large amount of staging corresponded to one of the coldest winters but this correlation did not hold true for the rest of the years. In 2004-05, a large amount of staging corresponded to a high discharge winter and in 1998-99 a small amount of staging corresponded to a low discharge with high cycling. These trends again, did not hold true for the rest of the years in the dataset with the exception of 2001-02 which also had a small amount of staging with a relatively high amount of cycling. The correlation coefficient (*Corr*) was calculated for the cumulative staging parameter versus average discharge (*Corr* = 0.237), discharge standard deviation (*Corr* = -0.330), and Cumulative DDF (*Corr* = 0.309). As can be seen from the values calculated, only small amounts of correlation exist and it is somewhat surprising to see a negative correlation between the average amount of cycling over the winter and the total amount of staging realized at the tailrace. The positive correlation between cumulative staging and DDF is expected and the positive correlation with average discharge could signify that a higher discharge may help the ice dam to continue to grow throughout the entire winter. This analysis highlights the truly dynamic nature of the anchor ice / aufeis dam at Sundance Rapids and some of the challenges that are present when trying to model the entire process numerically.

The average annual generation revenue lost over this 13 year dataset was $2.925 million. The Megawatt-hours (*MWh*) lost due to the tailrace staging was calculated using

$$MWh = eQ\rho_w g\Delta_{tr} 10^{-6} \ , \qquad \textbf{(5.1)}$$

where $e$ = generation efficiency (0.90 for this analysis), $Q$ = Limestone GS plant discharge (cms), $\rho_w$ = density of water (kg/m$^3$), $g$ = gravity constant (m/s$^2$), and $\Delta_{tr}$ = hourly staging at the tailrace (m). Without placing too much emphasis on the MWh's lost at the Limestone GS, this quantity provides a single parameter for comparison that combines the impacts of staging, flow, and cycling into a single parameter along with the progressive formation of the anchor ice and aufeis dam. The amount of MWh's lost each hour was then multiplied by the value of this power on the export market which was provided by the Resource Planning and Market Analysis Department at Manitoba Hydro and incorporated numerous assumptions regarding market conditions, generation capacity, system development and domestic load (2008 estimate). The value of a MWh on the export market varies by the month and the time of day (Table 5.2). For this analysis, "on-peak" hours were assumed to be 6 am to 10 pm with the rest of the day being "off-peak".

**Table 5.2** – Value of a MWh on the export market (2008 estimate).

| Month | On-Peak ($/MWh) | Off-Peak ($/MWh) |
|---|---|---|
| November | 65.21 | 37.92 |
| December | 72.53 | 42.25 |
| January | 71.86 | 42.97 |
| February | 68.54 | 43.33 |
| March | 61.88 | 37.19 |
| April | 58.56 | 34.67 |

### 5.1.1 Numerical Model

The model domain extends from the Limestone Generating Station along the Nelson River approximately 4.5 kilometers downstream. A finite element mesh was constructed over this domain using the commercially available SMS software package. The final mesh consisted of 6351 triangular elements and 3281 nodes (Figure 5.5). The surface area of the elements ranged in size from about 265 $m^2$ in the area surrounding the rapids to nearly 4000 $m^2$ in other areas of the model. The domain was divided into 6 different material types to allow for variation in the model parameters throughout the calibration process and during the model runs (Figure 5.5). The locations of 3 water level gauges are also identified in Figure 5.5 and will be referenced in the hydrodynamic calibration and verification below. Bathymetry data of the entire reach under consideration was obtained from a detailed survey conducted in 2004 by Manitoba Hydro. Figure 5.6 shows the fine resolution of the bathymetry data collected throughout the domain with the exception of the area in and around Sundance Rapids. This missing data was filled in later by manually adjusting the bathymetry values at the rapids during the hydrodynamic calibration with the assistance of LIDAR (LIght Detection And Ranging) data collected during a very low flow period in September 2004 (Figure 5.7). The hourly flow through the Limestone Station was specified as the single upstream boundary to the model and a constant elevation boundary was specified at the downstream end of the model as the only outflow boundary. The outflow elevation boundary was specified according to a rating curve developed for that location by Acres Manitoba (Acres, 2000) in a previous study.

### 5.1.2 Hydrodynamic Calibration and Verification

The numerical model was first hydrodynamically calibrated for open water conditions using a one week dataset beginning August 23, 2006 @ 12:00 pm. The discharge through the Limestone GS ranged between 1702 and 4719 cms for this calibration period which represents medium to high flows through the station. The measured water levels from the tailrace and the 3 water level gauges in the reach (Figure 5.5) were compared dynamically to the simulated values at the same locations. Once the initial comparison was made, the Manning's "*n*" values for the various sub-reaches and to some extent the rapids bathymetry as well, was iteratively modified until an acceptable comparison of the water levels could be made. Figures 5.8 and 5.9 show the water level comparisons over the calibration period. Also included in the plots is the water level predicted by a rating curve for that particular location which was developed by Manitoba Hydro using many years of observational data. This will provide some context to how the measured data fits in with the longer record of data.

From this collection of plots it can be seen that the model is able to simulate the open water hydrodynamic conditions quite well. Generally, there is a better comparison of the water levels at higher flows and in most cases the simulated water levels dip below the measured values during the low flow cycles. This can partially be attributed to the uncertainty in the bathymetry at the rapids and the ability to resolve the small outcrops with the model. Another observation with the measured data is that during the low flow cycles, the first gauge (UH738) measured water levels that are actually 0.2 m higher than the tailrace water levels which are measured 0.8 km upstream of this gauge. This could

be partially due to the Limestone River which outlets into the Nelson River near this gauge but it could also be a small gauge issue as well. This highlights the importance of providing the rating curve on the plot as well for the relevant context. It can be seen that the simulated values are well within 0.1 m of the rating curve at the tailrace, almost identical to the rating curve at UH738, within 0.15 m at UH740, and almost identical to the rating curve at UH706. The result at UH706 is expected because this gauge is downstream of the rapids and only about 1 km away from the downstream boundary of the model with a specified water level.

Once the calibration was deemed complete, the model was verified using a different one week dataset with a larger flow range. The verification dataset began on September 28, 2006 @ 12:00 pm and it represented almost the maximum range of flows expected downstream of the Limestone GS during winter periods. The flow range during this one week period was from 412 cms (one-unit operation) to 4289 cms (ten-unit operation). The comparisons between the measured and simulated water levels for the verification time period can be found in Figures 5.10 and 5.11. Very similar trends in the observations from the calibration run can be seen here as well with the deviations during the low flow cycles being slightly magnified in the verification run due to the much lower flow. Again the simulated water levels match very well with measured values at high flow conditions and to the rating curves over most of the flow range. During the low flow cycles, the differences between the measured and simulated values approach 0.3 m which is acceptable given the complex nature of the hydraulic conditions in this reach and that the simulated water levels match fairly well with the rating curves.

Table 5.3 below lists the different sub-reach / material types defined in the numerical model (Figure 5.5) as well as the Manning's "*n*" values that were determined through the calibration and verification procedure above. The minimum (*htlow*) and rewet (*hthigh*) water depths used for calibration and verification were 0.1 and 0.2 m respectively which is significantly lower than the minimum water depths required for a stable model prior to the improved dry bed treatment.

**Table 5.3** – Calibrated Manning's "n" values for each sub-reach / material type.

| Sub-reach / Material Type | Manning's "*n*" |
|---|---|
| Tailrace | 0.030 |
| Main Channel | 0.040 |
| Sundance Rapids | 0.065 |
| Rock Outcrops | 0.075 |
| Main Channel Downstream | 0.030 |
| Sundance Rapids - Channels | 0.065 |

The elevated Manning's "*n*" values for the Sundance Rapids sub-reaches were necessary in order for the model to capture the large head losses experienced by the flow when traveling through the rapids. The water depths and velocity vectors determined by the model during an 800 cms flow condition are shown in Figure 5.12. The elements with at least one dry node are blanked from the plot and it can be seen that the majority of the flow passes through a few preferential channels with the significant portion passing through the south portion of the rapids.

### 5.1.3 Season Ice Simulations

In order to capture the complete ice dam formation process at Sundance Rapids it is necessary to conduct entire season simulations, typically from sometime in November (when daily air temperatures drop consistently below 0 ºC) to around the end of March. Given the resolution of the model required to properly resolve the ice dam formation each of these simulations could take up to 1.5 weeks to run. Advancements in computing speed and compiler options continue to make this more manageable but the computing time is still significant.

It was investigated whether or not a coarser element mesh would be feasible for this study and it was found that in regards to the ice processes during freeze-up conditions, the model was not particularly sensitive to a change in model resolution. An adjustment to many of the calibration parameters could make up any differences resulting from a change in model resolution but the model becomes unstable when trying to model dry/wet bed conditions with a low resolution mesh and the ability to model these conditions is particularly important in this study. A higher resolution could be beneficial with the obvious trade off of more computing time but the resolution of the bathymetry data collected provides a practical upper limit as well.

Due to the length of time required to run a complete season, a selection of 6 winter seasons were chosen to represent the range of conditions expected to influence the formation of the ice dam at Sundance Rapids as well as the range of Limestone GS

tailrace staging due to the ice dam itself. This includes high (2005-06) and low (2003-04) flow winters, cold (1995-96) and warm (1999-00) winters (relatively speaking), and low (2005-06) and high (2001-02) amounts of cycling over the winter. The seasons chosen for the following analyses are identified in Table 5.4 below along with their start times, end times, and season length.

**Table 5.4** – Selected winter seasons chosen for ice simulations.

| Winter | Start Time | End Time | Season Length (hrs) |
|---|---|---|---|
| 1995-96 | November 1 12:00 am | April 9 12:00 am | 3840 |
| 1999-00 | November 12 12:00 am | April 1 12:00 am | 3384 |
| 2000-01 | November 16 12:00 am | April 1 12:00 am | 3264 |
| 2001-02 | November 19 12:00 am | April 1 12:00 am | 3192 |
| 2003-04 | November 1 12:00 am | April 1 12:00 am | 3648 |
| 2005-06 | November 13 12:00 pm | April 1 12:00 am | 3324 |

The ability of the model to simulate the ice dam formation over the entire winter will be evaluated. To this end, the measured tailrace water levels at the Limestone GS will be compared to the simulated water levels at the upstream end of the model as the anchor ice / aufeis dam forms throughout the winter. As well, the ability of the model to replicate 3 specific quantities will be evaluated throughout. These quantities include the maximum amount of staging realized throughout the winter, the cumulative amount of staging, and

the cumulative Megawatt-hours (MWh) lost throughout the season. This will give a representation of how well the model performs from a higher level which is appropriate given the majority of the comparison will be made with the tailrace levels about 3 km upstream of the ice dam formation and the variability in the ice dam effects is quite large.

#### 5.1.3.1 Water Temperature and Frazil Concentration

In order to conduct a proper analysis of the complete ice season simulations, tailrace water levels without any ice formation needed to be generated for each of the seasons. These "open" water levels will be used to determine the measured and simulated levels of staging throughout the season analysis. As a check, these tailrace water levels from the model were compared to the "open-water" levels provided by the one-dimensional HEC-RAS model described previously and were found to match up very well (Figure 5.13).

Included in these simulations, the heat transfer calculations were enabled using the input weather data and the finite element water temperature and frazil concentration calculations were carried out at the same time. The simulation of surface ice processes were not enabled and neither were the anchor ice calculations (*i.e.*, no mass exchange at the top or bottom boundaries of the river). Enabling these calculations did not impact the water levels but provided additional information leading into the further analysis. It also provided water temperature and suspended frazil contours in absence of any other ice processes occurring (Figure 5.14). It can be seen from the figure that due to the inflow water temperature of 0.02 ºC, the water temperature becomes supercooled very quickly as it exits the tailrace and a small amount of supercooling is present throughout the reach as

the heat loss at the surface is balanced by suspended frazil generation. This inflow water temperature was based on a single set of measurements taken in the tailrace of the Limestone GS by Manitoba Hydro and is a reasonable value given that the reservoir water temperature has been measured to be even closer to 0 ºC and only a small amount of heat will be added to the water as it passes through the generating units. The shallow areas of the model, along the shorelines and in Sundance Rapids, are showing higher levels of supercooling at this point in the simulation. This is not surprising given the processes simulated. If the surface ice processes were included, many of the areas along the shoreline would be covered with small amounts of border ice which would insulate the surface from further heat loss and reduce the levels of supercooling in those areas.

#### 5.1.3.2 Simulation of Ice Dam Formation at Sundance Rapids

The simulation of ice dam formation was conducted for the six seasons listed in Table 5.4 under a range of parameter values directly related to the anchor ice and aufeis growth processes described in Chapter 3. There are also many parameters in the model that are consistent throughout the season simulations below and are listed in Table 5.5. These parameters are not expected to have a significant impact on the ice dam formation process.

**Table 5.5** – Model parameters consistent for all ice season simulations.

| Parameter | Description | Value |
|---|---|---|
| $\alpha$ | Probability of deposition of a frazil particle reaching the surface | 0.00, 0.001, 0.01 |
| $\beta$ | Rate of re-entrainment of frazil ice at the surface [$s^{-1}$] | 1 x $10^{-5}$ |
| $v_b$ | Buoyant velocity of suspended frazil particles [m/s] | 0.0005, 0.001 |
| $\rho_s$ | Density of snowfall [$kg/m^3$] | 170 |
| $T_{cr}$ | Critical surface water temperature for border ice formation [ºC] | -0.25 |
| $V_{cr}$ | Critical water velocity above which border ice will not form [m/s] | 0.4 |
| $e_a$ | Initial porosity of anchor ice formation | 0.4 |
| $d_f$ | Diameter of suspended frazil particles [m] | 0.002 |
| $t_f$ | Thickness of suspended frazil particles [m] | 0.00013 |
| *htlow* | Water depth at which a node becomes "dry" [m] | 0.15 |
| *hthigh* | Water depth at which a "dry" node becomes "rewet" [m] | 0.30 |
| $\rho_b$ | Density of river bed material [$kg/m^3$] | 2650 |
| $h_{ia}$ | Linear coefficient for ice growth calculations [$W/m^2/ºC$] | 12.2 |
| $\alpha_{ia}$ | Constant for linear ice growth calculations [$W/m^2$] | 50 |

All 6 seasons of interest were each run under a "low", "medium", and a "high" ice dam formation scenario for a total of 18 season simulations. Within these scenarios, the model parameters most influential to the formation and evolution of the ice dam were adjusted consistently across the 6 different seasons for direct comparison as a set of simulations.

The relative amounts that the parameters were adjusted were in response to the analysis of previous simulations. These parameters included the accretion rate of suspended frazil to bed ($\gamma$), the bed particle diameter ($d_s$), the inter-particle resistance ($c_{ohb}$) and the maximum thickness of a single aufeis layer ($h_{aufmax}$). $\gamma$ and $h_{aufmax}$ were mostly used to control the ice dam formation while $d_s$ and $c_{ohb}$ helped to simulate the decay of the ice dam in the spring as well as limit the ice growth at certain locations. Typically, the bedrock outcrops were specified as having a small $d_s$ but a very large $c_{ohb}$ and the gravel bed locations had higher $d_s$ values but little to no inter-particle resistance was specified. The bedrock outcrops also had the highest values of $\gamma$ specified as it was expected that most frazil accretion would occur in these areas. The hydrodynamic time step varied between 0.40 and 0.20 s depending on the severity of the ice dam formation and the hydraulic conditions (*i.e,* more severe hydraulic conditions and ice dam formations required a smaller time step for model stability) and the ice dynamic time step for the free drift calculations was 1.0 s. The free drift calculations track the surface ice parcel position but do not consider the interaction between adjacent parcels and do not consider the development of any internal stresses in the parcels. These calculations were employed to help reduce the computation time and were applicable in this case due to the low surface ice concentration generated in this short reach. The coupling time between hydrodynamics and ice dynamics was 900 s and the dry bed check interval was 450 s.

The range of values for these parameters used in each of the three scenarios is listed in Table 5.6. Given the very dynamic nature of the ice dam formation and the range of conditions observed in the field, it is expected that some seasons will fit better under the

"low" formation scenario while others will be more accurately represented by the "medium" or "high" formation scenario.

**Table 5.6** – Range of parameters significant to ice dam formation.

| Parameter | Low | Medium | High |
|---|---|---|---|
| $\gamma$ (m/s) | $1 \times 10^{-6}$ – $6 \times 10^{-5}$ | $1 \times 10^{-6}$ – $1 \times 10^{-4}$ | $1 \times 10^{-6}$ – $2 \times 10^{-4}$ |
| $d_s$ (m) | 0.005 – 0.05 | 0.005 – 0.04 | 0.005 – 0.025 |
| $c_{ohb}$ ($N/m^2$) | 0 - 2000 | 0 - 3000 | 0 - 3000 |
| $h_{aufmax}$ (m) | 0.05 | 0.06 | 0.07 |

To illustrate the incremental effects of the above parameter adjustments in Table 5.6 on the ice dam formation and associated tailrace staging, the measured tailrace water levels are plotted with the tailrace levels throughout the 2001-02 winter for the low, medium, and high scenario (Figure 5.15). It is clear from the figure that the above adjustments impact the ice dam formation and tailrace staging significantly with the medium scenario having by far the best fit for this particular season. As a further comparison, the relative staging for each of the scenarios is plotted with the measured staging values in the bottom half of Figure 5.15. One thing that is apparent from the plots of tailrace staging is that the measured staging values have significantly more variation throughout the winter. It is not uncommon for staging of over 1.0 m to be followed by a value of -0.5 m in the same day or the next day. These variations are partially due to timing phases of the measured cycles when compared to the simulated "open-water" levels. The measured values will naturally

have more variability when compared directly to the smooth simulated cycles from the model. The simulated staging will also never have a value below 0 which is because the lowest values that could be simulated at a given point in time would be the completely ice free condition so it will not be possible to capture in the model the negative relative staging values seen in the measured data. A couple other contributions to this water level variation will be identified and discussed below.

As mentioned above, the ability of the model to capture three higher level parameters used to represent the impacts of the ice dam on the tailrace levels throughout the winter was also assessed. The three parameters compared are maximum amount of tailrace staging, cumulative staging over the winter, and total MWh's lost over the winter. The plots in Figure 5.16 show the simulated quantities plotted versus the measured data for all seasons and all scenarios. Values plotted near the 1:1 black line show cases where the simulated and measured quantities are very close to one another. From a visual inspection of the plots it is clear that collectively, the medium ice growth scenario captures the cumulative staging and MWh's lost more accurately and the high ice growth scenario better represents the maximum staging levels for the collection of seasons simulated. The relatively higher cumulative values in all scenarios can be attributed to the lower amounts of variation in the simulated staging values and therefore would cause the area under the plots to be greater. Three statistical parameters will be used to numerically quantify the goodness-of-fit of these simulated datasets to the measured values. The parameters include the maximum error (simulated vs. measured), the root mean squared error (RMSE), and the coefficient of variation of the RMSE (CV(RMSE)). CV(RMSE) is

simply the RMSE normalized by the measured dataset mean. The results of the statistical parameters are summarized in Table 5.7 and support observations obtained through visual inspection.

**Table 5.7** – Statistical parameters used to evaluate scenario simulations.

| Quantity | Statistical Parameter | Low Scenario | Medium Scenario | High Scenario |
|---|---|---|---|---|
| Cumulative Megawatt-Hours (MWh) | Maximum Error | 61496 | 33085 | 60964 |
| | RMSE | 47251 | 24465 | 42961 |
| | CV(RMSE) | 0.791 | 0.410 | 0.719 |
| Cumulative Staging (m) | Maximum Error | 2018 | 1846 | 2379 |
| | RMSE | 1403 | 986 | 1694 |
| | CV(RMSE) | 0.809 | 0.499 | 0.889 |
| Maximum Staging (m) | Maximum Error | 2.685 | 1.979 | 0.945 |
| | RMSE | 1.613 | 0.993 | 0.526 |
| | CV(RMSE) | 0.736 | 0.517 | 0.264 |

A collection of figures (Figures 5.17 – 5.28) illustrate graphically the ability of the model to simulate the tailrace staging effects at the Limestone GS for the 6 chosen seasons as well as the properties of the ice dam for each of the seasons including ice thickness, dry bed locations, ice dam porosity, and bed shear velocity contours. The low and medium ice growth scenarios were chosen to best represent one season each (2003-04 and 2001-02 respectively) and the high ice growth scenario was chosen to best represent the other four seasons. While there are many consistencies in the ice dam formation from year to year, the variations in some of the characteristics and the absence of a direct correlation

between the driving parameters and the ice dam properties observed make it particularly difficult to simulate with a single set of parameters.

The model was able to best represent the tailrace staging and ice dam conditions for seasons 2001-02 and 2003-04 which had low to medium amounts of overall staging. In these seasons, the peak water levels themselves are simulated very well and to a smaller degree so are the low water levels. For the seasons with higher levels of staging, the model deviations from the measured values become a little more noticeable and a few general trends can be pulled out from the dataset.

While the peak water levels are often adequately represented in the model, the low water levels are often not captured as well. The simulated water levels during the low flow cycles are typically higher than the measured values at the same time, especially when significant ice dam formations are present. This can be partially attributed to the fact that while the model tracks a porosity of the anchor ice and ice dam, once the ice accumulation creates a dry node condition there is no flow passing through that node in the model. It is expected that in the natural condition, the ice dam would have some residual porosity especially near the bed material which could pass some flow throughout the winter. Small channels between the rock outcrops could remain open even with large amounts of solid ice dam above it. This effect would also be more prominent in cases where the ice dam begins as an anchor ice formation that transitions into an aufeis process later in the season. For seasons with very low flow (2003-04) or large amounts of cycling coupled with a low to mid-range average discharge (2001-02), this effect could

be less significant because the dominant process in the ice dam formation is likely aufeis from a very early point in the season. The porosity near the bed would then be minimized and the relative amounts of conveyance not being accounted for in the model would be less so the low water levels are more accurately captured. This effect on the low water levels would also contribute significantly to the larger variations observed in the measured data.

Also tied into this characteristic of the ice dam is the fact that the observed tailrace staging decreases a lot quicker than what is simulated in the model. Adjustments to the model parameters help to trigger some release at the appropriate time but as evident in the plots, the model does not de-stage quick enough when compared to the measured values. A possible contributor to this quick release could be the higher volumes of substrate flow discussed above and another is evident in the heat transfer plots for each of the seasons. As a whole, it seems significant decay of the ice dam and the tailrace staging often begins to occur whenever the level of heat transfer (loss) goes below 100 $W/m^2$. In the model, since the inflow water temperature is 0.02 ºC, it does not take much heat loss to continue to have supercooled conditions at Sundance Rapids. This could signify that the theoretical heat transfer calculations slightly overestimate the amount of heat loss in this particular reach or, the bond strength of the ice dam to the bed material is weakened even under a reduced level of supercooling and not necessarily only under positive water temperatures. The contribution of even a small bed heat flux to the underside of the ice dam could also potentially be enough to weaken the bond at the bed material and lead to the thermal release of these large quantities of ice. This is consistent with field

observations of anchor ice (see Chapter 1) that have shown that anchor ice can grow quite quickly on a single cold night and then partially or completely release the following day when air temperatures rise slightly or solar radiation reaches the anchor ice. The impact of the large hydraulic drag forces present once the ice dam formation is significant will also contribute to the rather sudden decay of this ice dam once it begins to weaken in the spring. Given all the contributions outlined above, it is not surprising that the tailrace staging levels show high amounts of variation.

Other general observations gleamed from the two-dimensional contour figures are the peak ice dam thicknesses range between 3 m and 5 m with larger thicknesses found on the south side of the rapids where the majority of the flow initially passes. The dry node locations are relatively consistent from year to year and match up quite well with observed ice dam locations. A range of porosities are found at the modeled ice dam locations but the existence of porosities close to 0 are found more commonly where aufeis is the dominant growth mechanism from early on in the winter season. This would lead to a strong ice dam which is able to withstand larger hydraulic forces. The modeled ice dam porosities during the higher flow seasons (2000-01 and 2005-06) are the highest because the ice dam formation is dominated by the anchor ice process for a longer period of time when the flows are higher and the outcrops and anchor ice remain flooded for an extended period. It was also observed that once a significant ice dam is in place, the modeled bed shear velocity is typically greater than 0.5 m/s in the open channels. This observation will lead into the further analysis below.

### 5.1.3.3 Effect of Limiting Shear Velocity Criteria

In the simulations discussed in section 5.1.3.2 above, the location of the ice dam is largely controlled by the bed material specifications throughout Sundance Rapids. Both field and laboratory studies (see Chapter 1) have attempted to relate the growth and distribution of anchor ice to hydraulic parameters like Froude number and Reynolds number. The critical values obtained for these parameters vary for each location and laboratory which indicates that these parameters are likely a function of the many driving characteristics of anchor ice formation and it may be difficult to obtain one set of values to apply to all locations. For this portion of the numerical model study, critical bed shear velocity parameters ($U_{*max}$, $U_{*min}$) will be used to dynamically control the locations of frazil ice accretion to the bed material.

Through an analysis of the bed shear velocities throughout the rapids, specifically during the initial formation period of the ice dam when the dominate process is anchor ice growth, critical bed shear velocities of 0.05 and 0.55 m/s were chosen as the minimum and maximum values, respectively. When these bed shear values are compared to threshold values from Julien (1998), they correspond to fine-medium gravel ($U_{*min}$ = 0.05 m/s) and small-medium boulders ($U_{*max}$ = 0.55 m/s) which shows that these approximations are reasonable given the process being modeled and the bed substrate material in the area. The same bed material properties were specified across Sundance Rapids with the intention of these simulations to try and isolate how the ice dam would form if these criteria were used to control the location of the ice dam in a more direct response to the hydraulic conditions.

**Table 5.8** – Sundance Rapids bed material parameters for shear velocity criteria runs.

| Parameter | With Shear Velocity Criteria |
|---|---|
| $\gamma$ *(m/s)* | $2.5 \times 10^{-4}$ |
| $d_s$ *(m)* | 0.01 |
| $c_{ohb}$ $(N/m^2)$ | 6000 |
| $h_{aufmax}$ *(m)* | 0.08 |

The 3 seasons with the highest average discharge (1999-00, 2000-01, and 2005-06) were chosen for these simulations because of the larger contributions of the anchor ice growth process in the early stages of these winters. Figure 5.29 summarizes the results of these simulations in terms of the 3 high level parameters discussed above for the entire season analysis. It can be seen from the plots that the results from this set of simulations falls between the medium and high ice growth scenarios from section 5.1.3.2. Table 5.9 provides a comparison of the statistical parameters obtained from this dataset to the values obtained from the best-fit scenario from section 5.1.3.2. Collectively, this dataset provides a comparable representation to the observed values with some improvement in the cumulative staging quantity.

**Table 5.9** – Statistical parameters from shear velocity criteria runs.

| Quantity | Statistical Parameter | Best-Fit Scenario (from 5.1.3.2) | With Shear Velocity Criteria |
|---|---|---|---|
| Cumulative Megawatt-Hours (MWh) | Maximum Error | 33085 | 35131 |
| | RMSE | 24465 | 25537 |
| | CV(RMSE) | 0.410 | 0.428 |
| Cumulative Staging (m) | Maximum Error | 1846 | 924 |
| | RMSE | 986 | 740 |
| | CV(RMSE) | 0.499 | 0.388 |
| Maximum Staging (m) | Maximum Error | 0.945 | 1.164 |
| | RMSE | 0.526 | 0.686 |
| | CV(RMSE) | 0.264 | 0.344 |

Figure 5.30 shows a plot of the tailrace water levels and tailrace staging for the 1999-00 season simulation with the shear velocity criteria being employed. The maximum tailrace water levels are a little lower than those obtained for the high ice growth scenario and likewise for the tailrace staging throughout the season as well. Other characteristics of the simulated ice dam formation and evolution are similar with the shear velocity criteria including the amount of tailrace staging and the simulated decay of the ice dam has similar properties as well.

The most significant difference in the ice dam formation with the shear velocity criteria included is the location of the main ice dam components and the location of the open water channels (Figure 5.31). Instead of having multiple open channels spread across the

width of the rapids as typically observed, a single large open channel is kept open in the southern portion of the rapids with an ice dam formed across the remaining width of the river. This is due to the fact that the southern portion of the rapids is where the majority of the flow passes during ice free conditions and the inclusion of the shear velocity criteria prevents the ice dam from forming at the preferential flow locations. The total width of the open water channel is larger than the summation of the multiple open channels in the previous simulations and the properties of the ice dam itself are very similar to the previous simulations as well. Some anchor ice continues to form in the open water channel (1.0 to 2.0 m thick) during the low flow cycles, when the bed shear velocity drops a little, which offsets some of the increased conveyance of the larger open water width. Given that the simulated water levels were not improved significantly under this setup and that the location of the ice dam no longer matches the observed location, further simulations under this setup were not warranted.

#### 5.1.3.4 Combined Shear Velocity Criteria with Material Specification

Given the ice processes being modeled and the limited resolution of the rock outcrops in the rapids, it is not surprising that the results from section 5.1.3.3 indicate a requirement for the modeler to specify some location specific bed material properties. As a natural progression from the simulations above, the same shear velocity criteria were included in a simulation setup similar to the high ice growth scenario from section 5.1.3.2 with a few modifications. All 6 seasons were run under this combined setup. The range of parameters used throughout Sundance Rapids can be found in Table 5.10.

**Table 5.10** – Sundance Rapids bed material parameters for combined runs.

| Parameter | Value From Combined Runs |
|---|---|
| $\gamma$ *(m/s)* | $0.5 \times 10^{-5}$ - $2.5 \times 10^{-4}$ |
| $d_s$ *(m)* | 0.005 |
| $c_{ohb}$ $(N/m^2)$ | 100 – 8000 |
| $h_{aufmax}$ *(m)* | 0.08 |

Figure 5.32 summarizes the results of combined runs in terms of the 3 high level parameters for the entire season analysis. It can be seen from the plots that the results from this set of simulations improves the results for all parameters and in particular, the cumulative staging over the season. Table 5.11 provides a comparison of the statistical parameters obtained from this dataset to the values obtained from the best-fit scenario from section 5.1.3.2 and from the shear velocity criteria runs. Collectively, this dataset provides an improved representation of the observed values for cumulative staging and MWh's lost through the season and less favorable results in the maximum staging parameter. It should be pointed out that a significant portion of the error in the maximum staging dataset is concentrated in the 1999-00 season simulation which has an exceptionally high amount of maximum staging (Figure 5.32).

**Table 5.11** – Statistical parameters from combined runs.

| Quantity | Statistical Parameter | Best-Fit Scenario (from 5.1.3.2) | With Shear Velocity Criteria | Combined Runs |
|---|---|---|---|---|
| Cumulative Megawatt-Hours (MWh) | Maximum Error | 33085 | 35131 | 33275 |
| | RMSE | 24465 | 25537 | 16474 |
| | CV(RMSE) | 0.410 | 0.428 | 0.276 |
| Cumulative Staging (m) | Maximum Error | 1846 | 924 | 887 |
| | RMSE | 986 | 740 | 506 |
| | CV(RMSE) | 0.499 | 0.388 | 0.266 |
| Maximum Staging (m) | Maximum Error | 0.945 | 1.164 | 1.899 |
| | RMSE | 0.526 | 0.686 | 0.959 |
| | CV(RMSE) | 0.264 | 0.344 | 0.481 |

A plot of the tailrace water levels and the tailrace staging throughout the 2001-02 staging is shown in Figure 5.33. From the plot, the tailrace levels are comparable to the medium ice growth scenario from section 5.1.3.2 but the improvement lies in the increased simulated variation evident under this combined setup. Some small parameter modifications and including the shear velocity criteria in with the material types helped to shape the ice dam outcrops slightly as they evolved over the winter. This essentially increased the conveyance during low flow conditions which added slightly more variation to the staging plots. Figure 5.34 shows the ice dam contours from this combined setup. The properties of the ice dam formation are similar to those obtained in previous simulations in section 5.1.3.2 with the aufeis growth process being a dominant process in the ice dam formation during this season.

Figure 5.35 illustrates the improved 1995-96 simulation results obtained from the combined run setup when compared to the measured tailrace levels and the ones obtained from the high ice growth scenario in section 5.1.3.2. The peak amounts of staging may not be entirely captured by the model in this setup but overall, this simulation provides for a much more comparable result. These results observed in the 2001-02 and 1995-96 combined runs, specifically the increased variation in the staging plots, is consistent in the results from the other seasons of interest as well.

### 5.1.4 Summary of Sundance Rapids Case Study

The results from this case study illustrate many of the capabilities of the numerical model described in Chapter 3. The model is able to capture a large portion of the variability in the effects of the Sundance Rapids ice dam on the tailrace water levels at the Limestone GS. The validity of the model results can largely be found in the comparisons with the field observations (section 5.1) and in the ideal channel simulation results presented previously in chapter 4. Some uncertainties do exist in the model results and these are largely found in the ice processes occurring near the bed material and the interaction of the anchor ice and aufeis with the bed material in the rapids. Other uncertainties lie in the source of the natural variability of the measured tailrace water levels and some hypotheses for this variability have been presented in the discussion of this case study (section 5.1.3). A few summary statements from the above analysis will be included below with further development details discussed in Chapter 6:

1) Analysis of ice dam effects for the 1993-2006 period showed many consistencies in the Sundance Rapids ice dam formation each year but did not yield any significant correlation or trends in the ice dam effects on the tailrace water levels which make this case particularly tough to model numerically. This can be attributed primarily to the independency and complexity of the ice processes involved.

2) The model is more successful in capturing the effects of the ice dam during seasons where low to medium staging effects are realized and during seasons dominated by the aufeis growth mechanism. This can be attributed to the possible existence of some residual porosity in the ice dam near the bed material which can allow for some flow through the ice dam. This can be especially prevalent when the early stages of ice dam formation are dominated by the anchor ice growth process.

3) The model runs that combined the critical bed shear velocity with the varying bed material types in Sundance Rapids were the most successful simulations in capturing the cumulative Megawatt-Hours lost and the cumulative staging throughout the winter. This is because the bed shear velocity criteria helped to dynamically shape the ice dam outcrops slightly as they evolved over the winter.

4) The model is able to simulate the location of the ice dam as well as much of the evolution throughout the winter. The simulated tailrace water levels were not

able to capture the full range of variability found in the measured water levels during the same time period and the decay and release process of the ice dam was delayed in the numerical model runs when compared to the field data. This can be attributed partially to the natural variability of the measured water levels and the simplified release mechanisms considered in the model. Evidence suggests other factors such as a bed heat flux and partial release on a daily basis may complicate the ice dam formation and release process as it occurs in nature.

5) The critical bed shear velocity criteria are calibration parameters that are a function of local hydraulic characteristics, bottom roughness, and the level of supercooling. Experimental studies in this area would be beneficial to the model.

6) Given the numerous driving parameters for ice dam formation at Sundance Rapids and the large amount of variability in the ice dam properties from year to year, the model does a good job of capturing many of the effects of the ice dam on the tailrace water levels and provides a good basis for future research and model development.

## 5.2 Case Study 2: Lower Nelson River

While the Sundance Rapids case study was the primary focus of model development, a larger scale field test of the surface ice components in the model (Chapters 2 and 3) is a secondary goal of this research. This test was necessary to ensure that the freeze-up

components of the model still functioned as they were intended in a large scale field application. The upstream extent of the model used for this case study is again the Limestone GS in northern Manitoba (see Figure 5.1). This model includes a 35 km reach of the lower Nelson River from the Limestone GS to a location about 5 km downstream of the planned Conawapa GS "B" axis (Figure 5.36). The Nelson River empties into Hudson Bay approximately 90 km downstream of this model. The characteristics of the flow regime and the nature of the river bed geometry together provide ideal conditions for very dynamic ice formations to form in this reach of the Nelson River, downstream of the Limestone GS, each winter. Specifically, very large areas of open water give ample time for large quantities of active frazil, anchor ice, and surface ice to form and evolve throughout the reach. Often, an ice cover will be initiated in the lower portions of the river and advance upstream towards the existing stations due to the accumulation of surface and suspended ice. The significant gravitational and hydraulic forces acting on the accumulated surface ice usually creates a mechanically thickened ice cover that can be up to 15 m thick in the vicinity of the planned axis of the Conawapa GS.

The extent of the numerical model created is shown below in Figure 5.36 along with the water depth and velocity contours for a discharge condition of approximately 6500 cms. Because of the larger spatial scale of this model, the finite element mesh of the model is of a lower resolution compared to the Sundance Rapids model but still has 5906 elements and 3280 nodes. The triangular element areas in this model ranged from 1500 $m^2$ to 8500 $m^2$. Between the current and proposed generating stations two sections of rapids exist that are of interest because of their significant impact on the ice processes in this section of

the river. At Sundance Rapids, a bed elevation drop of 2.5 m occurs over a length of 400 m and at the longer of the two rapid sections, Lower Limestone Rapids, bed elevation relief of 11 m is realized along a 3 km section of the river. The relative locations of these rapid sections are identified as well as the generating station axes. There is approximately 32 m of head loss from the upstream end of this model to the downstream end.

From the two-dimensional velocity contours shown in Figure 5.36, the spatial distribution and range of water velocities throughout the study reach are clear. The slowest flowing section of the reach is just downstream of Sundance Rapids with an average velocity of 1.26 m/s which coincides with a Froude number of 0.15 in this area. In contrast, velocities reach as high as 5.70 m/s in the Lower Limestone Rapids area, which correspond to super-critical Froude numbers as high as 1.51 in isolated areas. The range and spatial distribution of depth and velocity throughout this section of the river will be important considerations when simulating the surface ice conditions.

### 5.2.1 Hydrodynamic Calibration

The model above was first calibrated for open water conditions using measured water levels at six gauges located throughout the reach. The relative locations and the names of each of the gauges can be found in Figure 5.36. A one week simulation was run using data from August 11, 2005 @ 12:00 am to August 18, 2005 @ 12:00 am. The measured flow through the Limestone Generating Station was used to set the upstream flow boundary condition and a seventh gauge (05UH769) was used to set the downstream level boundary condition. This time period was chosen because good data was available

from all the gauges and it was during the open water season prior to the winter that we intended on conducting our thermal ice simulations. It was also determined that due to the morphology of this section of the Nelson River and the relatively short growing season at this northern location, the effects of summer vegetation growth on the calibrated bed roughness values would be negligible.

Comparisons between the measured and modeled water levels at all of the gauges are shown in Figure 5.37. From this figure it is quite clear that the measured and modeled water levels at all locations match quite well. The average difference between the measured and modeled values is on the order or 2-3 cm with a maximum deviation of less than 0.250 m for the one week simulation.

The above calibration resulted in a range of values being specified for the Manning's bed roughness coefficient ($n$). The $n$ values used in the model ranged from a minimum of 0.025 in the tailrace section just downstream of the Limestone Generating Station to a maximum value of 0.0535 in the Sundance Rapids area. The large value specified in the area of Sundance Rapids is required to capture the amount of head loss experienced at this location. A second data set for later in this open water season (September 20-22, 2005) was used to verify the above calibration and was also successful with the water level comparisons yielding similar results (Figure 5.37).

### 5.2.2 Thermal Ice Simulations

Manitoba Hydro has monitored this reach of the Nelson River extensively since 1997 and has conducted a winter observation program at various times throughout the ice season depending on the variability of the ice conditions at that time. Chosen for the simulation of surface ice conditions was a time period surrounding March 3, 2006. This time period was chosen because a detailed monitoring report was available at this time and the combination of the flow and weather conditions for the 2005-06 winter suppressed the formation of ice cover in the lower sections of the Nelson River all the way to Hudson Bay. Without the dynamic formation of ice cover and associated water level staging, mass exchange of suspended frazil to the surface and border ice formation are the dominant ice processes over this winter.

At the upstream end of the model, the discharge through the Limestone Station was used along with a constant inflow water temperature of 0.02 °C. This temperature has been measured in the tailrace channel and considered valid provided an ice cover exists on the forebay of the station. The absence of an ice cover downstream of this reach allows for the downstream level boundary to be specified using an open water rating curve for that location. Simulated ice conditions will be compared to photographs taken between 12:00 and 14:00 hrs on March 3, 2006. The focus of the comparisons will be on the border ice extents and the surface ice conditions. The calibrated model parameters related to these surface ice processes can be found in Table 5.12.

**Table 5.12** – Model parameters calibrated for surface ice conditions.

| Parameter | Description | Value |
|---|---|---|
| $\alpha$ | Probability of deposition of a frazil particle reaching the surface | 0.00 – 0.50 |
| $\beta$ | Rate of re-entrainment of frazil ice at the surface [$s^{-1}$] | 0.00 |
| $v_b$ | Buoyant velocity of suspended frazil particles [m/s] | 0.001 |
| $T_{cr}$ | Critical surface water temperature for border ice formation [ºC] | -0.25 |
| $V_{cr}$ | Critical water velocity above which border ice will not form [m/s] | 0.7 |
| $d_f$ | Diameter of suspended frazil particles [m] | 0.002, 0.02 |
| $t_f$ | Thickness of suspended frazil particles [m] | 0.00013, 0.0013 |

#### 5.2.2.1 Water Temperature and Frazil Concentration

The contours of frazil concentration and water temperature for March 3, 2006 @ 12:00 hrs are shown in Figure 5.38. Quality observed data for both the water temperature and frazil concentration is not yet available but the ability to obtain reasonable results is still important. The detailed thermal budget calculations outlined in Chapter 3 are utilized in this simulation. From the figure it can been seen that the location of maximum supercooling is near the Sundance Rapids area and the increasing frazil concentration downstream helps to keep the water temperature close to 0°C for much of the reach. Some level of supercooling exists throughout this reach at least in part due to the suppression of a competent ice cover and continued heat transfer away from the water. The active frazil concentrations that exist because of this show a potential for anchor ice

growth throughout the reach contingent on two factors: 1) turbulent mixing is high enough to bring suspended frazil down to the bed surface, and 2) bed particles are stable enough to withstand the buoyant and drag forces of the attached frazil particles. It has been observed throughout the monitoring program that anchor ice and aufeis accumulations do exist at numerous locations throughout this reach often in the rapid sections where cobbles, boulders, and bedrock outcrops provide the competent bed material for the anchor ice to accumulate.

#### 5.2.2.2 Border Ice Extents

As outlined in Chapter 2, border ice grows outward from the existing ice cover or the banks of the river by two distinct mechanisms, both of which are considered within this numerical model. Border ice extents calculated by the numerical model are shown in Figure 5.39 with specific areas highlighted for further comparison.

In Figures 5.40 and 5.41, photographs obtained from the monitoring report dated March 3, 2006 are presented to compare the simulated border ice extents to those observed at this time. The numbered areas on the photographs correspond to the same areas identified in Figure 5.39. Areas 1 through 4 are identified in Figure 5.40 and the border ice in area 1 does match up quite well with observed extents and it should be noted that the island is included in the simulated border ice locations as it was a part of the finite element mesh. If one is to look at the simulated border ice found in area 2, it does not match up exactly with the large amount of snow covered area seen in Figure 5.40. This comparison though is actually much more favorable than it looks at first glance because

much of the snow covered area identified in area 2 of Figure 5.40 was left out of the finite element mesh because of the high elevations at these locations. The simulated extent of the border ice combined with the relative location of the mesh boundary does provide a relatively favorable comparison with observed data.

Border ice areas identified as 3 and 4 are highlighted in the bottom photo of Figure 5.40. The simulated extents of the border ice in this area on both sides of the river correspond quite closely to the observed extents seen in the photograph. Again, the small island visible in area 4 has been included in the finite element mesh and is tagged as border ice in Figure 5.39.

A final comparison of border ice extents can be shown for the area identified as area 5 in Figure 5.41 as well as for the area just upstream of the Conawapa 'B' axis along the north shore of the river (area 6). It is tough to identify exactly the extent of the border ice found in area 5, largely because of the angle of the photograph shown in the top of Figure 5.41. It can be concluded though that the border ice in this area seems to fill much of the bay and extends to the edge of the main flow area. The simulated location of border ice in this area was found to be very much the same (Figure 5.39). It can also be seen from Figure 5.41 that small portions of border ice do exist along the north bank of the river at the Conawapa 'B' axis and upstream of this location (area 6). Small amounts of border ice are simulated at these locations in Figure 5.39 but the extents here are slightly underestimated by the model under the current configuration.

### 5.2.2.3 Surface Ice Concentration ($C_a$)

The simulated surface ice concentrations were compared to observed estimates of the surface frazil ice coverage documented within the report. These estimates were made by experienced field personnel with extensive knowledge of this reach of the river and were expressed as an approximate areal percentage. It was stated in the report that for the section of the river extending from 4.5 km upstream of the Lower Limestone Rapids to 8.5 km downstream of the rapids, surface frazil ice covered approximately 25% of the open water area. It was also reported that the surface frazil ice concentration increased to about 30-40% in the reach downstream of the Conawapa 'B' axis. The simulated surface ice concentrations are shown in Figure 5.42. It can be seen that these simulated concentrations match up reasonably well with the estimated observed values if regionally averaged values are considered. It should be noted that a significant portion of the surface frazil ice mentioned above is not visible in many of the photographs (Figures 5.40-5.41) largely due to the cloud cover conditions that day, the resolution of the photograph, and the angle the photo was taken.

The rapids entrainment portion of the ice mass exchange model detailed in Chapter 3 was employed in this model at the Lower Limestone Rapids. Here, the rapids entrainment parameter ($R_a$) was specified as 0.75. From the surface ice concentration in Figure 5.42 there is a decrease in surface ice concentration at the Lower Limestone Rapids as would be expected. Here, larger portions of the surface ice parcels are entrained into the flow and tracked as a second (larger) class of suspended frazil particles. The concentration of these frazil particles ($C_{vB}$) is shown in Figure 5.43 with the maximum concentration being

at the Lower Limestone Rapids where all the entrainment is occurring and then decreasing in the downstream direction due to the relatively quick rise of these entrained particles as expected.

### 5.2.3 Summary of the Lower Nelson River Case Study

A numerical model was hydrodynamically calibrated for a section of the lower Nelson River extending approximately 35 km from the Limestone GS to about 5 km downstream of the proposed Conawapa GS 'B' axis. This model was used to field test some of the freeze-up model components detailed in Chapters 2 and 3. In particular, the surface ice mass exchange model (Chapter 3) and the border ice formation model (Chapter 2) were tested and compared to a set of field observations taken in March 2006 as a part of the Manitoba Hydro winter monitoring program. In general, good comparisons were made between the observed and simulated conditions for most sections of the reach and the model components were found to function as expected when applied to a field case.

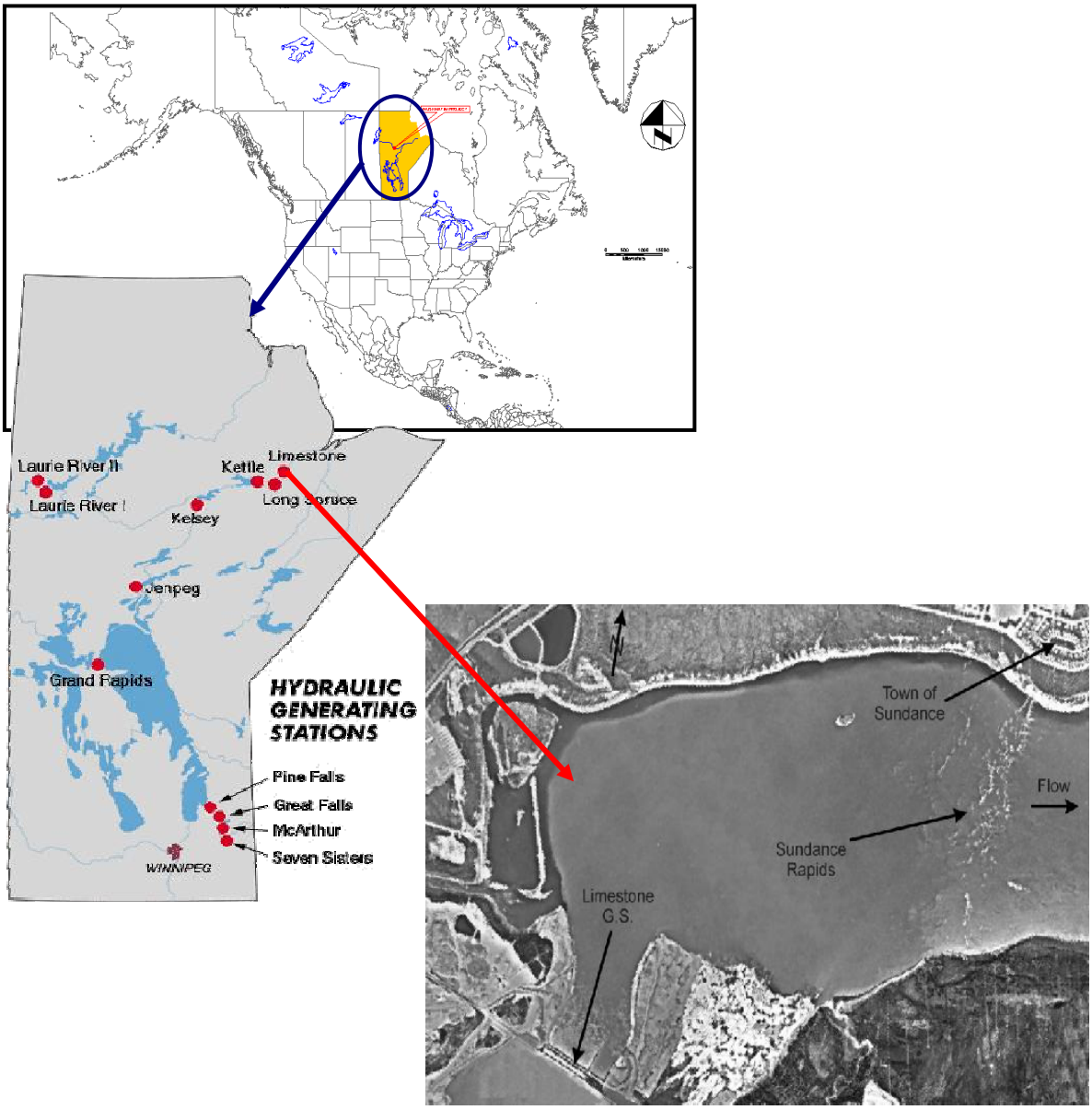


**Figure 5.1 -** Aerial view and location of Sundance Rapids (Malenchak *et al*., 2005).


**Figure 5.2 -** A typical anchor ice dam formed at Sundance Rapids (Malenchak *et al*. 2005).

**Figure 5.3 -** Evolution of 1999-2000 Sundance Rapids ice dam, December 14 (top), January 16 (bottom).

**Figure 5.4 -** Evolution of 1999-2000 Sundance Rapids ice dam, February 15 (top), March 17 (bottom).

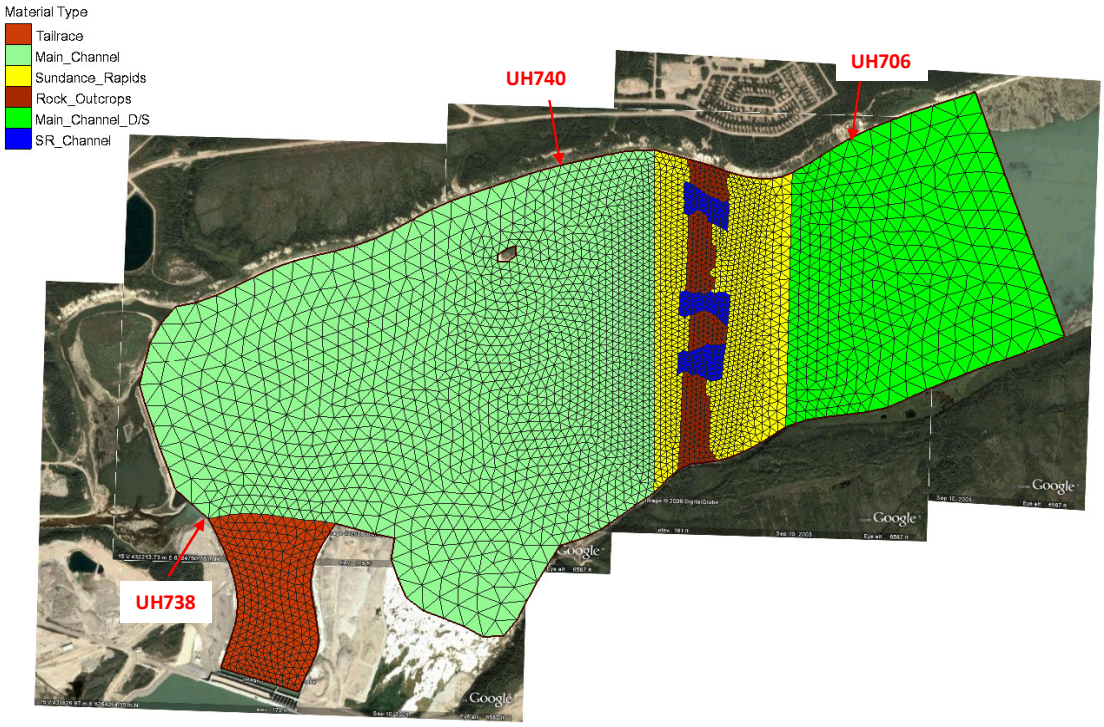


**Figure 5.5 -** Numerical model extents with material types and water level gauges.

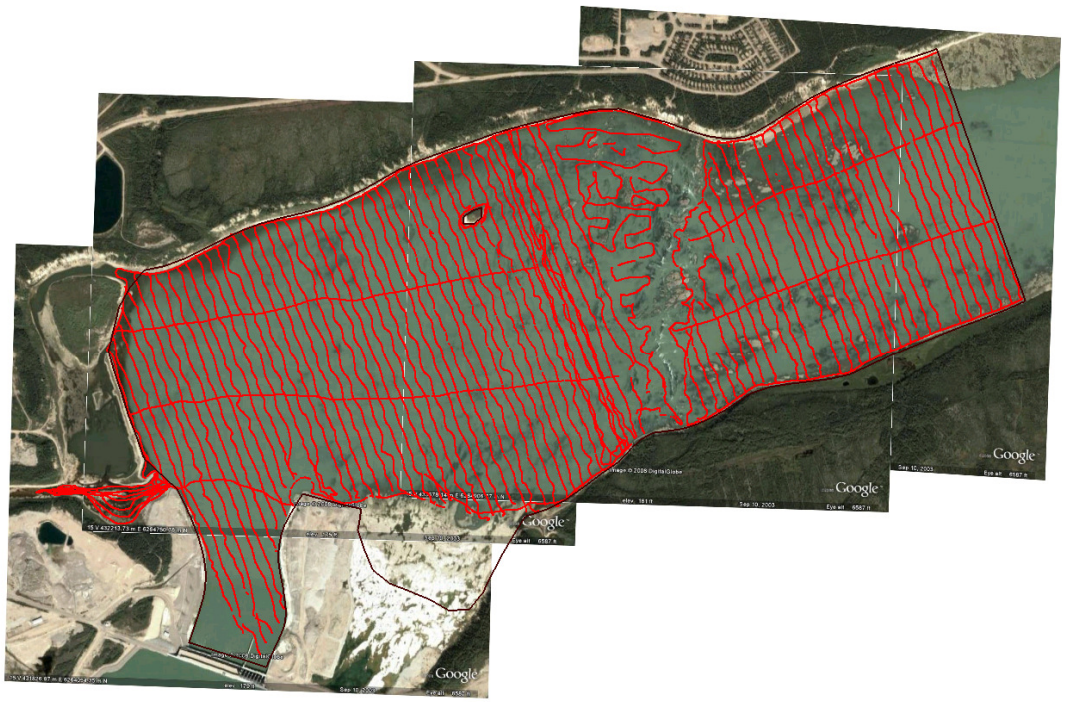

**Figure 5.6 -** Detailed bathymetry data collected by Manitoba Hydro, 2004.


**Figure 5.7 -** LIDAR data points collected September 18, 2004.

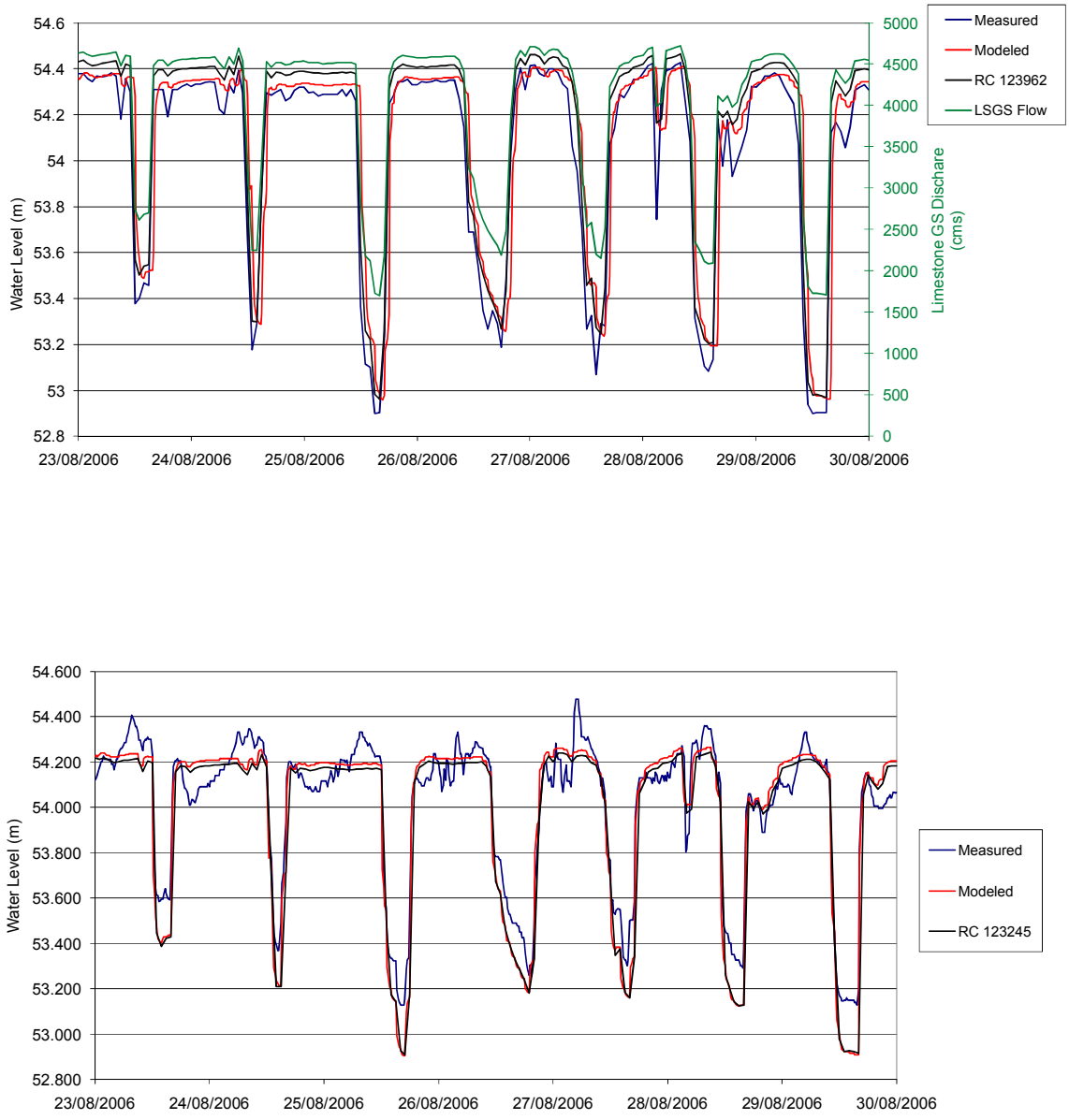


**Figure 5.8 -** Calibration water levels at the tailrace (top) and UH738 (bottom).

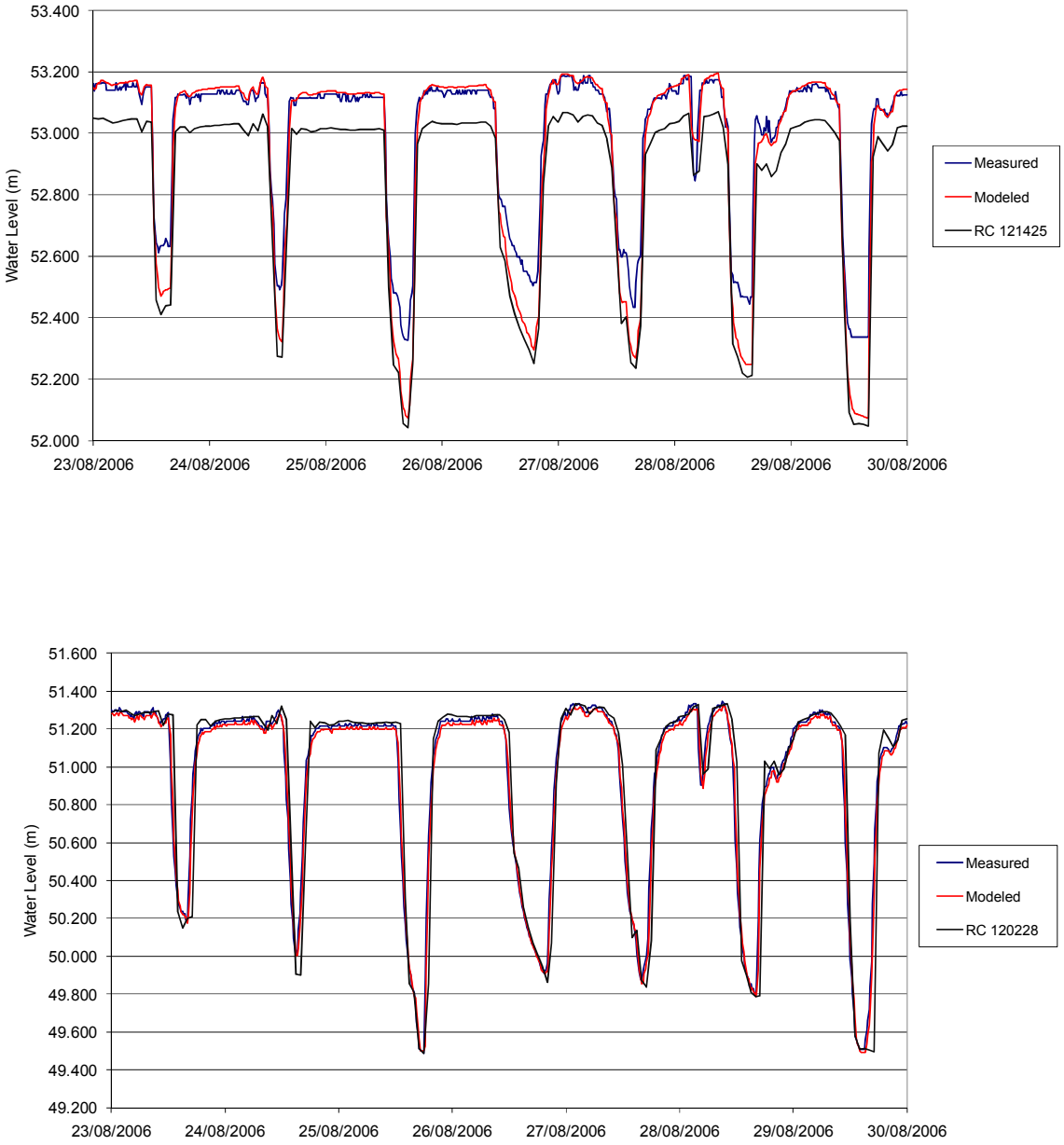


**Figure 5.9 -** Calibration water levels at the UH740 (top) and UH706 (bottom).

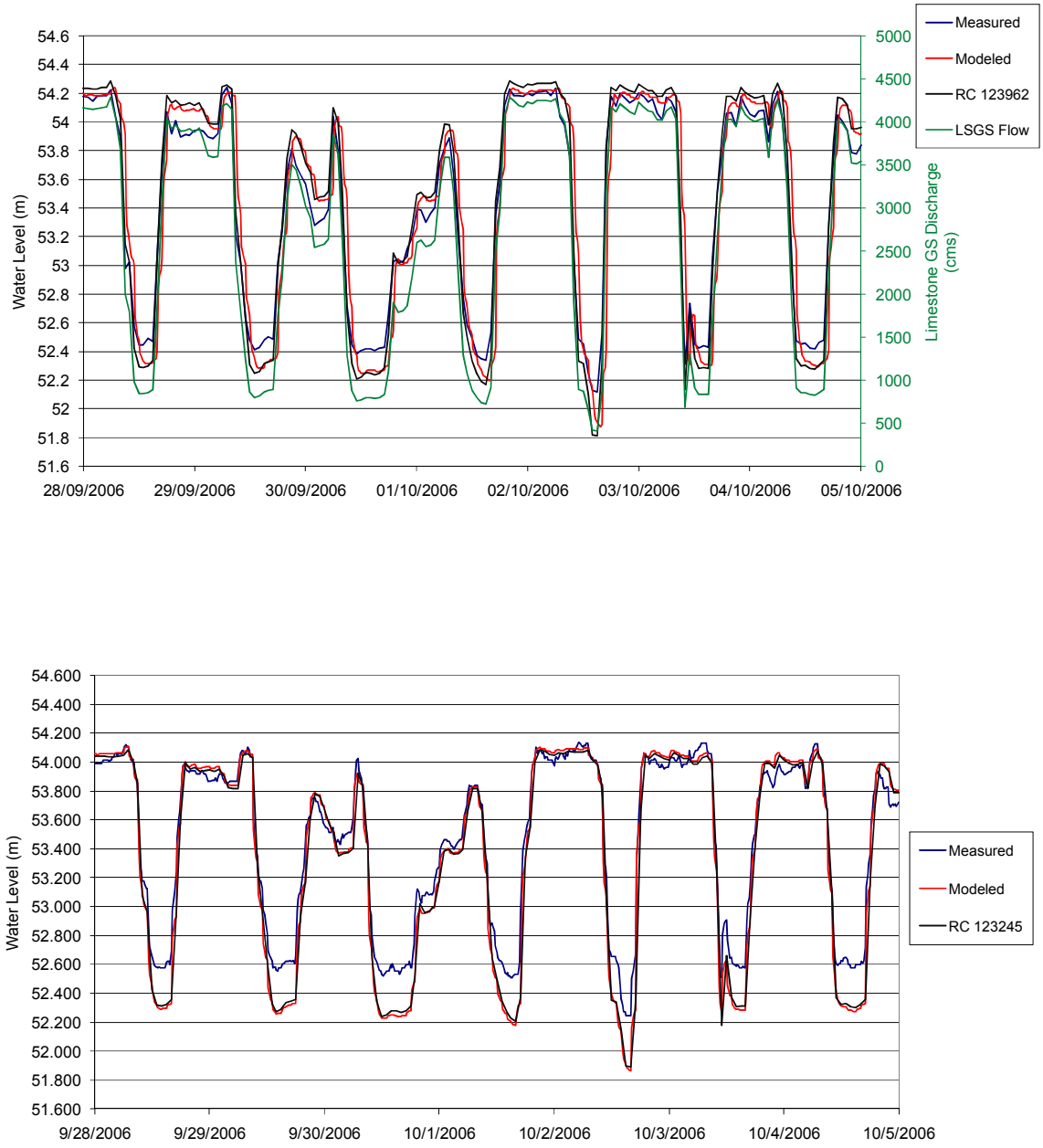


**Figure 5.10 -** Verification water levels at the tailrace (top) and UH738 (bottom).

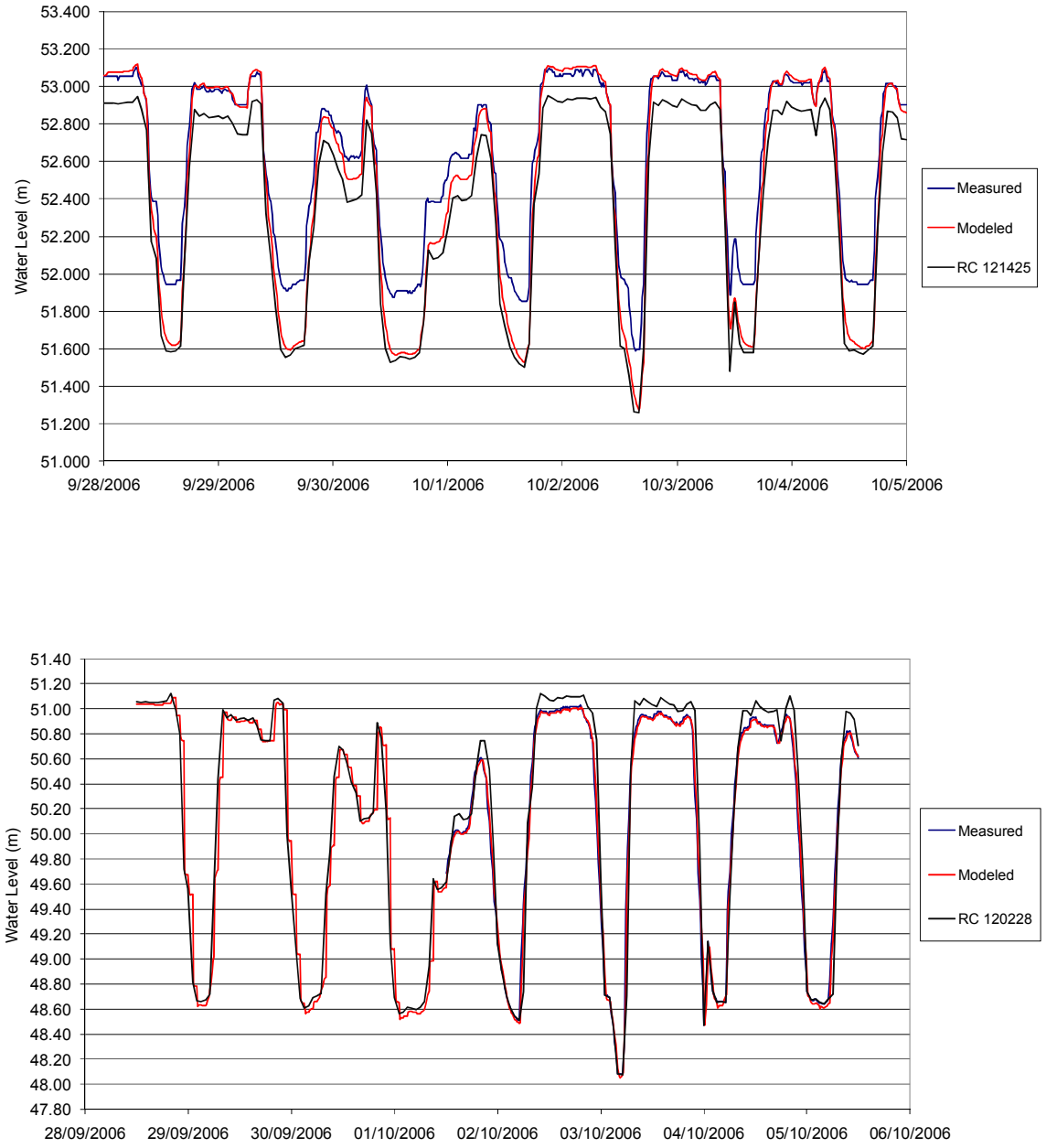


**Figure 5.11 -** Verification water levels at UH740 (top) and UH706 (bottom).

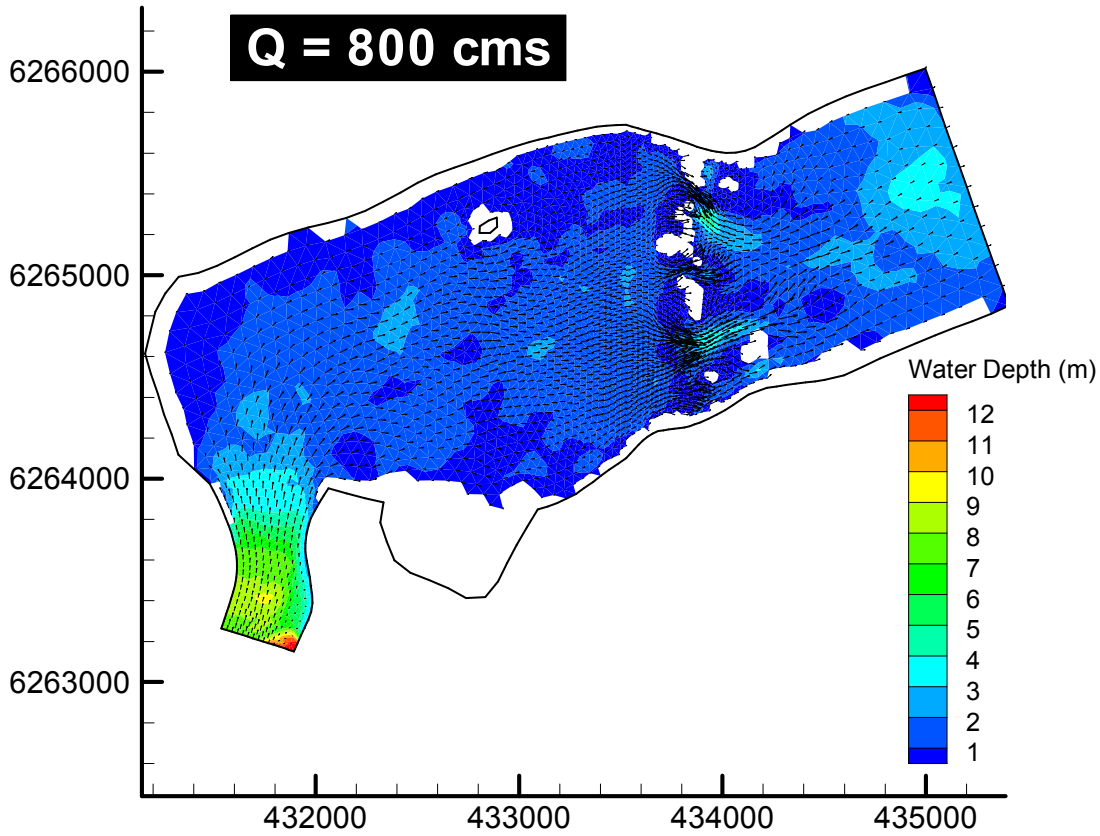


**Figure 5.12 -** Water depth and velocity vectors during an 800 cms flow condition.

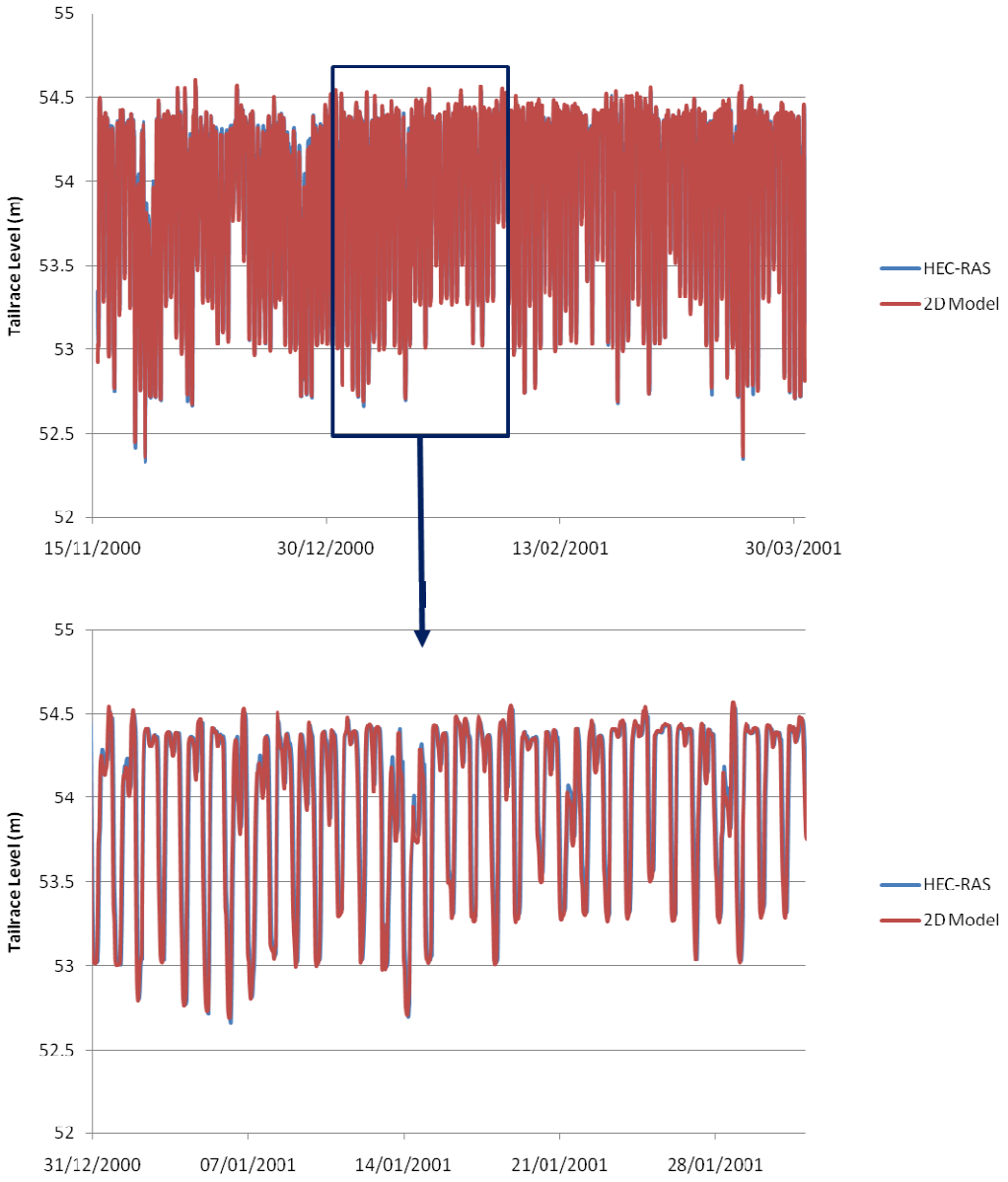


**Figure 5.13 -** Comparison of tailrace "open-water" levels over 2000-01 season.

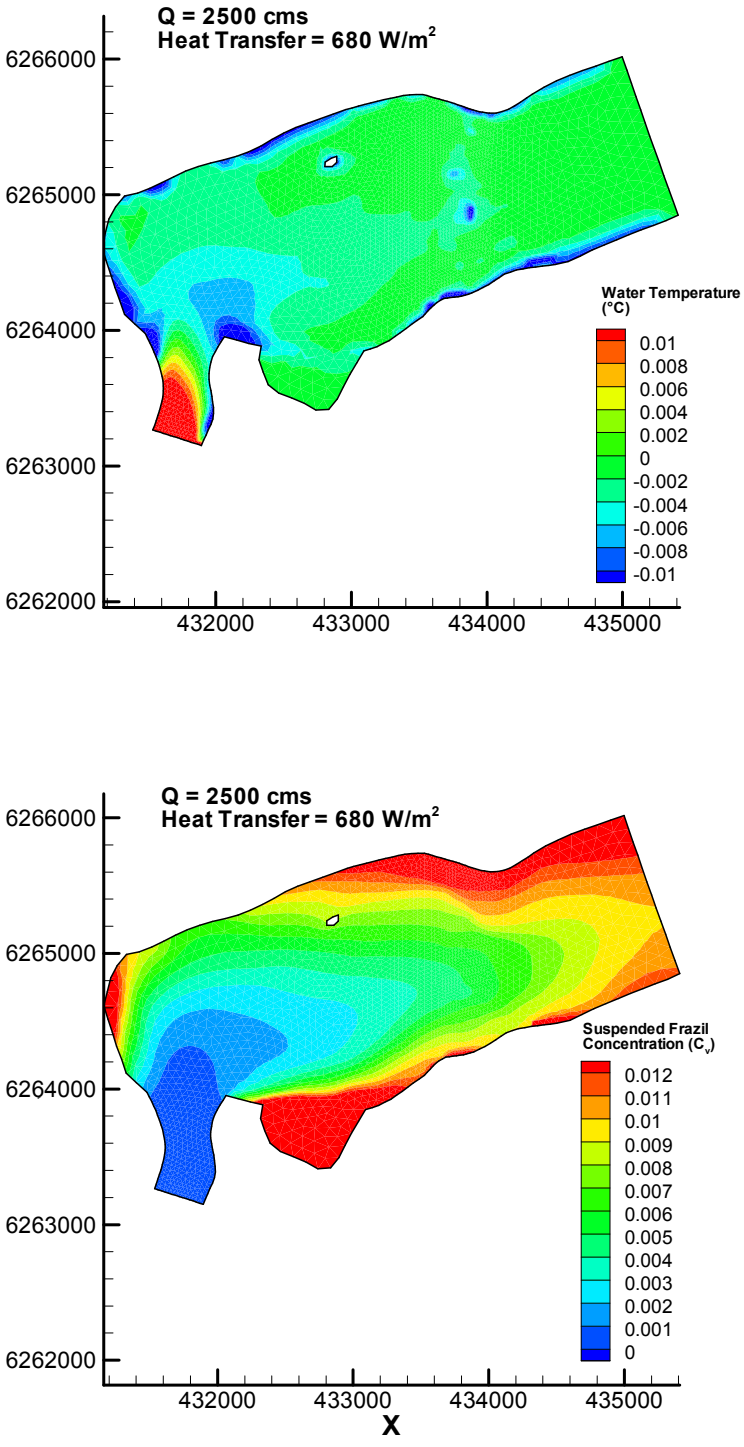


**Figure 5.14 -** Water temperature and suspended frazil contours with no surface ice.

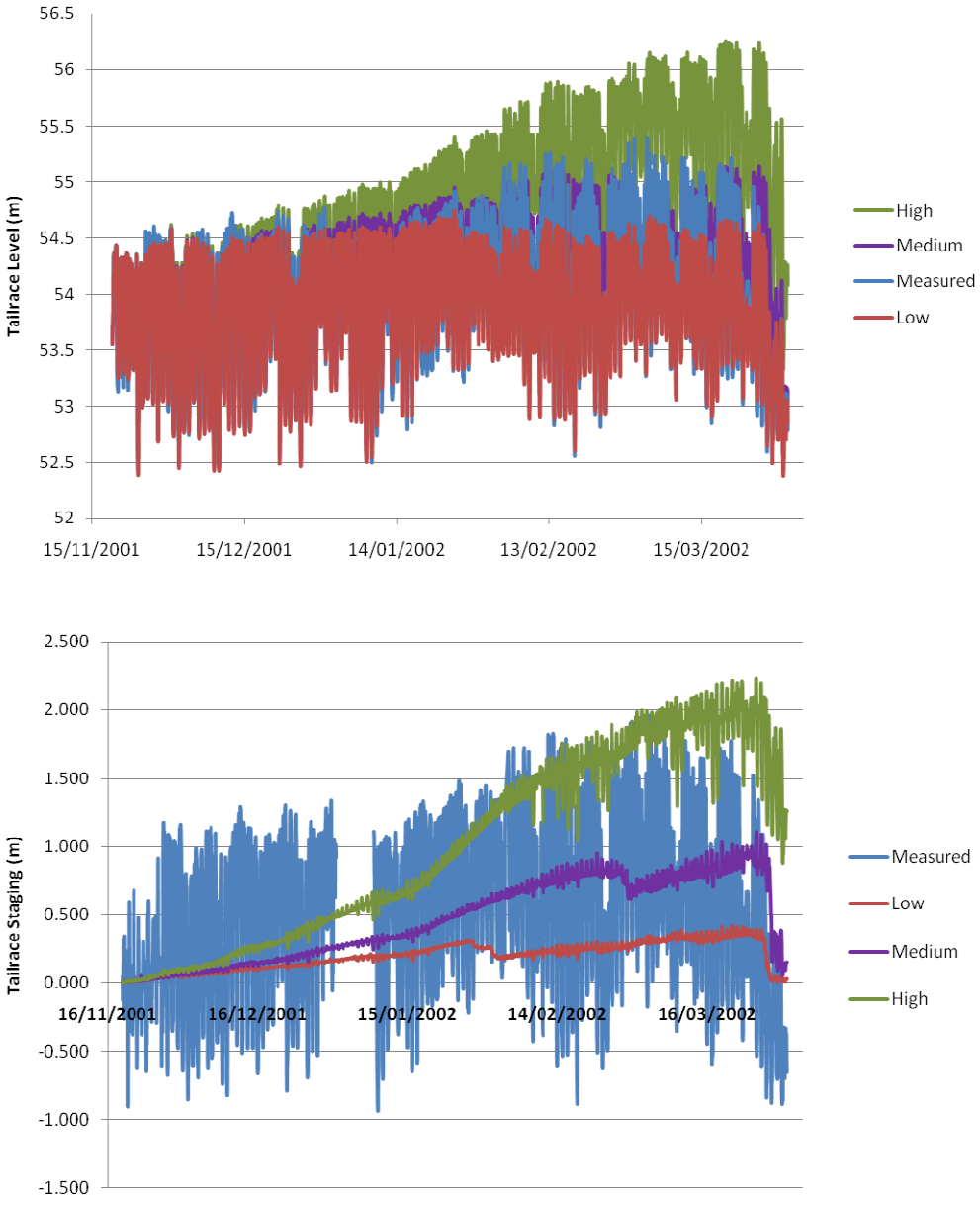


**Figure 5.15 -** 2001-02 tailrace waters levels (top) and tailrace staging (bottom) under low, medium, and high scenarios.

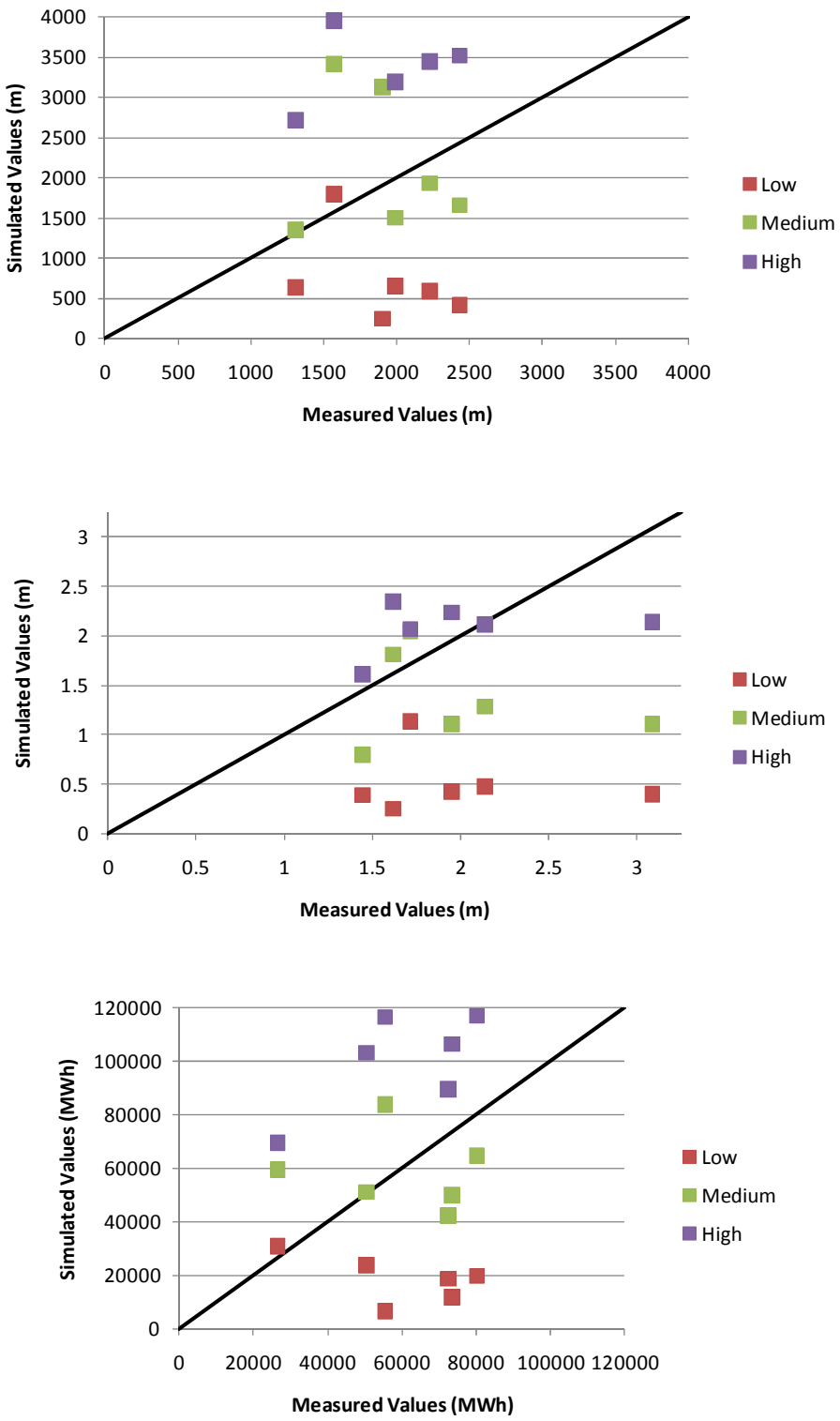


**Figure 5.16 -** Cumulative tailrace staging (top), maximum tailrace staging (middle), and MWh lost (bottom) for all scenarios.

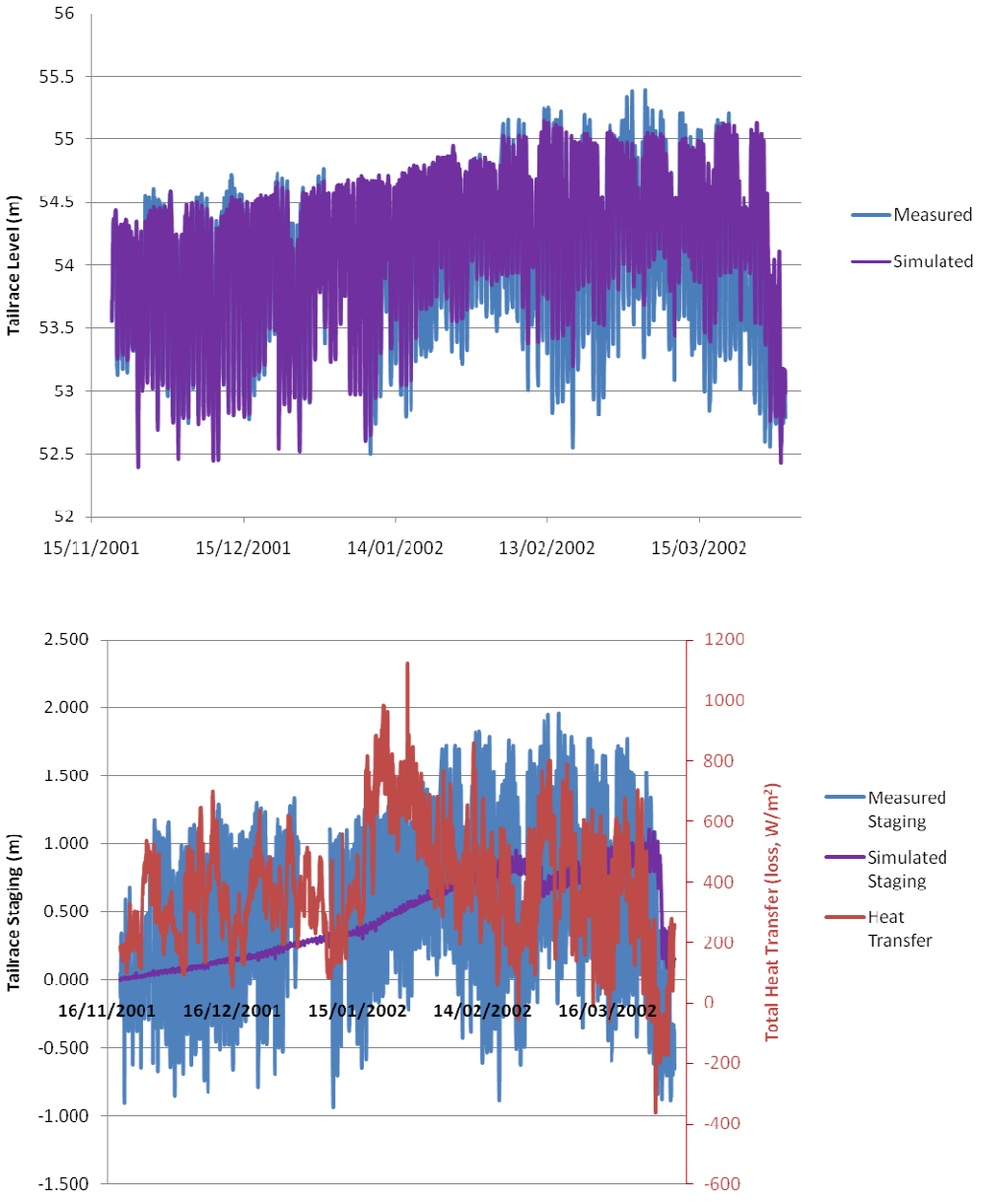


**Figure 5.17 -** 2001-02 tailrace water levels and tailrace staging (medium scenario).

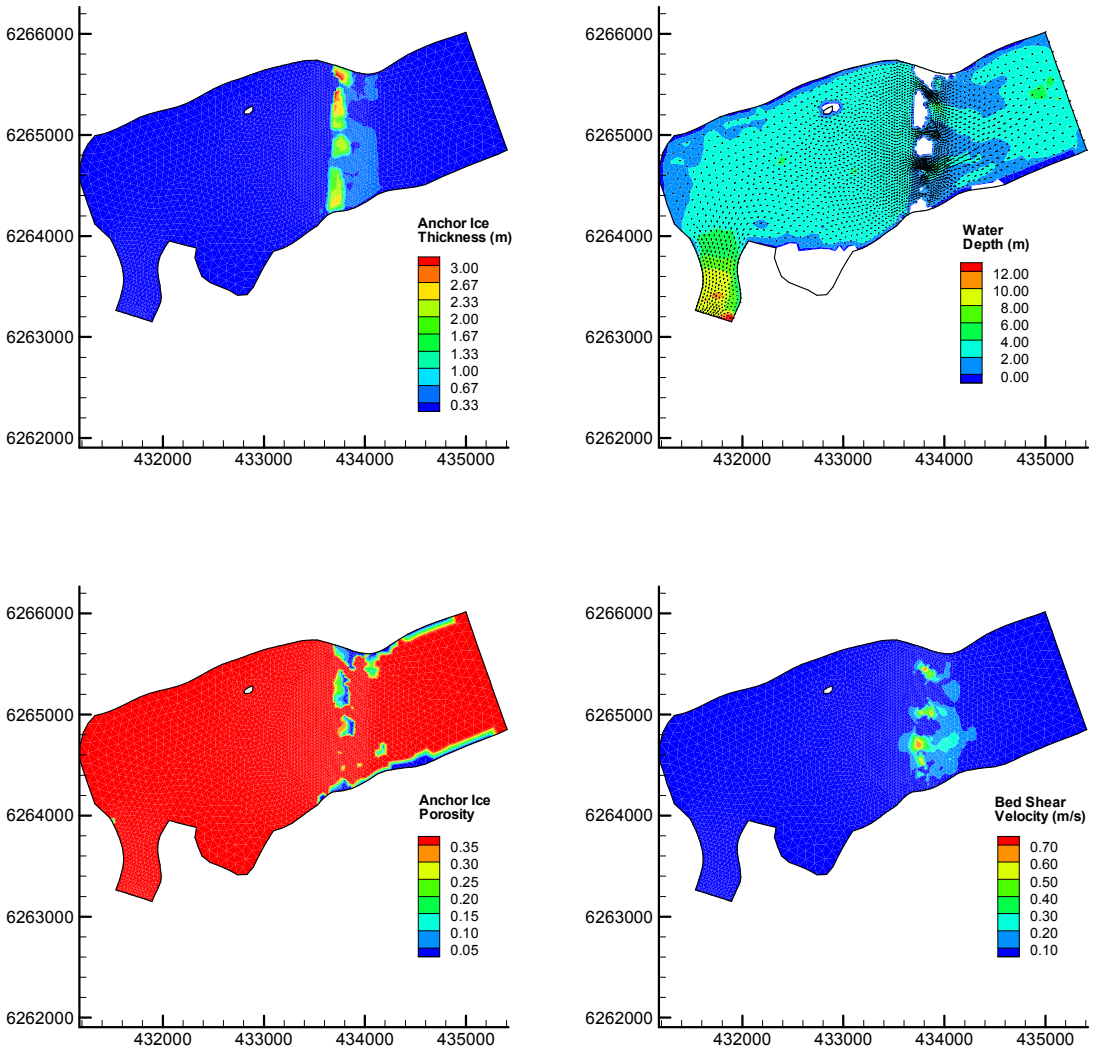


**Figure 5.18 -** February 18, 2002 simulated ice dam formation (medium scenario).

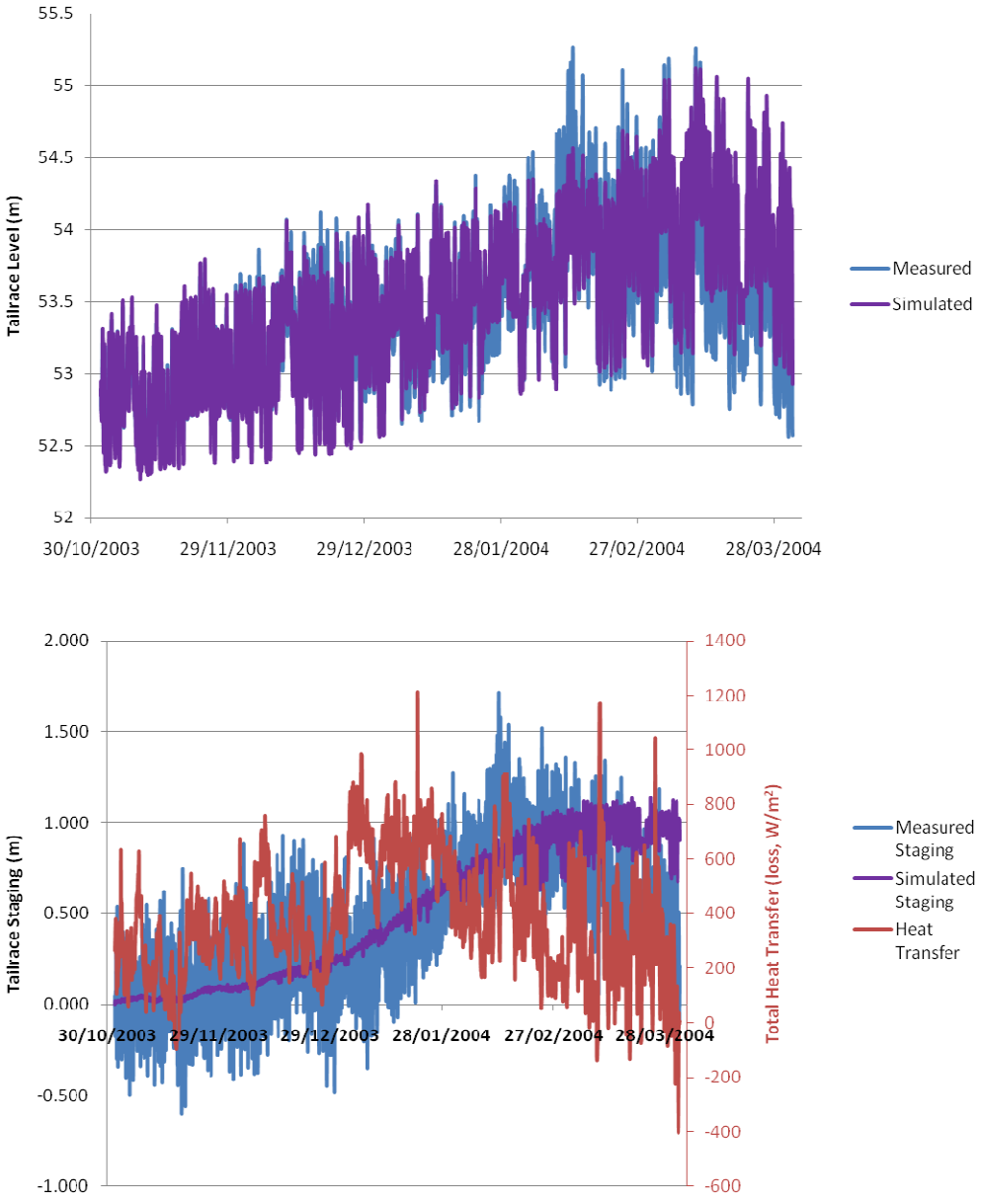


**Figure 5.19 -** 2003-04 tailrace water levels and tailrace staging (low scenario).

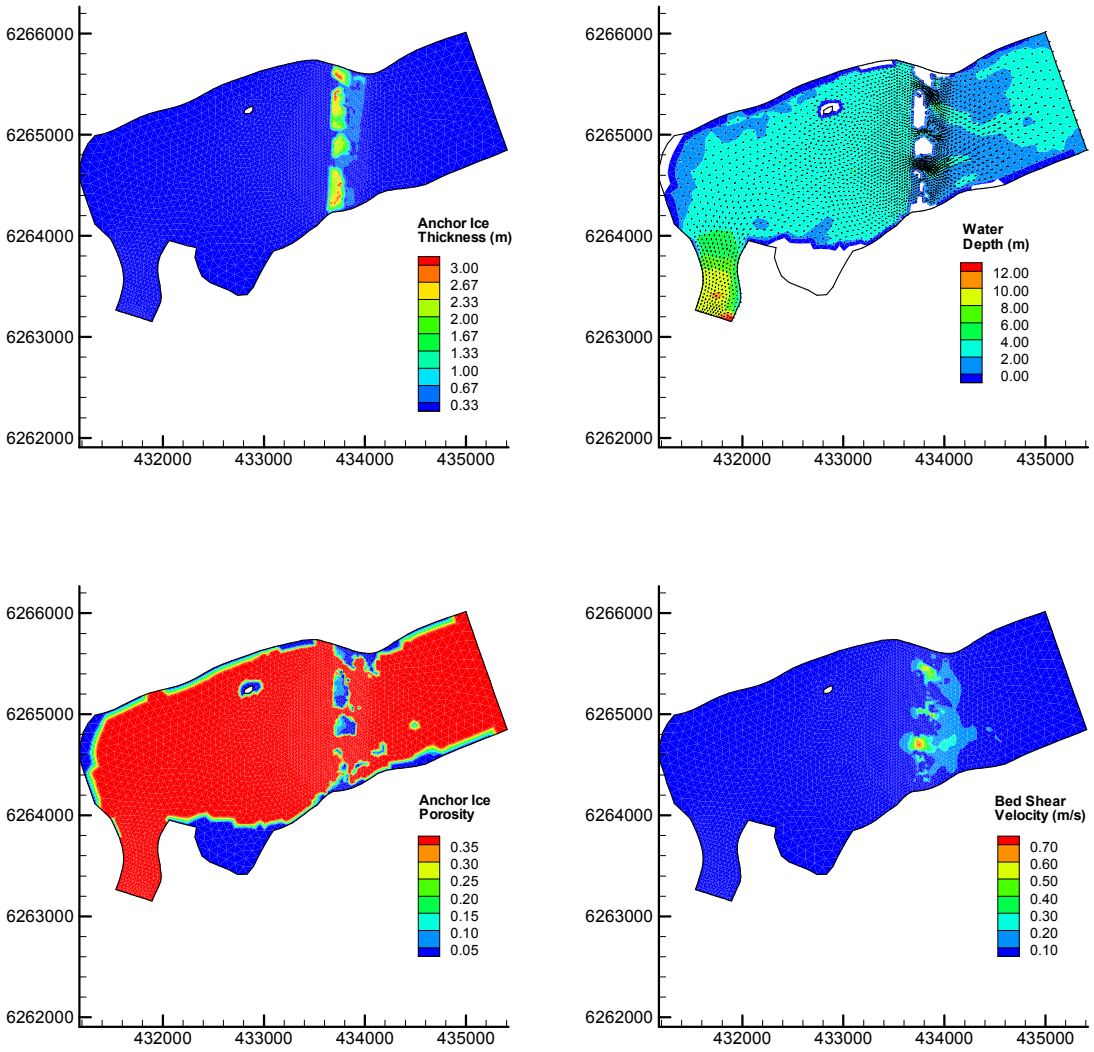


**Figure 5.20 -** February 21, 2004 simulated ice dam formation (low scenario).

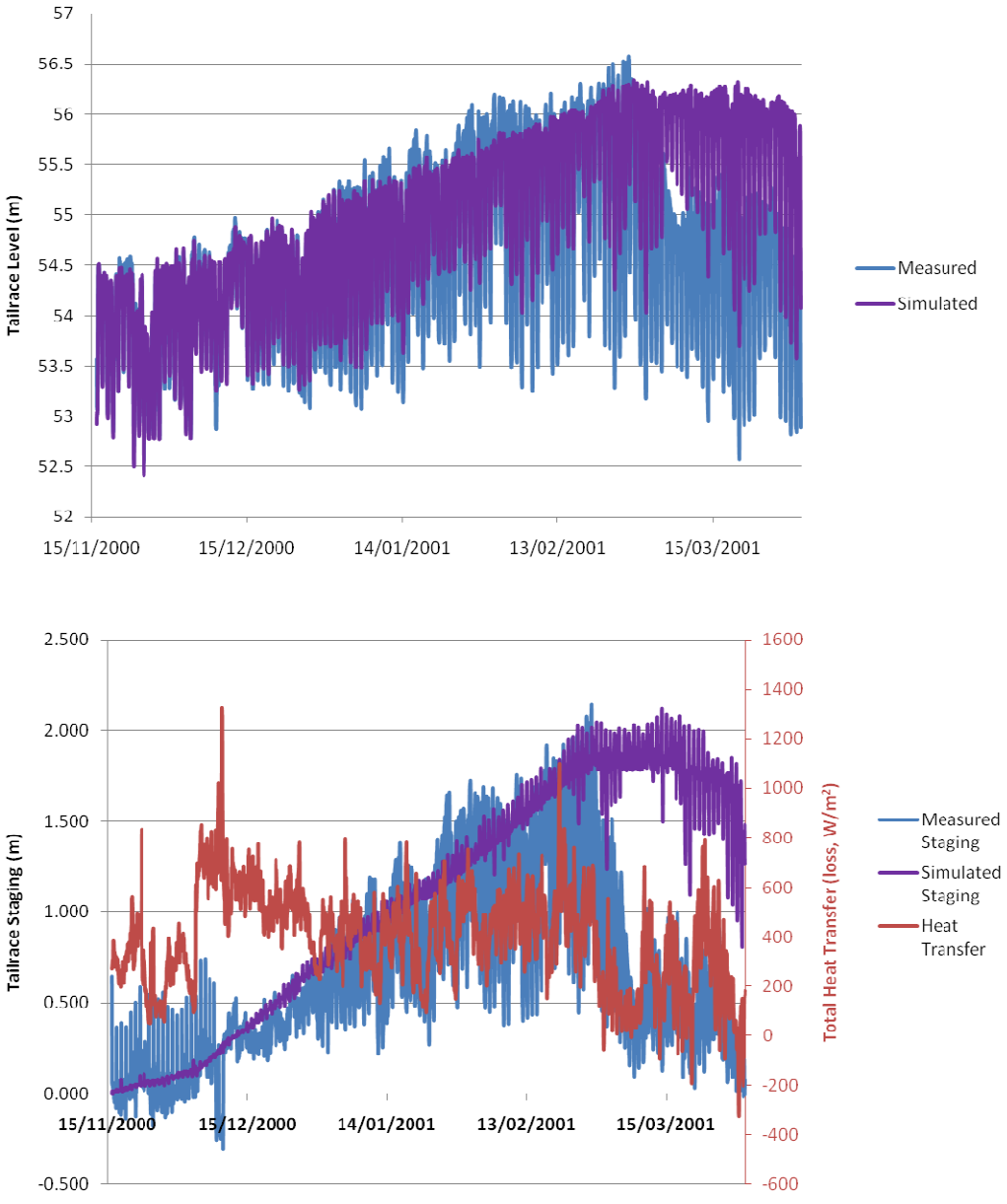


**Figure 5.21 -** 2000-01 tailrace water levels and tailrace staging (high scenario).

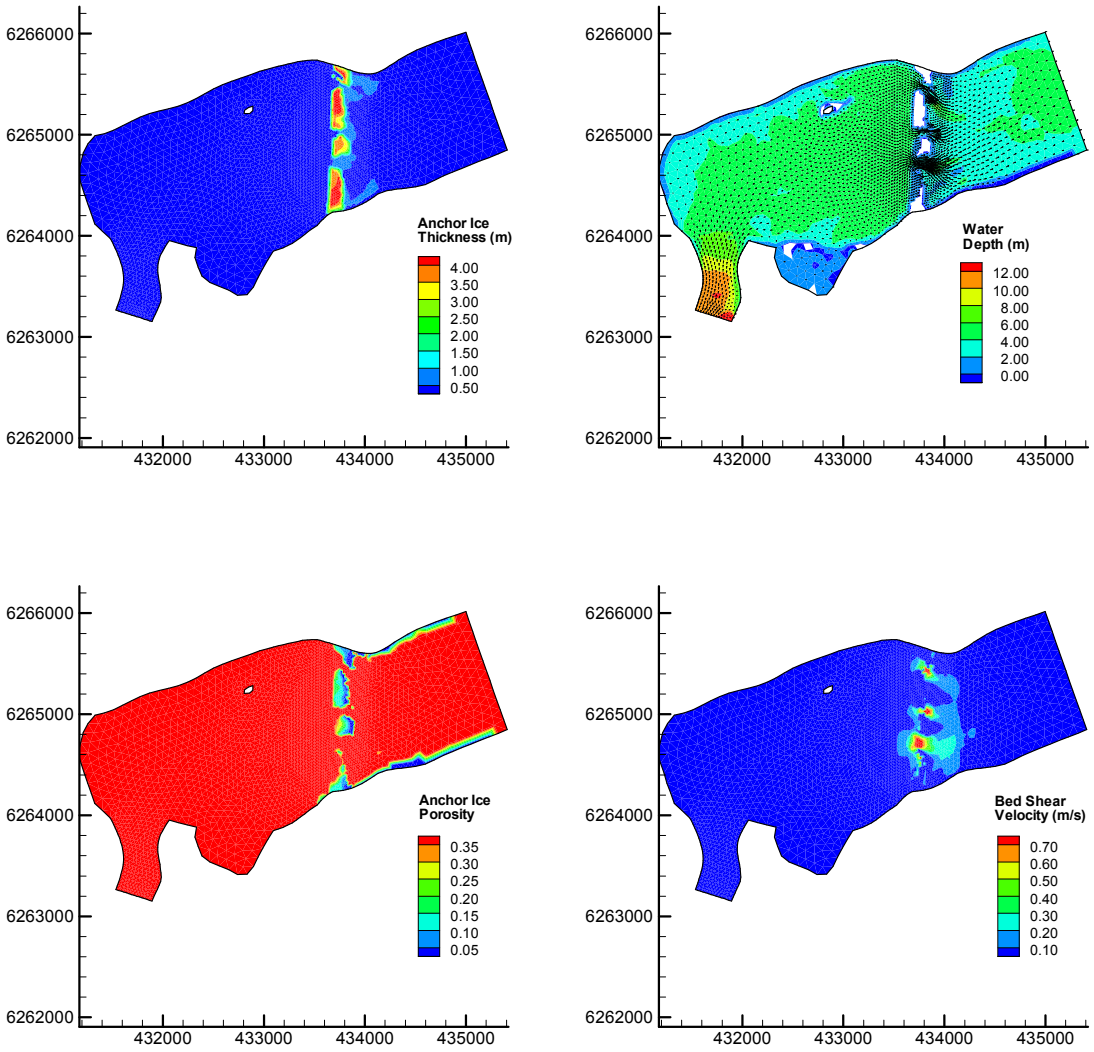


**Figure 5.22 -** February 24, 2001 simulated ice dam formation (high scenario).

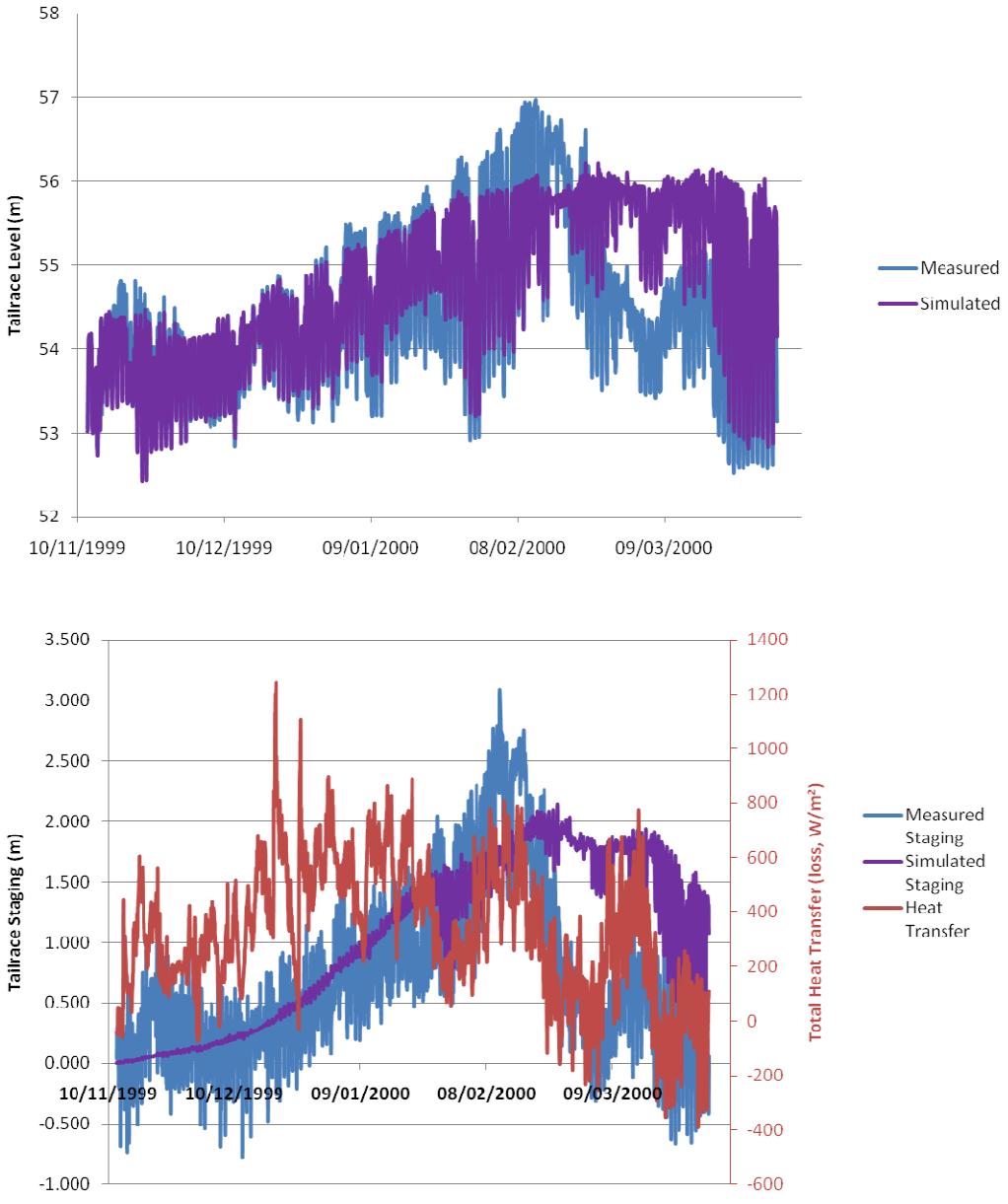


**Figure 5.23 -** 1999-00 tailrace water levels and tailrace staging (high scenario).

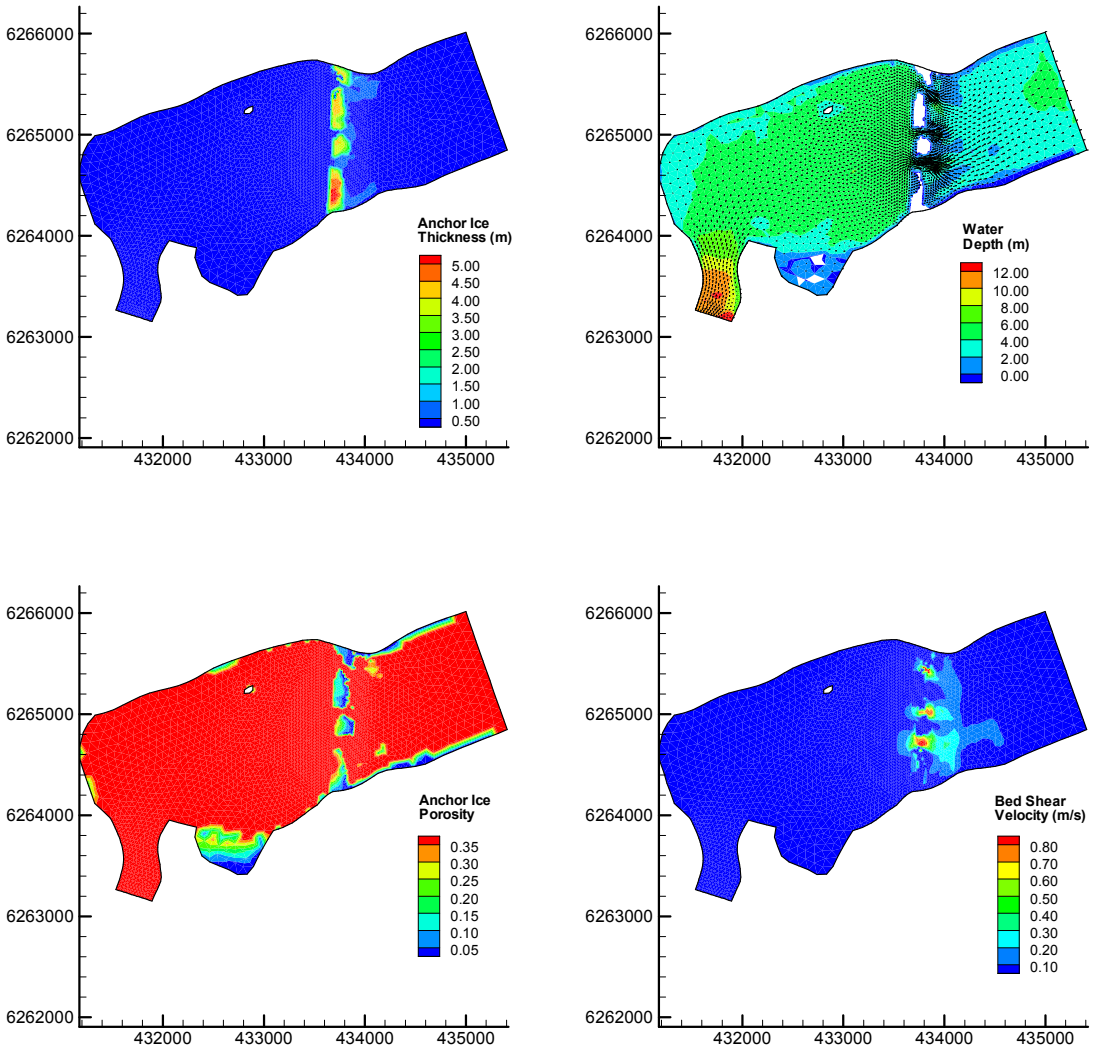


**Figure 5.24 -** February 22, 2000 simulated ice dam formation (high scenario).

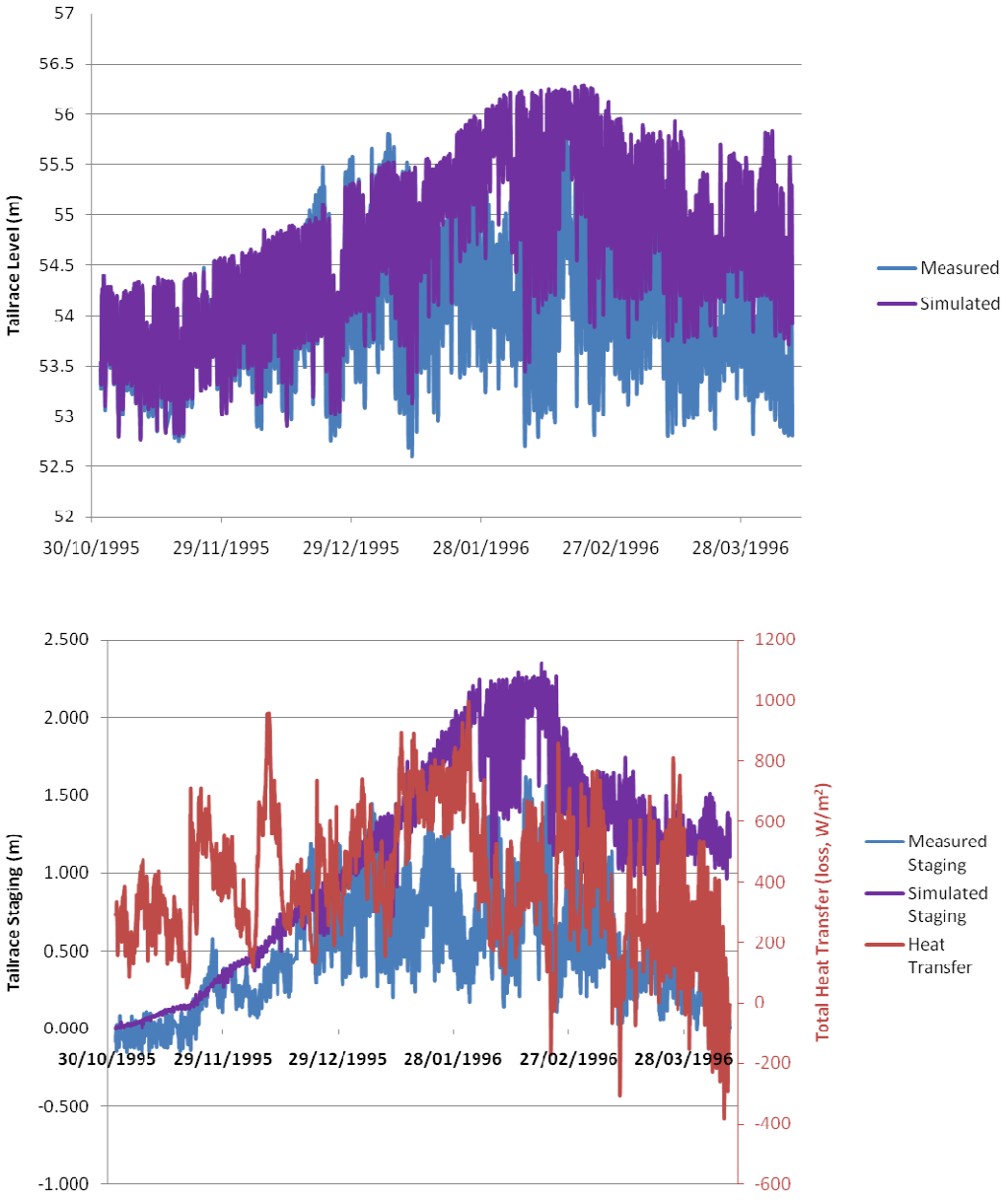


**Figure 5.25 -** 1995-96 tailrace water levels and tailrace staging (high scenario).

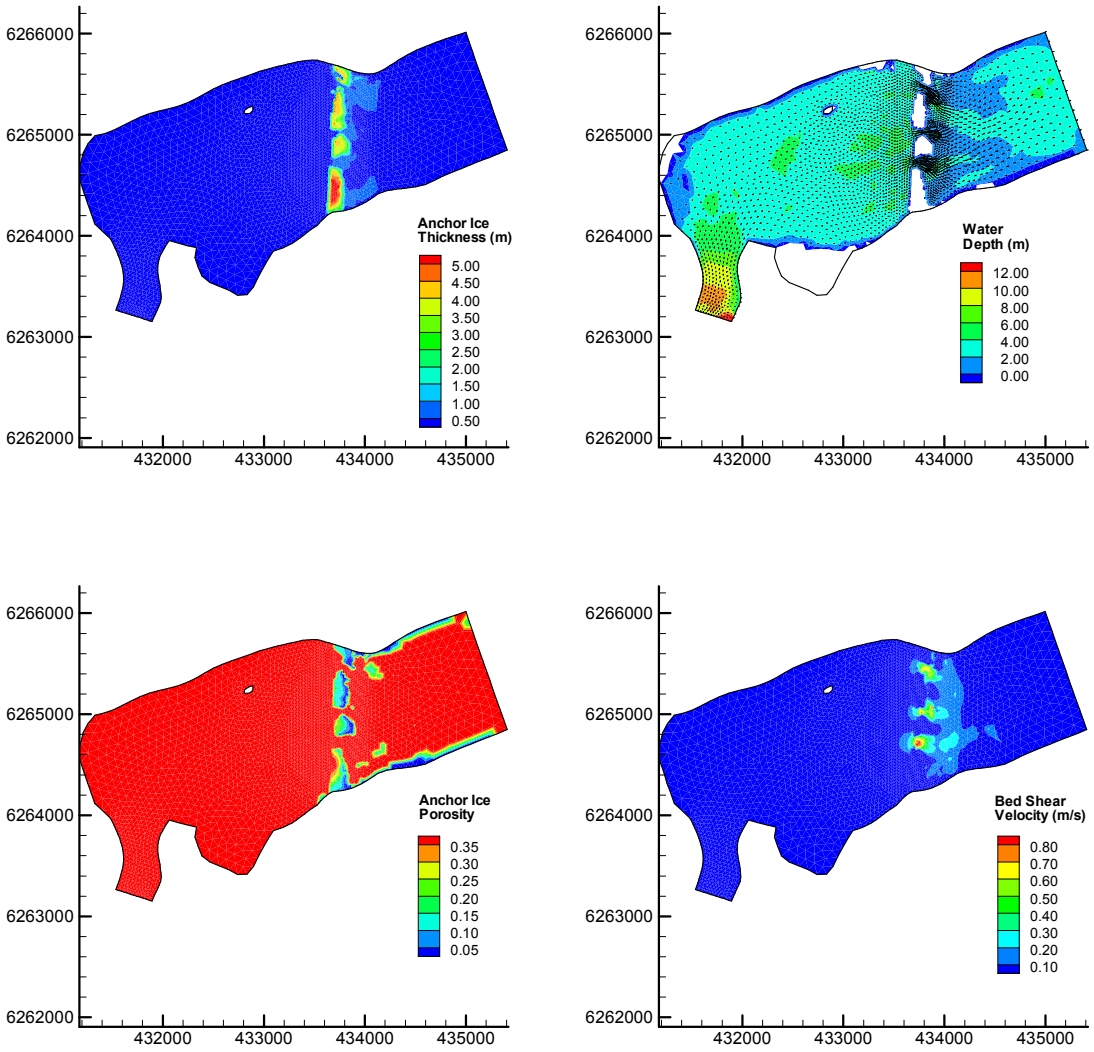


**Figure 5.26 -** February 7, 1996 simulated ice dam formation (high scenario).

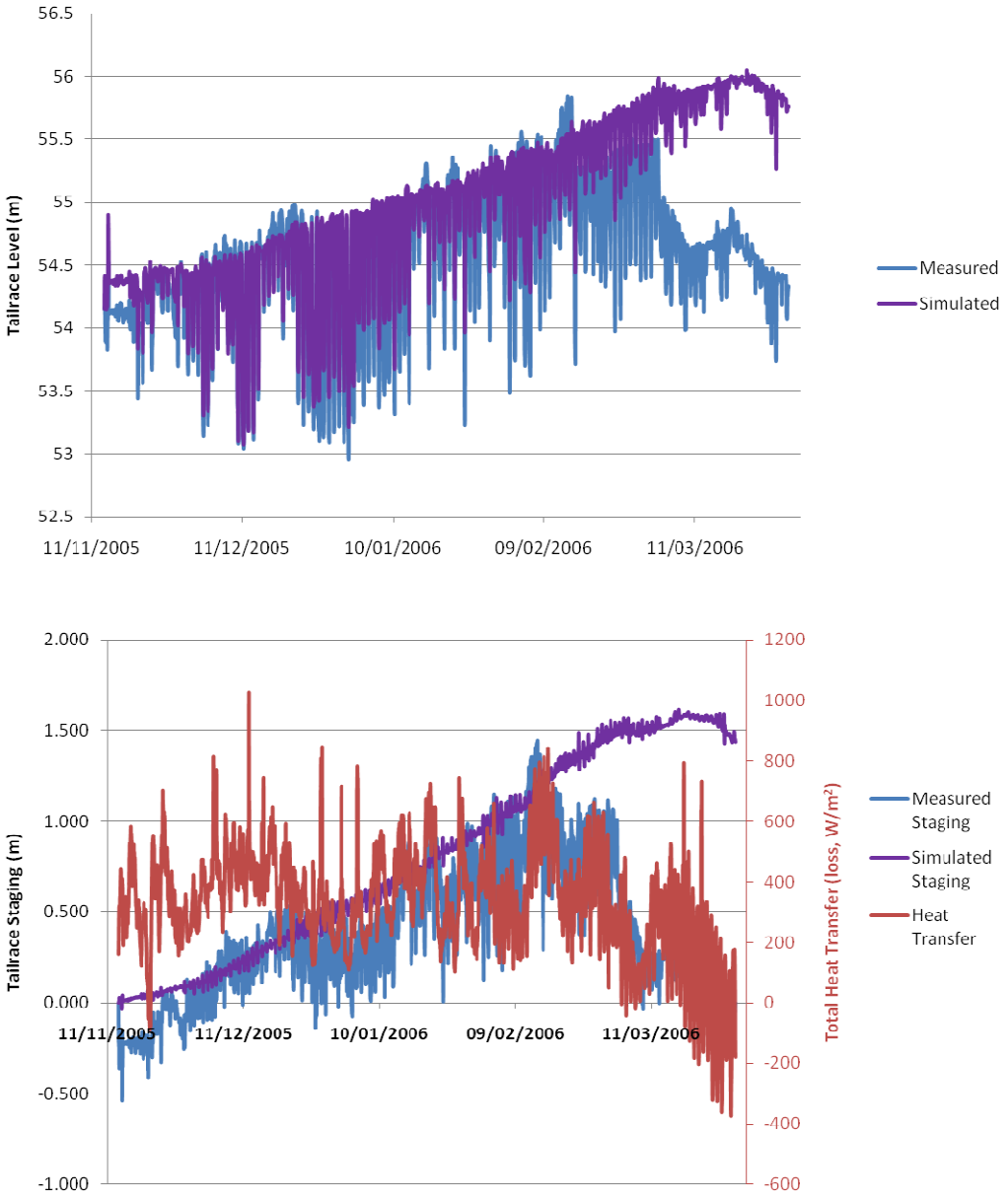


**Figure 5.27 -** 2005-06 tailrace water levels and tailrace staging (high scenario).

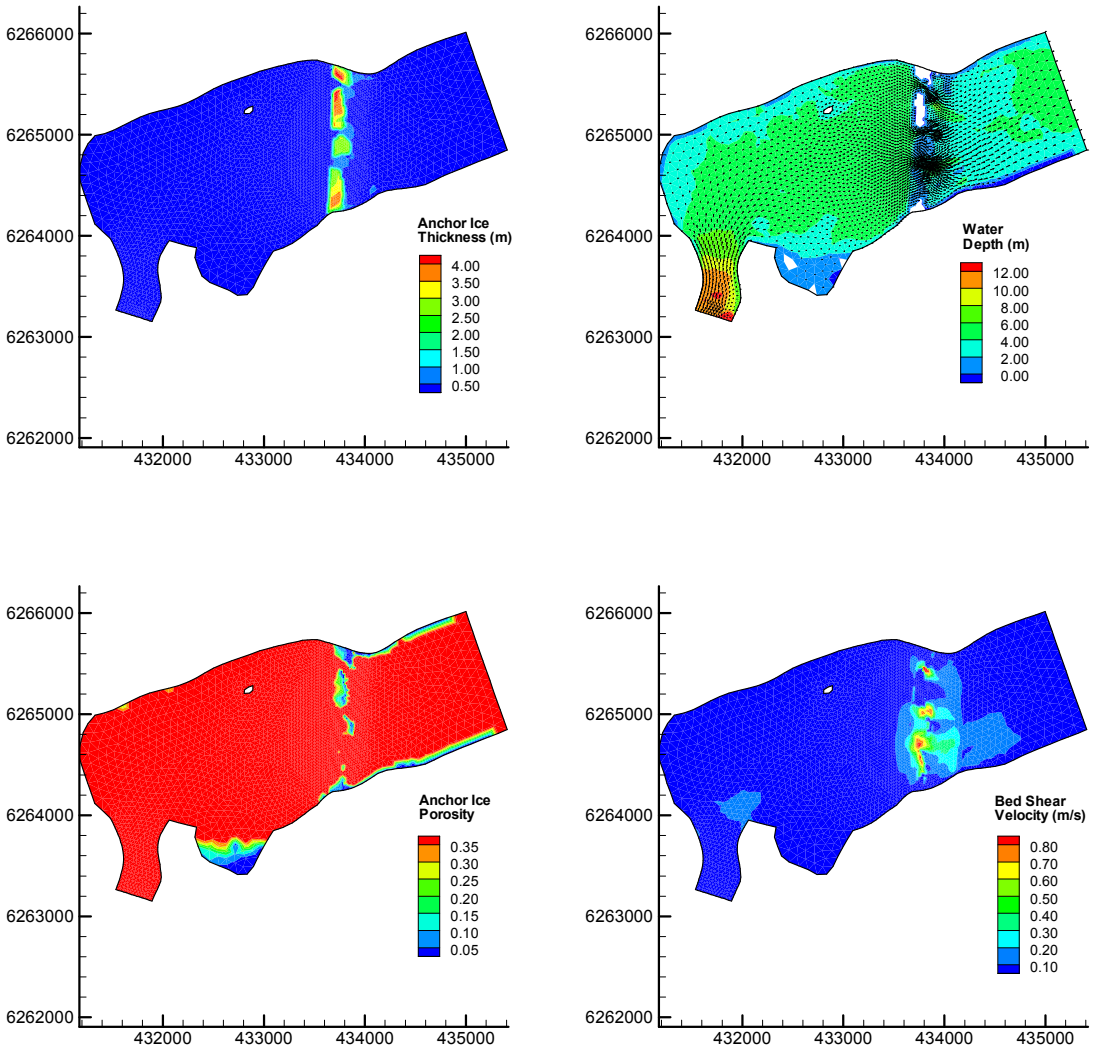


**Figure 5.28 -** February 23, 2006 simulated ice dam formation (high scenario).

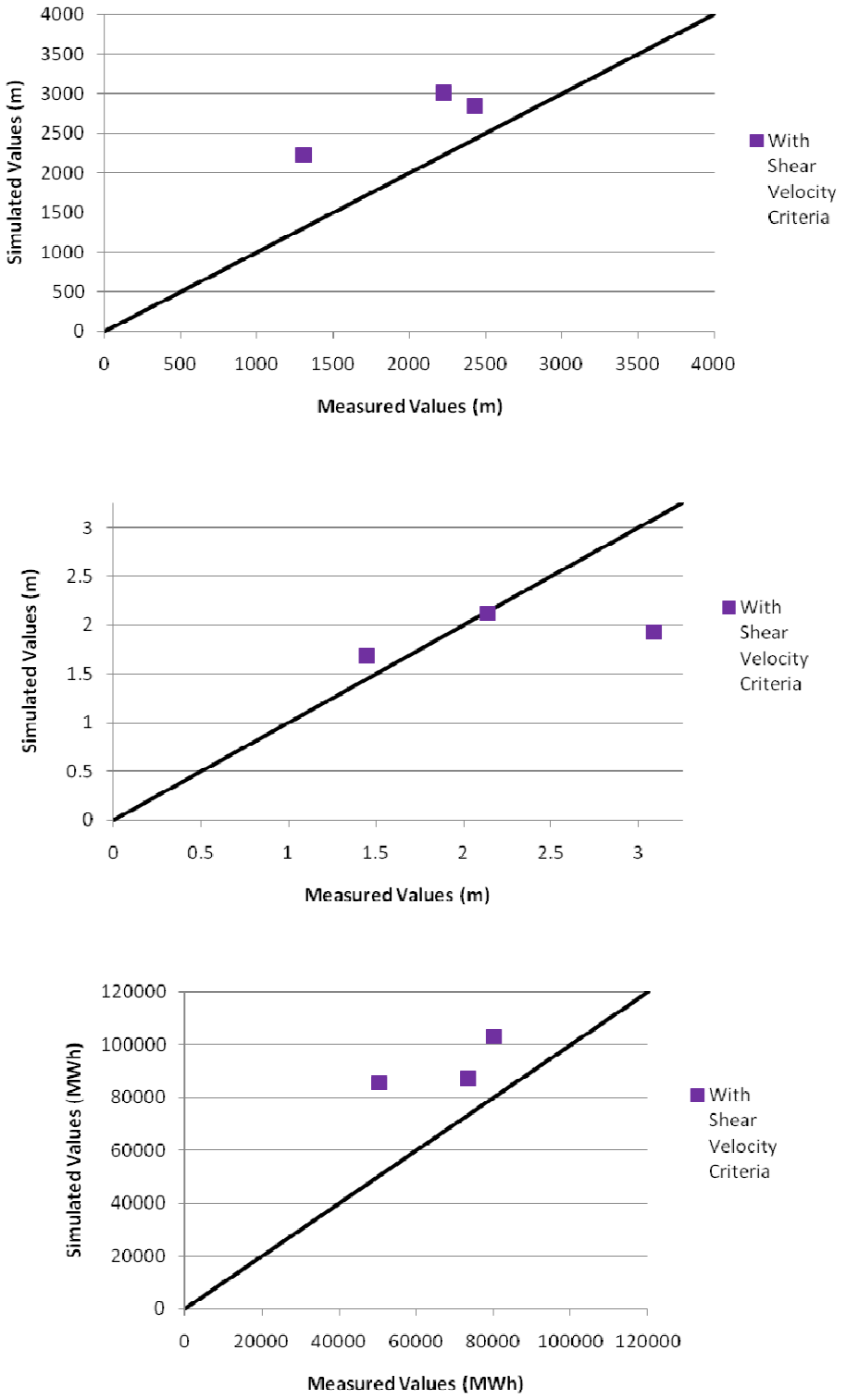


**Figure 5.29 -** Cumulative tailrace staging (top), maximum tailrace staging (middle), and MWh lost (bottom) for the shear velocity criteria runs.

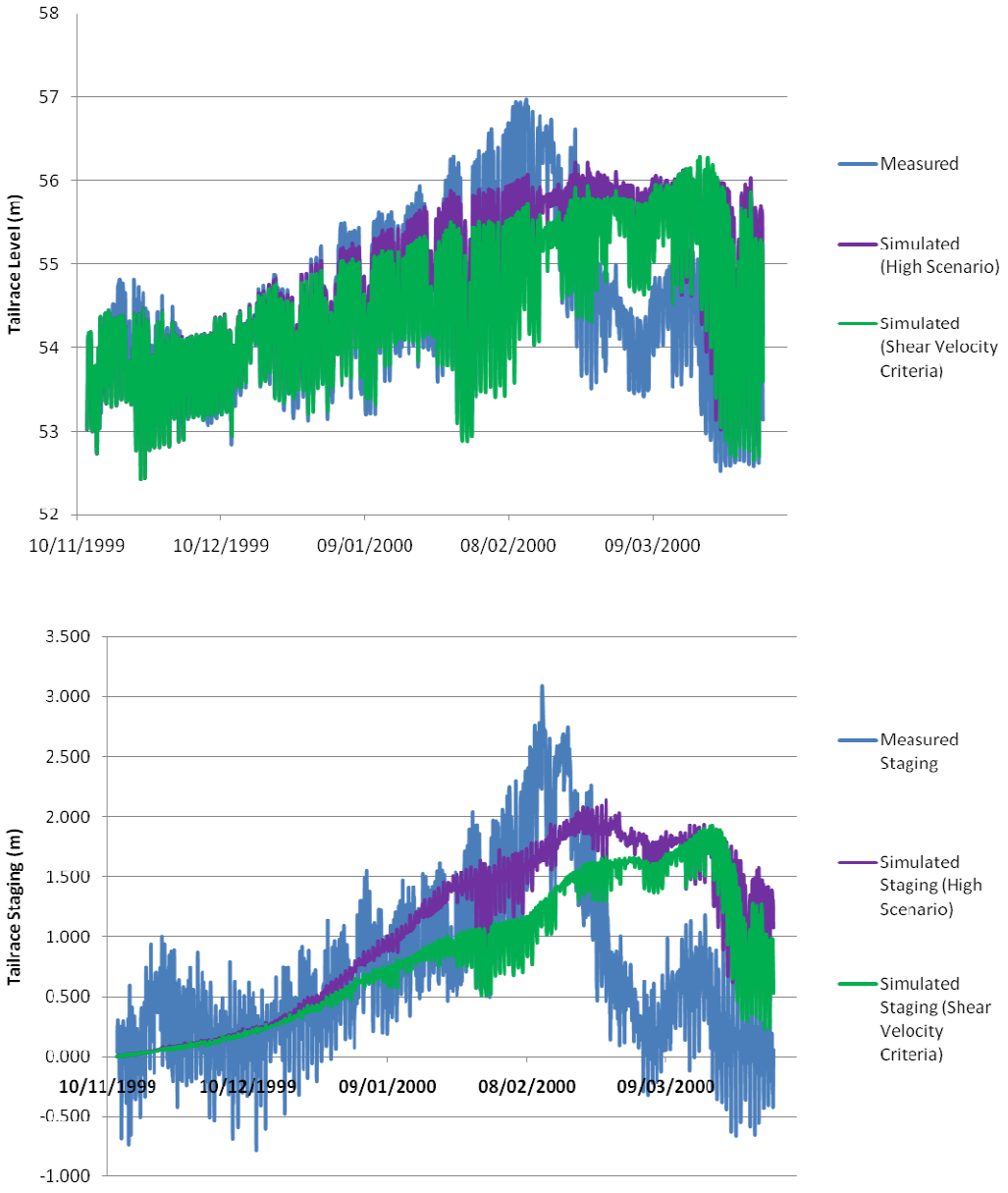


**Figure 5.30 -** 1999-2000 tailrace water levels and tailrace staging (with shear velocity criteria).

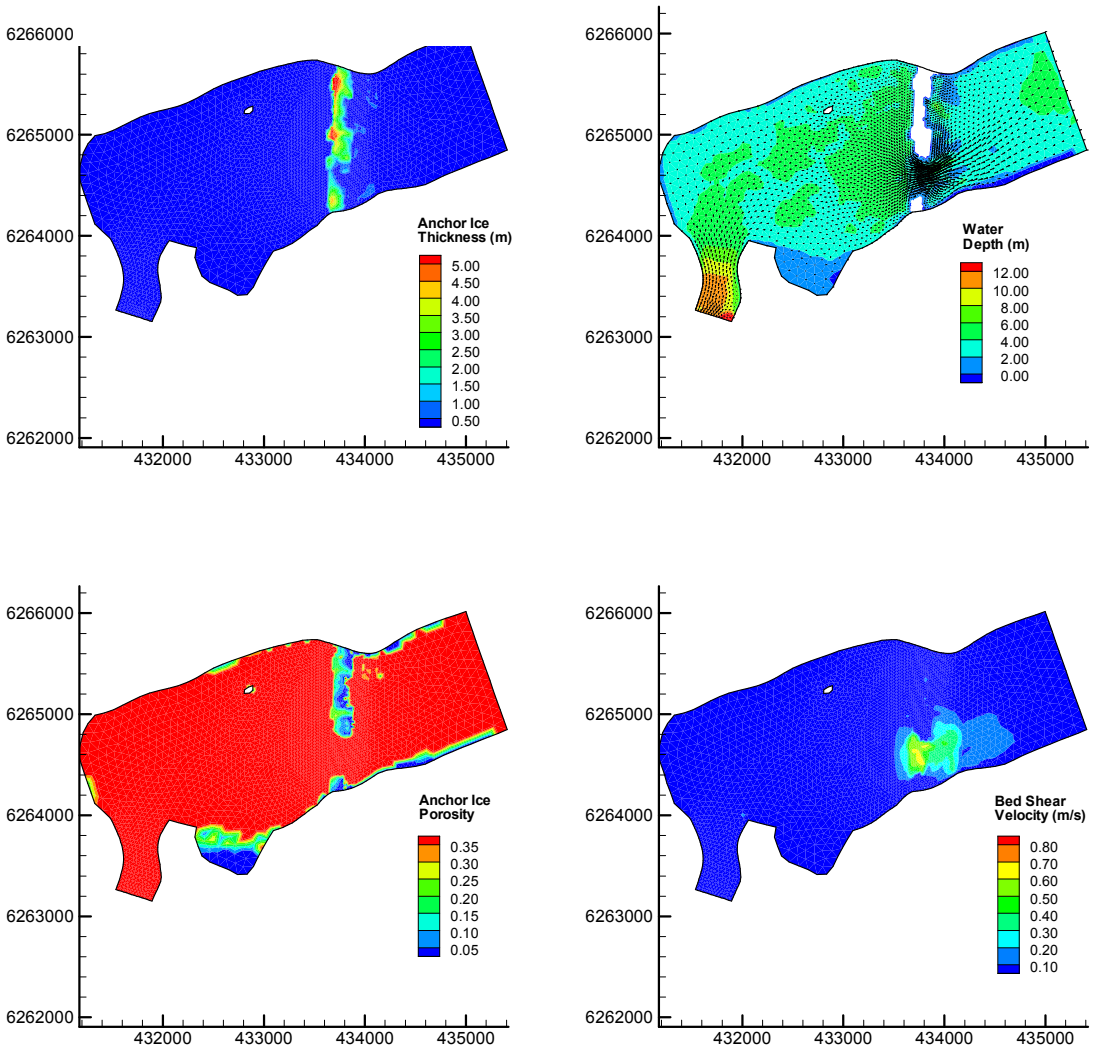


**Figure 5.31 -** February 23, 2000 simulated ice dam formation (with shear velocity criteria).

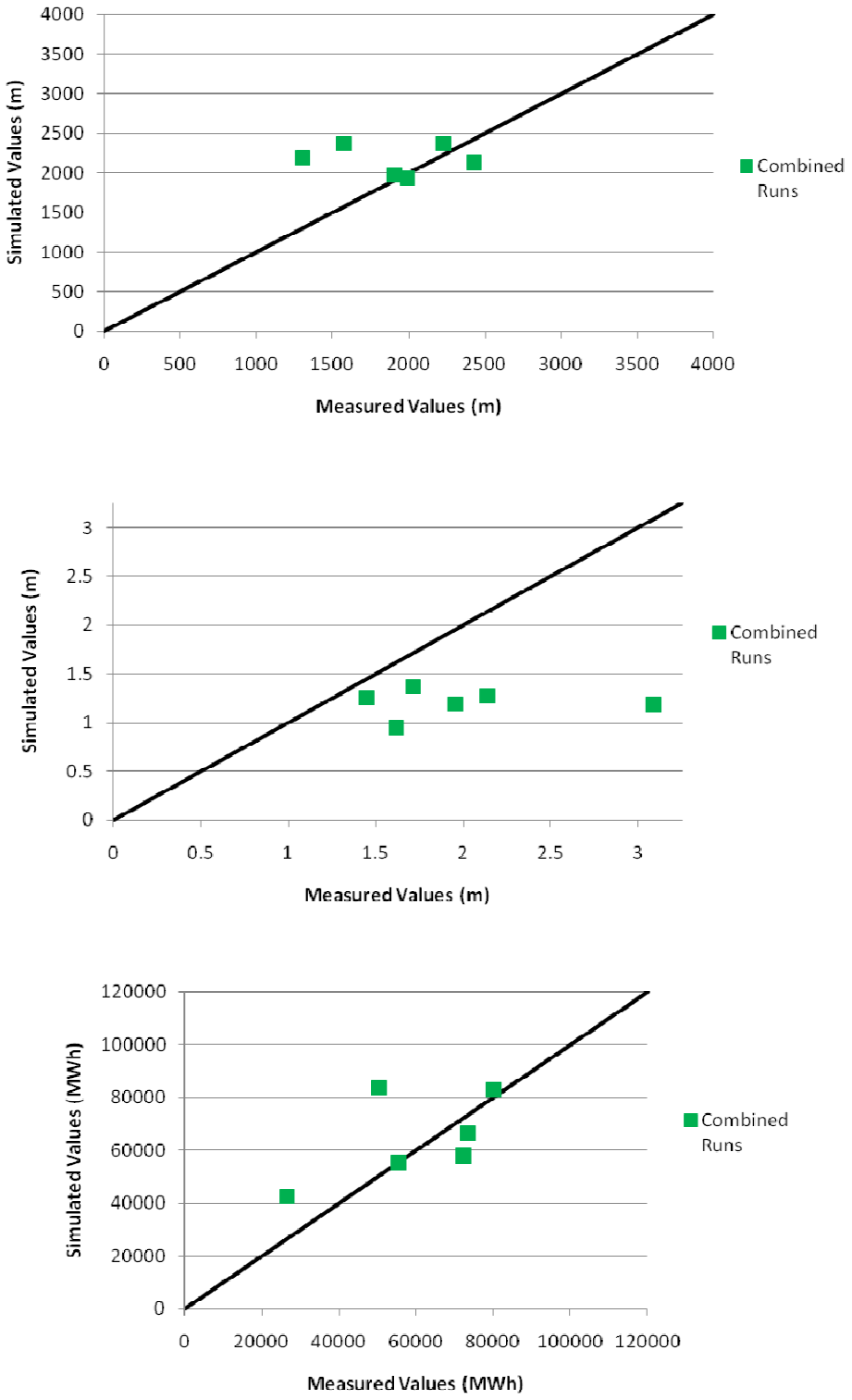


**Figure 5.32 -** Cumulative tailrace staging (top), maximum tailrace staging (middle), and MWh lost (bottom) for the combined runs.

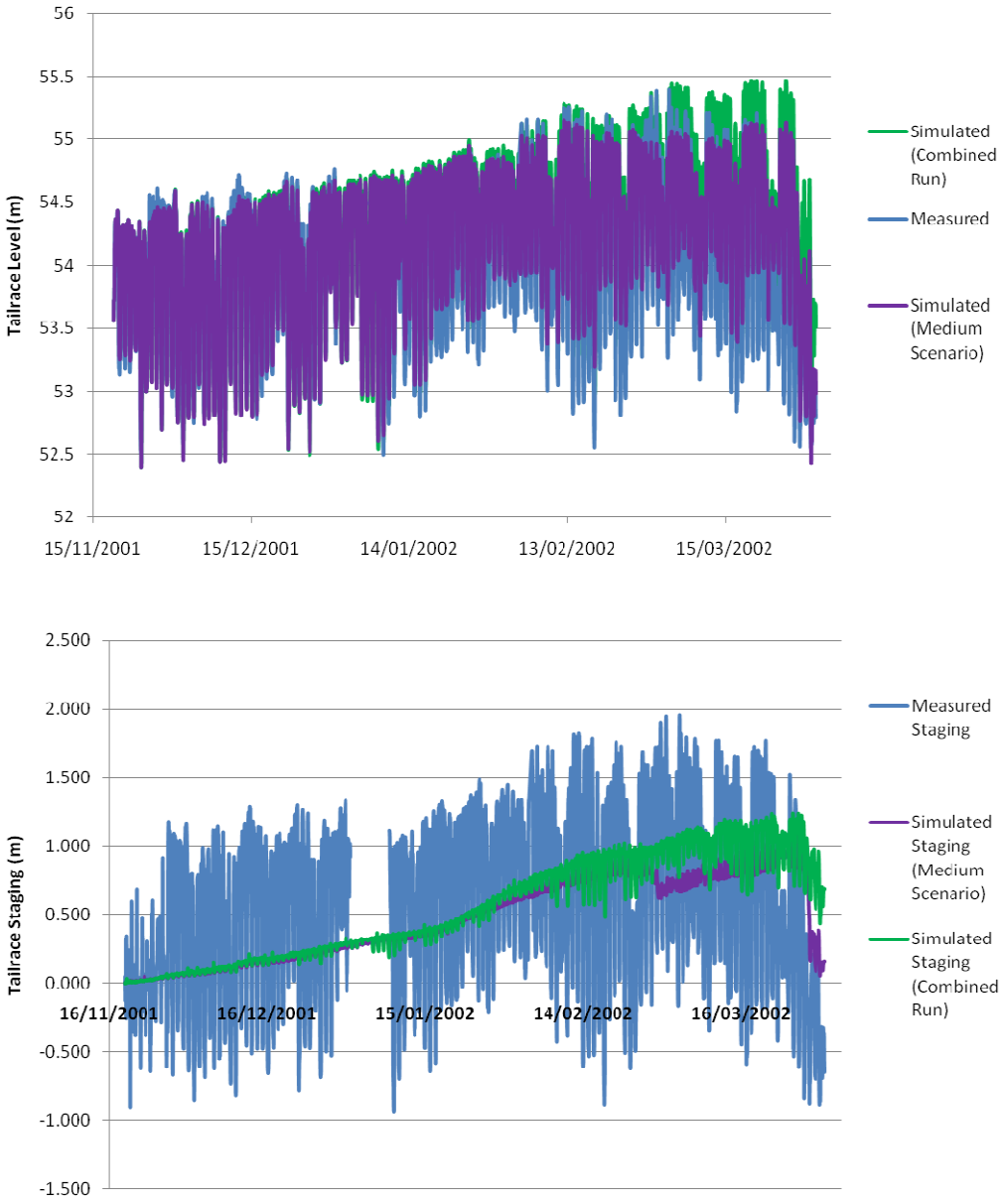


**Figure 5.33 -** 2001-02 tailrace water levels and tailrace staging (combined run).

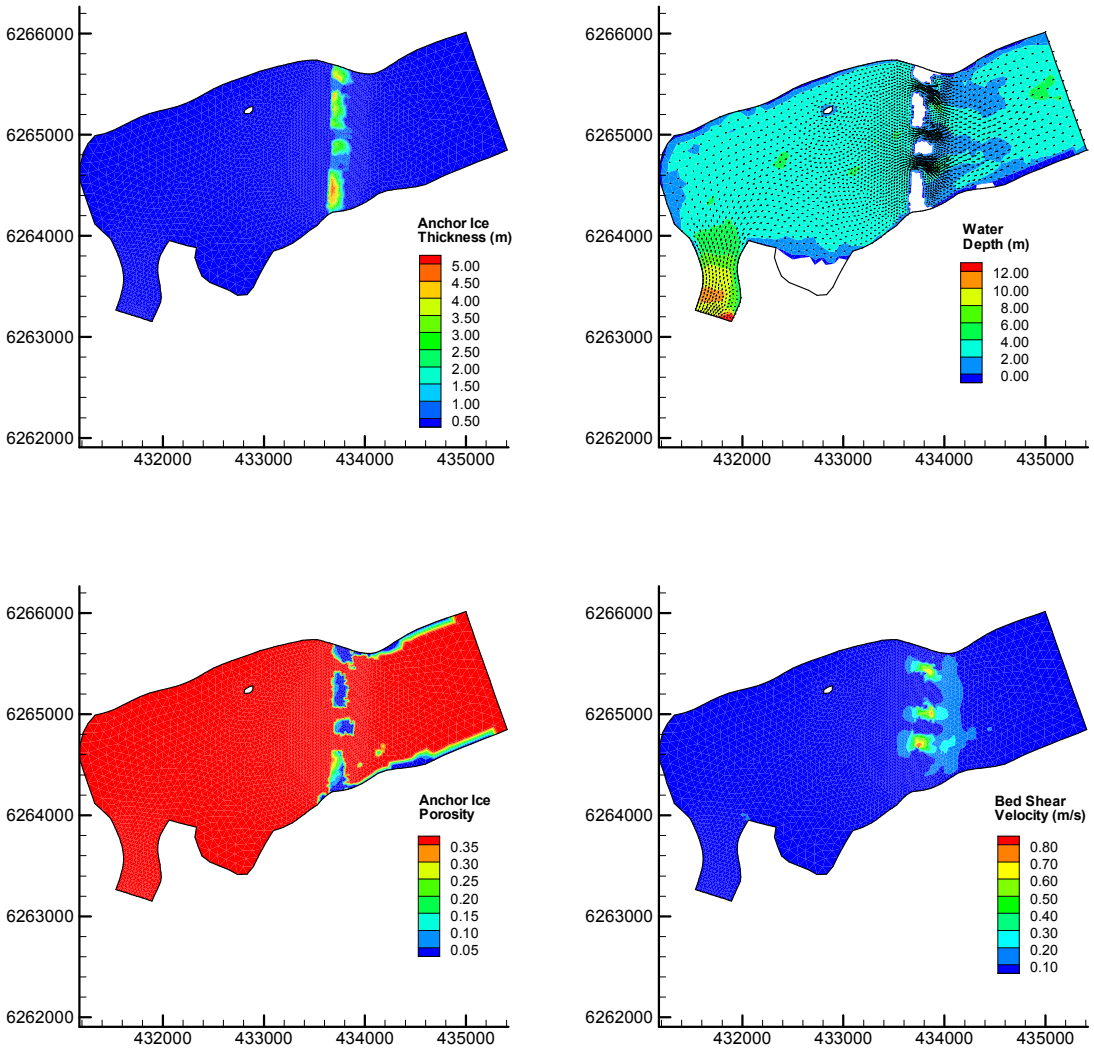


**Figure 5.34 -** March 10, 2002 simulated ice dam formation (combined run).

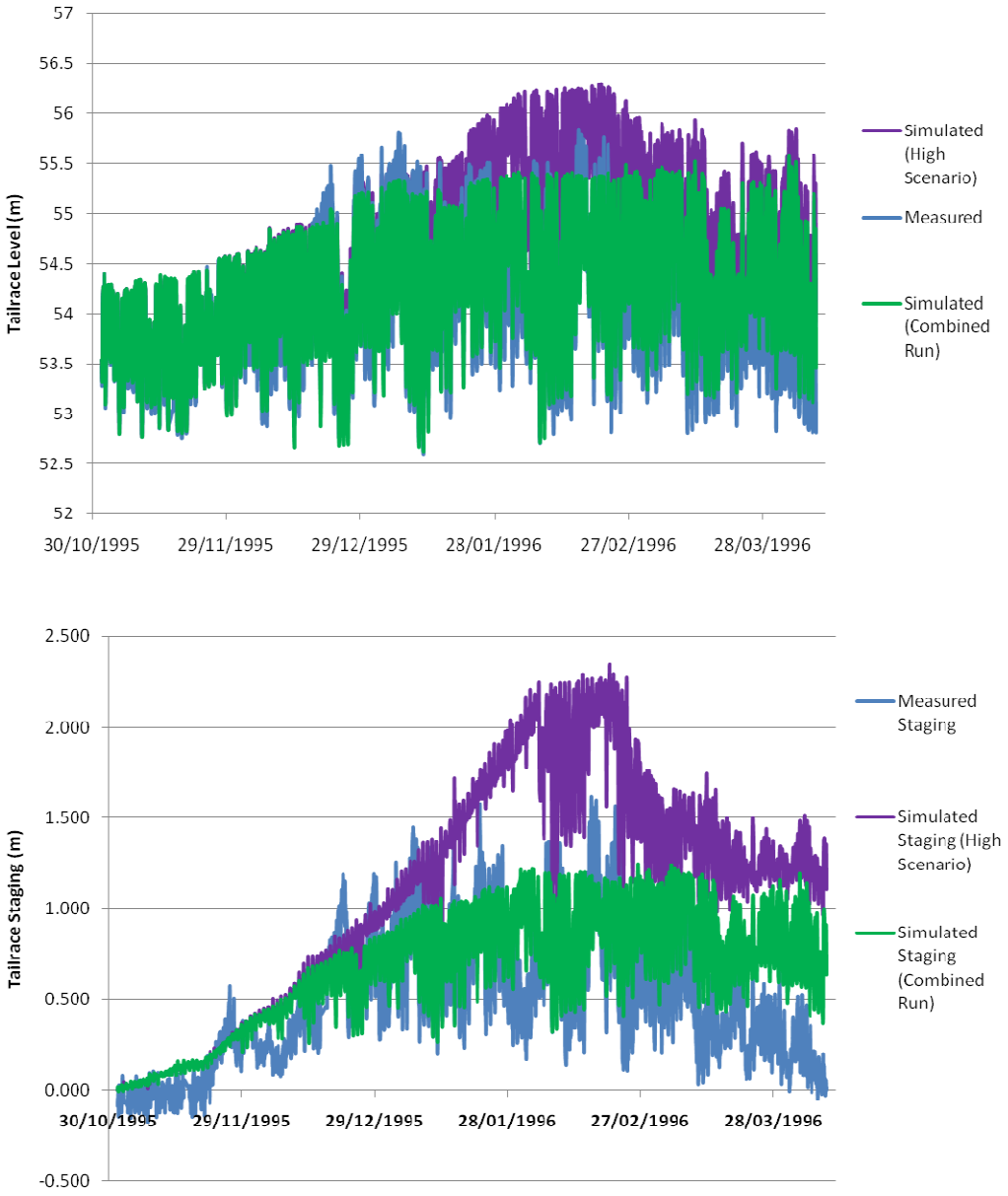


**Figure 5.35 -** 1995-96 tailrace water levels and tailrace staging (combined run).

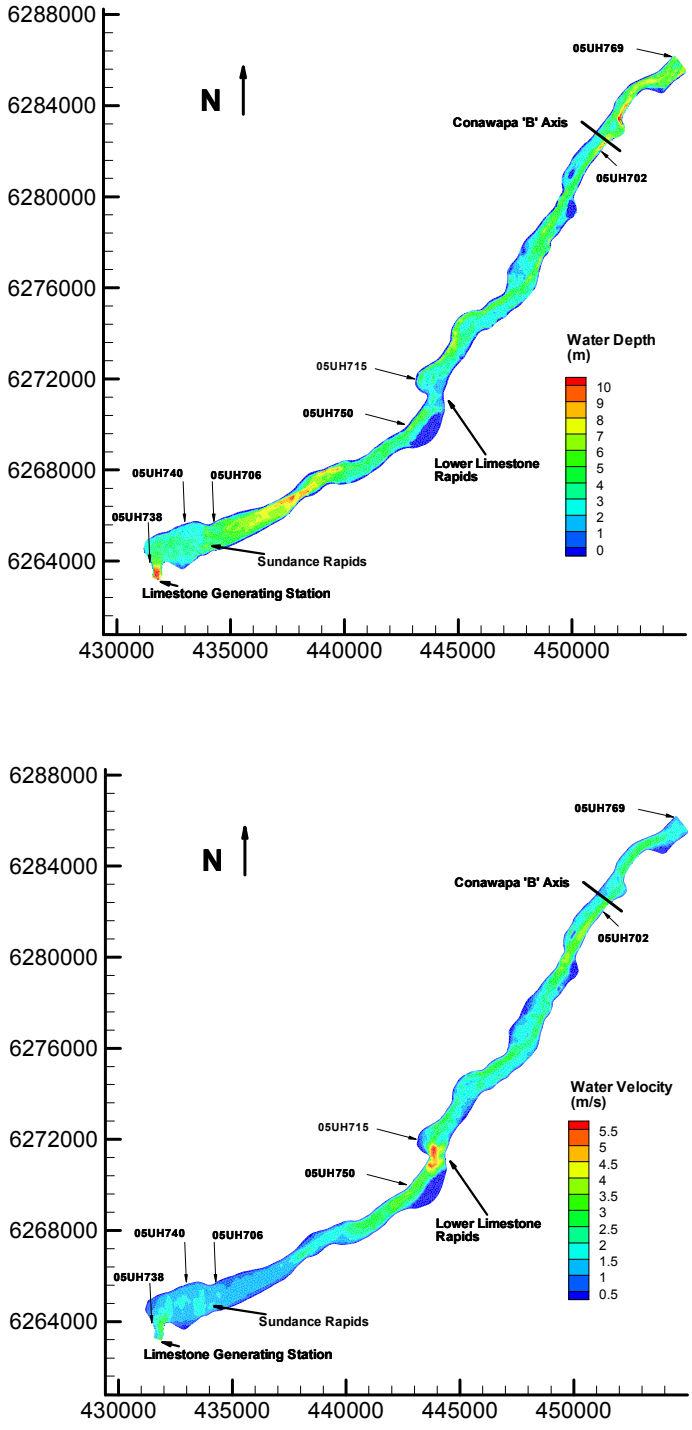


**Figure 5.36 -** Lower Nelson River numerical model extents with water depths and velocities (Q = 6500 cms).

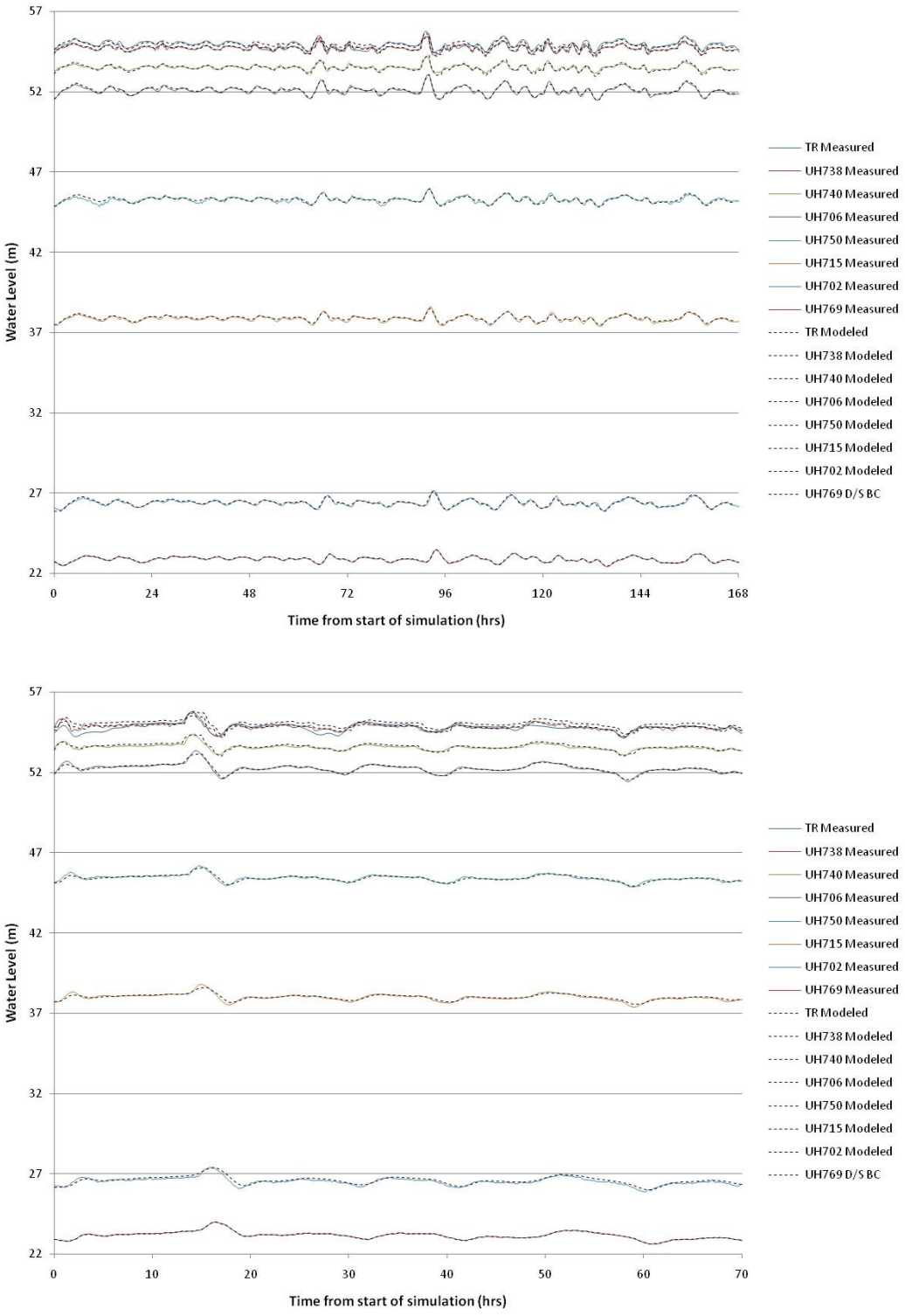


**Figure 5.37 -** Open water calibration (top, August 11-18, 2005) and verification runs (bottom, September 20-22, 2005).

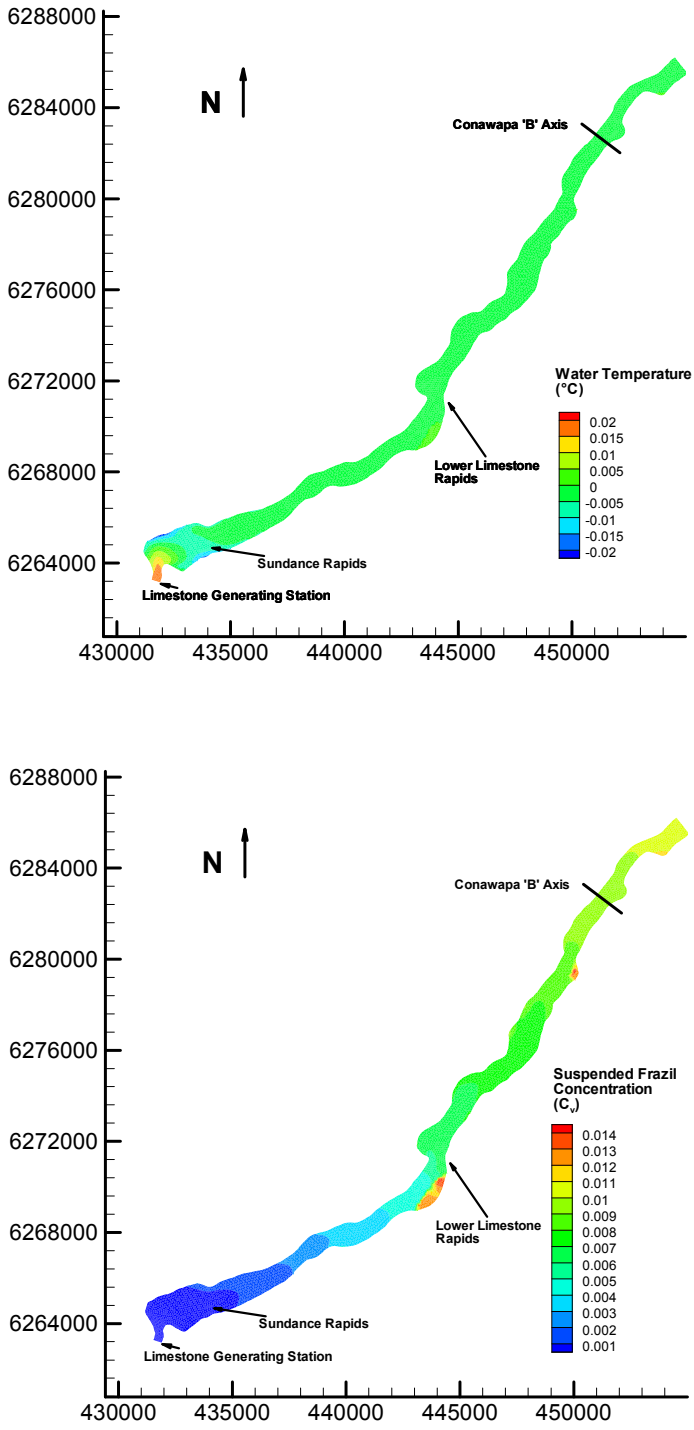


**Figure 5.38 -** Water temperature (top) and suspended frazil concentration (bottom) for March 3, 2006 @ 12:00 pm.

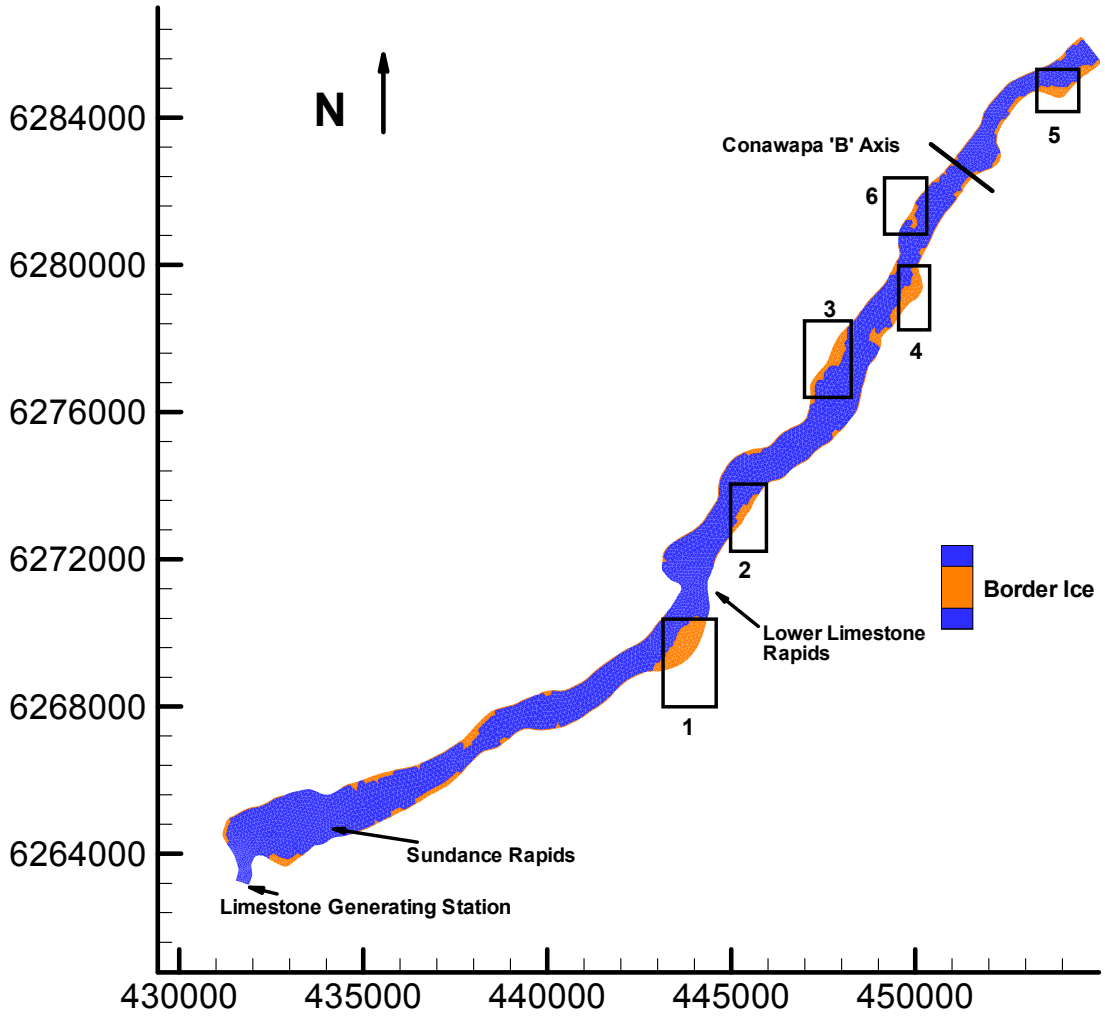


**Figure 5.39 -** Border Ice extents on March 3, 2006 @ 12:00 pm.

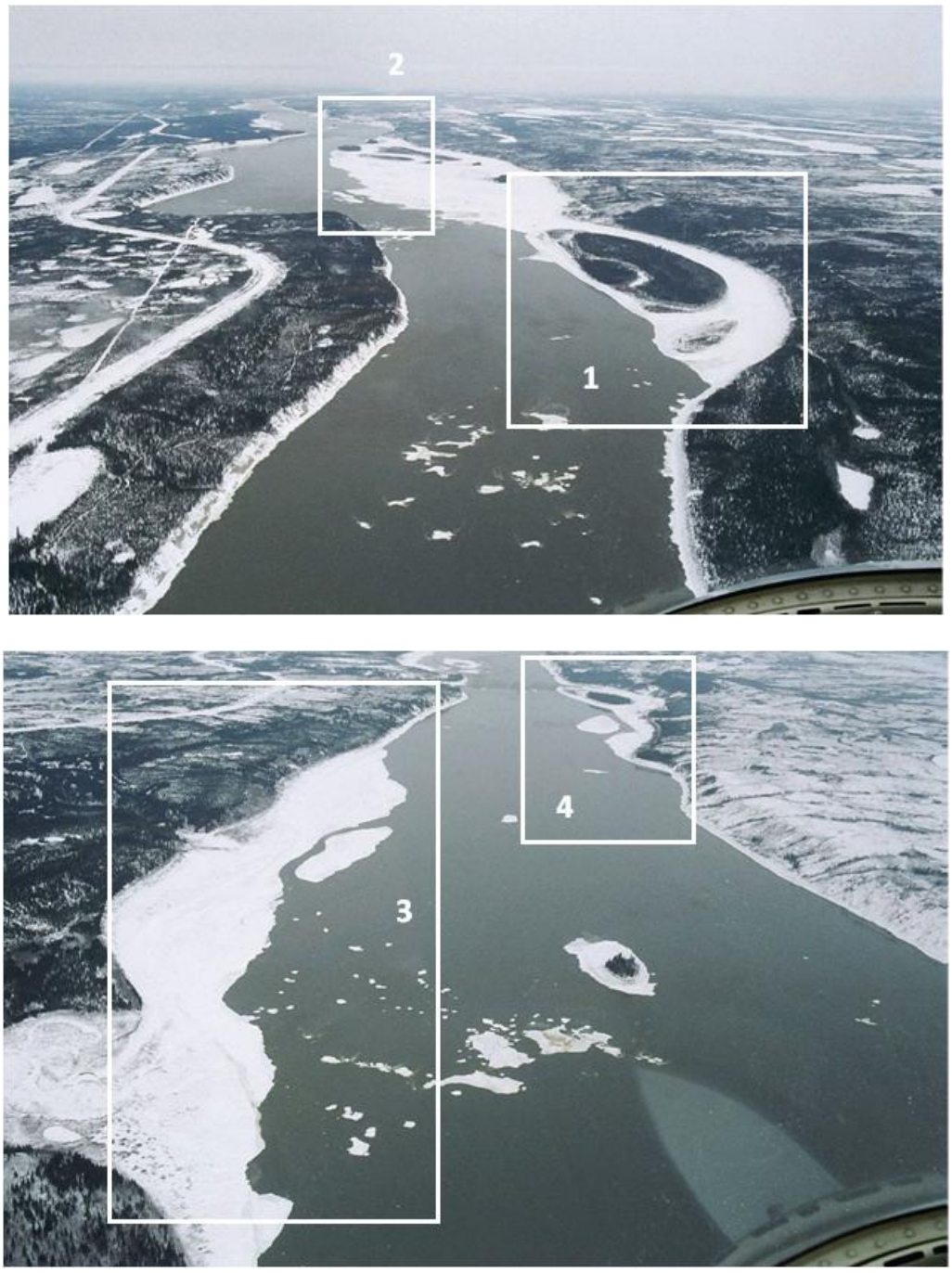


**Figure 5.40 -** Observed Border Ice conditions on March 3, 2006 @ 12:00 pm. Near Lower Limestone Rapids (top) and just downstream of the rapids (bottom).

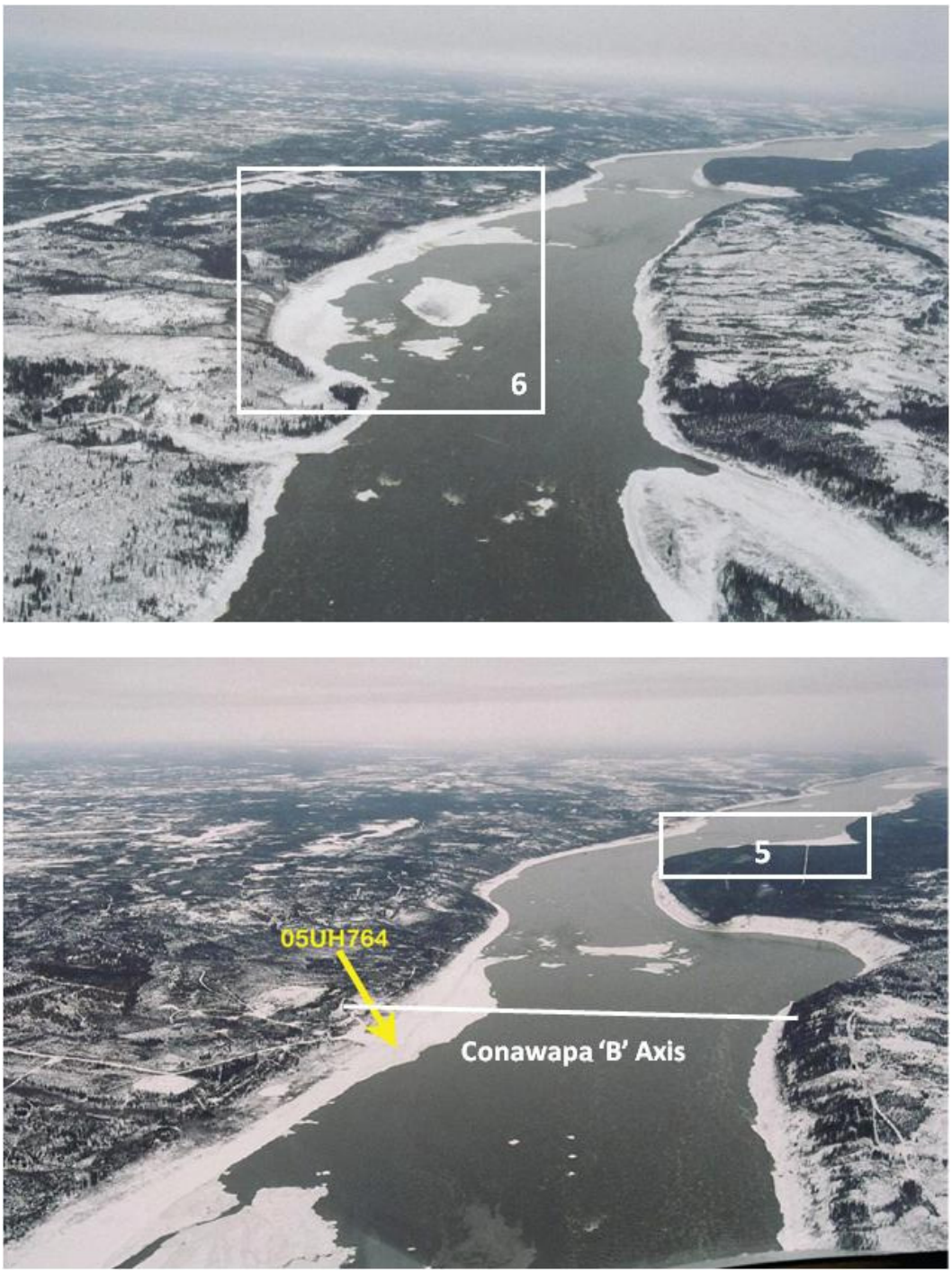


**Figure 5.41 -** Observed Border Ice conditions on March 3, 2006 @ 12:00 pm. Upstream (top) and at the Conawapa "B" axis (bottom).

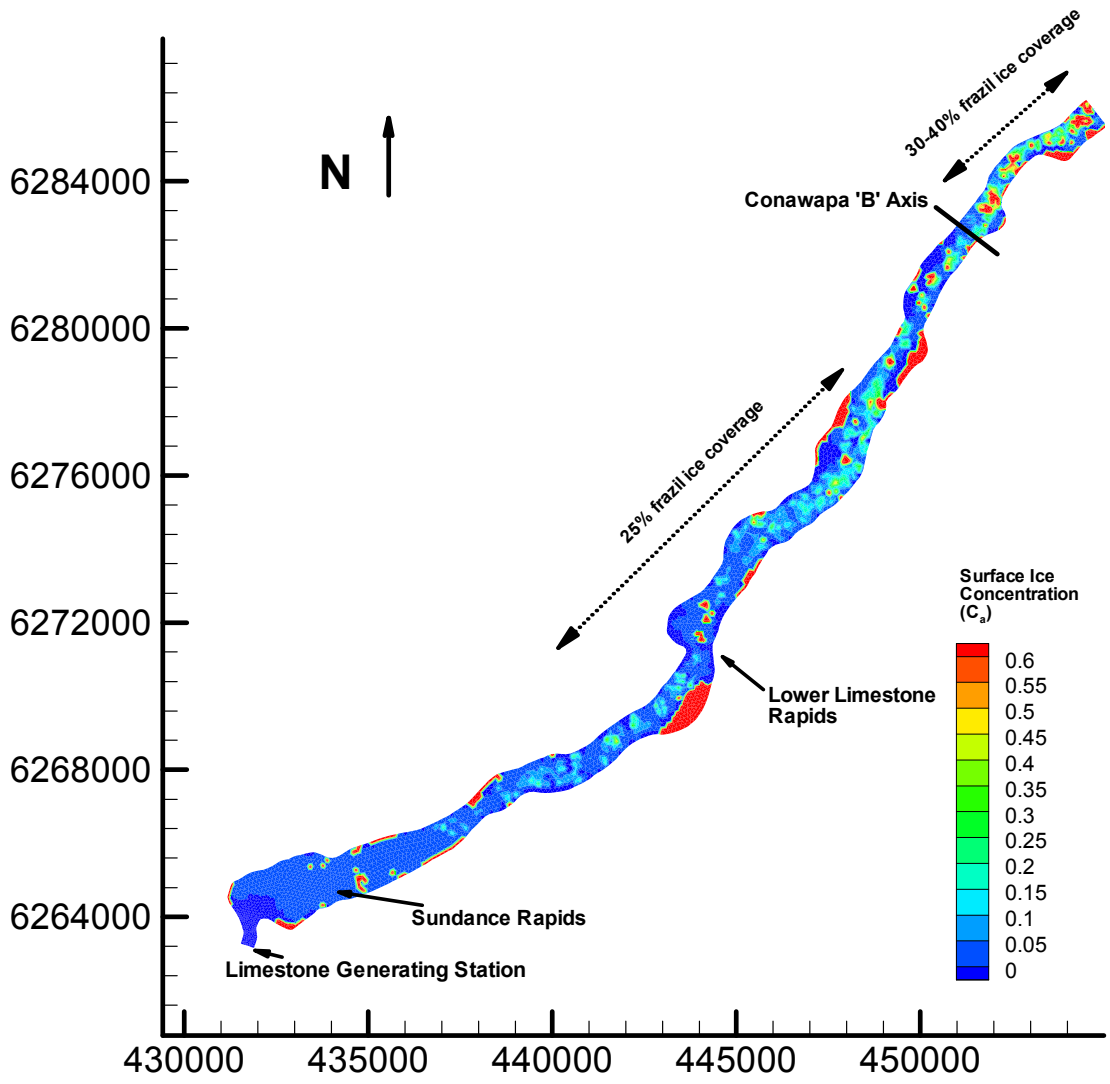


**Figure 5.42 -** Surface Ice concentration contours on March 3, 2006 @ 12:00 pm.

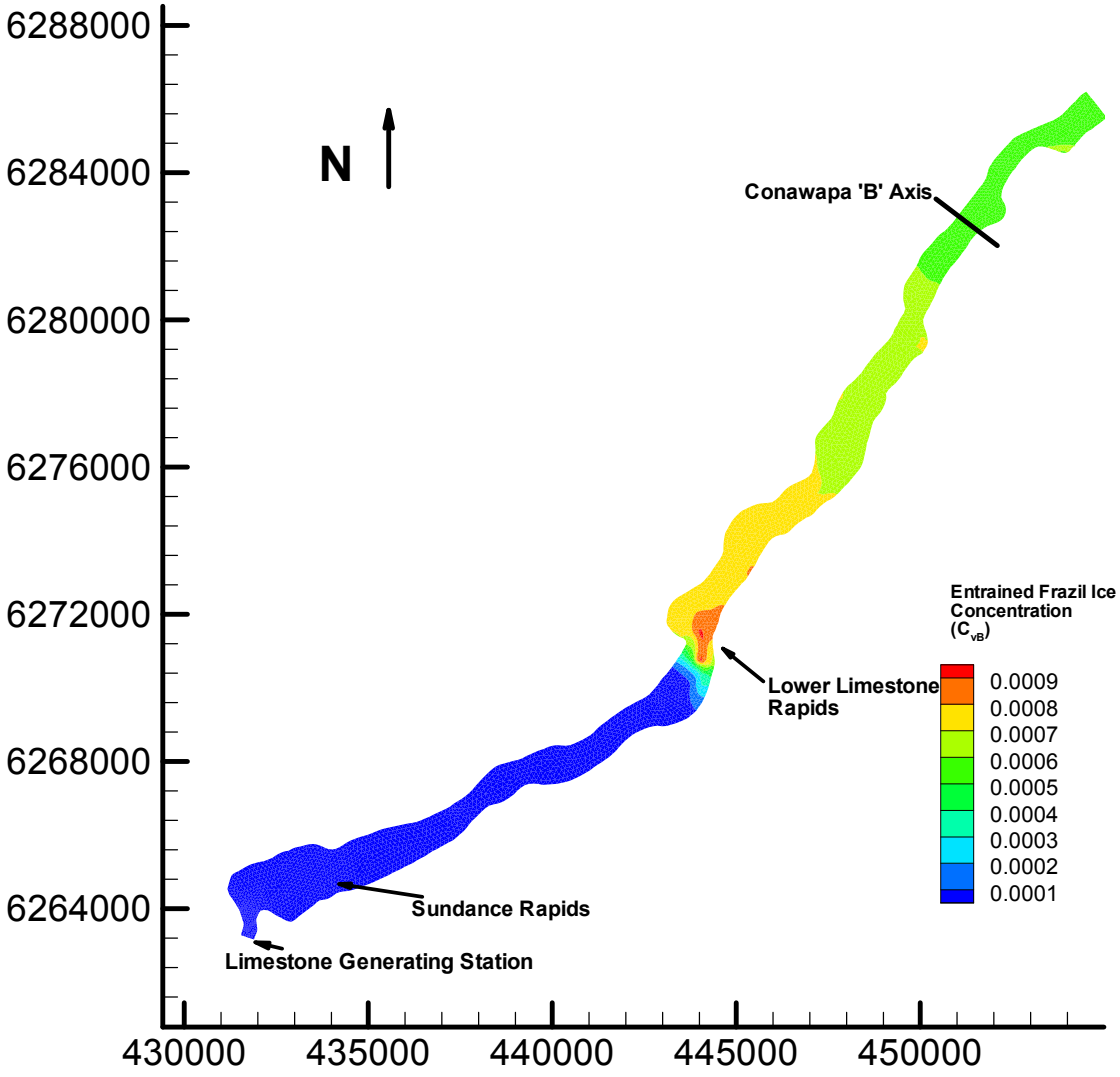


**Figure 5.43 -** Entrained frazil ice concentration on March 3, 2006 @ 12:00 pm.

CHAPTER 6

# Summary and Future Work

## 6.1 Summary and Conclusions

The existence of river ice can have a profound impact on water resources infrastructure development in cold regions of the world. Major engineering concerns related to river ice are ice jam flooding, operation of hydropower facilities, inland navigation passages, water transfers and environmental, ecological, and morphological effects (Shen, 1996). Under turbulent conditions, the formation of a solid ice cover may be suppressed for some time. The continued heat transfer away from the open river water will allow the water to become supercooled and frazil ice particles to form. These frazil particles may stick to underwater objects and produce what is known as anchor ice (Schaefer, 1950; Wigle, 1970; Tsang, 1982). The effects of anchor ice on the hydraulic characteristics of the flow have been well documented (Arden and Wigle, 1972; Parkinson, 1984; Marcotte and Robert, 1986; Yamazaki et al., 1998; Girling and Groeneveld, 1999).

The simulation of the entire river ice process (or portions thereof) using numerical models continues to be the most efficient means of studying river ice and the impacts it has on engineering projects. It should be noted that some river ice phenomenon often cannot be adequately represented by a 1-dimensional numerical model, which is why a 2-dimensional model like the one developed and applied in this thesis must be employed for certain processes. Advancements in the fundamental understanding of these processes as well as in the computational methods used to simulate them require that these models continually be developed in the future.

In this thesis, a literature review of comprehensive river ice models as well as anchor ice and aufeis simulation models was presented along with a summary of field and laboratory studies of these ice formation processes (chapter 1). A high level summary of the complete two-dimensional numerical model was then discussed which included an overview of the computational structure of the CRISSP2D model itself (chapter 2). A coupled sub-model of anchor ice and aufeis growth and evolution was developed for this thesis and the details were presented in chapter 3. Aside from the specific anchor ice and aufeis model components, this model also included developments in the dry bed treatment in the model, additions to the surface ice mass exchange model which included specific treatment of surface ice parcels at a rapids section of the river, and additions to the detailed thermal budget calculation model. Detailed testing of this model was then carried out in an ideal channel setting (chapter 4) and in 2 field case studies on the Nelson River in northern Manitoba, Canada (chapter 5).

From the work completed in this thesis, a few significant summary statements and conclusions can be made regarding the formulation of the model and its ability to model the complex anchor ice and aufeis formation and evolution processes. These processes are often the predominant ice processes in rapids sections of the river and the numerical modeling of these processes is the primary contribution of this thesis. These statements and conclusions are summarized in the following list:

1) A numerical sub-model which includes the anchor ice and aufeis growth processes in detail has been developed and tested in an ideal channel setting. The model includes improved dry bed treatment and a surface ice mass exchange model which incorporates the rapids entrainment process of surface ice.

2) Analysis of ice dam effects for the 1993-2006 period identified many consistencies in the Sundance Rapids ice dam formation each year but did not yield any significant correlation or trends in the ice dam effects on the tailrace water levels which make this case particularly tough to model numerically. This can be attributed primarily to the independency and complexity of the ice processes involved.

3) The model is more successful in capturing the effects of the ice dam during seasons where low to medium staging effects are realized and during seasons dominated by the aufeis growth mechanism. This can be attributed to the possible existence of some residual porosity in the ice dam near the bed material which can

allow for some flow through the ice dam. This can be especially prevalent when the early stages of ice dam formation are dominated by the anchor ice growth process.

4) The model runs that combined the critical bed shear velocity with the varying bed material types in Sundance Rapids were the most successful simulations in capturing the cumulative Megawatt-Hours lost and the cumulative staging throughout the winter. This is because the bed shear velocity criteria helped to dynamically shape the ice dam outcrops slightly as they evolved over the winter.

5) The model is able to simulate the location of the ice dam as well as much of the evolution throughout the winter. The simulated tailrace water levels were not able to capture the full range of variability found in the measured water levels during the same time period and the decay and release process of the ice dam was delayed in the numerical model runs when compared to the field data. This can be attributed partially to the natural variability of the measured water levels and the simplified release mechanisms considered in the model. Evidence suggests other factors such as a bed heat flux and partial release on a daily basis may complicate the ice dam formation and release process as it occurs in nature.

6) Given the numerous driving parameters for ice dam formation at Sundance Rapids and the large amount of variability in the ice dam properties from year to year, the model does a good job of capturing many of the effects of the ice dam on

the tailrace water levels and provides a good basis for future research and model development.

7) When applied to a larger field test case, the model performed well in the areas of border ice formation and surface ice mass exchange processes.

## 6.2 Future Work

The work presented in this thesis has been successful to date and has established some areas for future work and development of the numerical model. Extended from the work and conclusions above, the following future work objectives have been identified:

1) Further laboratory or numerical/physical model study on the functional relationship between the frazil ice accretion rate to the bed ($\gamma$) and the hydrodynamic (and meteorological) variables such as vertical mixing, buoyant velocity of the frazil particles, and the velocity and depth of flow will be useful.

2) The critical bed shear velocity criteria in the anchor ice model are calibration parameters that are a function of local hydraulic characteristics, bottom roughness, and the level of supercooling. Experimental studies in this area to further define these criteria in relation to the driving parameters would be beneficial to the further development of the model.

3) The Sundance Rapids ice dam case study highlights the many complexities of the formation and evolution of the ice dam. Further study on the decay and release of the ice dam including the primary drivers in this process (*i.e.*, solar radiation, bond strength to the bed material, bed heat flux, ice dam porosity, and hydrodynamic drag forces) would be beneficial to the model for this unique application.

4) The assembly and analysis of existing border ice datasets could lead to further model development in this area and an expansion of the simplified model formulations for dynamic and static border ice growth.

# References

Acres Manitoba Limited, 2000. Limestone Ice Mitigation Study. Report submitted to Manitoba Hydro.

Alekseyev, V.R., 1973. Conditions involved in formation and distribution of naleds in southern Yakutia. In Alekseyev, V.R., et al., "Siberian naleds". Draft translation 399, U.S. Army Cold Regions Research and Engineering Laboratory, Hanover, New Hampshire, pp. 43-58.

Alfredsen, K., Stickler, M., and Pennell, C., 2006. Ice formation and breakup in steep streams. Proceedings of the 18th IAHR International Symposium on Ice, Sapporo, Japan, pp. 117-124.

Andersland, O.B., and Ladanyi, B., 2003. Earthwork in cold regions. Frozen Ground Engineering, 2nd edition, Wiley, New York, pp. 230-232.

Anderson, E.R., 1954. Energy budget studies. IN: Water-loss investigations, Lake Hefner Studies, Technical Report, USGS professional paper No. 269.

Andersson, A., and Andersson, L., 1992. Frazil Ice Formation and Adhesion on Trash Racks. Proceedings from the 11th IAHR Symposium on Ice, Banff, Canada, pp. 671-682.

Andrishak, R., and Hicks, F., 2008. Simulating the Effects of Climate Change on the Winter Regime of the Peace River. Canadian Journal of Civil Engineering, Vol. 35, 2008, pp. 461-472.

Arden, R.S., and Wigle, T.E., 1972. Dynamics of Ice Formation in the Upper Niagara River. Proceedings, The Role of Snow and Ice in Hydro, IAHS-UNESCO-WMO, Banff, Alberta, Canada, pp. 1296-1313.

ASCE Task Committee on Hydromechanics of Ice, 1974. River Ice Problems: A state of the art survey and assessment of research needs. Journal of Hydraulic Engineering Division, American Society of Civil Engineers, 100(1), pp. 1-15.

Ashton, G.D., 1980. Freshwater ice growth, motion, and decay. In Dynamics of Snow and Ice Masses (S.C. Colbeck, Ed.), Academic Press, New York, pp. 261-304.

Ashton, G.D., 1982. Theory of Thermal Control and Prevention of Ice in Rivers and Lakes. Advances in Hydroscience. V.13, pp. 131-185.

Ashton, G.D. (editor), 1986. River and lake ice engineering. Water Resources Publications, Littleton, Co.

Barnes, H.T., 1928. Ice Engineering. Renouf Publishing Company, Montreal, Canada.

Beltaos, S., 1993. Numerical Computation of River Ice Jams. Canadian Journal of Civil Engineering, 20(1), pp. 88-99.

Bijeljanin, M., and Clark, S., 2011. Prediction of River Ice Formation on the Upper Nelson River Using Numerical Modeling. 20th Canadian Hydrotechnical Conference, CSCE, Ottawa, Ontario, Canada.

Bisaillon, J., and Bergeron, N., 2009. Modeling anchor ice presence-absence in gravel bed rivers. Cold Regions Science and Technology, 55(2), pp. 195-201.

Bolsenga, S.J., 1978. Preliminary observations on the daily variation of ice albedo. Journal of Glaciology, 18(80), pp. 517-521.

Brady, D.K., Graves, W.L., and Geyer, J.C., 1969. Surface heat exchange at power plant cooling lakes. The Johns Hopkins University, Baltimore, Maryland, USA, Research Project R-P-49, Report no. 5.

Brayall, M., and Hicks, F., 2009. 2-D Modeling of Ice Process on the Hay River NWT. Proceedings from the 15th CRIPE Workshop on River Ice, St. John's, Newfoundland and Labrador, pp. 318-331

Carey, K., 1973. Icings Developed from Surface and Ground Water. CRREL Monograph IIID3.

Carlson, R.F., and Kane, D.L., 1973. Hydraulic influences on aufeis growth. Proceedings of the First Canadian Hydraulics Conference, University of Alberta, Edmonton, Alberta, pp. 165-175.

Carson, R., Beltaos, S., Groeneveld, J., Healy, D., She, Y., Malenchak, J., Morris, M., Saucet, J-P., Kolerski, T., and Shen, H.T., 2011. Comparative Testing of Numerical Models of River Ice Jams. Canadian Journal of Civil Engineering, Manuscript submitted: #10-177

Carstens, T., 1966. Experiments with supercooling and ice formation in supercooled water. Geofysiske Publikasjoner, v. XXVI, pp. 1-18.

Carstens, T., and Lia, L., 1998. Snow and ice blocking of tunnels. Proceedings from the IAHR Symposium on Ice, Potsdam, USA, pp. 85-91.

Daly, S.F., 1991. Frazil ice blockage of intake trash racks. Cold Regions Technical Digest, No. 91-1.

Daly, S.F., 2010. Environmental conditions during frazil ice blockage of a water intake in Lake Michigan, Proceedings of the 20th IAHR International Symposium on Ice, Lahti Finland.

Dingman, S.L., and Assur, A., 1969. The effects of thermal pollution on river ice conditions – Part II, Cold Regions Research and Engineering Lab, U.S. Army, Hanover, N.H.

Doering, J.C., Berkeris, L.E., Morris, M.P., and Girling, W.C., 2001. Laboratory Study of Anchor Ice Growth. Journal of Cold Regions Engineering, ASCE 15 (1), pp. 60-66.

Doganovskiy, A.M., 1973. On participation of naleds in river runoff in upper reaches of Yana and Indigirka rivers. In Alekseyev, V.R., et al., "Siberian naleds". Draft translation 399, U.S. Army Cold Regions Research and Engineering Laboratory, Hanover, New Hampshire, pp. 236-245.

Einstein, H.A., and El-Samni, A., 1949. Hydrodynamic Forces on a Rough Wall, Reviews of Modern Physics, 21(3).

Fischer, H.B., List, E.J., Koh, R.C.Y., Imberger, J., and Brooks, N.H. 1979. Mixing in Inland and Coastal Waters. Academic Press, San Diego, California, USA.

Flato, G.M., and Gerard, R., 1986. Calculation of Ice Jam Profiles. Proceedings of the 4th Workshop on Hydraulics of River Ice, Subcommittee of Hydraulics of Ice Covered Rivers, National Research Council of Canada, Montreal, Quebec, paper C-3.

Foulds, D.M., and Wigle, T.E., 1977. Frazil – the invisible strangler. Journal of the American Waterworks Association, pp. 196-199.

Girling, W.C., and Groeneveld, J., 1999. Anchor Ice Formation Below Limestone Generating Station. Proceedings from the 10th Workshop on River Ice, Winnipeg, Manitoba, Canada, pp. 160-173.

Greene, G.M., 1981. Simulation of Ice-Cover Growth and Decay in One-Dimensional on the Upper St. Lawrence River, NOAA TM ERL GLERL-36, Great Lakes Environmental Laboratory, Ann Arbor, MI. p. 82.

Hammar, L., and Shen, H.T., 1994. Anchor Ice Growth and Frazil Accretion. Proceedings from the 12th IAHR Symposium on Ice, Trondheim, Norway, pp. 1059-1066.

Hammar, L., and Shen, H.T., 1995. Anchor Ice Growth in Channels. Proceedings from the 8th Workshop on the Hydraulics of Ice Covered Rivers, Kamloops, BC, Canada, pp. 77-92.

Hammar, L., Kerr, D.J., Shen H.T. and Liu, L., 1996. Anchor ice formation in gravel-bedded channels. Proceedings of the 13th IAHR International Symposium on Ice, Beijing, China, pp. 843–850.

Haynes, F.D., Haehnel, R.B., and Zabilansky, L.J., 1993. Icing Problems at Corps Projects. Technical Report REMR-HY-10, Waterways Experiment Station, Vicksburg, Mississippi.

Healy, D., and Hicks, F., 1999. Comparison of ICEJAM and RIVJAM Ice Jam Profile Models. Journal of Cold Regions Engineering, 13(4), ASCE, pp. 180-198.

Hicks, F. E., and Steffler, P.M., 1990. Finite Element Modeling of Open Channel Flow. Water Resources Engineering Report No. 90-6. Department of Civil Engineering, University of Alberta, Edmonton, Alberta.

Hicks, F. E., and Steffler P.M., 1992. A Characteristic-Dissipative-Galerkin Scheme for Open Channel Flow. ASCE Journal of Hydraulic Engineering, Vol. 118, No. 2, pp. 337-352.

Hirayama, K., Terada, K., Sato, M., Hirayama, K., Sasmoto, M., and Yamasaki, M., 1997. Field measurements of anchor ice and frazil ice. Proceedings of the 9th CRIPE Workshop on River Ice, Fredericton, New Brunswick, pp. 141-151.

Hu, X., Pollard, W.H., and Lewis, J.E., 1999. Energy exchange during a river icing formation in a subarctic environment, Yukon Territory. Geographie physique et Quaternaire, V.53, N.2. p. 29.

Huusko, A., Greenberg, L., Stickler, M., Linnansaari, T., Nykanen, M., Vehanen, T., Koljonen, S., Louhi, P., and Alfredsen, K., 2007. Life in the ice lane: the winter ecology of stream salmonids. River Research and Applications, 23, pp. 469-491.

Huokuna, M., 1990. The Finnish River Ice Research Project – the Numerical Model in Use. Proceedings from the 10th IAHR Symposium on Ice, Helsinki, Finland, V.3, pp. 215-230.

Jasek, M., Marko, J., and Fissel, D., 2010. Acoustic detection of ice and water velocities on the Peace River during the 2008-2009 winter. Proceedings of the 20th IAHR International Symposium on Ice, Lahti, Finland.

Ji, S., Shen, H.T., Wang, Z., Shen, H.H., and Yue, Q., 2004. Ice Dynamics Model with a Viscoelastic-Plastic Constitutive Law. Proceedings from the 17th IAHR Symposium on Ice, St. Petersburg, Russia, pp. 274-281.

Judge, D., Lavender, S., Carson, R., and Ismail, S., 1997. Headpond Ice Jams – Where will they occur? Proceedings of the 9th Workshop on River Ice, Fredericton, New Brunswick, Canada, pp. 73-87.

Julien, P.Y., 1998. Erosion and Sedimentation. Cambridge University Press, Cambridge, UK.

Kane, D.L., Carlson, R.F., and Bowers, C.E., 1973. Groundwater pore pressures adjacent to subarctic streams. In proceedings, North American Contribution, Second International Permafrost Conference, Yakutsk, USSR, National Academy of Sciences, Washington, D.C. pp. 453-458.

Kane, D.L., 1981. Physical mechanics of aufeis growth. Canadian Journal of Civil Engineering, Vol. 8, pp. 186-195.

Kempema, E., Reimnitz, E., and Barnes, P., 2001. Anchor-ice formation and ice rafting in southwestern Lake Michigan, U.S.A. Journal of Sedimentary Research, V 71(3), pp. 346-354.

Kempema, E.W., Shaha, J.M., and Eisinger, A.J., 2002. Anchor-ice rafting of coarse sediment: observations from the Laramie River, Wyoming, USA. Proceedings of the 16th IAHR Symposium on Ice, Dunedin, New Zealand.

Kempema, E.W., and Konrad, S.K., 2004. Anchor ice and water exchange in the hyporheic zone. Proceedings of the 17th IAHR Symposium on Ice, St. Petersburg, Russia. pp. 251-257.

Kempema, E.W., and Ettema, R., 2009. Variations in anchor-ice crystal morphology related to river flow characteristics. Proceedings of the 15th CRIPE Workshop on River Ice, St. John's Newfoundland, pp. 159-168.

Kennedy, R.E., 1944. Computation of daily insolation energy. Bulletin of the American Meteorlogical Society, V. 30.

Kerr, D.J., Shen, H.T. and Daly, S.F., 1997. Anchor ice formation and growth on gravel channel bed. Proceedings of the 9th CRIPE Workshop on River Ice, Fredericton, New Brunswick, pp. 153-171.

Kerr, D.J., Shen, H.T., and Daly, S.F., 2002. Evolution and Hydraulic Resistance of Anchor Ice on Gravel Bed, Cold Regions Science and Technology, 35, pp. 101-114.

Lal, A.M.W., and Shen, H.T., 1989. An Unsteady Flow Model for the Upper Niagara River. CEE Report 89-12, Clarkson University, Potsdam, New York, USA.

Lal, A.M.W., and Shen, H.T., 1991. Mathematical Model for River Ice Processes. Journal of Hydraulic Engineering, ASCE, 117 (3), pp. 851-867.

Lehtonen, J., 1991. Improvement of icing on main road 21 at Haukijoki, Muotkatakka, Lammaskoski, and Pitkaranta. Construction and monitoring in 1986-1988 (in Finnish). Technical Research Centre of Finland, Research Notes 1218, p. 60.

Li, H., 2005. A Two Dimensional Thermal Ice Model for River Channels. PhD Dissertation, CEE Report 05-02, Clarkson University, Potsdam, New York, USA.

Liu, L., and Shen, H.T., 2003. A Two Dimensional Characteristic Upwind Finite Element Method for Transitional Open Channel Flow. CEE Report 03-04, Clarkson University, Potsdam, New York, USA.

Liu, L., and Shen, H.T., 2005. CRISSP2D Version 1.0 Programmer's Manual. CEE Report 05-19, Clarkson University, Potsdam, New York, USA.

Malenchak, J., Morris, M., and Shen, H.T., 2005. Preliminary Evaluation of CRISSP2D to Model Anchor Ice on the Nelson River. Conference Poster: 13th Workshop on the Hydraulics of Ice Covered Rivers, CRIPE, Hanover, NH, USA.

Malenchak, J., Morris, M., Shen, H.T., and Doering, J., 2006. Modeling Anchor Ice Growth at Sundance Rapids. Proceedings from the 18th IAHR Symposium on Ice, Sapporo, Japan.

Malenchak, J., Morris, M., Shen, H.T., and Doering, J., 2008. Numerical Simulation of Ice Conditions on the Nelson River. Proceedings from the 19th IAHR Symposium on Ice, Vancouver, Canada.

Malenchak, J., Doering, J., and Shen, H.T., 2011. Modeling of Anchor Ice and Aufeis Formation at Sundance Rapids. Proceedings from the 16th CRIPE Workshop on River Ice, Winnipeg, Canada.

Marcotte, N., and Robert, S., 1986. Elementary Mathematical Modeling of Anchor Ice. Proceedings from the 8th IAHR Symposium on Ice, Iowa City, Iowa. pp. 493-506.

Martin, J.L., McCutcheon, S.C., and Schottman, R.W., 1999. Hydrodynamics and transport for water quality modeling. Lewis Publishers.

Matousek, V., 1984. Types of Ice Run and Conditions for their Formation. Proceedings from the IAHR Symposium on Ice, Hamburg, Germany, pp. 315-328.

Matousek, V., 1984a. Regularity of the Freezing-up of the Water Surface and Heat Exchange between Water Body and Water Surface, IAHR Symposium on Ice, Hamburg, Germany, pp. 187-200.

Matousek, V., 1990. Thermal Processes and Ice Formation in Rivers. Papers and Studies No. 180. U.S. Geological Survey Library, Columbia Environmental Research Center, Columbia, MO.

Mellor, M., 1966. Light scattering and particle aggregation in snow-storms. Journal of Glaciology, 6, pp. 237-248.

Michel, B., 1963. Theory of formation and deposit of frazil ice. Proceedings of Eastern Snow Conference, pp. 130-142.

Michel, B., 1967. Morphology of Frazil Ice. Proceedings of the International Conference on Low Temperature Science, Hokkaido University, Sapporo, Japan, pp. 119-128.

Michel, B., 1971. Winter regime of rivers and lakes. Cold Regions Science and Engineering Monograph III-B1a. U.S. Army Cold Regions Research and Engineering Laboratory, p. 131.

Michel, B., 1972. Properties and processes of river and lake ice. In: The Role of Ice and Snow in Hydrology. International Association for Scientific Hydrology, Publication No. 107, Vol.1, pp. 454-481.

Michel, B., Marcotte, N., Fonesca, F., and Rivard, G., 1982. Formation of Border Ice in the St. Anne River. Proceedings of the Workshop on the Hydraulics of Ice Covered Rivers, Edmonton, Alberta, Canada, pp. 38-61.

Miles, T., 1993. A study of border ice growth on the Bruntwood River. M.S. Thesis, Department of Civil Engineering, University of Manitoba.

Morse, B., and Richard, M., 2009. A field study of suspended frazil ice particles. Cold Regions Science and Technology, 55. pp. 86-102.

Newbury, R.W., 1968. Nelson River: A study of subarctic river processes. Ph.D. Thesis, John Hopkins University, Baltimore.

Osterkamp, T., and Gosink, J., 1982. Frazil ice formation and ice cover development in interior Alaska streams. Journal of Cold Regions Science and Technology, V.8, pp. 43-56.

Paily, P.P., Macagno, E.O., and Kennedy, J.K., 1974. Winter-regime thermal response of heated streams. Journal of the Hydraulics Division, ASCE, V. 100, N. HY4, pp. 531-551.

Pariset, R., and Hausser, H., 1961. Formation and Evolution of Ice Covers in Rivers. Transportation Engineering Institute of Canada, 5(1), pp. 41-49.

Parkinson, F.E., 1984. Anchor Ice Effects on Water Levels. Proceedings of the Workshop on the Hydraulics of River Ice, Fredericton, New Brunswick, Canada, pp. 345-370.

Piotrovich, V.V., 1956. Formation of depth-ice. Translated from Priroda, Vol. 9, pp. 94-95, by Defense Research Board, D.S.J.S., Department of National Defence, Canada, T235R.

Petryk, S., 1995. Numerical Modeling. In: River Ice Jams. Water Resources Publication, L.L.C. Colorado, USA.

Petryk, S., Carson, R., Hodgings, D., Parkinson, F., and Beltaos, S., 1990. Development of a Comprehensive Numerical River Ice Model. ASCE Technical Council on Cold Regions Engineering: Monograph – Cold Regions Hydrology and Hydraulics: A State of the Practice Report, pp. 739-760.

Prowse, T.D. and Gridley, N.C., (Eds.) 1993. Environmental aspects of river ice. NHRI Science Report No. 5, Environment Canada, Saskatoon.

Prowse, T.D., 2001. River-ice ecology II: Biological aspects. Journal of Cold Regions Engineering, 15(1), pp. 17-33.

Qu, Y., 2006. A Theoretical and Experimental Study of Anchor Ice. PhD Thesis, Department of Civil Engineering, University of Manitoba.

Qu, Y., and Doering, J., 2007. Laboratory study of anchor ice evolution around rocks and on gravel beds. Canadian Journal of Civil Engineering, 34, pp. 46-55.

Rimsha, V.A. and Donchenko, R.V., 1957. The investigation of heat loss from free water surfaces in wintertime (in Russian), Trudy Leningrad Gosud. Gidrol. Inst., V. 65, pp. 58-83.

Rousseau, Sauve, Warren, Inc., and Hydro-Quebec, 1983. Simulation des conditions de glace en riviere – documentation de programme. Montreal, Quebec, Canada.

Saarelainen, S., and Vaskelainen, J., 1988. Problems of Arctic road construction and maintenance in Finland. Proceedings of 5th International Conference on Permafrost, V.2, Tronheim, Norway, pp. 1466-1491.

Schaefer, V.J., 1950. The Formation of Frazil and Anchor Ice in Cold Water. Transactions of the American Geophysical Union, 31(6), pp. 885-893.

Schohl, G., and Ettema, R., 1986a. Naled Ice Growth. IIHR Report No. 297 – Iowa Institute of Hydraulic Research, Iowa University, Iowa City, Iowa, p. 187.

Schohl, G., and Ettema, R., 1986b. Theory and laboratory study of naled ice growth. Journal of Glaciology, 32(186), pp. 168-177.

Schohl, G., and Ettema, R., 1990. Two-dimensional Spreading and Thickening of Aufeis. Journal of Glaciology, 36(103), pp. 169-178.

She, Y., Hicks, F., Steffler, P., and Healy, D., 2008. Effects of Unsteadiness and Ice Motion on River Ice Jam Profiles. Proceedings from the 19th IAHR Symposium on Ice, Vancouver, Canada, pp. 375-383.

Shen, H.T., 1996. River Ice Processes – State of Research. Proceedings of the 13th IAHR Symposium on Ice, Beijing, China, pp. 825-833.

Shen, H.T., 2002. Comprehensive River Ice Simulation Systems – Task 2 Report. Submitted to CEA Technologies, Inc. (Contract T012700-0401)

Shen, H.T., 2003. Research on River Ice Processes: Progress and Missing Links. Journal of Cold Regions Engineering, ASCE, 17(4), pp. 135-142.

Shen, H.T., 2006. River Ice Processes and Hydraulics. Lecture Notes. Department of Civil and Environmental Engineering, Clarkson University, Potsdam, New York.

Shen, H.T., 2010. Mathematical modeling of river ice processes. Cold Regions Science and Technology, 62, pp. 3-13.

Shen, H.T., Chen, Y.C., Wake, A., and Crissman, R.D., 1993. Lagragian Discrete Parcel Simulation of River Ice Dynamics. International Journal of Offshore and Polar Engineering, 3(4), pp. 328-332.

Shen, H.T., and Chiang, L.A., 1983. Simulation of Growth and Decay of River Ice Cover. Journal of Hydraulic Engineering, ASCE, 110(7), pp. 958-970.

Shen, H.T., Lal, A.M.W., 1986. Growth and decay of river ice covers. Proceedings, Cold Regions Hydrology Symposium, AWRA, Fairbanks, pp. 583‑591.

Shen, H.T., Lal, A.M.W., 1991. Mathematical model for river ice processes. Journal of Hydraulic Engineering, ASCE, 117(3), pp. 851-867.

Shen, H.T., Van DeValk, W.A., 1984. Field investigation of St. Lawrence River hanging ice dams. Proc. IAHR Ice Symposium, Hamburg, pp. 241‑249.

Shen, H.T., Su, J., and Liu, L., 2000. SPH Simulation of River Ice Dynamics. Journal of Computational Physics, 165(2), pp. 752-770.

Shen, H.T., and Wang, D.S., 1995. Undercover Transport and Accumulation of Frazil Granules. Journal of Hydraulic Engineering, ASCE, 120(2), pp. 184-194.

Shen, H.T., Wang, D.S. and Lal, A.M. W., 1995. Numerical Simulation of River Ice Processes. Journal of Cold Regions Engineering, ASCE, 9(3), pp. 107-118.

Shen, H.T., and Yapa, P.D., 1984. Computer Simulation of Ice Cover Formation in the Upper St. Lawrence River. Proceedings from the Workshop on the Hydraulics of River Ice, Fredriction, New Brunswick, pp. 227-246.

Shen, H.T., and Yapa, P.D., 1985. A Unified Degree-Day Method for River Ice Cover Thickness Simulation. Canadian Journal of Civil Engineering, V.12, pp. 54-61.

Simonsen, C.P.S., and Carson, R.W. 1977. Ice Processes During the Construction of Limestone Generating Station. Proceedings from the 3rd National Hydrotechnical Conference, Quebec City, Quebec, p. 19.

Slaughter, C.W., 1990. Aufeis formation and prevention. Cold Regions Hydrology and Hydraulics, American Society of Civil Engineers, New York, pp. 433-458.

Sokolov, B.L., 1978. Regime of naleds: Permafrost: the USSR contribution to the Second International Conference, National Academy of Sciences, pp. 408-411.

Stickler, M., and Alfredsen, K., 2009. Anchor ice formation in streams: a field study. Hydrologic Processes, 23(16), pp. 2307-2315.

Streitz, J.T., and Ettema, R., 2002. Observations from an aufeis windtunnel. Cold Regions Science and Technology, 34, pp. 85-96.

TALAS, 1995. RIVICE Model Documentation: Volume II – Technical Appendices, Report submitted to the River Ice Model Project Steering Committee, November, 1995.

Terada, K., Hirayama, K., and Sasamoto, M., 1998. Field measurement of anchor and frazil ice. Proceedings of the 14th IAHR International Symposium on Ice, Potsdam, New York, pp. 697-702.

Tesaker, E., 1994. Ice Formation in Steep Rivers. Proceedings from the IAHR International Symposium on Ice, Trondheim, Norway, pp. 630-638.

Tetres, 2004. Selection of energy budget coefficients and field data for the lower Nelson River. Report submitted to Manitoba Hydro.

Theriault, I., Saucet, J-P., and Taha, W., 2010. Validation of the Mike-Ice model simulating river flows in presence of ice and forecast of changes to the ice regime of the Romaine river due to hydroelectric project. Proceedings from the 20th IAHR Symposium on Ice, Lahti, Finland.

Tsang, G., 1982. Frazil and Anchor Ice – A Monograph. NRC Subcommittee on Hydraulics of Ice Covered Rivers, Ottawa, Ontario, Canada.

Tsang, G., 1988. Development of Mathematical Modeling for Prediction of River Cooling and Frazil and Anchor Ice Formation. Proceedings from the 5th Workshop on the Hydraulics of River Ice/Ice Jams, Winnipeg, Manitoba, Canada, pp. 393-416.

Tuthill, A.M., Wuebben, J.L., and Gagnon, J.J., 1998. ICETHK User's Manual. CRREL Special Report 98-11, US Army Corps of Engineers, September, 1998.

van Everdingen, R.O., 1982. Management of groundwater discharge for the solution of the icing problems in the Yukon. In: The Roger J.E. Brown Memorial Volume, Proceedings Fourth Canadian Permafrost Conference, National Research Council of Canada, Ottawa, pp. 212-226.

Vinson, T.S., and Lofgren, D., 2003. Denali park access road icing problems and mitigation options. Proceedings of the 8th International Conference on Permafrost. A.A. Balkema, pp. 331-336.

Wang, D.S., and Shen, H.T., 1993. Frazil and anchor ice evolution in rivers. Report 93-09, Department of Civil and Environmental Engineering, Clarkson University, Potsdam, New York.

Wang, D.S., Shen, H.T., Zhu, Q., Huo, S., Li, Z., and Wang, Z., 1996. Simulation and analysis of ice conditions in the lower Yellow River. Proceedings of the IAHR Symposium on Ice, Beijing, China, pp. 721-728.

Wigle, T.E., 1970. Investigations into Frazil, Bottom Ice and Surface Ice Formation in the Niagara River. Proceedings from the IAHR International Symposium on Ice, Reykjavik, Iceland, p.16.

Wojtowicz, A., Hicks, F., Andrishak, R., Brayall, M., Blackburn, J., and Maxwell, J., 2009. 2-D Modeling of Ice Cover Formation Processes on the Athabasca River, AB. Proceedings from the 15th CRIPE Workshop on River Ice, St. John's, Newfoundland and Labrador, pp. 99-117.

Wojtowicz, A., 2010. 2-D Modeling of Freeze-up Processes on the Athabasca River downstream of Fort McMurray, Alberta. MSc Thesis, Department of Civil and Environmental Engineering, University of Alberta, Edmonton, Alberta.

Yamazaki, M., Hirayama, K., Sakai, S., Sasamoto, M., Kiyohara, M., and Takiguchi, H., 1996. Formation of Frazil and Anchor Ice. Proceedings from the IAHR International Symposium on Ice, Beijing, China, pp. 488-496.

Yamazaki, M., Hirai, Y., Hasegawa, K., and Hirayama, K., 1998. Anchor Ice Formation and Discharge Change on a Cold Region River. Proceedings from the IAHR Symposium on Ice, Potsdam, USA, pp. 77-84.

Yu, W.B., Lai, Y.M., Bai, W.L., Zhang, X.F., Zhuang, D.Sh., Li, Q.H., and Wang, J.W., 2005. Icing problems on road in Da Hinggangling forest region and prevention measures. Cold Regions Science and Technology, 42, pp. 79-88.

Zbigniewicz, H., 1997. Lake Winnipeg Regulation Ice Stabilization Program. Proceedings from the 9th Workshop on River Ice, Fredericton, New Brunswick, Canada, pp. 43-53.

Zufelt, J., Daly, S.F., and Gelvin, A., 2009. Observations aufeis formation in Jarvis Creek, Alaska. Proceedings from the 15th CRIPE Workshop on River Ice, St. John's, Newfoundland and Labrador, pp. 169-174.